Dissertation

submitted to the
Combined Faculties for the Natural Sciences and for Mathematics
of the Ruperto-Carola University of Heidelberg, Germany
for the degree of

Doctor of Natural Sciences

put forward by

Diplom-Physiker Marcus Hauser
born in Heidelberg, Germany

Oral examination: 04.07.2011

The Automatic Telescope for Optical Monitoring

Design and implementation of the
instrument control and pipeline analysis software
and
first results from the AGN monitoring program

Referees: Prof. Dr. Stefan Wagner
Prof. Dr. Werner Hofmann

Das Automatische Teleskop für optisches Monitoring

In dieser Dissertation wird die Entwicklung, Integration und die Ergebnisse der ersten Betriebsjahre von **ATOM**, dem **A**utomatischen **T**eleskop für **O**ptisches **M**onitoring, beschrieben. Es ist jetzt eines der weltweit ersten funktionierenden Systeme, welches vollautomatisch Beobachtungen durchführt und dabei selbstständig auf Wetteränderungen reagiert.

Basis dieses Systems ist das 75 cm Teleskop der Landessternwarte Heidelberg. Dieses wurde aufgerüstet und nach Namibia verlegt, um dort Teil des H.E.S.S.-Experiments zu werden. ATOM überwacht für H.E.S.S. tatsächlich oder potentiell im *TeV* Bereich emittierende extragalaktische Ziele (Aktive Galaktische Kerne, AGK) im optischen Spektralbereich, um Langzeitlichtkurven zu erstellen und bei eventuellen Ausbrüchen die Cherenkov-Teleskope zu alarmieren. Dafür wurde eine komplett neu entwickelte Datenreduktionspipeline erstellt, welche die im automatischen Betrieb gewonnen Daten selbstständig analysiert und flusskalibrierte Lichtkurven erstellt.

Alle von Namibia aus beobachtbaren, im Hochenergiebereich detektierten AGK wurden (ebenso wie einige andere AGK) intensiv auf Fluss- und Farbvariationen untersucht, sowie Korrelationen zwischen den ATOM-Beobachtungen und den Messungen des *Fermi*-Satelliten im GeV Bereich bestimmt. Darüber hinaus wurde durch diese Arbeit die Rahmenbedingungen für einen stetig wachsenden photometrischen Katalog von über 200 AGK zur Verfügung gestellt.

The Automatic Telescope for Optical Monitoring

This thesis is presenting the development and commissioning phase as well as results from the first years of operation of **ATOM**, the **A**utomatic **T**elescope for **O**ptical **M**onitoring. It is now one of the worldwide first operational telescope systems that is performing observing runs in a completely automatic way whilst being able to respond to changing weather conditions without any human interaction.

The basis for this system is the 75 cm telescope of Landessternwarte Heidelberg. It was upgraded and relocated to Namibia to be part of the H.E.S.S. experiment. ATOM is now monitoring potential or detected *TeV* emitting extragalactic sources (Active Galactic Nuclei, AGN) for H.E.S.S. in the optical spectral range to create long-term lightcurves and sent alerts in case a source is entering a flaring state. For that purpose, a complete new data reduction pipeline was developed. This pipeline is analysing the images recorded by ATOM and is producing flux calibrated lightcurves in an automatic way

All *TeV*-detected AGN, which are observable from Namibia, have been studied for flux and color changes (as well as some other AGN). For some sources, potential correlations between ATOM observations and measurements in the *GeV* energy range performed by the *Fermi* satellite have been investigated. Furthermore, this work is providing the framework for an increasing photometric catalog consisting of more than 200 AGN.

Contents

1. Introduction

This thesis is about the development of the *Automatic Telescope for Optical Monitoring* (ATOM), a project which consists of transforming a 30 year old telescope, sitting in an not operational condition at Landessternwarte Heidelberg, into a fully automatic telescope running in Namibia, monitoring a large list of Active Galactic Nuclei for activity and producing long term monitoring lightcurves. I will describe the developed soft- and hardware for this project, its operation procedures and present some of the results found in the first years of operation. But the starting point should be an introduction to the astrophysical objects, which are the reason for all this intellectual and instrumental effort.

The layout of this thesis is the following: in this first chapter, I will introduce the scientific objects under investigation with ATOM and briefly present the organizational environment of this project.

Chapter 2 consists mainly of hardware description, where the main emphasis will be on the instrument, which was designed by me and not on the telescope itself (my own contribution to the pure telescope refurbishment was mostly limited to organizational and administrative support and participation in testing procedures).

Chapter 3 is devoted to my testing of CCD cameras, the tests applied to select the best camera system for ATOM and the performance tests in the preparatory phase before commissioning ATOM in Namibia.

The operation mode of the telescope system now in production is described briefly in chapter 4, and the automatic data analysis pipeline is described in detail in chapter 5.

The remaining chapters are describing scientific applications of the data taken with ATOM; first atmospheric extinction measurements and their correlation with H.E.S.S. parameters (chapter 6), and secondly the behavior of Active Galactic Nuclei in chapter 7.

The thesis is closed with the summary and outlook chapter 8 and an appendix holding supplementary material.

1.1. Active Galactic Nuclei

The main targets for observation by ATOM are extragalactic objects called *Active Galactic Nuclei* (AGN). These objects are located at the center of a galaxy, a compact region which emits a much higher luminosity than normal galaxies at at least some or even all parts of the electromagnetic spectrum. A galaxy which hosts an AGN is called *active galaxy*. Many of them are showing a *jet*, originating in the central compact region and extending into intergalactic space.

The luminosity is believed to be produced by accretion of matter onto a supermassive black hole at its center. By today's knowledge, AGN are the most luminous persistent sources of electromagnetic radiation in the universe[1] and therefore detectable up to high

[1] A gamma-ray burst (GRB) is on average more luminous, but is only a burst and has a lifetime of

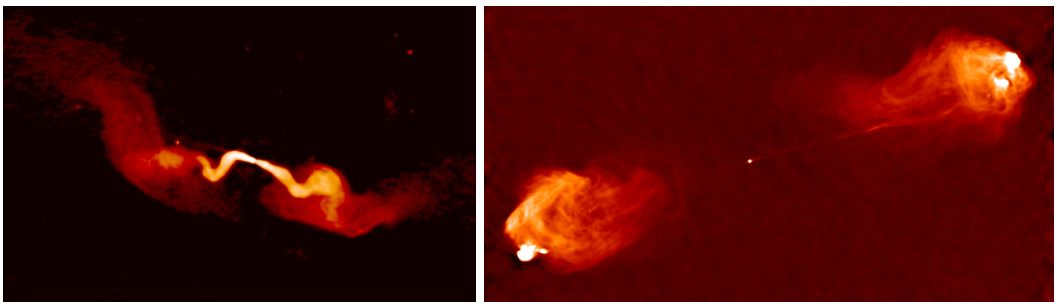

Figure 1.1.: Radio maps showing two different types of radio galaxies. *left:* 3C 31 (NGC 383) as an example for an *Fanaroff-Riley type I* radio galaxy. Note that the most luminosity is coming from the jet at the inner part of the extended object. *right:* Cygnus A, an example for a *Fanaroff-Riley type II* galaxy with its significant lobes at the end of the jet. *(Image courtesy of NRAO/AUI)*

redshifts.

1.1.1. Observational appearance

The universe presents AGN in very different observational fashions to us. Some have huge jets, some don't. Some are bright in only some wavelength regimes, others are luminous from radio to VHE energies. One can start to organize this so called **AGN zoo** by its radio features:

radio quiet AGN are bright in visible part of the electromagnetic spectra, whereas the luminosity in radio is negligible compared to the higher frequencies. The discrimination between radio quiet and radio loud is done by the flux ratio between radio and optical band, so radio quiet is defined as $F_{5\,Ghz}/F_{440\,nm} \lesssim 10$ (Kellermann et al. (1989), Urry and Padovani (1995)).

Subclasses are the

QSO, or *Quasi Stellar Objects*, which were first believed to be stars due to their point-like morphology. They were found to be something different than stars when one started to look at their spectra, which are dominated by a strong continuum emission (optical, sometimes extending to the x-ray regime), overlaid by narrow and broad optical emission lines. Their (in some cases later found) host galaxies can be of any type of the Hubble sequence.

Seyfert Galaxies are nearly always Spiral or Irregular Galaxies. They are showing strong continuum emission from the galactic nucleus. Further subdivision into *type I* or *type II Seyfert galaxies* is done by the presence or absence of broad emission lines.

radio-loud AGN are typically hosted by elliptical galaxies. Their radio emission from jet-related emission regions is dominating the overall radio luminosity and in some cases also the total energy emission. Subclasses are

$\lesssim$ days, whereas AGN are emitting over cosmological timescales.

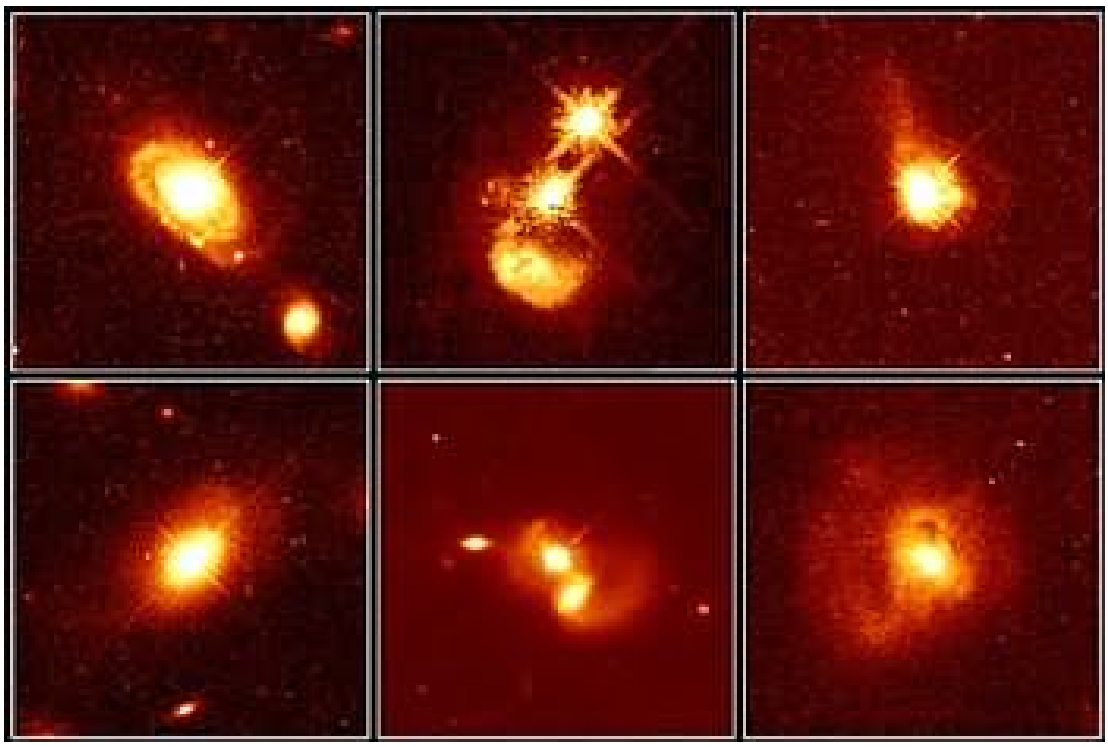

Figure 1.2.: Collection of HST images of quasars hosted by galaxies of different type. *(Image credit: Bahcall et al., STScI/NASA, 1996)*

Radio galaxies, which are emitting radio energy not only from the central region, but also from the outer parts of the galaxy. Further sub-classes were suggested by Fanaroff and Riley (1974) after studying a sample of 57 radio galaxies from the 3C catalog (Bennett (1962)). The authors divided their sample into *type I* and *type II* sources, depending whether most of the radio luminosity is coming from the jet near to the central object, or from radio lobes further out (see fig. 1.1 for an example).

Quasars are more-or-less QSOs emitting also at radio frequencies. They are extremely luminous (up to 10^{48}erg/s), and their spectrum consists of a strong continuum in the optical, overlaid with broad and narrow emission lines. They are embedded in host galaxies of any type of the Hubble sequence, but ellipticals are dominant (examples given in fig 1.2). Further sub-classification can be done by separating this type of AGN by their spectral index (radio wavelength) into *flat spectrum radio quasars* (FSRQ) or *steep spectrum radio quasars* (SSRQ), with the dividing line at $\alpha_r = 0.5$ (Urry and Padovani (1995)).

Blazars are the most enigmatic incarnation of AGN. Their optical spectrum is nearly featureless, no spectral lines are visible. The redshift / cosmological distance of these kind of objects can therefore only be determined if one is able to measure spectral lines of the host galaxy, but for many of these sources no host galaxy has been detected yet. If a host galaxy is detected,

it has always been an elliptical one. Most of these sources are showing flux variability on all timescales and wavelengths.

1.1.2. Physical model

Despite the very different observable appearance of these powerful extragalactic objects (emitting at luminosities of up to 10^{45-49} erg/s), astronomers came up with ideas of a common physical model for these kind of objects. The nowadays widely-accepted unified model was presented in Urry and Padovani (1995): the model describes an AGN as a supermassive black hole (SMBH) of $10^{6-8} M_{\odot}$, surrounded by an accretion disk and an optically thick torus. The SMBH is emitting a *jet* perpendicular to the disk/torus plane, which is surrounded by two kinds of matter blobs, emitting the narrow line and broad line emission seen in some type of AGN. The different observational incarnations of AGN are then explained by different viewing angles onto the black hole (BH) (see fig. 1.3). The main target for ATOM monitoring, blazars, are for example AGN where the observer is looking at (very) low angles ($< 15°$) directly into the jet.

Non-thermal emission in blazars

The spectral energy distribution (SED) of blazars is showing a double-hump structure (see figure 1.4). The two humps, one peaking in the optical/UV/x-ray regime, the other one in the MeV-GeV part of the spectrum, are typically described using a *synchrotron self Compton* (SSC) scenario (see e.g. Maraschi et al. (1992), Tavecchio et al. (1998) or Fossati et al. (1998)).

The idea of these models is that electrons, being accelerated in the magnetic field of the AGN, emit synchrotron radiation. This synchrotron radiation is observed as the low-energy hump. The high-energy hump is caused by the low energy synchrotron photons being upscattered by the highly relativistic electrons via *inverse Compton scattering*, thus reaching energies up to the TeV range.

A slightly different model to SSC is the *external Compton* (EC) model, where the to-be upscattered photons do not come from the synchrotron emission, but from an external photon field (e.g. from thermal emission from the accretion disk), see e.g. Dermer and Schlickeiser (1993).

A different approach to explain the SED is done by *hadronic models*, where the high energy hump of the SED is created by protons accelerated to VHE energies. These can produce VHE photons via π^0 decay (Pohl and Schlickeiser (2000)). The high energy hump can also be explained by synchrotron radiation of relativistic protons. In these scenarios, the low energy hump is often still explained by synchrotron emitting electrons (Mannheim et al. (1991), Mannheim and Biermann (1992), Mücke et al. (2003)).

1.2. Multiwavelength observations

Today, it is unclear which of the models described in sec. 1.1.2 represents nature best. Some observations can be described with one or multi-zone SSC models, other with hadronic models or even both. The key to understanding is more simultaneous data, sampling both the low and high energy hump at the same time. Each model is making

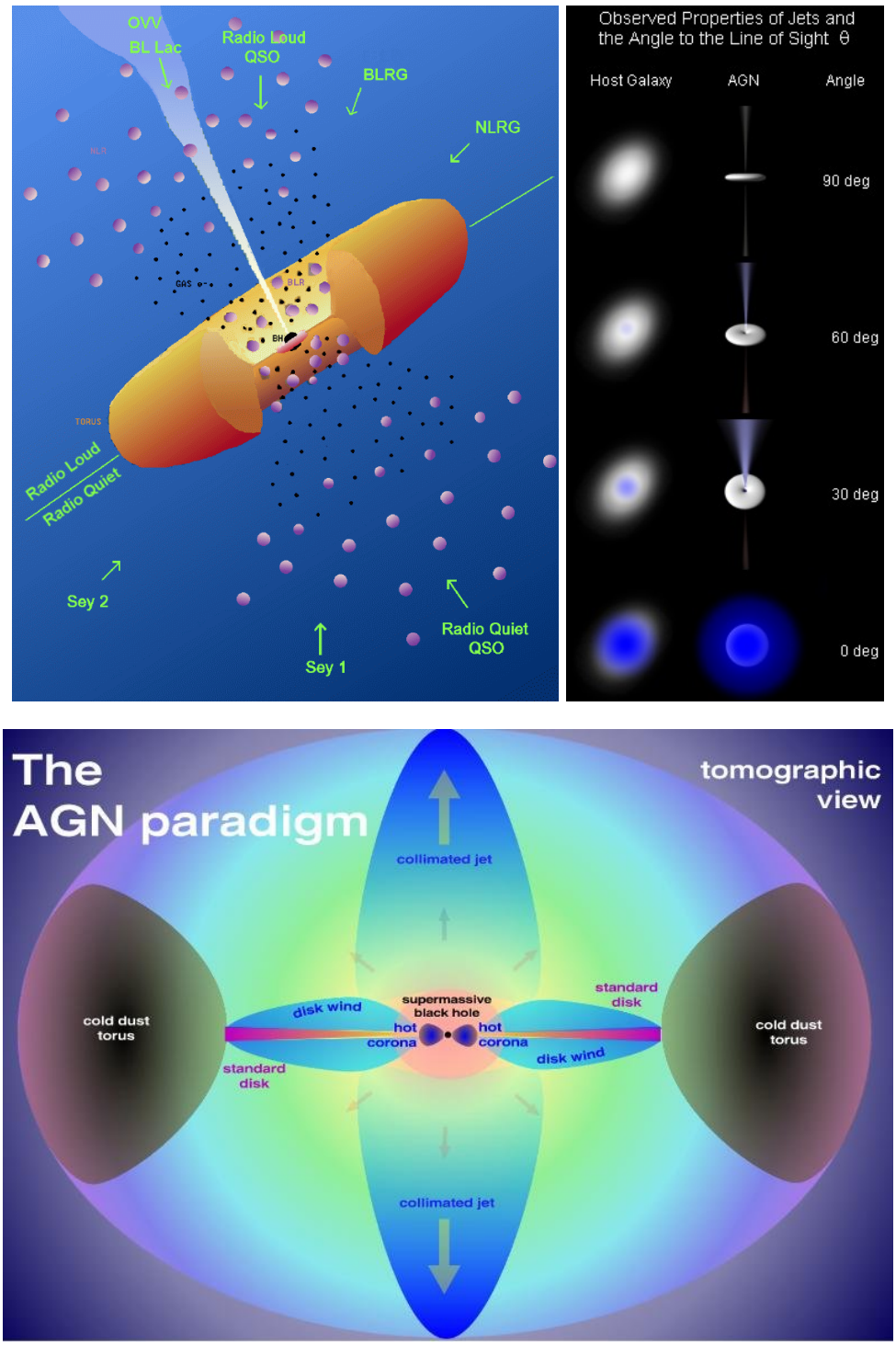

Figure 1.3.: Schematic sketch of the unified model of AGN. The central object is a SMBH, surrounded by a hot corona, standard disk and a cold dust torus. The jet is ejected perpendicular to the other components. The different observational incarnations of AGN can be explained by different viewing angles onto the AGN and therefore shading/ non-shading of the hot inner parts.
Image credit: Beppo SAX calendar 1999 and Ron Kollgaard (Wikipedia) (top), Müller (2005, fig. 4.1)(bottom)

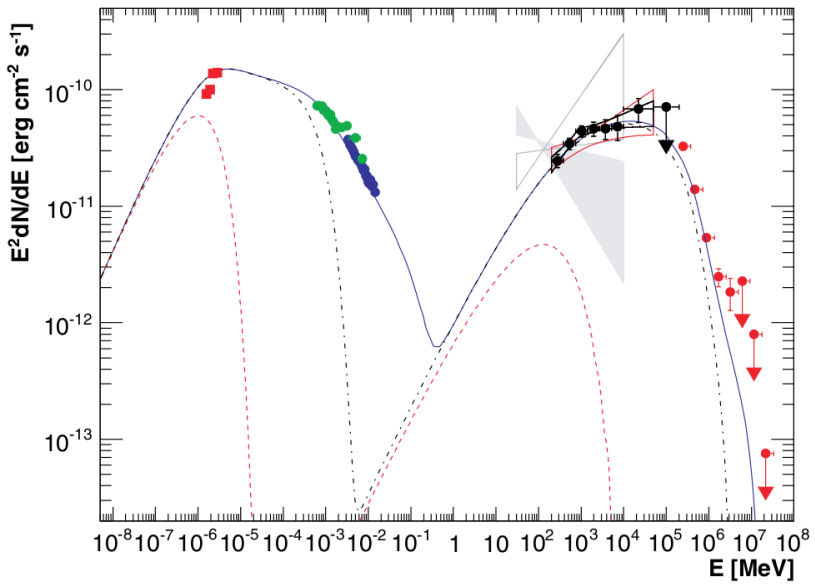

Figure 1.4.: Example of an blazar SED: the points are measurements of different instruments, covering over 14 orders of magnitude in energy. The characteristic two-hump structure is clearly visible. The lines represent different components of an SSC model tuned to describe this dataset. (SED first published in Aharonian et al. (2009), optical points provided by ATOM, VHE points by H.E.S.S.)

different predictions about the peak position and the ratio between the low and high energy hump.

Also long term monitoring can help to understand these sources, if variability is detected. For example, a flare in the low energy hump (e.g. detected in optical wavelength) is in the SSC scenario assumed to be followed by an increase in the high energy regime. To detect such flares, a dedicated monitoring telescope, concentrating on blazars, is desirable. Such a system is introduced in section 2 and described in the rest of this thesis.

Figure 1.5.: The H.E.S.S. telescopes

1.3. The H.E.S.S. experiment

ATOM is part of the *High Energy Stereoscopic System* (H.E.S.S.) experiment. It is one of the mayor *Imaging Atmospheric Cherenkov Telescope arrays* (IACT) of the world, sensitive to cosmic electromagnetic radiation in the energy range between 100 GeV to 100 TeV ($10^{11} - 10^{14}\,eV$, very high energy (VHE)). The telescopes are located in Namibia (southern Africa), in the Khomas highlands, in the vicinity of the Gamsberg[2]. A detailed description of this experiment can be found in e.g. Hinton (2004) and Aharonian et al. (2006).

H.E.S.S. is operated by a collaboration of $\approx$ 200 scientists from different European countries.

1.3.1. Technical description

The exact geographical position of the experiment is 16°30′10” E, 23°16′22.1” S at 1800m a.s.l. on Farm Goellschau (see figure 1.6). The site is equipped with 4 identical telescopes (see figure 1.5 and 1.6), positioned on a square grid with the neighboring telescopes being separated by $\approx$ 120 m. The first telescope started observations in 2002, whilst the full array is operational since December 2003. At present time, a fifth telescope is under construction. This telescope, being much larger than the operational four, will improve the sensitivity of the H.E.S.S. experiment and extend the accessible energy range to lower energies.

[2]The Gambsberg and the adjacent Hakos mountains are well known for excellent astronomical weather conditions for most time of the year.

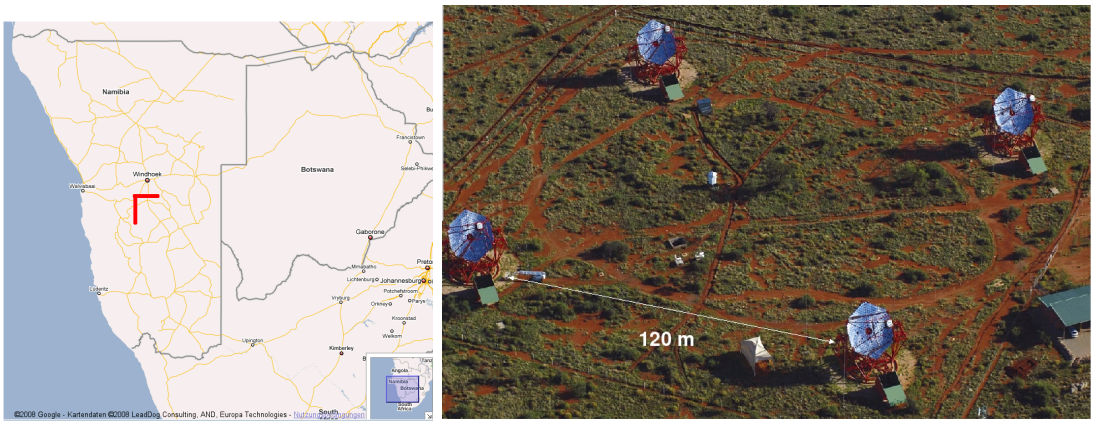

Figure 1.6.: *left:* map of south-west Africa (taken from Google maps). The location of H.E.S.S. and ATOM is marked by the red bars. *right:* A bird’s eye view of the H.E.S.S. telescopes.

The telescope bodies are constructed on a steel space frame structure, with the dishes being 13 m in diameter. Each telescope dish is equipped with 382 round mirrors (60 cm diameter each), forming a segmented main mirror with 15 m focal length and a f/d ratio of 0.8. The total mirror surface per telescope is $108m^2$.

The cameras are located at the prime focus of the telescopes. Each camera detects light using 960 photo multiplier tubes (PMT) and images a field-of-view (FoV) on the sky of about 5° in diameter. The cameras have an individual mass of ≈ 800 kg and a dimension of 1.6 m diameter and 1.5 m length.

1.3.2. IACT observing techniques

VHE photons cannot be detected directly on the surface of Earth, since they are absorbed by the atmosphere. This absorption process takes place in the upper atmosphere, were the primary photon interacts with atmospheric nuclei and creates a particle cascade though pair production and bremsstrahlung, until the energy of the secondary γ-rays drops below the rest mass of the resulting electron-positron pair ($E < 2 * m_e c^2 = 2 * 511\,\text{keV} = 1.022\,\text{MeV}$). As long as the created particles are moving at local superluminal velocity in the atmosphere, they emit Cerenkov light. The maximum of Cerenkov light is created at an altitude of ≈ 10 km.

This light pool travels towards the Earths surface in form of a very short (order of ns) flash of a blue light cone. Based on the recorded light distribution in the cameras, the energy and direction of the primary VHE photon can be computed. If the shower is recorded by more than one telescope, the direction of the shower can be determined much more accurate than using only one telescope (that is why it is called *High Energy Stereoscopic System*). A schematic view of this process is given in figure 1.7 and a detailed explanation can be found in e.g. Aharonian et al. (2006).

1.3.3. Atmospheric influences on H.E.S.S. measurements

With the atmosphere being an essential part of the whole detection process, it is important to know –or being able to make useful assumptions about– its influence on the particle shower and the light travel. This is mainly done by comparing the recorded light distribution with Monte-Carlo models of shower evolvement in the atmosphere (Bernlöhr (2000), Bernlöhr (2008)). Fine-tuning of these models could be done by including atmospheric transparency measurements that were acquired simultaneously to the TeV data. One possibility are simultaneous LIDAR measurements, another one is the classical (optical) astronomical atmospheric extinction determination. The latter one is described in section 6.

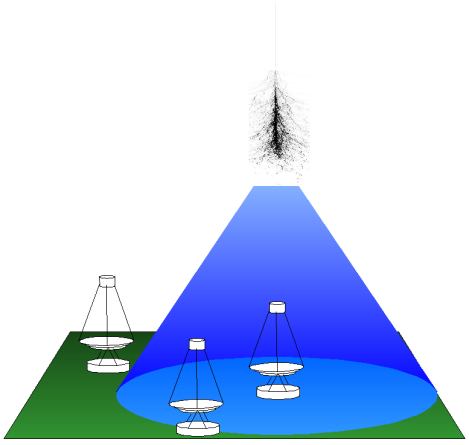

Figure 1.7.: Schematic view about recording of a VHE photon introduced particle shower. The shower starts to evolve in $\approx$ 10 km altitude, the resulting Cherenkov light cone is about 100 m wide when reaching the H.E.S.S. telescopes at 1800 m a.s.l.

2. Automatic Telescope for Optical Monitoring

2.1. Project goal

As pointed out in the previous chapter (1.1.2), simultaneous multiwavelength observations are crucial for the understanding of AGN physics. The best possibility to get optical measurements simultaneously to the VHE measurements by the H.E.S.S. telescopes is obviously an optical telescope completely assigned to and operated by the H.E.S.S. collaboration itself. Placing the VHE and optical telescopes on the same site eliminates the risk that simultaneous optical-TeV measurements fail because of bad weather at one of the (different) telescope sites or different observing windows because of different geographical positions introduce time lags in observations.

In addition to AGN physics, atmospheric extinction measurements by an optical telescope located next to the IACTs could probably help to calibrate the shower images recorded by the IACT cameras.

2.2. Telescope

Figure 2.1.: Images of ATOM at the H.E.S.S. site in Namibia.

The telescope was build by *Zeiss* as a prototype for an computer controlled azimuthal telescope mount in the late 1970s. It was operated for several decades at Landessternwarte Heidelberg[1] and used for many astronomical projects.

[1] http;//www.lsw.uni-heidelberg.de

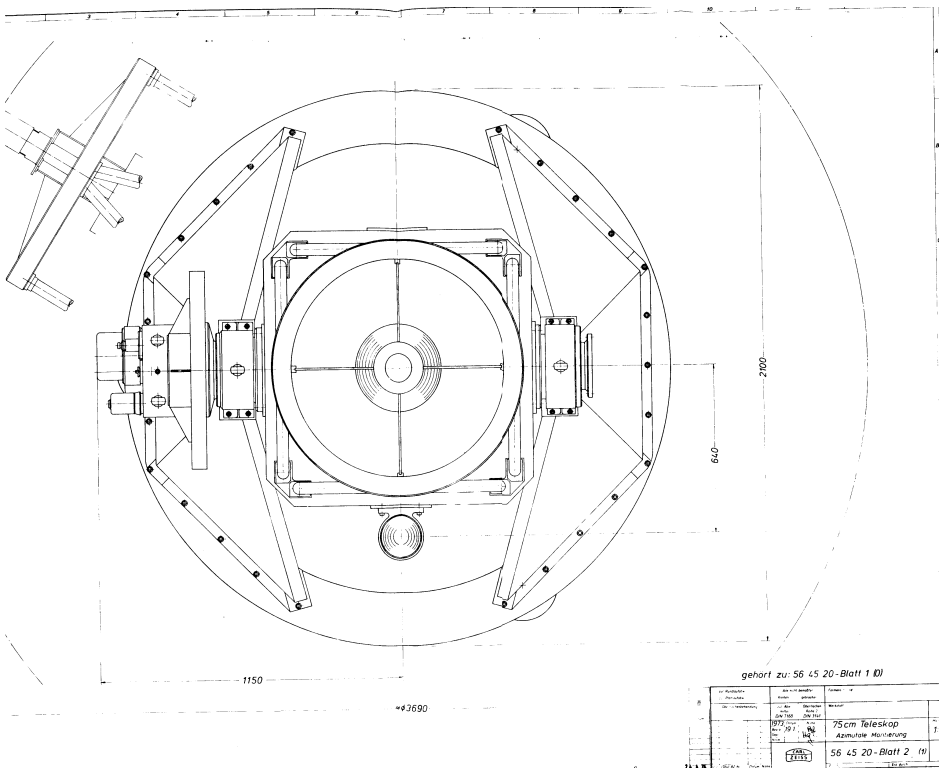

Figure 2.2.: mechanical drawing of ATOM, view from above

Its main mirror has a diameter of 75cm, the focal length of the optical system is 600 cm. The main technical data of ATOM can be found in table 2.1, mechanical drawings in figure 2.3 and 2.2.

Only small mechanical modification were applied to the telescope for the robotic mode (mainly the motorized mirror cover and some sensors for hydraulic pressure), whereas the old and not operational electronic control components were rebuild from scratch at Hamburger Sternwarte[2]. The mirrors were re-coated in summer 2005, just before shipping the telescope to Namibia.

The telescope control software `telops`[3] is not part of this PhD thesis, but was developed by H.-J. Hagen (Hamburger Sternwarte). A description can be found in the ATOM user manual (Hauser (2006)).

[2] http://www.hs.uni-hamburg.de
[3] telescope operating system

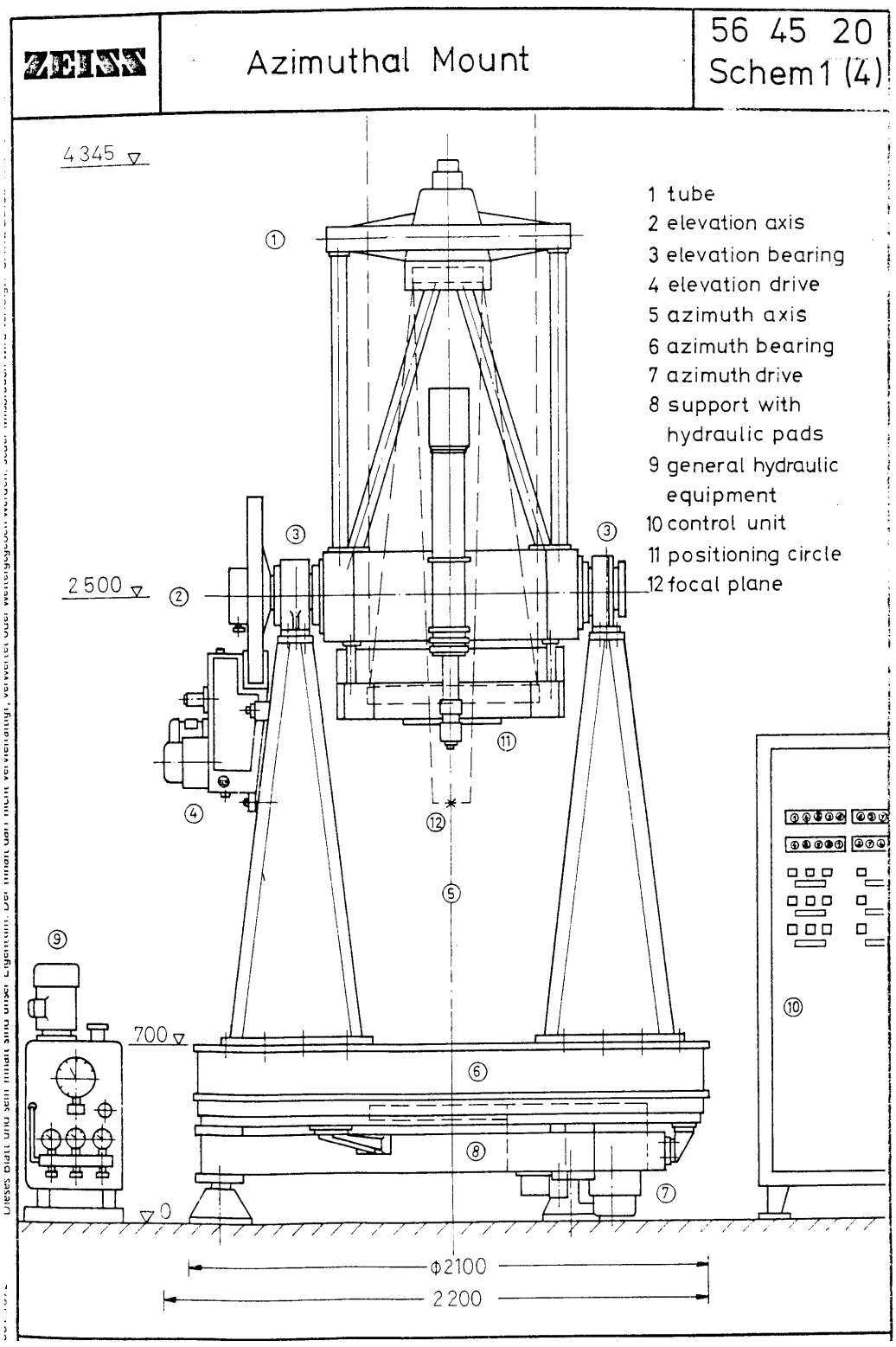

Figure 2.3.: mechanical drawing of ATOM, side view

Optical system	
free aperture	75 cm ⌀
focal length	600 cm
aperture (f) ratio	f/8
focal plane	5.2 cm ⌀ $\hat{=}$ 30 arcmin
	$\hat{=}$ 0.036 arcsec/μm $\hat{=}$ 28 μm/arcsec
distance between focus and rear of primary cell	35 cm
primary mirror	
material	Zerodur
outer diameter	78 cm
diameter of central bore	21.5 cm
maximum thickness	11.75 cm
focal length	225 cm
secondary mirror	
material	Zerodur
outer diameter	32.5cm
focal length	-126.5cm
attached finder telescope	
free aperture	11 cm ⌀
focal length	110 cm
aperture (f) ratio	f/10
Field of view	3°⌀
weights	
weight of main mirror	100 kg
weight of secondary mirror	17 kg
max. weight attached to rotatable flange	75 kg
total weight of telescope	4200 kg

Table 2.1.: Technical data of ATOM

Figure 2.4.: ATOM control electronics. Some main components: *cabinet 1, upper part:* manual control panel used for on-site control without any computer involved;*bottom:* transformators for the telescope servodrives; *cabinet 2, 2nd panel from above*: main PLC of control system; *bottom:* telescope control PC `attel`(relocated to cabinet 3 in the meantime). *cabinet 3*: computer for instrument control, network and telephone access for ATOM building.

2.2.1. Control electronics

The original telescope control electronics were replaced completely for the ATOM project by Hamburger Sternwarte, following the strategies they were using for automation of their Oskar-Lühning-Teleskop[4]. In particular, all ATOM motors are now operated using industrial approved programmable logic controllers (PLCs)[5], resulting in a very stable system.

2.2.2. Pointing corrections

The telescope control software `telops` by H.-J. Hagen includes a pointing model that accounts for

- deviations of the bottom plate of the telescope from being exactly horizontal
- offsets in the axes encoder zeropoints (e.g. "north" is not really azimuth=0.0°)
- flexure in the telescope structure due to gravitational bending
- atmospheric refraction (static model only, no meteorological information is used)

[4]OLT, see http://www.hs.uni-hamburg.de/EN/Ins/Olt/
[5]type Möller `PS 4-341-MM1`

date	#images	<dAz>	med(dAz)	RMS	<dElev>	med(dElev)	RMS
2007	11469	-10	-8	80	+47	+59	80
2008	9227	-19	-30	84	+50	+70	94
2009	10113	-52	-92	120	+44	+67	137
2010a	3223	-33	-90	171	+12	+3	186
2010b	3576	-20	-20	37	-53	-59	43

Table 2.2.: Angular offsets between telescope and real celestial coordinates from data visualized in figure 2.5, separated by years. *All numbers are given in arcseconds.* The measurements were converted from the measured offsets in α, δ to azimuth and elevation because ATOM is an Az Alt mounted telescope.
#images gives the number of acquired frames for which a valid WCS could be found (this is also the number of points shown in each panel of fig. 2.5); *<dAz>* mean deviation in azimuth; *med(dAz)* median deviation in azimuth; *RMS* is the 1σ root-mean-square of the distribution. Next 3 columns are giving the same for the deviations in elevation. The data from year 2010 is split in two periods because the pointing model parameters were adjusted in August 2010. See text for more details.

The initial parameters for this model have been determined in a few nights after the assembly of the telescope in Namibia by measuring the offset between star positions according to `telops` and on the real sky. The so-found model allows for a pointing accuracy of $\ll 3$ arcmin on all relevant positions in the sky[6]. Note that the FoV with the current instrumental setting is 8x8 arcmin, so this accuracy is sufficient for normal operation. The mentioned pointing accuracy of $\ll 3$ arcmin is valid for pointing the telescope to an arbitrary positioning on the sky, re-pointing the telescope to the same *Az/Alt* coordinates within a time span of $\approx$ months results in an accuracy of ≈ 20 arcsec.

To check for the stability and correctness of the pointing model mentioned above, the angular distance between nominal telescope coordinates and WCS coordinates were investigated. The WCS positions were derived from a fit of astrometric catalog star positions to the star positions detected in all images recorded during the normal observations (the astrometric fit is part of the ATOM data analysis pipeline and is described in section 5.1.3).

Since the basic coordinate system of ATOM is not Hour Angle and Declination like for a classical parallactic mounting, but azimuth and elevation, the found true α, δ values were transformed into true azimuth and elevation at time of observation and compared with the azimuth and elevation reported by the telescope control system. Note that this position includes already the corrections of the pointing model. The found deviations are shown in fig. 2.5, separated by years; the statistical properties of the measured deviations are listed in table 2.5. The more interesting relation for pointing correction between raw encoder values and true sky position cannot be shown for the first years of operation, since the raw encoder values are only stored in the FITS images since March 2010, when in became apparent that an update of the pointing model parameters is necessary and that the neeed raw encoder values were not recorded before.

Since the color scale in fig. 2.5 is constant for all panels, it is easy to see that the pointing offset is growing with time. Most obvious change is probably the change in

[6]The pointing accuracy is worse at elevation angles <20deg, but observations this near to the horizon are not performed during normal operation.

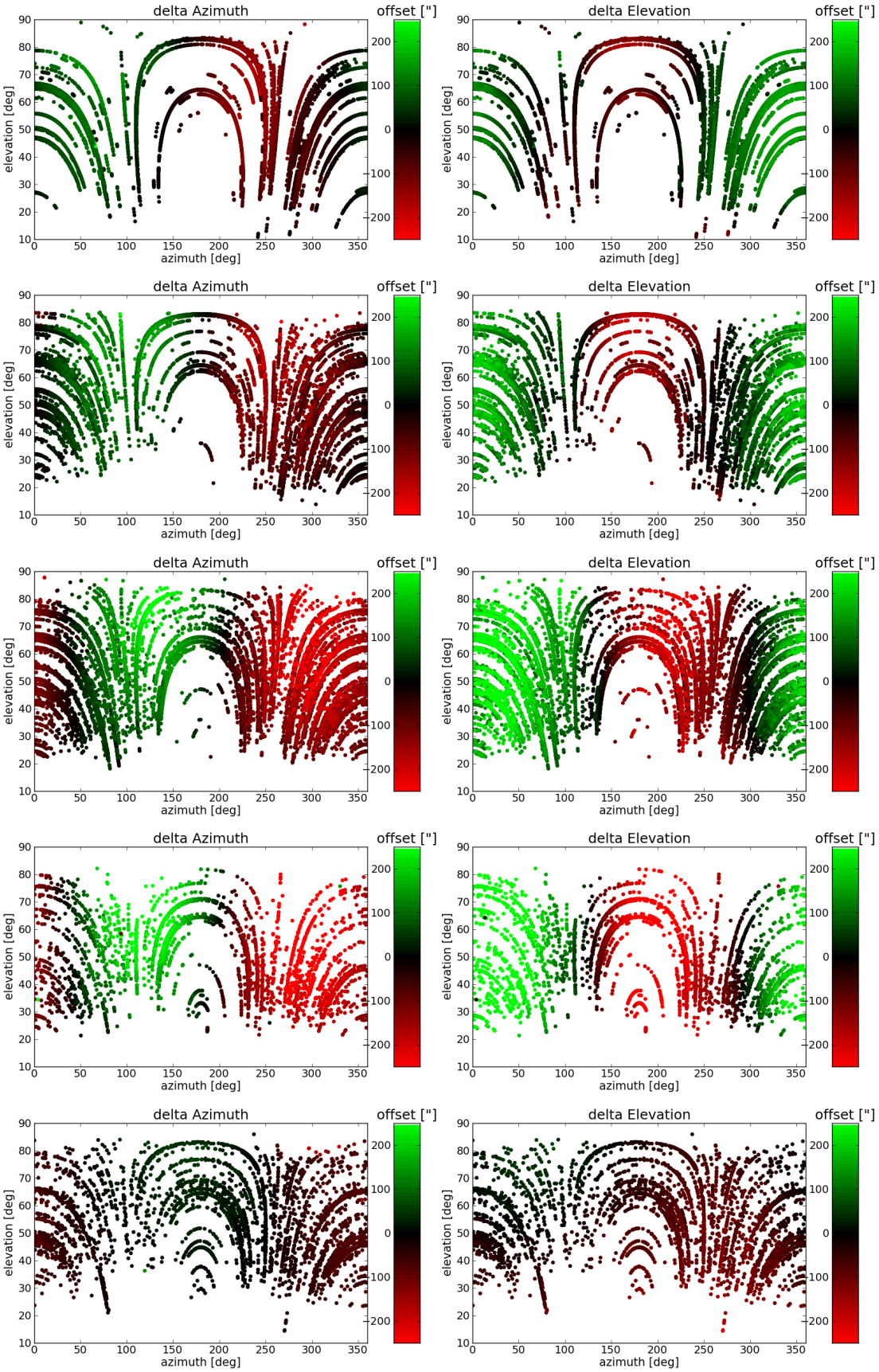

Figure 2.5.: Angular offsets between telescope and true celestial coordinates. From top to bottom: year 2007, 2008, 2009 , 2010 until August, 2010 after August with new pointing parameters. See text and table 2.2 for further description and numerical properties.

$\Delta Elevation$ at an azimuth of ≈ 270 deg between 2008 and 2009 (row 2 and 3), when it turned from an positive (shown in green) to negative (shown in red) offset. This may very well be explained by e.g. a tipping of the concrete baseplate the telescope is standing on over the years.

Using the offset data collected May to July 2010, 1451 supporting points for the pointing model were gained and updated parameters for the pointing model were computed by H.-J. Hagen and are used by the telescope control system since August 2010. The effect of the new pointing parameters is clearly visible in the bottom panel of figure 2.5, where the now much smaller pointing offsets using the new parameters in the 2nd half of 2010 are shown.

In principle, it would be possible to update the pointing model parameters constantly, all necessary input parameters (encoder values, true sky position) are available from the FITS headers of ATOM images after they are processed by ADRAS (see chapter 5) each morning, but this is not implemented in the software.

Such a software upgrade would to be "nice to have", but is not essential for the project, since ATOM is finding its targets also now.

2.3. Instrument

The ATOM instrument consists of the main imaging CCD camera with a filter wheel in the upstream light beam (see chapter 3 for detailed description of the camera selection process). A small part of the focal plane image is fed into a guiding camera attached to the side using a small plane mirror. Each component is described in the following.

2.3.1. Main camera

The main CCD camera of ATOM is placed at the Cassegrain focus of the telescope. It is an *ALTA E47+* from Apogee Instruments Inc.[7], housing a *E2V 47-10 grade 0* CCD chip (see E2V (2000) for a detailed CCD chip description). The spectral sensitivity of this chip is given in figure 2.12.

The camera is equipped with a thermoelectric cooler being able to cool the CCD down to 55 K below ambient, camera control and data transfer is done via a standard Ethernet connection.

Nominal resolution of the camera system is 1024x1024 pixels, the physical size of the CCD is (1056 + 2x 8 dark reference) x 1027 pixels, each with a size of (13x13) μm. Due to limitation in the software drivers (Mills (2005)), the maximum read-out region is limited to 1040x1024 with the 8 rightmost columns being dark reference columns.

The camera resolution on the sky is 0.47 arcsec/pixel, thus leading to a field-of-view (FoV) of 8x8 arcmin. The size of the FoV in comparison to the Crab nebula is illustrated in figure 2.8.

2.3.2. Filter wheel

The filter wheel (fig. 2.9) is able to house 6 filters. It was custom build at the LSW workshop according to a design by me. The filters are placed in a revolver magazine and

[7] since 2010: *Apogee Imaging Systems*, http://www.ccd.com

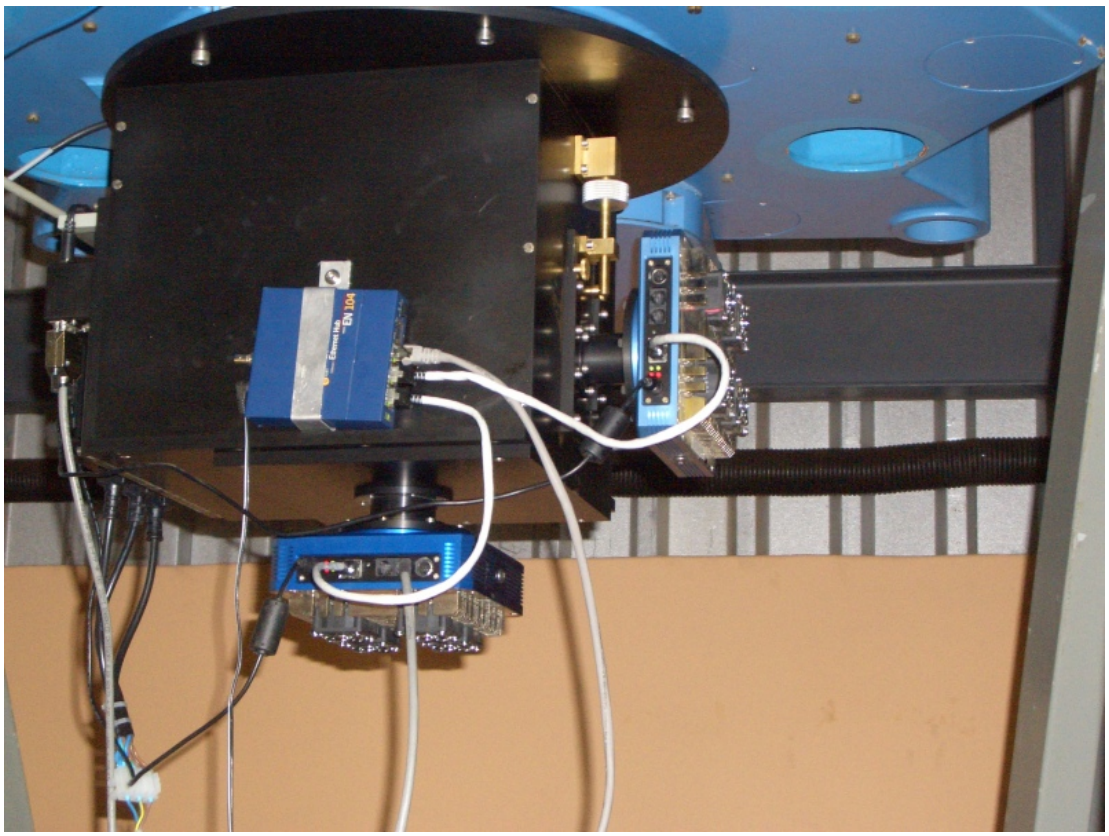

Figure 2.6.: Instrument below the mirror cell: Main camera is at the bottom, the guiding camera to the right. The device in the front is a small Ethernet hub which distributes the control signals to/from the cameras. The control cable of the filter wheel unit can be seen at the left. It is connected to the RS-232 port of the guiding camera, which acts as a signal/media converter to tunnel the signals from the control computer via Ethernet to the filter wheel unit.

are moved by a little DC motor. Motor and control electronics were bought from *maxon motors*. Unfortunately, they do not offer control software for Linux, so a significant amount of work was necessary to develop a software which can control the filter wheel motor in all ways necessary for this project. The resulting C library `libEPOS` (Hauser (2006)) is freely distributed[8] and already used by some other projects.

Also attached to the filter wheel is a framework holding the different power supplies for both CCD cameras and the filter wheel.

The filters are 2 inch in diameter and fixed in standard filter housings. We are using the *Johnson-Cousins UBVRI broad-band photometric system* as defined by Bessell (1990) (see figure 2.10 for transitivity curves). In addition to the five real filters, the last available filter position is loaded with a piece of black paper. This is used to block the optical path whilst performing dark exposures and to save the underling CCD entrance window from dirt during standby times.

In 2008, the U band filter was removed from the filter wheel to allow observations in white light.

[8] http://www.lsw.uni-heidelberg.de/users/mhauser/libEPOS/ and http://sourceforge.net/projects/libepos/

Figure 2.7.: ATOMs main CCD camera (image credit: *Apogee Imaging Systems*)

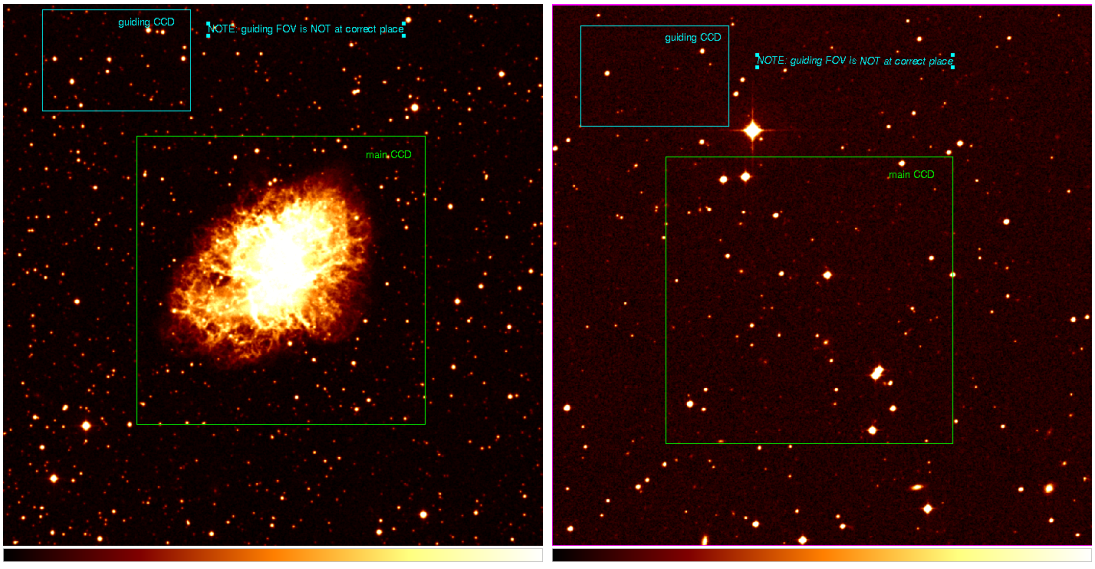

Figure 2.8.: Illustration of ATOM main camera field of view (FoV). The size of images shown here is 15x15 arcmin, indicated FoV of main CCD camera (green box) is 8x8 arcmin. The blue box denotes the size of the FoV of the guiding camera. The correct position of the guiding FoV is 30 arcmin away from the main FoV, it was moved here for illustration purposes. *left:* crab nebula; *right*: PKS 2155-304

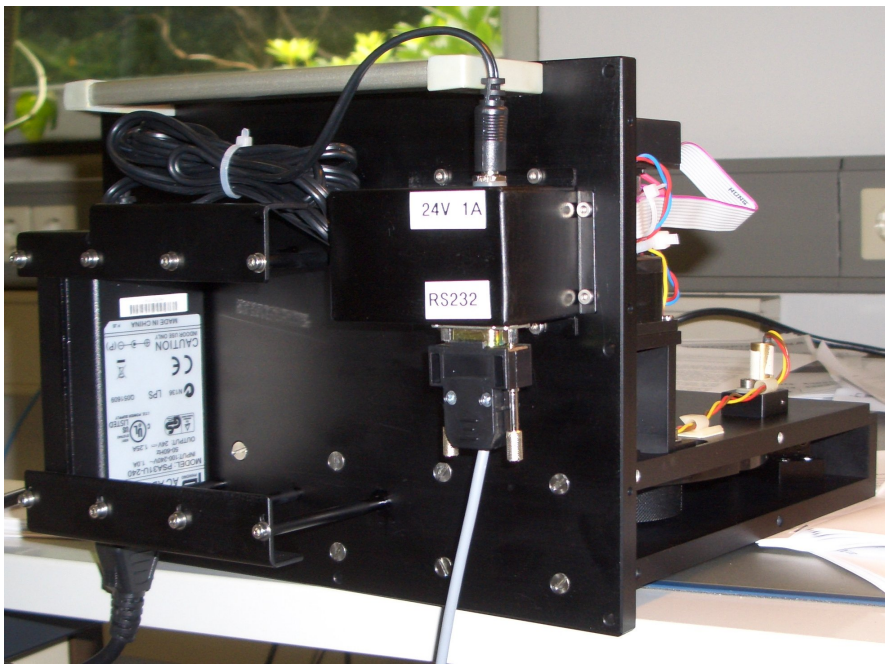

Figure 2.9.: ATOM filter wheel unit

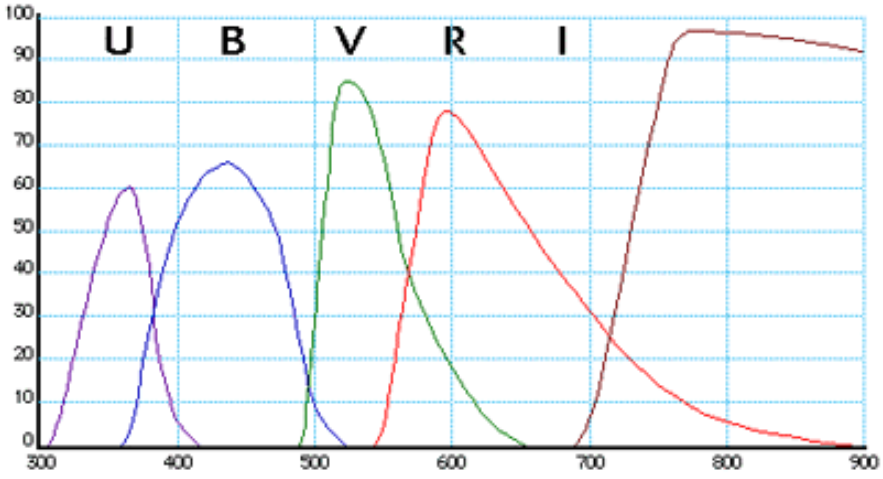

Figure 2.10.: filtercurves as given from the vendor

	main camera	guiding camera
RON [e^-]	9.5	≈ 14
gain [e^-/ADU]	1.35 ± 0.07	1.67 ± 0.02
bias level [ADU]	$2038 \pm 11 @ -25°C$	2742 ± 8
read-out time (full frame)[sec]	8.1	2.7

Table 2.3.: The main performance characteristics of the ATOM CCD camera systems (own measurements).

2.3.3. Autoguiding system

The guiding camera is attached to the side of the instrument box. It is -similar to the main CCD camera- an *Apogee ALTA E1* (similar housing (see figure 2.7) and same software interface as main camera, but smaller and less sensitive (and thus cheaper) CCD chip). The FoV of the choosen guiding camera (see sec. 3.4.1) is (4.1x2.8) arcmin. Since the center of the guiding camera is located 50 mm (which transforms to 30 arcmin on the sky) away from the image plane rotator axes, the accessable FoV of the autoguiding system projected on the sky has the form of a circular ring with an outer/inner radius of 30 arcmin $\pm$ half the width of the projected size of the CCD. By turning the image plane rotator axis, the guiding system can for any telescope pointing position choose its guiding area out of an area on the sky of

$$\mathrm{FoV}_{\mathrm{autoguider}} = \pi\left(r_a^2 - r_i^2\right) = \pi\left(\left(30' + \frac{4.1'}{2}\right)^2 - \left(30' - \frac{4.1'}{2}\right)^2\right) \quad (2.1)$$

$$= 772.8\,\mathrm{arcmin}^2 \approx \underline{0.21\,\mathrm{deg}^2} \quad (2.2)$$

During the first commissioning run in November 2005, the angular distance between the center of the main camera and the center of the guiding camera was measured to be 33'40" to the south, thus leading to a accessible FoV of $\approx$ 0.24 deg^2. The explanation for this discrepancy of 3.7 arcmin is that the LSW workshop modified the initial design of the instrument to give more room to the turning filter wheel. This accessible FoV for the autoguider is large enough to allow guided observations on practically every position on the sky.

The correct mounting orientation of the guiding camera with respect to the instrumental box / the telescope can be seen in figure 2.6.

An overview of the orientation of the different cameras in the telescopes focal plane is given in figure 2.11.

2.3.4. Instrument operation software – `instops`

As described in the previous sections, the instrument consists of two CCD cameras and a filter wheel unit. The development of control software for these devices was a major task of this thesis.

While there exists some low-level software library for camera control (Mills (2005), with unfortunately really bad/non-existing documentation), there was no Linux compatible software for the motor control of the filter wheel available. But the documentation published by *maxon motor* is really helpful for developing own software (see maxon

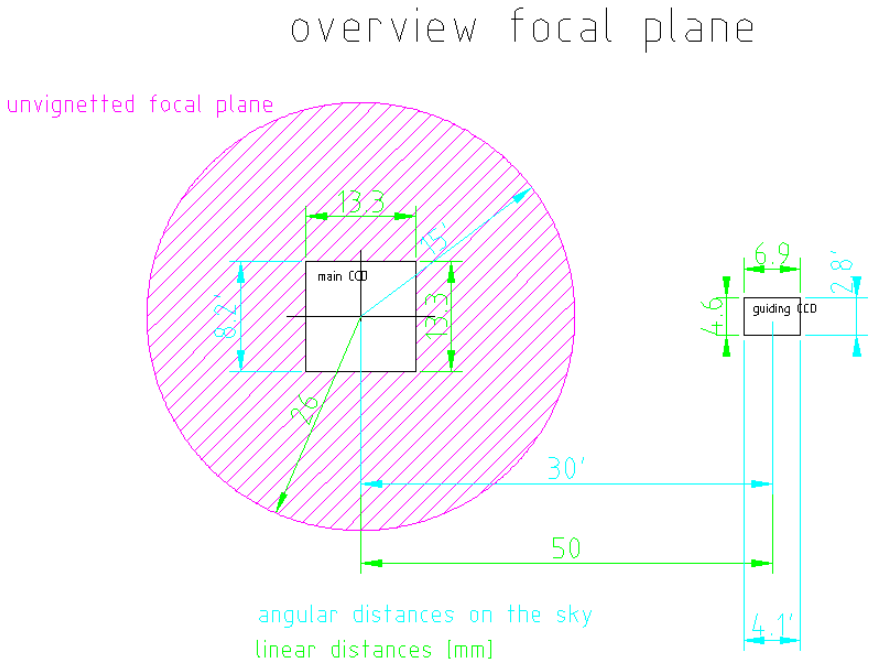

Figure 2.11.: overview of image plane

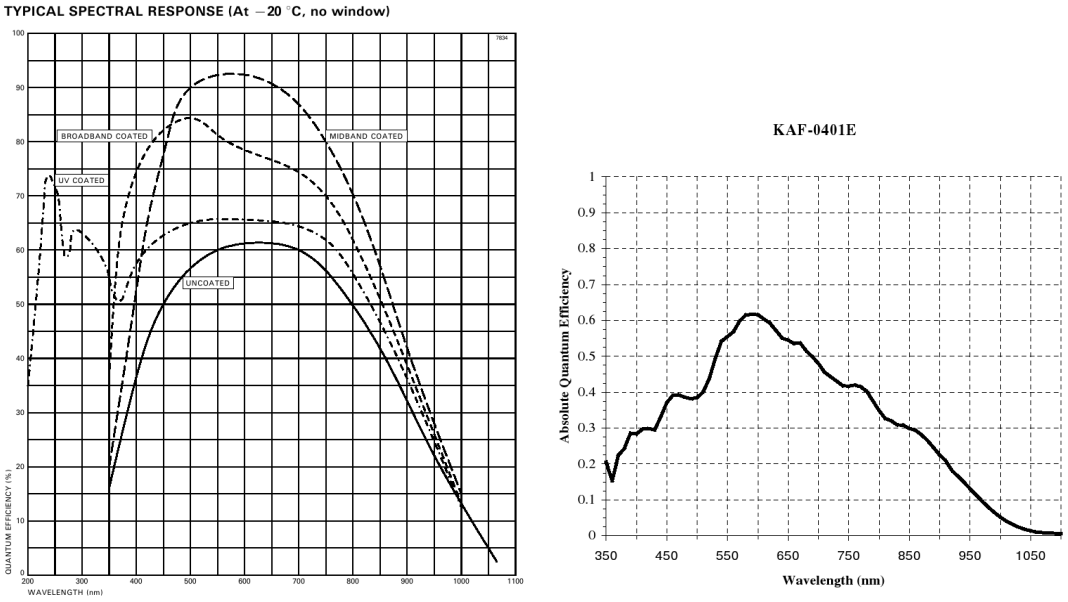

Figure 2.12.: spectral sensitivity of used CCD chips. *left:* main camera CCD chip e2v 47-10 (E2V (2000)). The CCD used by ATOM is *broadband coated*. *right:* guiding camera CCD chip KAF-0401ME (Eastman Kodak Company (2000))

motors (a), maxon motors (b) and maxon motors (c)). So at first there was the need to develop a software library to be able to control the motor control device *EPOS*[9].

This software, called `libEPOS`, is now able to communicate via RS-232 protocol to the control device, verify all commands via CRC-32 checksums and to position the filter wheel at any of the six pre-defined positions.

`libEPOS` is published online and can be freely used by anyone interested. Two projects (one in Spain, one in Switzerland) have already communicated that they use `libEPOS` for their work. For an detailed description and code download, see the project website at http://www.lsw.uni-heidelberg.de/users/mhauser/libEPOS/.

Based on the Apogee drivers and `libEPOS`, an instrument control software called `instops` (for `inst`rument `op`eration `s`oftware) was developed. It is implemented as a server daemon written in C and C++ (the C++ part was necessary to be able to use the Apogee camera drivers). All incoming and outgoing communication has to be broken down in a complete single line of plain ASCII text each. A detailed list of all commands and examples are given in the ATOM user manual (Hauser (2006)).

Software architecture

The schematic design of the `instops` software is given in figure 2.13. All interaction interfaces to the (software) world outside is marked in green, the hardware interfaces are omitted in this diagram.

There are several processes spawned by the main `instops` process. This is due to the fact that it was found that the camera control functions implemented in the Apogee camera library (Mills (2005)) have a chance of $\approx 10^{-5}$ to throw a *segmentation fault* when called. In the multi-process design implemented here, the main `instops` process monitors its child processes and re-spawns them if one crashes. The advantage over concentrating all into a single process and restarting this in case of a crash by `init` (or any other monitoring process) is that a crash in the guiding routine does not terminate a multi-minute (or even longer) science exposure. The guiding process can restart immediately with its previously determined guiding star and the subwindow centered on it[10]. Since it was found that the telescope tracking on most part of the sky is good enough to do >5 min exposures without guiding correction, a segmentation fault in the autoguider process should not destroy an ongoing science exposure. Nor should a failure of the main camera process interrupt the telescope autoguiding. Up to now, there was no incident found where a crash in the camera software modules killed the whole `instops` process.

The information exchange between the different processes is via a shared memory segment, to which `instops` and every of its child processes is attached.

The task of each single module is described below:

shared memory segment: a shared memory segment is in the UNIX world a part of computer memory to which several different processes can attach, read and write. Usually, each piece of memory can only be accessed by the process (read: *program* for most cases) which allocated it. It is not visible (or accessible) for other processes.

[9] for a device description, see http://www.maxonmotor.de/ and search for `EPOS`

[10] Note that the re-start of a camera control process after a crash takes about 40 seconds due to some re-initializing of the camera firmware.

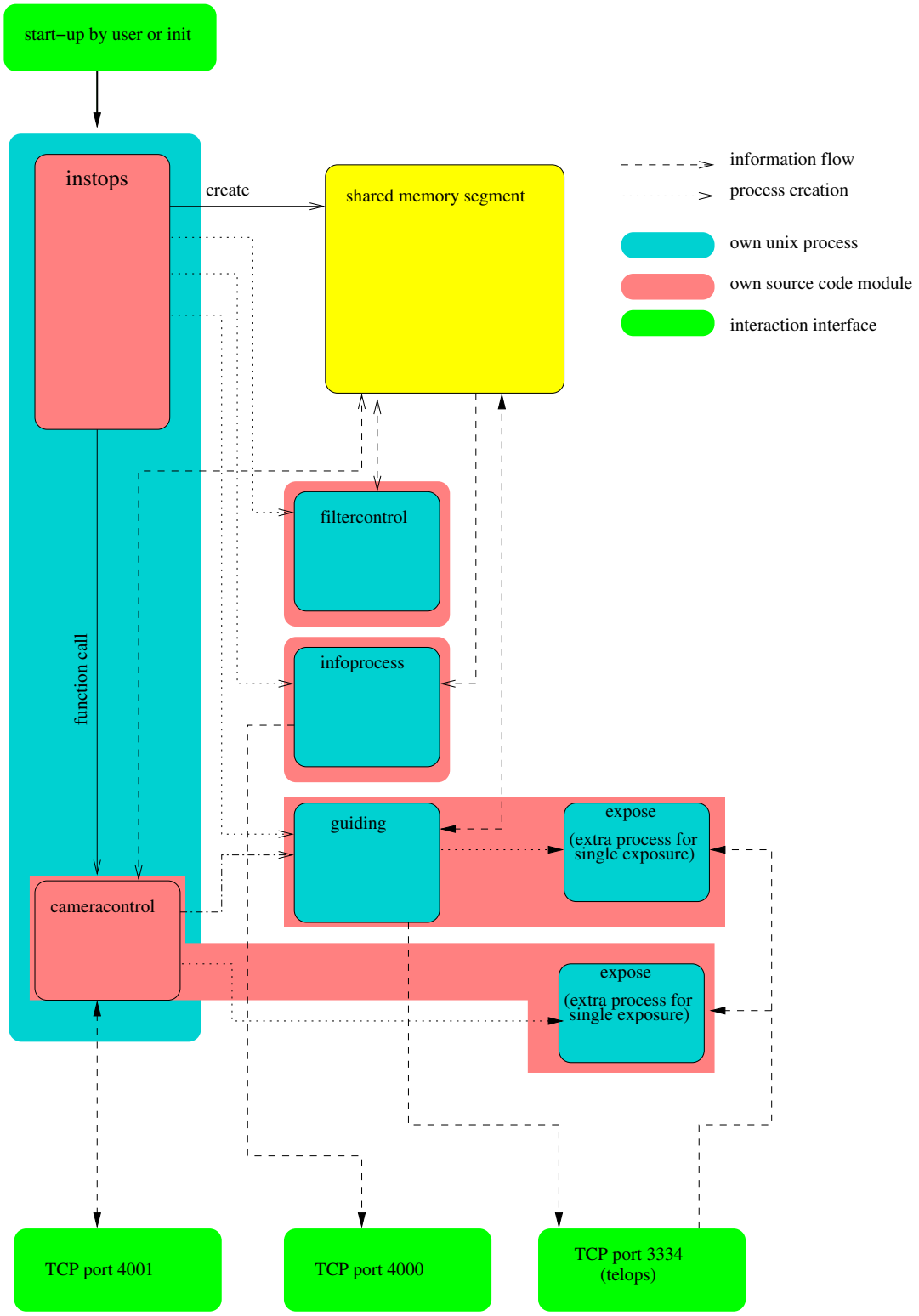

Figure 2.13.: Schematic overview of `instops` software components. See text for explanation.

byte number	name	description	type	size [bytes]	remarks
1	STATUS -0 -1 -2 -3 -4 -5 -6 -7	several status infos	bit pattern	1	8 bit-wide pattern in use cooling enabled requested temperature reached shutter open during exp. exposing logging enabled unused stop request
2	TEMPERATURE	CCD temperature	float	4	read-only
6	FANMODE	camera fan mode	signed short	2	[0..3]; 0:off, 3:max
8	ROIXS	ROI: X_{start}	signed short	2	start of ROI- X axis
10	ROIXE	ROI: X_{end}	signed short	2	end of ROI- X axis
12	ROIYS	ROI: Y_{start}	signed short	2	start of ROI- Y axis
14	ROIYE	ROI: Y_{end}	signed short	2	end of ROI- Y axis
16	EXPTIME	exposure time [s]	double	8	
24	TEMPSETP	CCD temp. set point	float	4	
28	TEMPHEAT	temp. heatsink	float	4	read-only
32	PATH	path to FITS storage	char[80]	80	
112	TARGETID	ATOM targetID	short int	4	
114	CAMERACONTROLPID	PID of camera control process	pid_t	4	read-only
118	INFOPROCESSPID	PID of info process	pid_t	4	read-only
122	FILTERWHEELPID	PID of filter wheel control process	pid_t	4	read-only
126	FILTERID	requested filter position	signed short	2	[0-5]: set filter 6: search for reference position
128	FILTERSTATUS	status of filter wheel unit	signed short	2	read-only; <0: some error -1 start-up error -2 no reference found -3 timeout while positioning -99 general error [0-5] present filter position 6 searching for reference position
130	GUIDINGPID	PID of autoguider process	pid_t	4	read-only
134	GUIDINGSTATUS	status of autoguider	signed short	2	read-only; <0: some error -1 unable to conect to camera 0 switched off 1 searching for guide star in FoV image 2 guiding ongoing, taking subframes 3 no guide star found
138	GUIDTEMP	autoguider CCD temperature	float	4	read-only
142	GUIDHEATEMP	autoguider heat sink temperature	float	4	read-only
146	GUIDFANM	fanmode of guiding camera	signed short	2	[0..3]; 0:off, 3:max
148	DS9	display images in DS9 via XPA	short int	2	0,1
150	LOOPS	number of images with same settings taken in a row	short int	2	0-255
152	CLIENT	IP:port of connected client	char[32]	32	read-only
184	AUTOFOCUS	adjust telescope focus based on guiding star morphology	short int	2	0-off; 1-on

Table 2.4.: Allocations in shared memory segment. The remark *read-only* means that the value cannot be changed by user interaction, but is set by the system.

Here, the shared memory is allocated by the `instops` main process at startup. It holds all information that is needed by more than one of the `instops` subtasks, e.g. the PIDs (process identification number) of the subtasks (for communication issues), the actual and requested filter wheel position, actual and requested CCD temperatures and other stuff. See table 2.3.4 for a complete overview.

camera control: this process is in charge of controlling the main camera. It sets and reads different temperatures (CCD chip, heatsink), sets the read-out region on the CCD, triggers exposures, saves acquired images to disk, and so on.
It is also responsible for communication to the 'outside' world (whether it is a human observer or a software robot), to receive commands and providing status information concerning the whole instrument.

camera control – expose: the camera control process spawns an extra process if an exposure is triggered. This extra process was introduced because the probability of a crash of the underling camera drivers was found to be significantly higher when reading out the CCD chip than all other command to the camera. So a crash during image readout does not affect the other `instops` components at all. But of course the to-be read-out image data is lost in that case[11]

filtercontrol: the ATOM filter wheel is controlled via this task. The code in here is mainly a wrapper around `libEPOS`, to make it fit into the framework of `instops` software.

infoprocess: as the name suggests, this process provides the instrument status as plain ASCII text to everyone interested via TCP/IP connections. It practically converts the content of the shared memory segment into ASCII and adding some words for explanation.

guiding: the guiding camera is controlled here. This includes not only the pure camera parameters and actions like temperature, read-out region and exposures, but also the autoguiding logic.
When asked to start autoguiding, this process first acquires a full-frame exposure and initiates a search for the brightest star in the image, which is isolated and not too near to the image borders. This star is used as a guide star until the end of autoguiding is requested. The star position is determined by calculating the center of mass (COM) of the light distribution on the chip. All further exposures are taken in subframe mode only, meaning only a small part of the CCD, centered around this guide star, is read-out. Omitting most of the CCD pixels during image read-out improves the read-out time ($< 1s$ instead of $\approx 5s$ for full-frame readout), thus leading to less dead-time and thus a higher duty cycle in consecutive guiding exposures. The COM of the guiding star is computed in each exposure and the offset to the previous exposure is transformed into a telescope offset on the sky. This offset is reported to the telescope control software `telops`, which corrects the telescope position. We now use exposure times of 30 sec, but this can be configured

[11] In 4 years of operation, this has happened ≈ 10 times. It has happened much more often during software development at LSW. The only obvious difference between development phase and operation is the used exposure time (was shorted during testing). So the risk of a crash seems to anticorrelate with exposure time.

Figure 2.14.: Rain detector from Thies Klimatechnik. See http://www.thiesclima.com/niederschlagswaechter.htm for technical data.

in the `instops` config file, together with other guiding parameters. See the ATOM user manual for a complete description of the parameters.

guiding – exposure: see the explanation of *camera control – expose* above.

2.4. Rain sensor

In 2007, ATOM was upgraded with the installation of a *rain sensor*. This device is able to detect precipitation and should prevent[12] the automatic system from opening the roof in case of precipitation.

2.4.1. Device

The device (see figure 2.14) was bought from *Thies Klimatechnik*. It detects precipitation by monitoring a 5x5 cm^2 area with a IR light barrier. Any interruption of the light beam triggers an event, and N events (N between 1 and 15) in a 50 sec time interval are considered to be rain. We are currently using $N = 5$.

2.4.2. Control software

The rain sensor control software is a small server process that monitors the status of the rain sensor. This status can be queried via a TCP/IP connection.

The information about rain detections comes from querying if a relay that is controlled by the rain sensor hardware and connected to the seriell port of a PC is triggered or not. The hardware status is queried once per second, and if rain is detected, a warning is broadcasted to all connected clients. Until the introduction of an "intelligent" robotic observation software (which should take care of making use of weather monitoring information, see also sec. 4), this control software also launches an emergency script

[12] *should prevent* means that the rain sensor is not blocking any operation, but it is providing status information (*raining right now* or time since last rain detection). Any remote and/or automatic system is expected to query the rain sensor status before deciding to open the roof.

(`stopTelescope.py`) which cancels any ongoing observation and closes the mirror cover as well as the building roof in case rain is detected[13].

The software also counts the time since last rain detection (or program start) and can communicate this upon request. This is used by the telescope startup scripts to prevent an accidental opening of the roof during (or shortly after) rain.

2.5. Cloud monitor

The ATOM cloud monitor hardware and control software is a contribution of Hamburger Sternwarte to ATOM. It was installed on site in July 2008. Note that beside the term *cloud monitor*, it is often named *sky monitor*.

The device consists of an CCD camera[14] behind a fisheye lens[15] and images the whole sky every few minutes. The presence (or absence) of clouds is detected by the non-detection (or detection) of stars on the sky. More details are given together with a description of the operation mode of the cloud monitor in sec. 4.2.

Since software revision 458 (2008-10-17), its values are read by `instops` and the sky transparency value is stored within the FITS headers every time a frame is written to disk.

The measurements are also written to protocol files, which are used as an input for correlation studies with the H.E.S.S. trigger rates and ATOM extinction measurements (see chapter 6). An image of the sky including the sky quality estimation is constantly updated on a webpage (see fig. 2.15).

[13] Note that this has not happened up to now (March 2011), since the cloud monitor terminates any ongoing observing run in case the sky gets cloudy.

[14] Model *SXVF-H5* by Starlight Xpress, see http://www.starlight-xpress.co.uk/SXV-H5.htm

[15] Model *ORIFL 190-3* by *Omnitec*, see http://omnitech.com/fisheye.htm

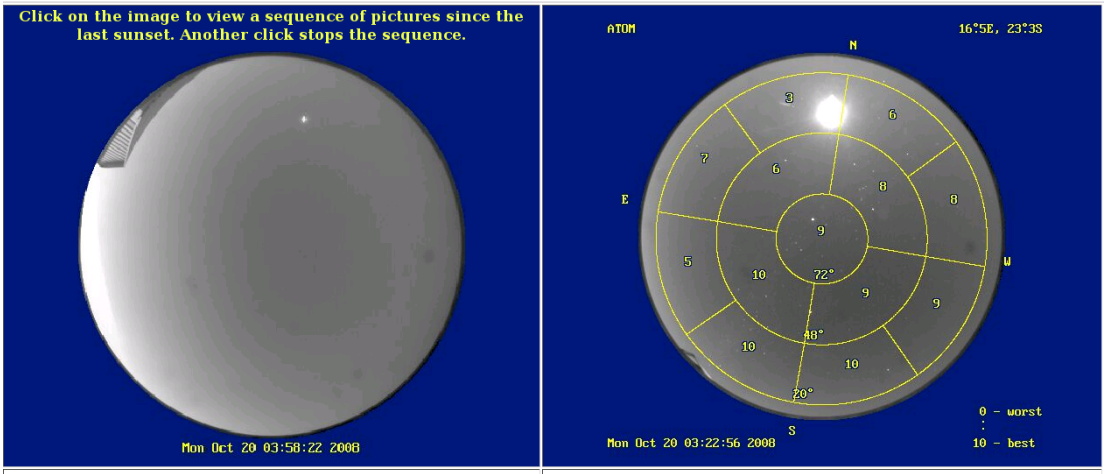

The latest picture taken by the sky monitor camera. (The sun was at least 4° below the horizon and there was no precipitation detection for 30 minutes.)	Automated estimation of transmission status for latest sky exposure with Sun at least 12° below the horizon.
Local time	Mon Oct 20 15:20:16 2008
Current elevation of Sun	35.8°
Current elevation of Moon	-65.8°

2008 June 16 18:04 | *H.-J.Hagen*

Figure 2.15.: *top:* HTML interface to cloud monitor measurements. The bright spot visible in the right hand panel is the moon.
bottom: photo of the sky monitor device and the rain sensor, mounted next to the ATOM building.

3. Test of different CCD cameras

Charge Coupled Devices (CCD) image sensors are *the* workhorse for optical and NIR observational astronomy since more than 30 years now. So why investing the huge effort to test several different CCD camera systems and not just make a quick survey around some observatories and use the CCD system for ATOM that all other observatories are using?

First of all, there is no such dominating system. The big instruments at the big telescopes worldwide have all build their own imaging system (based on CCD devices bought from a few companies selling these), but often with own control electronic, tailored to their specific needs. Since the required infrastructure and money for such an approach did not exist for ATOM, we needed to buy a commercial CCD camera system off-the-shelf.

Secondly, almost all CCD imaging systems used in professional astronomy are cooled by usage of liquid nitrogen (LN2) to operating temperatures of $\approx -120°$C to reduce (and nearly eliminate) dark current.

This option was not considered for ATOM, since there is no suitable source for LN2 at the H.E.S.S. site. Although one could use a closed-cycle cooling system to avoid the necessity for LN2 refills, this device would add aditional complexity (and thus higher risk of failure) to the project. And the anticipated exposure times for ATOM allowed to plan with a moderate cooling system without suspecting too much noise because of dark current (this assumption was proven correct in the tests described in the following sections).

So the following requirements came up for the market survey conducted to find the best suited CCD camera system for ATOM:

1. thermo-electrical cooling (TEC) via Peltier-elements, since no LN2 is available at the H.E.S.S. site.

2. availability of drivers/control software for the *GNU/Linux* operating system.

3. control cable length of $\geq$ 5m to avoid the necessity to mount the camera control computer on the telescope tube. This is not desirable, since the reliability and lifetime of a PC which is moved around and tilted during operation would most probably be way too short for an automatic system.

4. a FoV of $\geq$ 5x5 arcmin on the sky to get enough reference stars around the target object for differential rphotometry.

5. a pixel scale between 0.3 and 0.6 arcsec/pixel

6. as sensitive as possible

7. still affordable

manufacturer & type	CCD	connection	max ΔT	price (2004)
Apogee Alta E47+	e2v 47-10	Ethernet	55K	9,700 €
OES	e2v 47-10	Ethernet	60K	16,700 €
Sensovation HR-100	e2v 47-10	Ethernet	100K	26,000 €
Princeton Instruments	e2v 47-10	USB	70K	31,600 €
Andor iXon DV 887	e2v 97	PCI card	70K	33,500 €

Table 3.1.: Main characteristics of CCD camera systems that were considered for ATOM. Column *connection* denotes the way the camera is connected to the controller PC. *max* ΔT gives the maximum temperature difference between CCD chip and ambient temperature that the TE cooler can provide. The camera from *OES* was not considered any more after we had word from Sternwarte Bamberg that the electronics of these cameras are quite unreliable. The device by *Princeton Instruments* was excluded from further considerations because of its price (Andor iXon, being even more expensive, was still kept inside the sample, because its high speed imaging would allow to probe AGN for fast flux variations – a science case none of the other camera systems would give access to).

With the telescopes projection scale of 28 μm/arcsec, the items number 4 and 5 translate to a sensor size of $A \geq (8.4\,\mathrm{mm})^2$ and a pixel scale of 8.3 to 16.6 μm. Obviously, requirement 6 is in our case not limited by technology but by the requirement 7.

The telescope itself does not limit the camera selection, as it was build to support much heavier instrumentation (up to 75 kg) and its optics provides a focal plane of 5.2 cm diameter. None of the possible instrumentation scenarios for ATOM is even close to these limits.

Looking through the CCD types available in off-the-shelf purchasable camera types, it was quickly realized that the quite cheap Kodak CCD types KAF-*something* are not suitable for our purpose because of a) small pixel sizes of $\leq 9\,\mu$m and b) low quantum efficiency (QE, typically $\leq 65\%$ at the peak). But the –in astronomy well known and commonly used– CCD type 47-10 from *E2V* (see E2V (2000)) satisfied our requirements with its size of 1024^2 pixels ($(13\,\mu\mathrm{m})^2$ in size) and high QE of $\geq 80\%$ in a large spectral range.

In addition to this conventional CCD type, the *low light level* (L3, sometimes also called electron multiplying CCD – EMCCD) chips (also from *E2V*) just arrived at the end user market in 2004. This camera type allows high-speed imaging, typical exposure times in astronomical usage would be of the order of 0.1–10 sec. A camera from *Andor Technologies* that is housing one of this new-type CCDs was also tested.

Table 3.1 gives a compilation of cameras that were tested for their acceptability for this project.

3.1. Common test procedures

3.1.1. Test setup

The technical setup as well as data analysis algorithms for all laboratory CCD camera tests were nearly identical for all tested cameras and are described in the following. If not mentioned explicitly in the camera specific sections, the here described setup was applied to all test candidates.

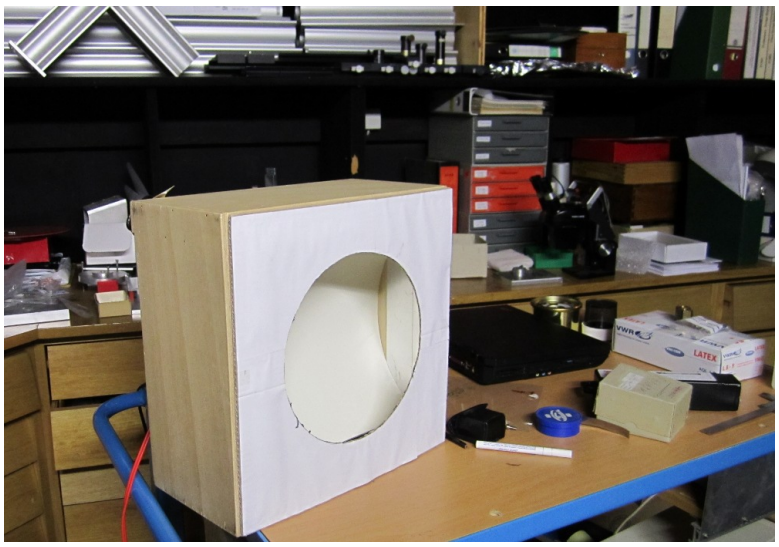

Figure 3.1.: The LSW flat field device for lab test. It hosts two light bulbs (one at top, one at the bottom), which -together with the curved projection screen- allow for a quite homogeneous and flat illumination pattern in its central region. The homogeneity is improved if the projection screen is placed outside the focal plane of the imaging optics (like it was done here).

All laboratory images were obtained in a dark, EM-shielded room. The room also provided a quite stable temperature during the whole tests. A Nikon photographic lens was attached to the cameras (which were by chance all equipped with a *C-mount* interface).

The tests covered the following tasks:

- understanding the camera software API and its stability as well as its completeness
- stability of CCD bias level and its dependence on temperature
- stability of CCD dark current and its dependence on temperature
- stability of CCD gain factor and its dependence on temperature
- CCD read out noise (RON)
- stability of CCD linearity and its dependence on temperature
- dynamic range of CCD chip

For taking bias and dark current frames, the lens was in addition to be placed in a dark room covered with a thick black cloth.

For flatfield images, a simple flatfield device (see figure 3.1) was used, which provides nearly homogeneous illumination across the field of view; the device was placed approximately 50 cm away from the camera.

3.1.2. Test data analysis

Bias level The *bias* level of a CCD camera can be expressed as either the mean or median value of a bias frame. A bias frame is an 'exposure' with zero exposure time with closed shutter, so that no signal is introduced by light. For this thesis, the bias level of any frame refers to the median signal level.

Read out noise The *read out noise* (RON) is the noise of the CCD signal after being processed by the read out amplifier and the *analog digital converter* (ADC). It is typically measured by fitting a Gaussian distribution to the pixel values of a bias frame. The width of the Gaussian distribution represents the RON.

Dark current The *dark current* is the signal introduced by thermal lattice vibration in the CCD detector material. It is obviously a function of detector temperature and time. It is measured the same way as bias level, but with non-zero integration time.

Gain factor and linearity One of the advantages of a CCD in comparison to photographic plates is the linear relation between incoming photon flux S and the (digitalized) output signal intensity I. The connecting factor between S and I is the gain factor g:

$$I = g \cdot S \tag{3.1}$$

The *gain factor* g is the combined conversion factor of the read out amplifier and the ADC. It tells how many electrons have to be accumulated per pixel to get one *analog digital unit* (ADU, sometimes also referred as *counts*).

All gain measurements in this work were obtained following the method described in Newberry (1998), which is summarized in the following:

The signal variance $\mathrm{V} = \sigma^2$ is dominated by the statistical noise σ of the incoming photons $\sigma = g \cdot \sqrt{\mathrm{S}}$, S = signal of incoming photons, g = gain. The readout noise is negligible at high signal levels. The mean intensity I is given by $\mathrm{I} = g \cdot \mathrm{S}$, so that the relation between gain g, intensity I and variance V can be expressed as

$$\frac{\mathrm{I}}{\mathrm{V}} = \frac{g \cdot \mathrm{S}}{g^2 \cdot \mathrm{S}} = \frac{1}{g} \tag{3.2}$$

So the determination of actual gain boils down to a simple linear fit of intensity vs. variance for high –but not too high– intensities.

Flat field effects (inhomogeneous CCD illumination, leading to a higher noise level) have been removed by subtracting two images with same system parameter settings and same illumination(after multiplicatively adjusting them to the exact same mean intensity) and using the variance of a homogeneous part[1] of the resulting frame. Consequently, this variance needs to be halved because of error propagation. The corresponding mean intensity value is taken from one of the input images.

Eq. 3.1 is of course not valid for arbitrary signal levels. At one stage, a single pixel cannot hold any more electrons and saturates. Thus from there on, I is constant despite of increasing S. The flux levels where eq. 3.1 is true defines the *usable dynamic range* of a CCD.

The number of electrons a single CCD pixel can hold during the integration time is called *full well capacity*. This is one of the main characteristics of a CCD chip and scales typically with the physical pixel size. The resolution of the ADC (16 bit for most cameras considered here, the *iXon* has a 14 bit ADC) and CCD full well capacity are the main input parameters for selecting the right gain factor for a camera system (simplified picture in an ideal world: no electrons $\rightarrow$ 0 ADU, full well capacity reached $\rightarrow 2^{16} = 65536$ ADU).

[1] a 50x50 pixel area was used here

The gain factor and usable dynamic (linear) range is determined by measuring I as a function of S. For simplicity reasons, the flux S of the test device was kept constant and the exposure time t_{exp} was varied.

3.2. EMCCD – Andor iXon DV 887

Electron multiplying charge coupled devices (EMCCD) are a new type of CCD detectors, meant for high speed read-out and *on chip* amplification of the accumulated charge before the read-out analog-digital-converter converts the charge into some digital signal. The composition of an EMCCD device is illustrated in figure 3.2, and the difference between conventional CCD and an EMCCD is described by *Andor Technology* as

> Unlike a conventional CCD, an EMCCD is not limited by the readout noise of the output amplifier, even when operated at high readout speeds. This is achieved by adding a solid state Electron Multiplying (EM) register to the end of the normal serial register; this register allows weak signals to be multiplied before any readout noise is added by the output amplifier, hence rendering the read noise negligible.

(taken from http://www.emccd.com/what_is_emccd/)

Following the two quite successful test runs using one *iXon DV887* by *Andor Technology PLC* for blazar monitoring on very short time scales done by S. Wagner and myself in cooperation with colleagues from the *Cork Institute of Technology (CIT)* in 2003 at the 2.2 m telescope of Calar Alto observatory, intensive laboratory tests of this camera type at LSW were conducted. The results of the two observing campaigns at Calar Alto[2] have been reported at the ENIGMA meetings (Smith et al. (2003)) and at SPIE 2004 (Smith et al. (2004)).

The usage of an EMCCD for ATOM would allow investigations on very short time scales, down to seconds and even sub-seconds time scales for the brighter sources. An access to this parameter space would justify the necessary additional financial investment[3] w.r.t. the other, conventional CCD cameras under investigation for ATOM. Because of the new technology used in this imaging system and the potential additional science cases, the iXon camera was tested more intensively than the other systems.

The report on the test of the *iXon DV 887* given in this section is a roundup of our test report to Andor (Pühlhofer et al. (2004))[4].

[2] Proposal #46, Spring 2003 (27.1. - 2.2., 7 nights) and Proposal #41, Autumn 2003 (17.9. - 22.9., 6 nights)

[3] Not only is the iXon the most expensive camera in the test sample, the high data rate of this device would require significantly more powerful IT infrastructure than what is needed for the other cameras.

[4] Note that despite the fact that the final test report was edited by my colleague G. Pühlhofer, the camera control software was completely my own creation, and the vast majority of performed tests and analysis was also done by me.

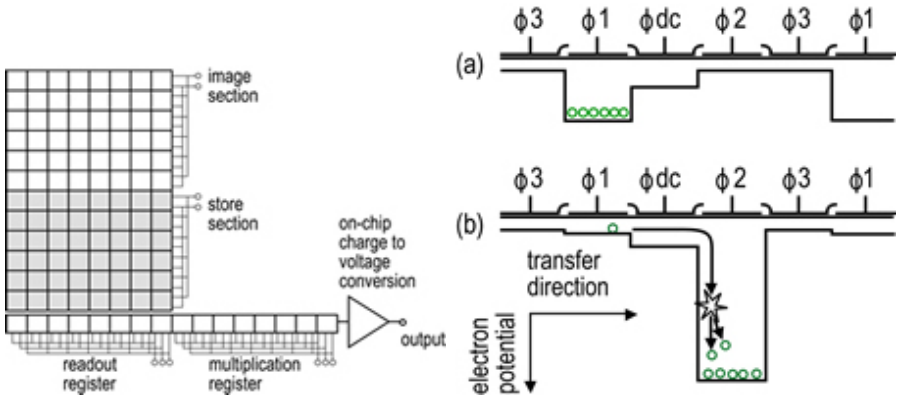

Figure 3.2.: Schematic layout of an EMCCD device. *left:* overview over the different sections. The *image section* is the light sensitive part of the CCD and corresponds to the surface of a conventional full frame CCD. The *store section* is not exposed to light. The combination of image and store sections corresponds to a conventional *frame transfer CCD*. The readout register is the same as in conventional CCDs. The technical innovation for EMCCDs lies in the *multiplication register*, which is described further in the *right illustration*: upper panel a) shows a conventional CCD pixel, where the accumulated charge (here in symbolized in green) is transfered to the next pixel by applying alternating electric potential to the different phases ϕ_i. The lower panel b) depicts the EMCCD multiplication register: for each pixel, there is a big potential well which introduces impact ionization cascades when charge is moved into it. Having several hundreds of these stages in a row allows for huge amplification rates. (image credit: *Andor Technology*)

3.2.1. Test setup

Most of the test data was obtained in single scan mode. The results from kinetics mode investigations are specially marked[5]. Only a minor fraction of the tests were done using kinetics mode, because I only managed to set up the software correctly for kinetics mode at a late stage of the tests.

All acquired data were full frame images with 512×512 pixels. This limited the minimum readout time in kinetics mode to $\approx 250\,\text{ms}$ according to the controller software.

For the single scan operating mode of the camera, the parameter space of gain, temperature and exposure time was investigated.

The actual gain of the iXon is a function of both gain setting and temperature.

[5] *kinetics mode* is according to the *Andor* nomenclature a camera operating mode where many frames are read-out in a row and stored in the computer memory instead of writing them to disk. Since writing to memory is of the order of 10^5 times faster than writing to disk, one is able to acquire much higher framerates in this mode (if the computer and not the camera is the bottleneck). But since one has typically much less memory than disk space, this mode cannot be used too long and requires to interrupt data taking to store the acquired data to disk once the memory is completely utilized.

For the kinetics mode tests, the parameter space was extended for

- nKinetics – number of kinetic cycles (i.e. number of frames for the iXon)
- kinCycleTime – time between two subsequent kinetic cycles; this was set to 250 ms, which was slightly above the allowed value given by the controller

3.2.2. Software

No end-user Linux software for operating this camera was provided by Andor. They only provided an API for the *C programming language* (Kernighan and Ritchie (1988)), which enabled me to develop own programs for camera control. Since the control to the camera is via an PCI controller card, an extra kernel module[6] is needed. This was provided by Andor in a *binary-only* way, so that we had no chance to investigate the cause of some software errors.

Memory problems

At the beginning of the iXon tests, two critical problems originating from the Andor kernel module concerning computer memory usage were found:

1. a memory leak which quickly allocated the whole available RAM (20MB per acquired frame), thus leading to a program crash
2. a memory limitation for the entire OS to 256MB RAM

After several bug reports, both problems were solved by Andor with a software upgrade (modified kernel module) during the tests[7].

Program crashes

The whole test was suffering from repeated program crashes, occurring after typically 10 to 50 frames (independent of single scan or kinetics mode). It was found later that the program is caught in an endless loop[8].

The only way to get out of this was to kill the task. Though everything seemed to be fine after that, (the operating system was still running without problems), the complete system froze when the program was rerun.

The only way found to avoid these program crashes was to make a break of about 10sec after about 5 images (these numbers where found empirically only). In rare cases, the program hang after one or two images taken in a rapid sequence. This behavior occurred not only with my own software, but also with Andor's example program `image.cpp`. A later found workaround was to remove and reload the Andor kernel module to continue.

While this workaround may be acceptable in manned lab experiments were low dead time is not crucial, it is fatal in nightly astronomical operation.

[6] in the world of Microsofts operating systems, this would be called a *driver*

[7] At a later time, I learned from other users of Andor cameras that this bug in Andor's kernel module has been reported to Andor more than a year before the tests at LSW.

[8] Endless is defined here as more than 30 seconds, exposure time was always set to sub-second values

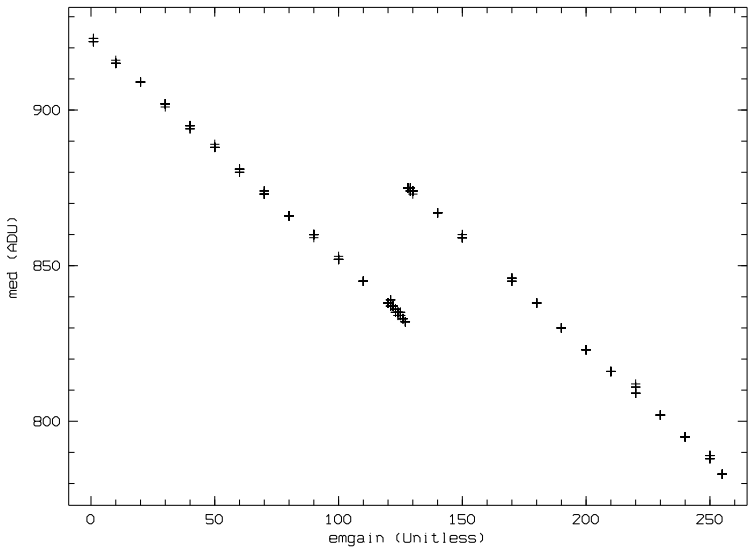

Figure 3.3.: Bias vs. gain (T = −58°C, t_{exp} = 0.01 sec. t_{exp} = 0 sec was not possible with the Andor Software API).

File system crashes The program crashed mentioned above led three time to a completely corrupted file system, requiring a complete new installation of the OS and user programs. Since the Andor software was supplied in a binary only form, no further investigations were possible.

3.2.3. Camera signal stability

Bias stability

Bias vs gain The bias varies with the gain in a linear decreasing way in a range of 920 to 780 ADU. A remarkable effect is observable when increasing gain from 127 to 128: a discontinuity raising the median of bias frames by 40 ADU (see figure 3.3).

Bias vs temperature Small variations of bias with temperature were observed. We measured a slight decrease (< 3 ADU/10K) of bias with decreasing temperature.

Bias vs time Bias varies also with time. The fastest variations were observable on the time scale of about ten minutes. When taking dark current measurements, a higher mean bias level for shorter, but later exposed frames was noticed, a behavior that could be explained by variations of bias.

If the software had to be restarted between these acquisition runs, bias shifted by up to 10 ADU (up to 1 for gain = 1, up to 10 for gain = 255).

Saturation level instability

An instability of the bias and saturation levels within a period of one week was found. The bias level shifted ≈ 9 ADU as well as the saturation level for each set of parameters changed. While saturation signal level of 14600 ADU was measured at one point in time, one week later the level has dropped to 14470 ADU. This effect is shown in figure 3.4.

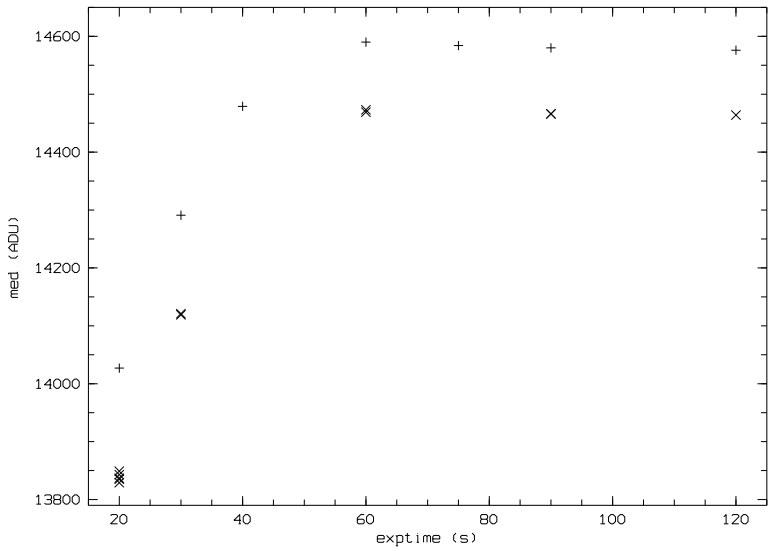

Figure 3.4.: Median signal vs. exposure time for flat field measurements taken one week apart (setup parameters T = −78°C, emgain = 250).
Data taken on 04.08.04 (+) and 10.08.04 (×). The effect of variations in the saturation level described in sec. 3.2.3 is clearly visible.

3.2.4. Dead time, minimum exposure time

Minimum exposure time in reality

The minimal exposure time for this camera that can be selected via the API is $2 \cdot 10^{-5}$s. Considering that the camera is equipped with an internal mechanical shutter, this is a surprisingly short minimum exposure time – if this software parameter has anything to do with reality.

To check for this, a quick test series was acquired: pointing the camera to our flat field device and keeping the illumination level constant, the exposure time was varied from the minimum value of 10^{-5}to10^{-1}s. Results are given in figure 3.5.

One expects that the API knows about the shutter timing characteristics and reports back the actual exposure timings (function *GetAcquisitionTimings()*).

But it was realized that one always gets back the entered exposure time if it was longer than $2 \cdot 10^{-5}$s.

Coming back to figure 3.5, one expects so see a linear rise, starting from minimal exposure time up to the saturation level. But one sees a plateau at about 3200ADU up to an exposure time of about 1 ms, thus indicating that the actual exposure time is equal for all settings shorter than this. The interpretation that this means that the shutter is not able to cope with shorter exposure times was later confirmed by Andor.

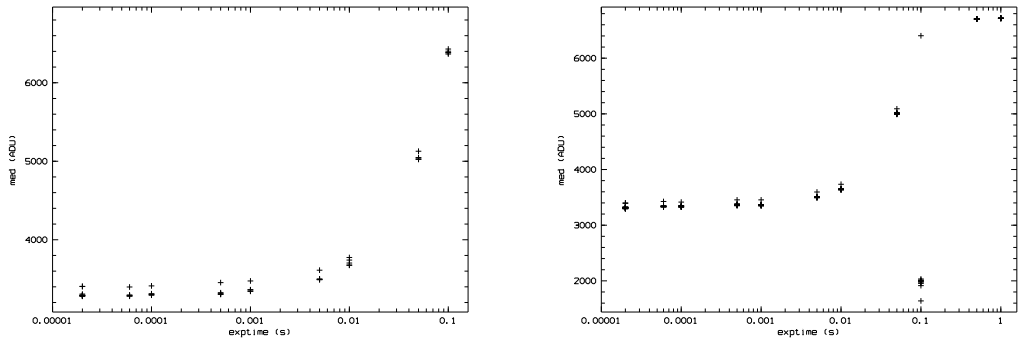

Figure 3.5.: *left:* Median vs. exposure time for flatfield (T = −78°C, gain = 1) *right:* Median vs. exposure time in kinetics mode. (T = −78°C, gain = 1)

Kinetics mode

A surprising behavior of the median signal level vs exposure time relation is observable in kinetics mode. The kinetic cycle time was set to 250 ms, the number of kinetic loops to 10. The numbers are shown in figure 3.5 (right-hand side). All non-kinectics related parameters are equal to the ones in section 3.2.4.

For a series of ten frames, the first frame has a larger median value than the last nine for every set of parameters, provided that exposure time is less than 0.1s. The gap averages 100 ADU. For an exposure time of 0.1 sec, the kinetics mode causes a gap of up to 6000 ADU. From the second to the tenth frame the median rises again by up to 800 ADU. The effect of gaps appearing does not occur for time settings above 0.1 sec. This effect was reproduceable several times.

According to Andor, this is due to the shutter functionality. No further explanation came with this statement.

3.2.5. Noise

Readout noise

To determine the noise characteristics, the signal statistics of individual frames were investigated. The signal distribution of bias frames could be described by normal distributions as expected. The variation of readout noise with gain is shown in fig. 3.6. The plateau level (for emgain < 200 for all parameter combinations) is about 1.6 ADU. For higher temperatures than used for the data in fig. 3.6 (T = −78°C), the rise of readout noise for increasing gain is less steep and therefore does not reach such a high level. E.g. the highest readout noise at $T = -78$°C is 2.8 ADU, at $T = -58$°C 1.9 ADU. Maybe this rise is due to additional noise produced and/or amplified by the multiplication process (which *is* temperature dependent).

Readout noise is showing the same characteristics and values when switching to kinetics mode.

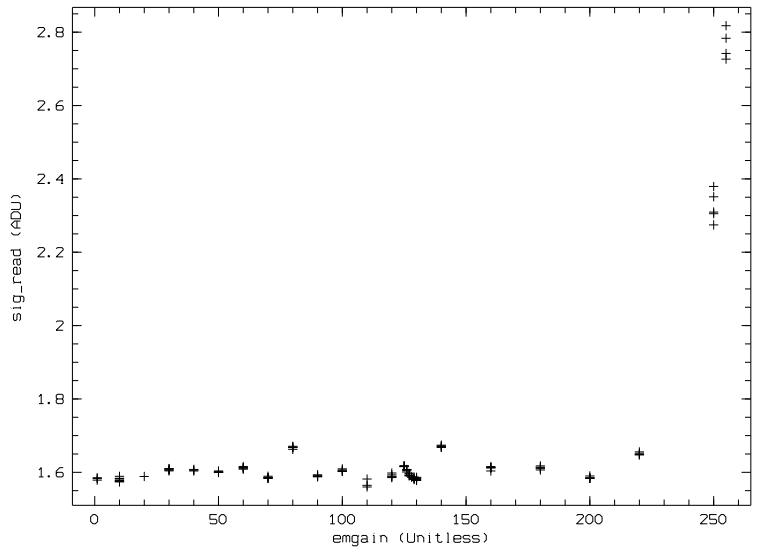

Figure 3.6.: Readout noise vs gain for T = −78°C

Dark current

Dark current was investigated as a function of gain and temperature. But because of the unpredictable variations of the bias level (see section 3.2.3), the dark current measurement did not yield the expected information about its variation with temperature. If one assumes bias variations of up to 10 ADU (maximum observed number), the dark current for temperatures below −40°C is smaller than 0.4 ADU/sec for high gains. For gain settings below 200, the dark current is likely to be less than 0.2 ADU/sec. This makes the dark current neglectable for the aimed exposure times of this high-speed camera

As a function of gain, the dark current shows the expected exponential correlation of charges multiplied in the gain register.

3.2.6. Sensitivity, actual Gain

Actual gain (not to be mixed up with the software adjustable EMCCD-gain) was determined as described in section 3.1.2.

Figure 3.7 shows the actual gain of the camera vs the software set gain. With an extrapolated software gain of *0* (measurements were only performed with software gains ≥ 1), one can determine the gain of the ADC to be about $0.03\,\mathrm{ADU}/e^-_{phot}$ or $33\,e^-_{phot}/\mathrm{ADU}$)(the vendor stated a value of $18\,e^-_{phot}/\mathrm{ADU}$ in the supplied performance sheet).

With the highest possible software-set gain of 255, an actual gain of about $10\,\mathrm{ADU}/e^-_{phot}$ was achieved, thus being well above the measured RON. But we were still getting a lower `EMgain` at maximum setting than it should be (350 vs. 1000 in the performance sheet)

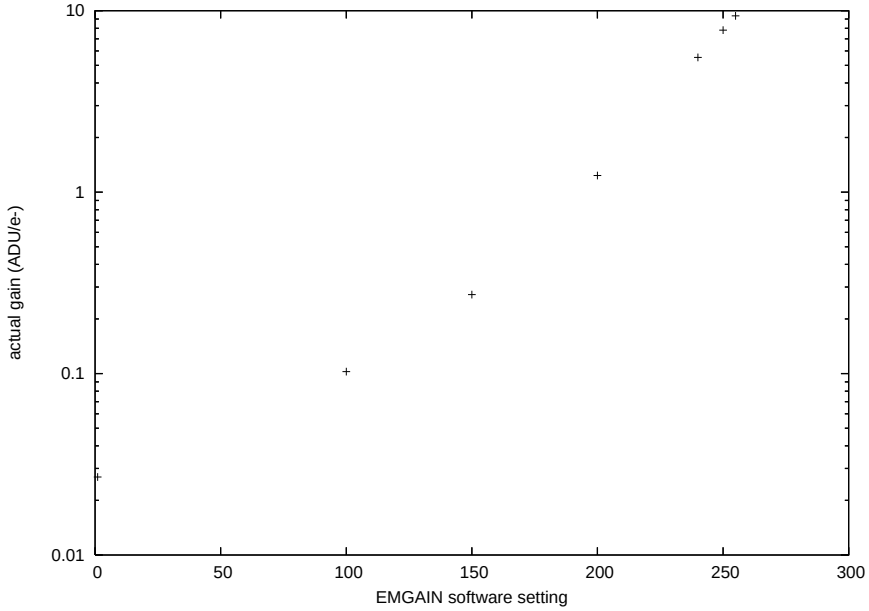

Figure 3.7.: Actual gain vs software-set gain (T = −58°C)

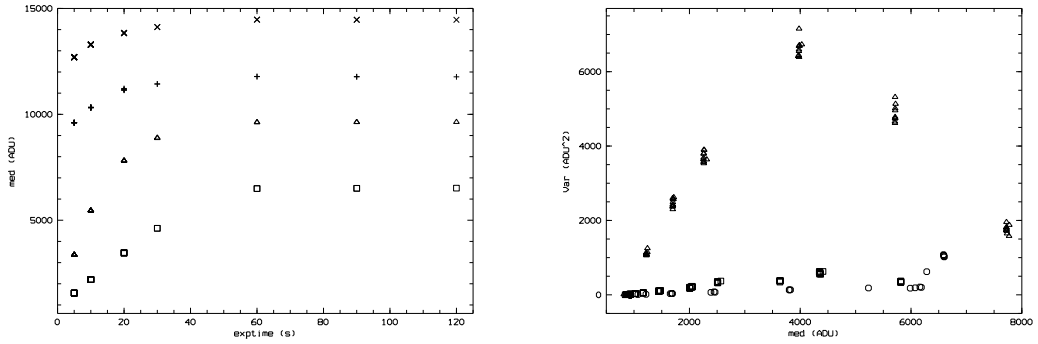

Figure 3.8.: *left graph:* Saturation level varies clearly with software gain setting (T = −78°C); □: gain = 1, △: gain = 100, +: gain = 179, ×: gain = 250 *right graph:* Check for linear response of the detector: shown is signal variance vs. median signal level. (T = −78°C); ○: gain = 1, □: gain = 100, △: gain = 200

3.2.7. Dynamic range

For measuring the dynamic range, the camera was illuminated with a constant light source. The integrated intensity was varied by changing the exposure time.

Saturation

The saturation level is considered to be reached once the signal level does not increase with increasing exposure time. It seems that the maximum value of the ADC converter is not adjusted according to the gain. As seen in figure 3.8 (left panel), the saturation level varies strongly with gain and does never reach the expected maximum value of $2^{14} = 16384$ for a 14 bit ADC.

Linearity

Fig. 3.8 (right panel) is showing variance vs median level of a small homogeneous part, obtained from several flats for several gains at T = −78°C. If we assume Var = σ^2 arising from statistical noise of incoming photons, the linear regime for the CCD ends at a median of about 4000 to 6000 ADU. Furthermore, this behavior seems to be nearly independent of gain and temperature.

3.2.8. Conclusion

The L3 design as realized in the iXon DV 887 is an extremely interesting concept for detection of low level signals. While it is in principle desirable for ATOM to use the iXon DV 887 instead of a conventional CCD model, several issues emerged from this test that voted clearly against this camera:

- Stability: The computer crashes with accompanying severe file system corruption are not acceptable.
- Overscan: there does not seem to be a method to measure an overscan or to read-out the dark reference columns and rows of the CCD87 chip, which are mentioned in the e2v CCD datasheet.
- Saturation / Dynamic range: The saturation level at low gains is quite low, resulting in a poor dynamic range.

Each of the above mentioned facts alone would be sufficient to question the eligibility of the *iXon* for daily astronomical work, but all three together are a clear rejection criterion.

Acknowledgments: I thank Olaf Koschützke (LOT Darmstadt) for lending us two times an *iXon DV 887* for test purposes. I thank Barry Smith (Andor, Ireland) for helpful hints concerning software problems.

Figure 3.9.: SamBa HR-100 (image taken from *Sensovation* web page)

3.3. Sensovations ultraCool SamBa HR-100

The *ultraCool SamBa HR-100* is a nice camera from *Sensovation*, a German company which main interests have been in medical and biological application of CCD cameras so far. The *HR-100* model is -in their point of view- also well suited for the astronomical market because of good TE cooling, allowing long exposure times with low dark current.

I had the chance to test 2 cameras, each fully functional, but not having passed the company internal quality control for different reasons. The main goal of the test was to ensure the ability to control the camera using a GNU/Linux system, since the company was only offering software for Microsoft Windows system.

3.3.1. Camera body

The HR-100 housing consists of a very mounting-friendly (in contradiction to the iXons curved surfaces) cuboidal main body with attached fan (see figure 3.9). All cable connectors are easily accessable. According to the specs, the internal TE cooler is able to cool the CCD to 100 K below ambient. All tests with the first camera were performed at an stable temperature of $-60°C$ (camera internal temperature control loop misfunction), whereas the 2nd test camera was only able to cool to $-46°C$ (due to vacuum leakage). Both restrictions were known in advance, but *Sensovation* was not able/willing to provide us with an 100% working camera for tests without waiting in the queue for more than a year.

3.3.2. Software interface

As mentioned above, *Sensovation* did not provide any Linux software for their cameras. But they did provide good documentation for older camera models that were applicable to the HR-100 software interface in most cases. Camera control exchange and data downloading is done via Ethernet. All control commands are sent in plain text to the camera on one TCP port, whereas data download triggered by some command sequence is handled through another TCP port.

All PC based software to acquire images from the camera was written from scratch for this test[9]. While I was just starting developing network communication software,

[9] I thankfully acknowledge the very helpful email support from *Sensovation* for understanding the correct syntax and order of all the necessary commands to acquire images with the HR-100.

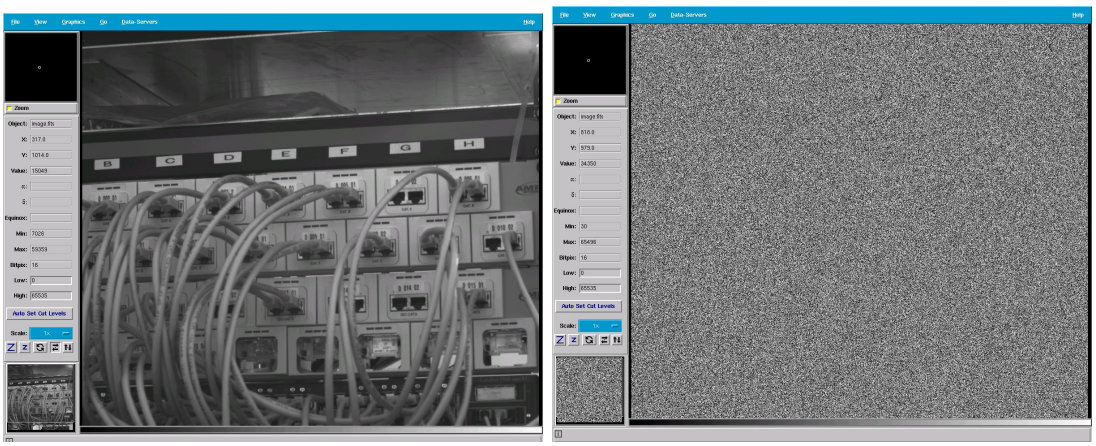

Figure 3.10.: First successful acquired and download image from a HR-100 with own Linux software (left). The right image shows the first try (should be same image as on the left-hand side) without converting the big endian numbers sent out by the camera to little endian host order.

the data download of image data from the camera clearly showed me the importance of correctly converting the endianess of numbers from network order (big endian) to host order (little endian). The effect of interpreting big endian numbers as little endian is demonstrated in figure 3.10.

3.3.3. Test parameters

The *HR-100* can be operated in two operation modes (called *HR* and *HSR*). The available documentation did not mention the intended use case for each mode. All tests have been performed using both operation modes. In addition, the camera gain can be set by software to four different values.
Due to the limited test period, all test were performed at a single temperature only.

3.3.4. Bias stability

To test for bias level stability, several images in complete darkness with exposure times $t_{exp} = 0$s were acquired in a row (see figures 3.11, 3.12). The bias level was stable at all parameter combinations. However, it was noticed that the signal level scatter is significantly higher when operating the camera in *HSR* mode.

3.3.5. Gain measurements

Gain measurements have been done according to the method described in section 3.1.2. The measurements are shown in figure 3.11 for the *HS* operation mode and in figure 3.12 for *HSR* resp. The results are summarized in table 3.2.

3.3.6. Conclusion

This camera is offering good performance and a well-usable software interface and seems on the technical site well suited for the ATOM project. But after tests of the *Alta E47+* system (see sec. 3.4.2), the slightly better performance of the *Sensovation HR-100* seemed not to justify the significantly higher price w.r.t the *E47+*.

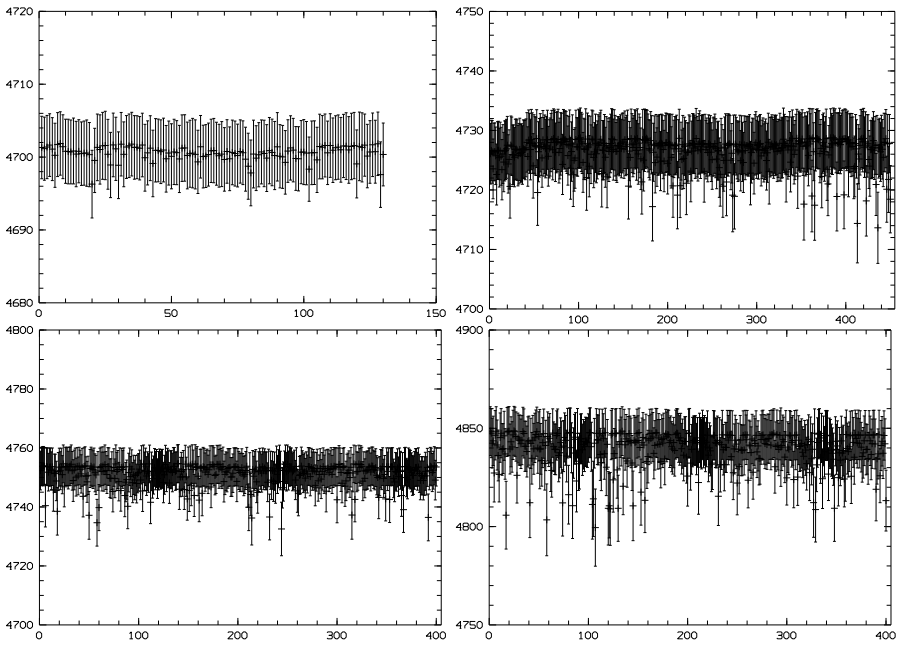

Figure 3.11.: Shown here is the bias level (median signal value and RMS over the complete CCD vs. a running number) at operation mode *HS*, software gain setting was changed from 1 (upper left) to 4 (lower right panel). The bias level is stable within errors.

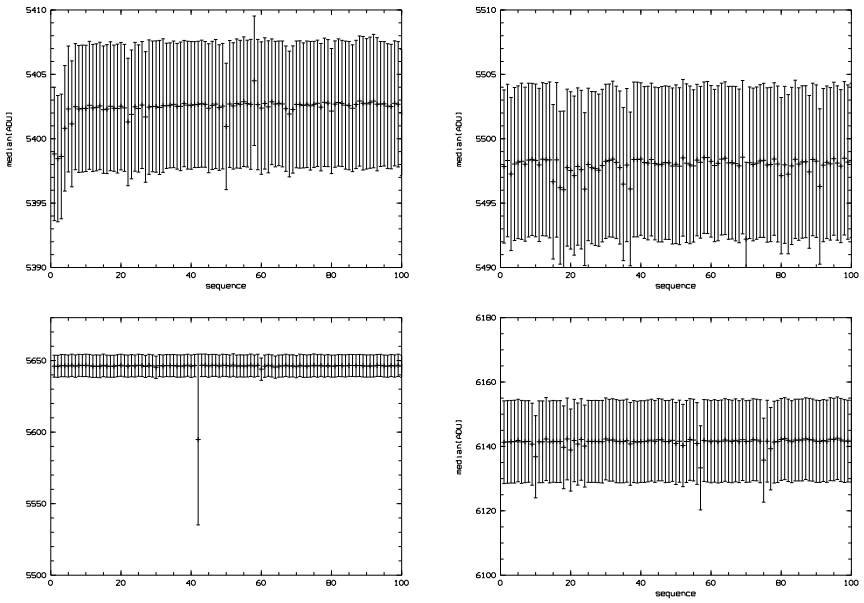

Figure 3.12.: Bias level; same as in fig. 3.11, but for operation mode *HSR*. During the measurement cycle with software gain setting 3, one outlying measurement was observed. This is not understood, but is a complete singular event. Since these measurements were performed unattended, it cannot be ruled out that e.g. a (very short) power glitch occurred, messing up CCD clocking and readout voltages. Otherwise, the bias level is stable within errors.

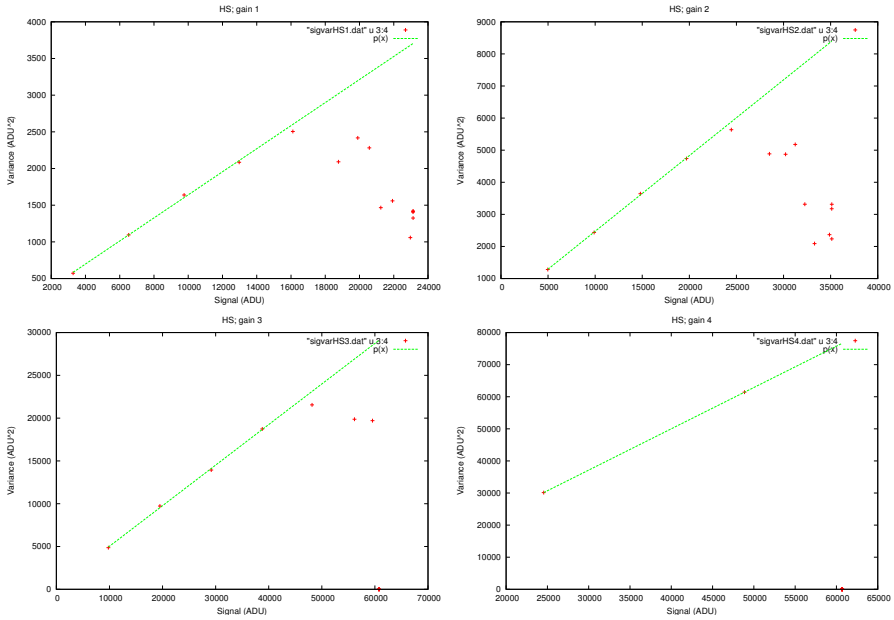

Figure 3.13.: Gain measurements of SamBa HR-100 camera for operation mode *HS* 1–4

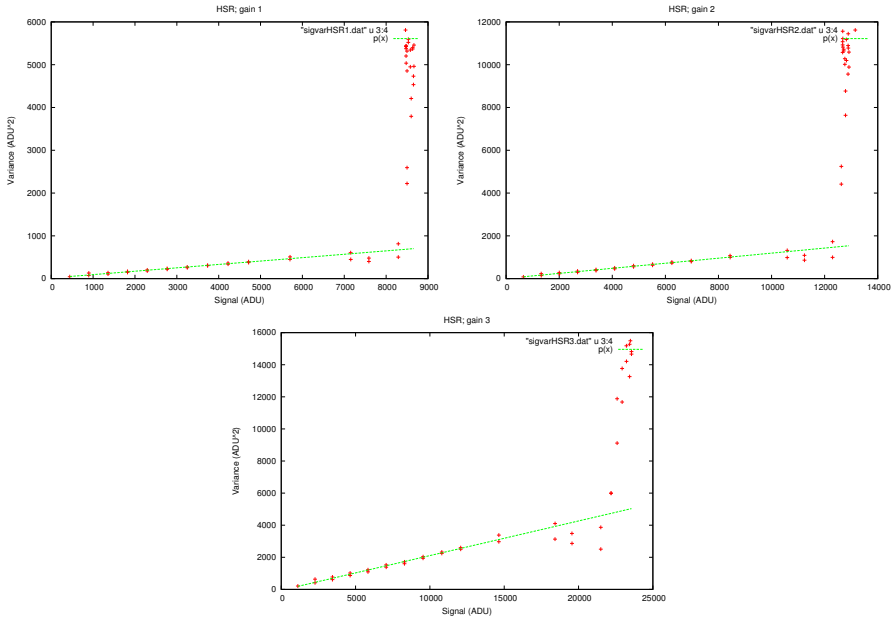

Figure 3.14.: Gain measurements of SamBa HR-100 camera for operation mode *HSR*. No data for the parameter combination operation mode *HSR*, gain 4 could be acquired because of time constraints.

operation mode	gain parameter	linear up to [ADU]	measured gain [e^-/ADU]
HS	1	15000	6.37 ± 0.17
	2	23000	4.28 ± 0.05
	3	44000	2.11 ± 0.04
	4	55000	0.73 ± 0.01
HSR	1	6000	12.5 ± 0.4
	2	10000	8.45 ± 0.23
	3	16000	4.54 ± 0.13
	4	*no data taken*	

Table 3.2.: summarized gain measurements of SamBa HR-100 camera

3.4. Apogee *Alta* platform

Apogee is manufacturing and selling CCD camera systems to the astronomical community for quite some time. When starting to look for a camera system for ATOM, they were just introducing their *Alta* camera platform into the market. Their product strategy is to offer one camera platform (one housing type in three different sizes) with the same hard- and software interface equipped with different CCD sensors. The computer interface is either USB or TCP/IP over Ethernet. This offers interesting prospects with regard to ATOM, since –in principle– it would allow us to use the same type of camera for guiding (with a small and cheap CCD) and for science (with a high quality CCD), thus cutting the necessary software development on the camera interface side by 50%. And an TCP/IP Ethernet connection between camera(s) and control computer has no practical limit in cable length, is robust against electromagnetic interference when using S-STP cables[10] and is using a connection-oriented protocol that has proven its reliability by being *the* protocol for ≈ 40 years of success of the Internet. The fact that this connection camera $\Leftrightarrow$ control computer does not require any special hardware to be added to an *off-the-shelf* computer makes it even more interesting for an automatic system like ATOM.

An *Alta E1* type camera was bought to be used as guiding device of ATOM. After successful tests of this camera, it was decided to use an Alta model housing a high quality CCD (the *E47+ model*) as science camera for ATOM. The tests and performance of these two cameras are described in the following sections.

3.4.1. Alta E1

The *E1* model is housing a *Kodak KAF-0401E* CCD chip (see Eastman Kodak Company (2000) for a detailed description of chip specifications). The 768x510 9μm pixel size transforms with the ATOM focal length to a FoV of (4.1x2.8) arcmin on the sky. Using the image plane rotator, this leads to an accessible FoV of nearly 800 arcmin^2 for the guiding camera as shown in eq. (2.1). This allows for finding a guide star for nearly every telescope pointing position in the sky.

Since chip size and camera interface matched our requirements for a guiding camera,

[10] at least when using cable length $\ll$ 100m as it is assumed here

an *E1* was bought to work as the guiding camera for ATOM. Before shipping it to the telescope being already in Namibia at this point in time, the characteristics of this camera were measured as reported in the following.

Cooling

To get the CCD to the lowest possible temperature, the cooling test was performed in the dome of the 70 cm telescope of LSW[11]

The requested CCD temperature was reduced stepwise until the device could not cool deeper. This was repeated with fan speeds `medium` and `fast`. As it can be seen in figure 3.16, a detector temperature of $-30°\mathrm{C}$ can be reached and held stable.

Dark current

The dark current was measured at a detector temperature of $-20°\mathrm{C}$. A lower detector temperature was not achievable due to a high ambient temperature in the Faraday cage (where the dark current measurements were taken). A signal increase of $0.0013\frac{\mathrm{ADU}}{\mathrm{s}}$ was found using a linear fit to the data taken at $T = -20°\mathrm{C}$. Using the results of section 3.4.1, this corresponds to $0.002\frac{\mathrm{e}^-}{\mathrm{s}}$. *Apogee* specs are giving $0.08\frac{\mathrm{e}^-}{\mathrm{s}}$ for $T = -25°\mathrm{C}$.

Hot pixels

An annoying problem with this camera –and as later visible also with its "big brother", the *E47+* (see 3.4.2)– is the relatively large number of *hot pixels*, i.e. pixels which are giving signal levels significantly higher than their surrounding neighboring pixels. This is shown in figure 3.18.

These pixels are spacially constant, which means they are a problem of the CCD chip itself and not originating from the read-out electronics. Further investigations showed that their intensity is a function of integration time and CCD temperature, thus allowing for a subsequent removal through image processing.

Gain and linearity

The measurements were taken as described in section 3.1.1. Individual test parameters were lamp voltage $U_{\mathrm{lamp}} = 2.0\mathrm{V}; I_{\mathrm{lamp}} = 513\mathrm{mA}$; lens aperture 5.6; focus infinitesimal, detector temperature $T = -20°\mathrm{C}$.

A linear fit results in a detector gain of $1.7\frac{e^-}{\mathrm{ADU}}$ (*Apogee* claimed $1.4\frac{e^-}{\mathrm{ADU}}$ in their test report.

Read-out noise

Apogee claimed a RON of 8 ADU, which could be verified in all 10 measurements (see figure 3.20 for pixel histograms).

[11] This was the coolest place available which offered power and network connection

Figure 3.15.: Camera body of an Apogee ALTA camera system.

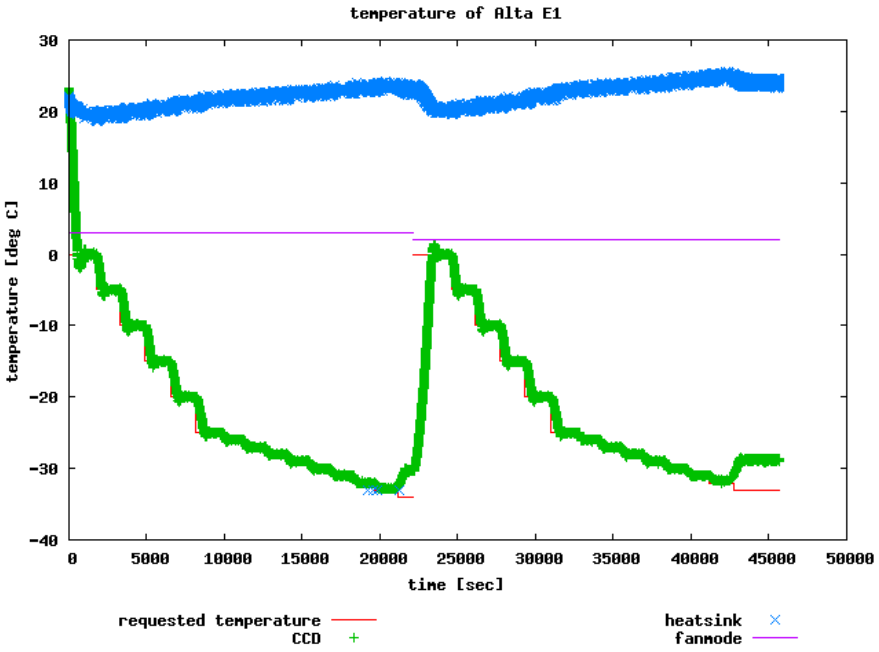

Figure 3.16.: Cooling capability of Alta E1: CCD temperature *vs.* time. The setpoint was ramped down in regular intervals until the Peltier cooler could not follow anymore. The experiment was repeated with the speed of the camera fans set from *fast* to *medium*. No significant change in the reachable maximum temperature difference CCD-ambient was found with the different fan speeds.

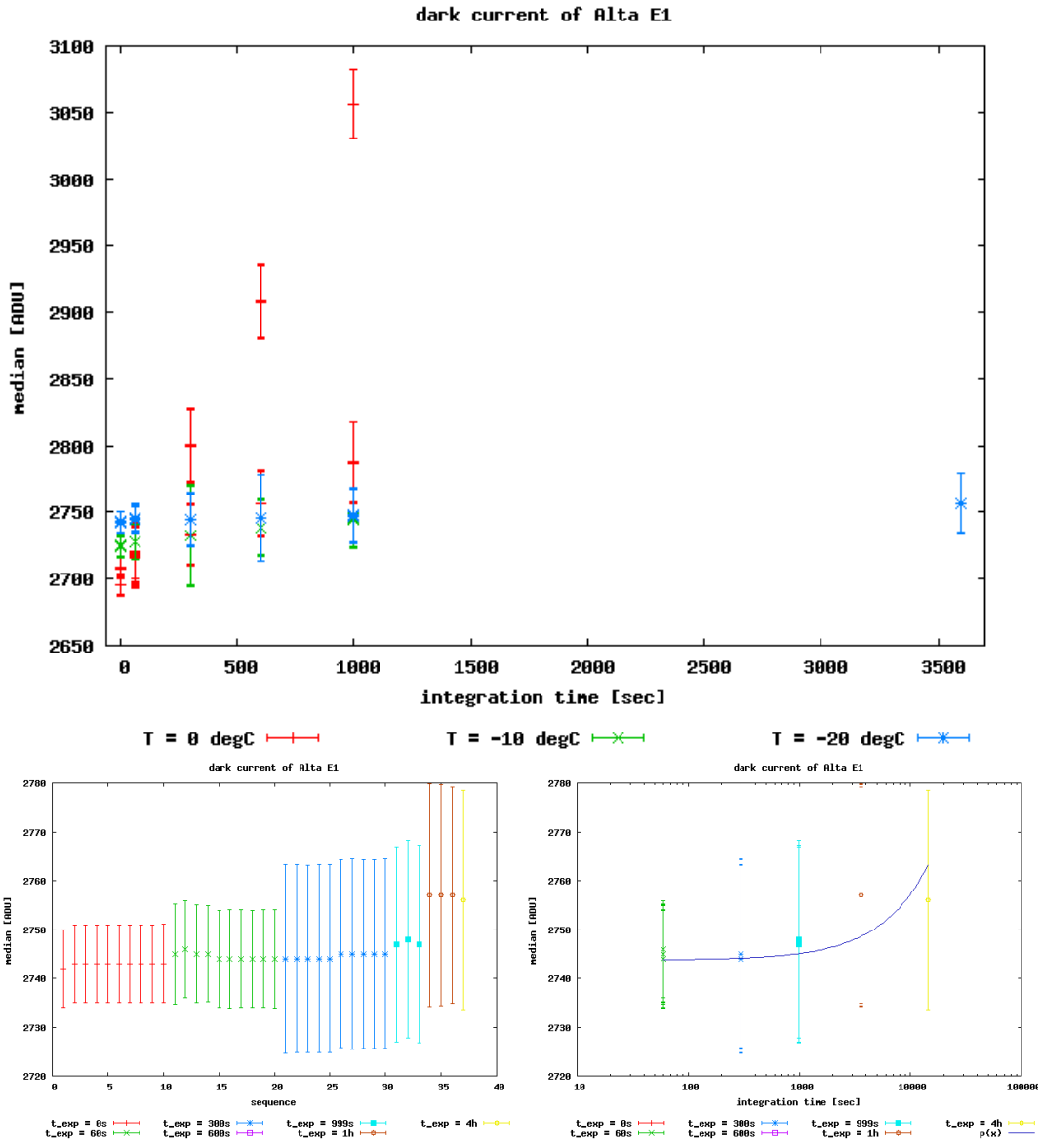

Figure 3.17.: *upper plot:* mean signal intensity in dark frames at different integration time and temperatures.
lower plots: measure dark current at $T = -20°\mathrm{C}$, the $\log(t)$vs. $< I >$ graph on the right side is also showing also a linear fit to the data.

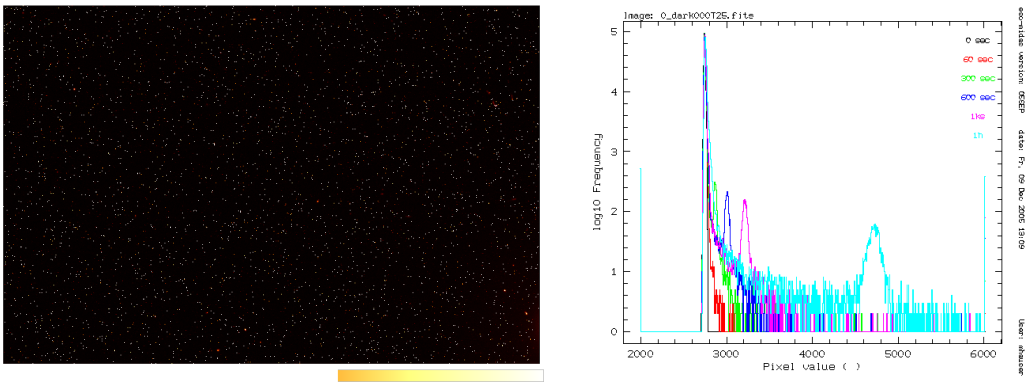

Figure 3.18.: *left:* one hour dark frame; *right:* histogram of signal values in dark frames of different integration time. The clearly visible peak at higher pixel values is due to the hot pixels. A signal increase with longer integration times can be seen.

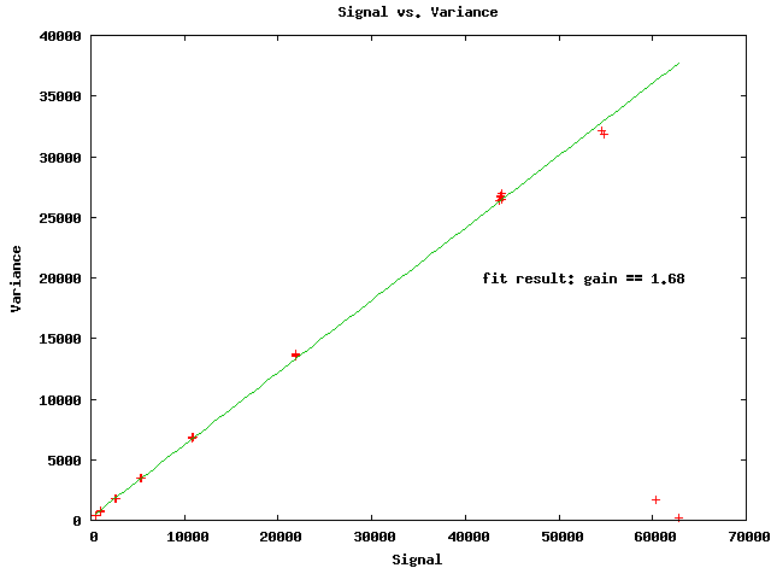

q

Figure 3.19.: Signal vs. variance plot to determine the detector system gain. Also noticeable here is that the dynamic range in which the camera is operating as a linear detector goes up until ≈54 kADU.

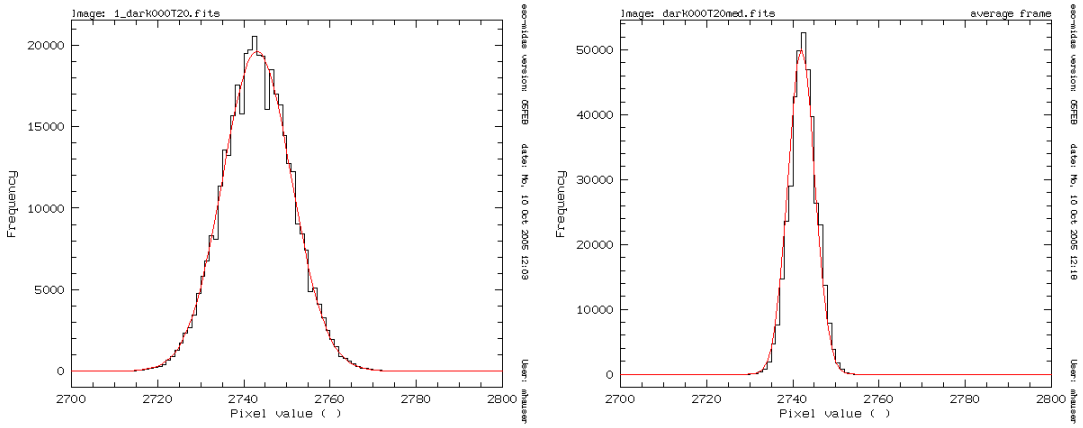

Figure 3.20.: Signal distribution per pixel in bias frames. *left:* single frame, FWHM=7.98 ADU; *right:* 10 frames median-averaged, FWHM=3.12 ADU.

3.4.2. Alta E 47+

After the first experiences with the *E1* model, it was decided to go for an *E47+* model to be used as the main/science camera for ATOM. This camera type is housing an *E2V 47-10 grade 0* CCD chip (see E2V (2000) for a detailed CCD chip description), the same type of CCD as the *Sensovations* camera described in section 3.3)[12].

Nominal (from the sales brochure) resolution of the camera system is 1024x1024 pixels, the physical size of the CCD is (1056 + 2x 8 dark reference) x 1027 pixels, each with a size of (13x13) μm. Due to limitation in the software drivers (Mills (2005)), the maximum read-out region is limited to 1040x1024 with the 8 rightmost columns being dark reference columns. When mounted on ATOM, the camera resolution on the sky is 0.47 arcsec/pixel, thus leading to a maximum FoV of 8x8 arcmin. This is illustrated in figure 2.8.

All data used in the following tests was acquired using `instops` (sec. 2.3.4) in October 2006. CCD test temperature was $-25°$C[13].

CCD cosmetics

The following pixel defects were found:

- bigger region around (380,320) having a higher intensity (few percent) at red wavelength w.r.t. the background. This effect is not visible at blue wavelengths. It can be corrected using flat fields (see figure 3.21).
- black spots (max. 80% intensity of surrounding pixels):
  - 4 pixel at (535,344)
  - 1 pixel at (728,735)
  - 5 pixel at (916,94)
  - 1 pixel at (1002,223)

  Since E2V specs allow up to 50 black spots for *grade 0* chips, this had to be accepted.

U band features

As it can be seen in figure 3.22, large structures are visible in U band (λ =360 nm). These are most probably due to the CCD coating. As demonstrated in figure 3.21, these artefacts can be removed using the flat fielding technique.

CCD gain

A CCD gain of of 1.14 e^-/ADU ($\pm$1%) (see figure 3.23) was measured. Apogee claimed 1.4 e^-/ADU in their test report.

[12]The specifications of the *Sensovations ultraCool SamBa HR-100* camera were superior to the *Apogee Alta E47+* in nearly all disciplines, but this camera system was also about three times more expensive.

[13]Apogee tested at $-32°$C, but this temperature was not reachable at LSWs ambient temperature.

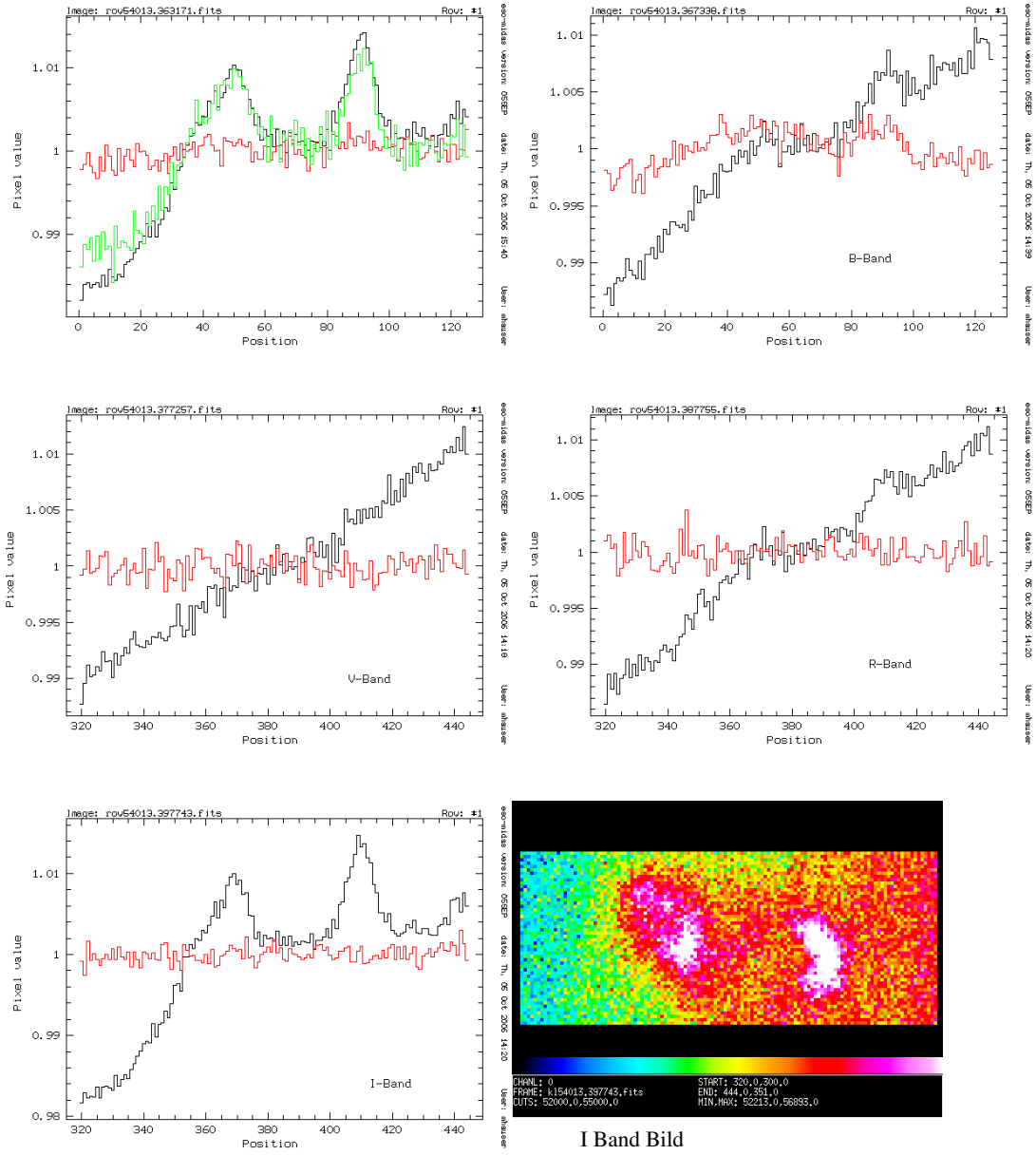

Figure 3.21.: Two bright spots are visible in red filterbands. Plots are showing line intensity (column 325..450), averaged over rows 300..351. Black lines are from raw frames, whilst red lines are after flat field correction. The peaks in U band graph were found not to be caused by inhomogeneous sensitivity in the U band, but by very red light passing through the U band filter. To test this, a very red light source (light bulb with $\approx 1500\,\mathrm{K}$) was used. The green curve in the upper-left plot is an exposure through an U band + blue-block filter (no transmission below 630 nm) in the optical path, so one would expect this filter combination to be completely opaque, which it is not $\rightarrow$ peak is coming from red light.

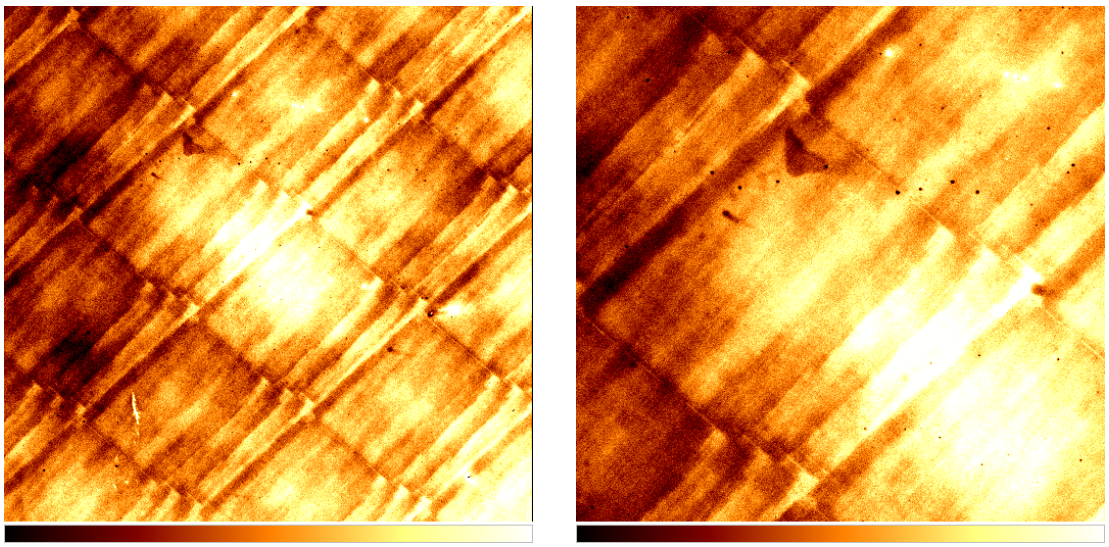

Figure 3.22.: Large structures visible when using U band filter.

Read-out noise

A RON of 7.00 ± 0.016 ADU was measured. According to section 3.4.2, this translates to $5\,e^-$. Apogee claimed $9.4\,e^-$ in their test report.

Cooling

The CCD was able to reach a temperature of -30°C whilst having a heatsink temperature of $+28$°C (using fastest fan speed; see also figure 3.24. The ambient temperature was about 21°C.

Apogee performed their tests with a "Delta of 54°C". Unfortunately, they did not specify if that is *CCD vs. ambient* or *CCD vs. heatsink*. The specification is 55°C below ambient.

3.4.3. Conclusion on Apogee cameras

Both Apogee cameras offer sufficient performance and were the cheapest camera systems in the test sample. The software interface is lacking a proper documentation, but is still usable.

A clear advantage of the common camera platform for scientific and guiding camera is that both are operated through the same software interface, thus reducing the development efforts and making maintenance easier.

The Apogee Alta platform was choosen for both the science and guiding camera for ATOM.

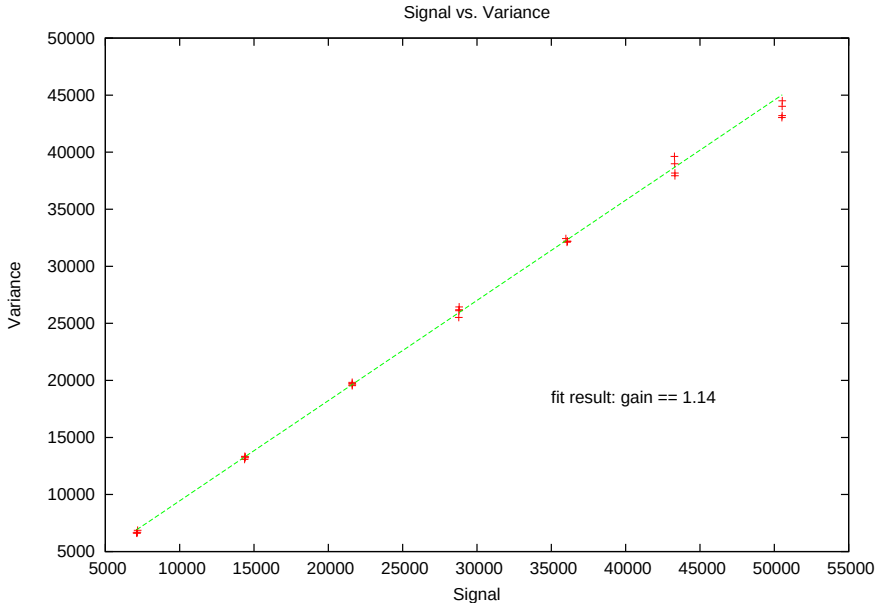

Figure 3.23.: Signal vs. variance plot for E47+. Exposure times ranges from 5 to 35 seconds.

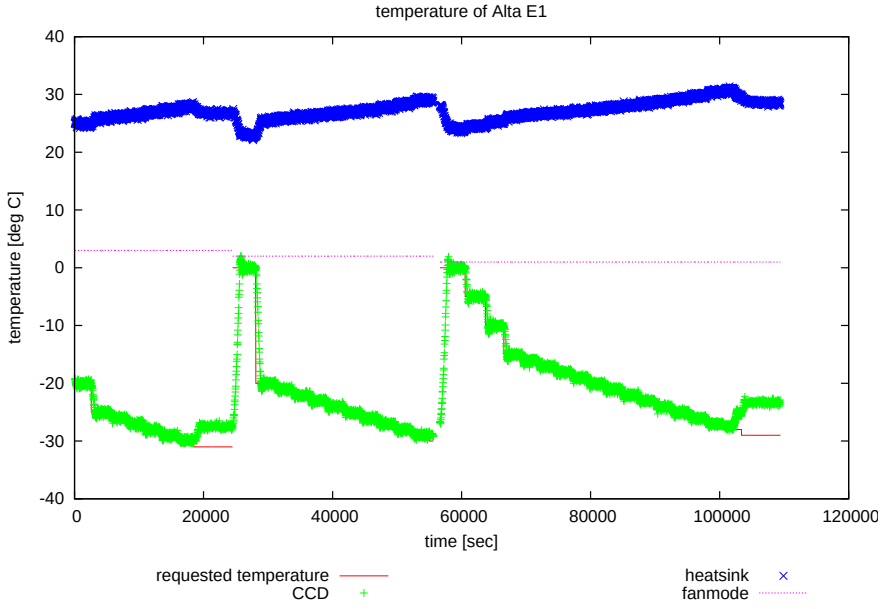

Figure 3.24.: Temperature of Alta E47+

4. Operating ATOM

ATOM is nowadays typically operated in an automatic way (although we are aiming for full robotic operation, this stage has not been reached yet). The software for basic automatic operation was written by B. Behera and is capable of distributing a pre-defined list of static commands to the telescope and instrument control software (which are described in sec. 2.2.1 and 2.3.4) in a pre-defined given order. A possible upgrade for this software would be the capability to make decisions based on dynamic input parameters like weather, upcoming ToO, changed target priorities and so on. For a detailed description of this automation software, see Behera (2010).

There are more tasks required to have ATOM running in an automatic way than just distributing predefined commands in fixed syntax to the hardware daemons (e.g. creating these commands, reacting to changing weather conditions...). Development and implementation of all these tasks has been a part of this thesis and is described in the following sections.

The operation of ATOM consists of the following daily duties for the person in charge of ATOM operation:

1. during daytime, check for the outcome of last nights observations (e.g. detected flares, technical problems, have a look at frames if ADRAS (the pipeline analysis task, see sec. 5) failed on processing them, etc.). Check for flares of AGN at any wavelength (most time reported via *Astronomers Telegrams*).

2. late afternoon, create the observing schedule for the upcoming night (see next section, 4.1). Pay attention to the planned H.E.S.S. schedule for the night and make sure ATOM observes all AGN on the H.E.S.S. schedule sometime during the H.E.S.S.observation of that source.

3. sunset in Namibia: check for weather by inspecting the webcams located at the H.E.S.S. site, approve automatic start-up of ATOM

4. shortly after start of observations, check if the system is running.

5. if possible, check occasionally during the night if everything is going well.

[During ideal times, tasks 3-5 were shared between all H.E.S.S. group members at LSW in a weekly turn]

4.1. Scheduling

The observing schedule for ATOM and thus the control files for the automatic observing software mentioned at the beginning of section 4 is created daily and based on two input parameters for each target: the weight w (representing the importance of the target) and the intended observing frequency f (time between two consecutive pointings). Together

with the date of the last successful observation (latency l), these three numbers are transformed into a priority P which then is used to choose the targets for tonight's observations.

To account for visibility conditions, the following modifications are applied to the target weights w based on the maximum target altitude $h_{\max}$ over ATOM whilst the sun is more that 12° below the horizon before the final calculation of observing priority P are done:

- $30° < h_{\max} \leq 40°$: weight w is decreased by 40%
- $20° < h_{\max} \leq 30°$: weight w is decreased by 60%
- $h_{\max} < 20°$: $w = 0 \Rightarrow$ target will not be on schedule.

At time of writing, the quantity $P = P(w, f, l)$ is computed like (with pressure p as an auxiliary quantity stating how urgent a observation is; $p > 1$: observations overdue)

$$P = w \cdot \underbrace{\frac{l \cdot f - 1}{6} + 1}_{\text{pressure } p} \tag{4.1}$$

In addition, P is reduced by 50% if the pressure $p < 0.95$ to damp the probability of observing targets more often than requested[1]. The parameters for calculation P as given above were found empirically and are giving a time-efficient scheduling for ATOM, allowing us to observe the ≈ 280 targets in the ATOM program with their different weights and frequencies. To give some numbers: during good observing periods (9 full night observations in 10 days), a source must gain on average a priority $P \geq 6.5$ to be on the schedule.

Figure 4.1 is demonstrating the overbooking of some RA bands with the requested observing frequencies of different targets.

The requested observing time per 1h RA band is computed as the sum over all targets in this RA band, taking into account the exposure times in B+R, a constant overhead C for telescope pointing and camera read-out and the observing frequency f. The average value of $C = 150\,\text{sec}$ was found empirically.

$$\text{req. time / RA band} = \sum_{\text{all targets in RA band}} (t_{exp,R} + t_{exp,B} + C)/f \tag{4.2}$$

The algorithm presented above is implemented in the software `scheduling_info.py` (see table F.3), the quantities w, f are stored in the target definition tables of ADRAS (chapter 5).

The next step in preparing the automatic observations is to translate the now fixed schedule in single commands to control the telescope and instrument. This is done by the program `createComSet` (see table F.3). It queries the ADRAS tables for exposure times in the different requested filter bands and checks for boundary conditions like angular distance to the moon and minimum and maximum[2] altitude during the exposures. Its

[1] It is not set to $P = 0$ because there is the slight chance that there is no competing object in a certain RA band, and it is ok to e.g. observe a monitoring target that should be observed once per week already after 5 days to reduce the overall pressure in the following night.

[2] remember that ATOM is a telescope with an AltAz mounting and thus has a zone-of-avoidance around the zenith when tracking.

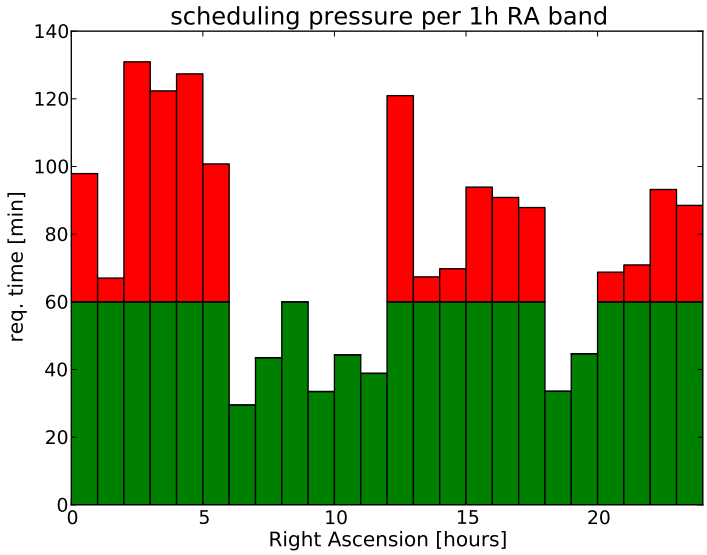

Figure 4.1.: Scheduling pressure for ATOM observations beginning of 2011. The red-colored RA bands are overbooked, partly by more than a factor of 2.

output is an control file which holds one command for the hardware control software per line together with rules which individual previous command(s) must have finished before it can be launched. This file is used as input to the "robot" program mentioned in the beginning of this chapter.

4.2. Usage of cloud monitor

The informations provided by the all-sky cloud monitor presented in section 2.5 is used to interrupt ongoing observations during the night if the cloud coverage is getting too heavy and to restart observations once the sky gets clear enough.

The cloud monitor provides an estimation of sky transparency (0: completely covered, 10: cloudless night) of 13 individual sectors on the sky. The transparency in each sector is estimated by counting stars and comparing the number of detected stars with the number of stars listed in the *Bright Star Catalogue* (Hoffleit and Jaschek (1982)) down to 7th magnitude.

The following sky transparency conditions have to be fulfilled to convince the sky monitoring software that the weather is good enough to open the roof of the ATOM shelter and start observations:

- at most 5 sectors rated *bad*
- at most 1 *critical* sectors rated *bad*

A sector is rated as *bad* if the sky quality is estimated to be ≤ 5. The *critical* sectors are the inner ones, i.e. with a zenith angle of less than 45°. On top of the general bad rating valid for all sectors, the critical sectors have an additional quality flag which is set to *bad* if the quality is ≤ 5

To prevent getting annoyed by short-term fluctuations, a permanent rating as *bad* for 5 consecutive measurements is required to trigger any action. For the *critical* ratings, this is shortened to 3 consecutive measurements[3]. The timing constraints (5 and 3 consecutive measurements) were relaxed to this values after the first studies of typical timescales of weather changes above Goellschau were done. This is described in sec. 6.2.2.

The software is also capable of the reverse process: start observations if the cloud coverage vanishes (or at least weakens). The same conditions as for stopping applies: if for 5 consecutive measurements the conditions do not request closing the roof, observations will be resumed.

At present stage, this procedure is suffering from one big limitation of the robot software: once it is running, it is impossible to interact with this program. So if clouds are moving in, the only possibility to stop the robot software is to hard kill it. This can lead to the situation that the operation is terminated in minute 29 of a 30 min exposure. And since there is no way of communication, the exposure will be corrupted because the shutter will stay open whilst the telescope is slewing to its parking position, mirror cover is closing, etc. A similar problem occurs when re-starting observations in the middle of the night: the system will not do anything until the next scheduled (based on the schedule crated during daytime, assuming uninterrupted observations) observation of the next target is about to start. Example: the system is re-started at minute 1 of a planned one hour observation of a faint source[4]. The system will then "*sit and relax*" for 59 min during acceptable observing conditions and wait for the pre-planned start of the next target in the schedule. If the cloud conditions change several times during the night, this may result in a night without any useful observation done despite of several usable hours of observing time (summed up).

The way out of this problem would be to upgrade the robotic software so that it would be able to communicate with the outside world (mainly with the weather information services) and to implement a dynamic scheduling algorithm.

The above described procedure is realized in the script `skyqual.py` (see F.3).

4.3. The rain sensor

The rain sensor, already presented in section 2.4, is of course also used during automatic operation. There is no big logic involved here. If rain is detected, a script[5] is called which checks for the status of the enclosure and –if found open– closes the roof instantly. The ATOM start-up scripts are checking the rain sensor, too. If rain is detected right now or was detected 30 min ago, the script[6] will refuse to open the enclosure.

[3] I am afraid of a single black rain cloud right above the telescope. Although such a condition of a single cloud bringing rain has not yet been spotted, it would be annoying if the first report of such a condition would be rain on the main telescope mirror.

[4] For faint sources, exposure times of e.g. 30 min in B and 20 min in R band are common. Including overhead, a two color observation of a faint source may take up to nearly one hour of scheduled observing time.

[5] `stopTelescope.py`, see appendix F

[6] `startTelescope.py`, see appendix F

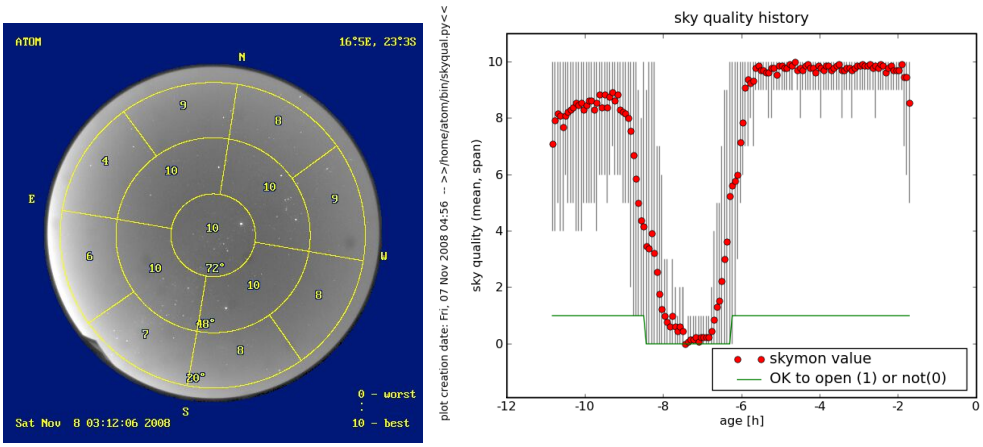

Figure 4.2.: Example of sky transparency estimation by the all sky cloud monitor.
left: image of the sky with the individual sectors and quality numbers overlaid. *right:* the trend over the whole night. The red points are the arithmetic mean over the whole sky per measurement, the grey bars are giving the span (minimum and maximum value in all sectors). The green line at the bottom shows the result of the *clear-to-open* estimation discussed in section 4.2 (0: close; 1: open).

4.4. Focussing the telescope

The telescope focus is mainly depending on the telescope temperature. Given the fact that the ATOM building roof is made of corrugated metal sheets and the building is not equipped with air-conditioning, one can easily imagine that there are significant temperature changes between hot Namibian afternoon hours and cold desert nights under a cloudless sky (see fig. 4.3). It was found that the focus can change quite rapidly (on timescale of tens of minutes), especially at the beginning of the night. Thus the focus has to be adjusted several times per night to assure a good image quality.

The usual way of finding the correct telescope focus is to image a star several times with different focus values, measure the FWHM of the stars light distribution on the CCD as a function of focus value, fit a 2^{nd} order polynom to the data and determine the minimum value. Although this procedure could be automated, it would still take at least ten minutes to get the correct focus and would require a break in the scientific data taking. Even more important, it is impossible with this procedure to adjust the focus during an ongoing exposure. And such *"focussing breaks"* would be needed several times per night.

Because of the above mentioned limitations, another method to find the correct telescope focus was implemented. Outside the central focal plane, the telescope optics is suffering from astigmatism. The FoV of the guiding camera is ≈ 34 arcmin away from the central optical axes, far enough that the astigmatism creates significant image distortion. This effect causes a point source (aka *star*) to appear not circular, but ellipsoid on the guider image plane, *if the telescope is out of focus*. The main axis of the image ellipsoid is then orientated either in the vertical or horizontal direction, depending on the telescope focus being *intra-* or *extra-focal* (see figure 4.4 for an example). This means that the images taken by the autoguider can be used to adjust the telescope focus even

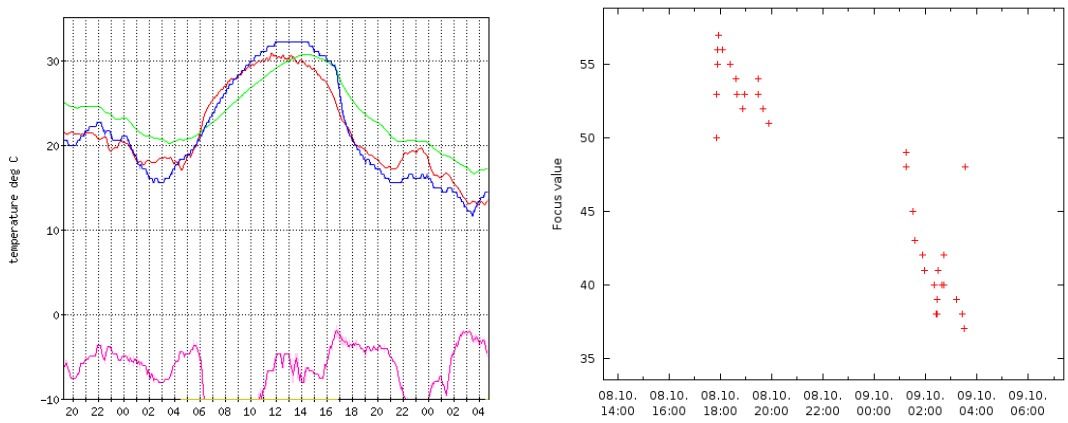

Figure 4.3.: Temperature changes at the telescope on Oct 09, 2010 (left graph) and the resulting telescope focus values (right graph)), determined with the method described in section 4.4. For the temperature graph, the *blue line* corresponds to the temperature measured directly at the telescope tube, *red* is the temperature outside the ATOM building and the *green line* is showing the temperature measured inside the building. The *pink line* at the bottom is giving the dew point. Note how fast the telescope temperature adapts to the outside temperature once the building is opened at sunset.

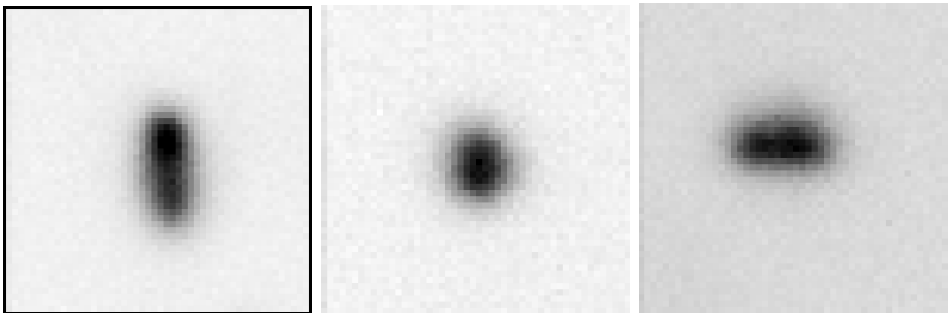

Figure 4.4.: Example of auto guider images at different focus values.
left: focus value too high; *middle:* focus ok; *right:* focus too low

during an ongoing scientific exposure without any overhead in terms of observation time.

To achieve this, the image analysis step inside the autoguider module of the `instops` software was improved. The system does fit a 2D Gaussian profile to the light distribution of the guiding star to determine the positional offset. This information is used for telescope guiding. What is new here -and now used for focussing- is that the relative extensions in the x and y directions are used to compute focus offset information.

The focus offset is computed the following way (Θ being the angle between $+x$ direction and the ellipsoid main axis, e ellipsoid elongation (see also fig 4.5). Tuning parameters are e_{thres} (elongation threshold) and ϵ (amplitude)):

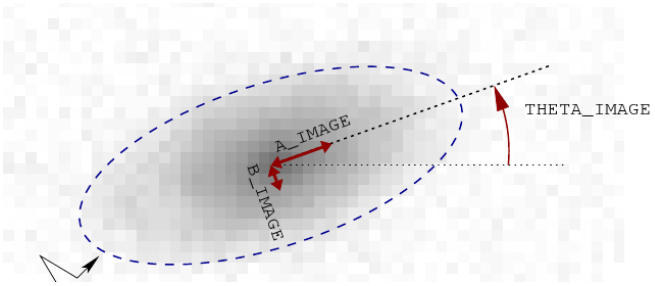

Figure 4.5.: Illustration of image parameters used for focussing (figure taken from Bertin and Arnouts (1996)).

$$\begin{aligned} |\text{focus\_offset}| &= (e - e_{\text{thres}}) \cdot \epsilon \\ \Theta &= \begin{cases} < 20 & \Rightarrow \text{sgn}(\text{focus\_offset}) = 1 \\ \geq 70 & \Rightarrow \text{sgn}(\text{focus\_offset}) = -1 \\ \text{undefined} \end{cases} \end{aligned} \tag{4.3}$$

It was found that a decent focus can be achieved by choosing the values $e_{\text{thres}} = 1.1$ and $\epsilon = 4$ for the tuning parameters. A maximum focus correction per step of 4 units was introduced to avoid messing up the focus completely in case of a very distorted image due to cosmics or other image artefacts.

Everything stated above requires of course that the focal plane of the autoguiding camera is the same as for the science camera to make this procedure work. Since the CCD of the guiding camera is physically not placed in the same plane as the science CCD (see section 2.3.3 for a description of the hardware layout), one has to make sure that the *optical length*[7] to the guiding CCD is the same as to the science CCD. The guiding camera can be moved along the optical axis to adjust for any possible offset. The procedure used here was first to focus the telescope without taking the autoguider into account and then secondly move the guiding camera to minimize the measured FWHM on the stars images on the guiding CCD *without changing the telescope focus*. After the guiding camera was in focus, it was checked that the telescope focus has not changed in between (i.e. that the science camera was still in focus). This was done once during commissioning in November 2006 and re-checked again in November 2009.

The result of this control focus run with the science camera in November 2009 is shown in figure 4.6. The best focus found using the automatic method based on the guiding image morphology before *and* after the focus run was 43, a value which matches the minimum FWHM found in the science camera exposures when varying the telescope focus. So the validness of my focussing method was confirmed.

4.4.1. Focussing problems during spring 2010

The effectivity of ATOM was lowered during spring-time 2010 because of some problems with the telescope focus. The found focus encoder values were several 10 units[8] lower

[7] The optical path to the science camera is shorter than the geometric one, because of the filter inside the beam to the science CCD.

[8] Scale is like 1 focus unit $\approx 30\mu$m linear movement of the secondary mirror along the optical axis of the telescope.

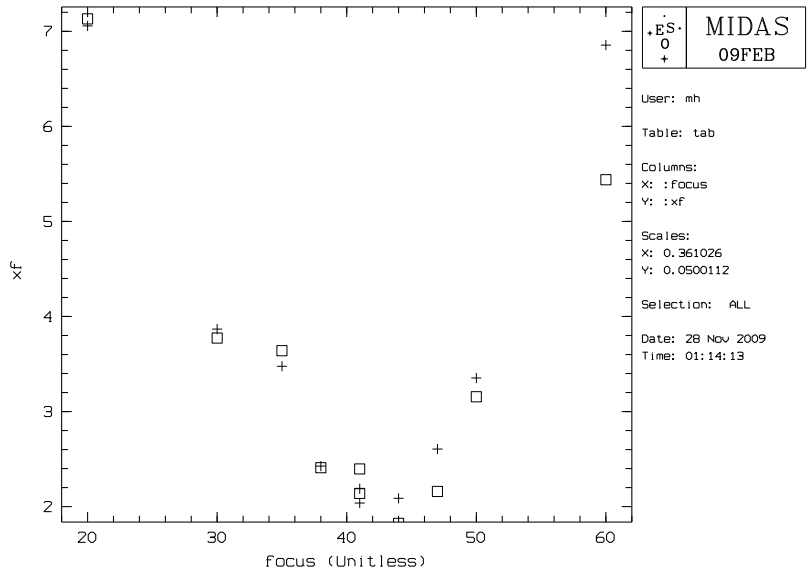

Figure 4.6.: Focus run in November 2009. Shown is the FWHM of a star in arcsec as a function of telescope focus. Note that the best focus value found by the automatic system based on the autoguider images before and after the focus run was *43*, a value which matches the minimum FWHM found on the science exposures.

than expected, with several big changes on arbitrary daily time scale over the following month (no big changes were found during any night). This is illustrated in fig. 4.7.

Focussing the telescope in incremental steps like described in the previous section was still working. The image quality was also not affected, which would be expected if e.g. one of the tree bolds holding the secondary mirror would been loose and the mirror is moving in an uncontrolled way. It looked like a systematic shift of the focus encoder scale, but the focus reference mark, being on the hardware side independent from the incremental encoder, could not have changed (it is glued on the moving part of the secondary mirror actuator) and was still giving signals. A visual inspection of the focussing hardware by the H.E.S.S. technical crew did not reveal any issue with the hardware.

This triggered investigations of the focus value vs. temperature relations. The focus value is expected to be a linear dependence of temperature changes, since the telescope tube should shrink linearly with decreasing temperature, thus requiring the secondary mirror to be moved further up (in our scale: to lower focus values) to keep the optical system stable.

Figure 4.8 is showing the correlation of focus value against the 3 measured temperatures at ATOM: a sensor at the telescope tube , outside and inside the building. As expected, the best correlation between temperature and focus value is coming from the temperature measurements at the telescope tube, the other two temperatures are mainly shown for completeness. Even for the "good" time period before 2010, the correlation coefficient is not ≈ 1 as one would expect, but with 0.6 much worse (χ^2 values of a linear fit to the data were totally off the wall). This is probably due to the fact that the thermometer at the telescope tube is not really measuring the average temperature of

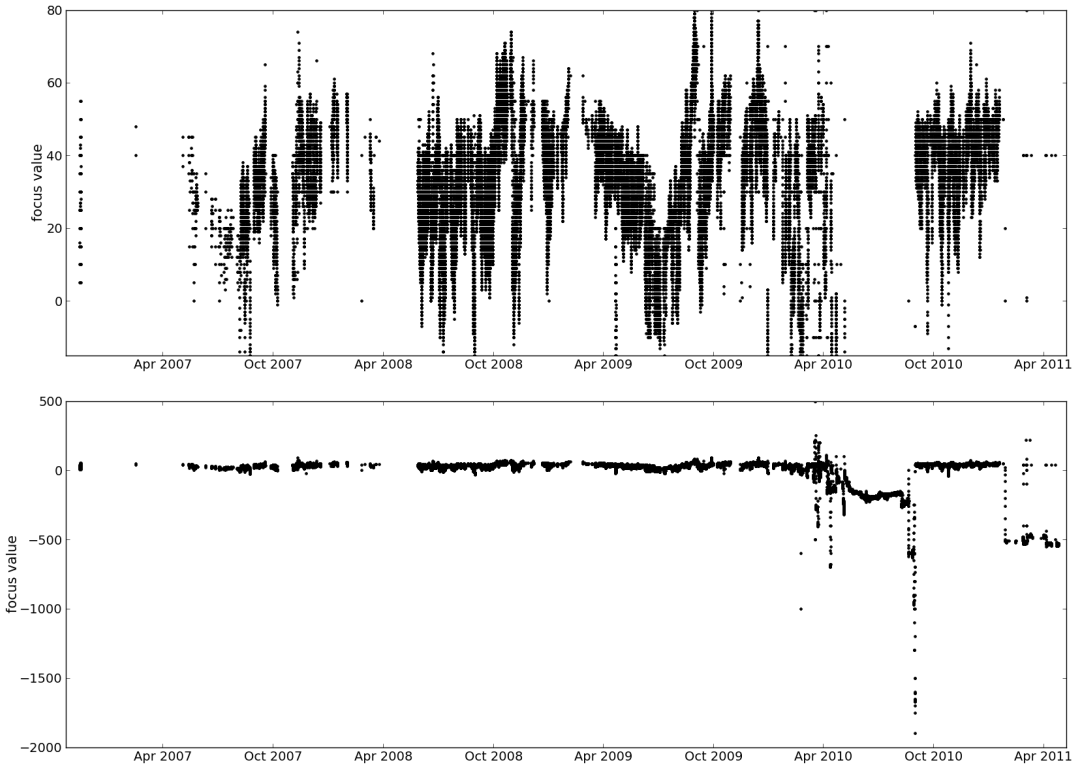

Figure 4.7.: Raw focus encoder values over time. Note that the typical dynamic scale during normal operation is [0,60]. The horizontal structure (white lines) in the zoom-in (upper panel) are due to the focus value being reported in integer numbers only. The unusual values were reported starting March 2010.

the whole tube, but only a spot, and thus introducing much scatter.

In Aug 2010, the complete focus gear and encoder part was dismounted. It was found that the glue fixing the slit disk of the encoder had gone bad, *sometimes* leading to lost encoder counts. This was fixed and the focus is behaving like in the first three years of operation now[9]. No large amount of observing time was lost because of this problem, since the large loss of counts occurred always in the morning when the secondary mirror was moved over 10's of units back to the estimated correct focus position at beginning of the next night, and not during the night. It only required a more intense human supervision of the start of operation in the evening, since the automatic focussing routine described before is only able to deal with deviations from the correct focus of $\lessapprox 10$ units. The effective loss of scientific observing time because of this was typically 5 to 20 min / night.

[9]Thanks Toni+Albert!

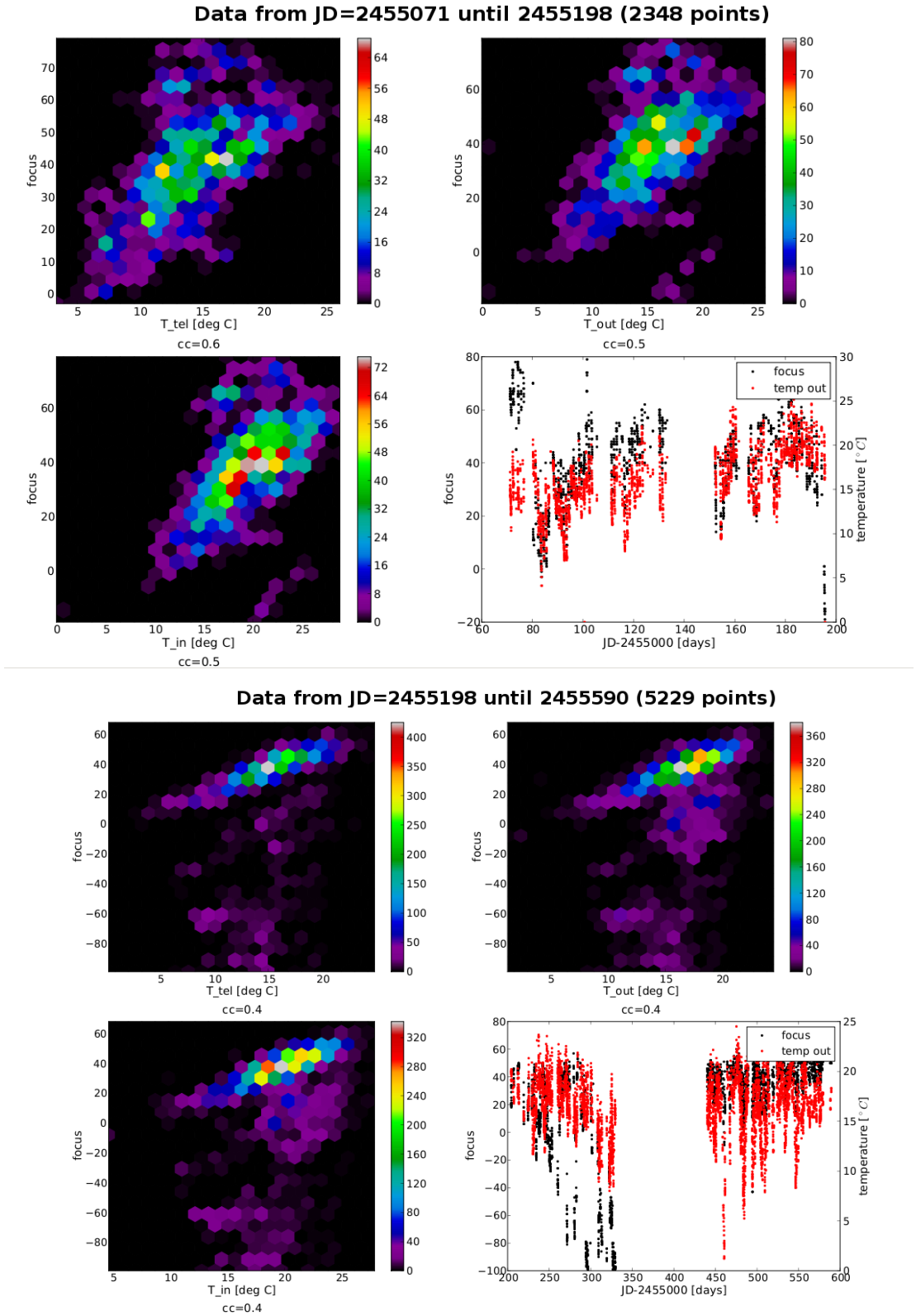

Figure 4.8.: Focus value vs. temperature. The upper panel is presenting all data before the problem occurred (all before 2010), the lower panel all data acquired after beginning of 2010. The three scatter plots in each panel are showing telescope temperature T_tel, outside temperature T_out and inside temperature T_in against focus value. Below the plot is the correlation coefficient (Pearsons 'r') of the two measurements given. As expected, the best correlation with the focus value is coming from the measurement at the telescope tube.

5. Automatic Data Reduction and Analysis Software – ADRAS

Since ATOM was from the beginning meant to be an automatic system, able to observe and photometrically analyze observations of AGN and other interesting point sources without human user interaction[1], it was clear that a pipeline system for data analysis is needed. This system needs – and now has – the capability to process incoming raw images to photometric calibrated data points. This ***A****utomatic* ***D****ata* ***R****eduction and* ***A****nalysis* ***S****oftware* (in short form: **ADRAS**) is after `instops` the 2nd major software contribution to the ATOM project from this thesis.

ADRAS is written in `python`[2], making heavily use of several python extension modules for MySQL database access[3], FITS file handling via `PyFITS`[4] and numerical array calculations by using `numarray`[5]. Graphical output is produced via `matplotlib`[6].

ADRAS is split in several sub-tasks. They are

1. **registration:** Any acquired raw FITS frame is fed into the ADRAS pipeline. This is the first step, where the basic properties of this frame (dark, flat field of science frame, temperature and exposure time, position on the sky, etc.) are extracted from the FITS header and stored in a database for further reference. This is implemented in the script `registerFrame.py`.

2. **standard image reduction:** Science frames are processed to remove any instrumental artefacts. This is described in section 5.1.

3. **photometry:** Objects on the FITS frames are detected and their flux is measured in arbitrary units, see sec. 5.2.

4. **photometric calibration:** The photometric flux scale of every FITS frame is fixed on some reference objects, see sec. 5.2.3.

5. **lightcurve creation:** All data determined in the previous steps is now compiled into a lightcurve. See sec. 5.2.4.

The usage of the corresponding software tools is described in detail in the ATOM user manual (Hauser (2006)), together with examples . In the following, the conceptual design of the pipeline is presented.

[1] well, I guess you remember what the "A" in ATOM stands for...
[2] http://www.python.org
[3] http://www.mysql.com/
[4] PyFITS is a product of the Space Telescope Science Institute, which is operated by AURA for NASA. http://www.stsci.edu/resources/software_hardware/pyfits
[5] http://www.stsci.edu/resources/software_hardware/numarray, also from STScI
[6] http://matplotlib.sourceforge.net/

5.1. Pipeline image reduction

5.1.1. Why image reduction

Image reduction means in the world of optical astronomy the reduction of the measured image to its scientific content, i.e. to remove instrumental effects on the content. The three main interfering effects are *bias*, *dark current* and *flat fielding* anomalies. The *bias* $\mathcal{B}$ is an additive component of the image signal, added by camera electronics so that even a signal of 0 intensity can vary (because of not avoidable noise) symmetrically around its true value[7]. For real cameras, this value is often also temperature dependent and may change on a timescale of months. *Dark current* D is another additive signal component. It originates from e^- being excited from the valence band to the conduction band in the semiconductor material of the CCD chip by thermal movement and is thus a function of integration time and temperature of the CCD[8]. A *Flat field* $\mathcal{F}$ is the answer of the complete detection system (CCD camera as well as telescope and other possible optics (e.g. filters) included in the measurement process) to an illumination with a spacially homogeneous light source. It holds for example information about vignetting, different quantum efficiency of different CCD pixels or obscuration of light by dust particles on the camera entrance window or filters. This is of course a multiplicative effect on the resulting signal.

The true signal S, which would be measured by an ideal instrument is therefore defined (R being the raw signal from the real camera device)

$$\mathcal{S} = \frac{\mathcal{R} - \mathcal{B}(T_{\mathrm{CCD}}) - D(T_{\mathrm{CCD}}, t_{\mathrm{exp}})}{\mathcal{F}} \tag{5.1}$$

(note that all terms here are of course 2D-matrices, corresponding to the image pixels, and not scalars)

5.1.2. Choosing appropriate calibration frames

The quantities of $\mathcal{B}$, $\mathcal{D}$, and $\mathcal{F}$ from eqn. (5.1) are defined though calibration frames. Many CCD cameras used in professional astronomy are cooled with liquid nitrogen and have at their operating temperature a negligible dark current. Therefore, for most of these cameras, a dark current correction is not done and images are only bias subtracted. Unfortunately, with our TE cooled CCD camera, the dark current is significant as it was shown in section 3.4.2. For simplicity reasons, ADRAS does not disentangle between bias and dark current corrections (this is no problem since both are additive terms) and we are only dealing with one additive term called $\mathcal{D} = \mathcal{B}(T_{\mathrm{CCD}}) + D(T_{\mathrm{CCD}}, t_{\mathrm{exp}})$ from now on.

Since even the combination of closed ATOM shelter, close mirror cover and closed camera shutter leads to a increased signal level in *dark frames* if once acquires them during daytime w.r.t. frames taken during nighttime, this prohibits calibration frames to be taken during daytime. Since nighttime should be spend for observations, only

[7] Signal values are based on electron counting. If a true signal of 0 would correspond to $0\,e^-$, any noise would be highly asymmetric (there are no negative counts) at no or low intensity, and only at S/N levels $\gg 1$ became symmetric.

[8] in an ideal world, the *dark current* is linear proportional to integration time and follows temperature in an exponential decrease with intensity halved every 8 K of decreasing temperature.

periods where no observations are possible during nighttime are used to acquire dark frames. This is done during bad weather or full moon nights[9].

Flat field frames are usually taken every evening as twilight flats.

Since the calibration matrices $\mathcal{D}$ and $\mathcal{F}$ may change with time[10], ADRAS is following a straight forward approach and simply chooses the images which were acquired in the nearest temporal proximity to the science exposure $\mathcal{R}$ to create suitable $\mathcal{D}$ and $\mathcal{F}$ calibration images for any given $\mathcal{R}$.

In addition to temporal proximity, the CCD temperature has to match also for $\mathcal{D}$ (it was found that a match of $\pm 2°$C is most suitable). To minimize the effect of *read-out noise* in $\mathcal{D}$ and $\mathcal{F}$, many single calibration frames[11] are median-averaged to build one $\mathcal{F}$ or $\mathcal{D}$ used for the reduction of $\mathcal{R}$. Finally, ADRAS has to consider that each $\mathcal{F}$ has to be corrected for dark current and normalized to a mean intensity $< I >= 1$ before averaging. And that one cannot use one $\mathcal{F}$ for different filters, but has to construct mean flat fields for each filter separately. Eqn. 5.1 turns now finally into

$$\mathcal{S} = \frac{\mathcal{R} - < \mathcal{D}(T_{\mathrm{CCD}}, t_{\mathrm{exp}}) >}{< \mathcal{F}(\mathrm{Filter}) >} \tag{5.2}$$

5.1.3. Astrometric calibration

The last step in (my definition of) standard image reduction is the refinement of the *World Coordinate System* (WCS) keywords stored in the FITS header. The WCS describes the mapping of image pixels x, y to α, δ (J2000) coordinates on the sky and is defined in Greisen and Calabretta (2002) and Calabretta and Greisen (2002)[12].

The image header is at this stage already holding α, δ coordinates which were taken from the telescope control system at time of the exposure. As described in sec. 2.2.2, these coordinates are not very accurate on the sub-arcminute level, and thus needed to be refined. This is done by using the software package `imwcs` (Mink (1997), Mink (2006)), which is fed by a list of pixel coordinates of bright objects detected in the image by a first quick run of the SExtractor software (described in sec. 5.2), applying a quite high detection thresholds of 6 standard deviations above the local background. `imwcs` takes this list of (x, y, flux) tuples and matches them against an astrometric catalog of star positions. If a match is found, the WCS keyword in the FITS header are updated to allow a mapping of (x,y) pixel coordinates to α, δ coordinates on sub-arcsecond accuracy.

The default catalog used for matching is the *UCAC 2* catalog (Zacharias et al. (2004b)). This catalogs contains the position of stars between $7 < \mathrm{mag}_R < 15$ for declinations $\delta < 45$ deg and is thus very well suited for ATOM data. For fields north of $\delta \approx 45$ deg,

[9] ATOM *can* in principle take useful data even at full moon nights, if one avoids a region of $\approx 15°$ around the moon. But this time is typically devoted for taking calibration frames. In addition, there is a safety issue: a few days around full moon, the H.E.S.S. technical and shift personal is typically *not* on site. And the ATOM enclosure is typically not opened if no one is available to close the roof in case of a complete system failure or longer power outage.

[10] E.g. additional or moving dust particles on any optical relevant surface will alter $\mathcal{F}$.

[11] There are typically 5 flat field frames per filter and per night available. Dark frames are acquired during nights not used for observations (typically full moon nights, so $\approx 2-3$ nights every 28 days). Using this approach, ADRAS can combine also $\approx 5-10$ dark frames for each combination of CCD temperature and integration time.

[12] Some errata dated 2007 are available from the authors webpage: http://www.atnf.csiro.au/people/mcalabre/WCS

the older USNO-A2 catalog is used (Monet et al. (1998)). Because of the low-bandwidth Internet connection of the H.E.S.S. site, both catalogs are stored on disk at the ATOM computers. This is also the reason that the more complete and newer catalogs USNO-B (Monet et al. (2003)) or NOMAD (Zacharias et al. (2004a)) are not used: because of their size (80 and 100 GB), they are meant to be used via online queries only.

Finally, ADRAS is storing the so-called *standard reduced frames* $\mathcal{S}$ on disk for further processing by the photometry package. The whole task is implemented in the script `standardRed.py`.

5.2. Photometry

5.2.1. Accuracy tests with different apertures

To check for the photometric accuracy achieved by the different photometric methods offered by the used photometry program SExtractor (Bertin and Arnouts (1996)), the differential magnitudes of reference star i vs. reference star j, measured with all available photometric methods that this software offers, are compared. Since these stars are assumed to be of constant magnitude, the scatter of $d_{ij} = m_i - m_j$ for many repeated measurements on many different observations of the same FoV can be used as a qualitative statement of photometric quality.

Different photometric methods

ADRAS is using SExtractor in version 2.5[13], which is only offering aperture photometry. There are rumors that the code includes first parts of a PSF fitting routine, but this is still unannounced and undocumented[14] and therefore not used inside ADRAS.

The difference in between all this various methods is the size and shape of the aperture. SExtractor offers fixed-size circular apertures and floating apertures with adaptive size and shapes. The background is treated equally in each method (see Bertin and Arnouts (1996) or Holwerda (2006) for details about the underling algorithms). Table 5.1 lists all aperture types used in this test.

Measurements

To check the photometric accuracy of different aperture types, the measured differential magnitudes of reference stars placed around PKS 2155-304 (see figure 5.1) are compared with values published by Hamuy and Maza (1989).

The mode of the distribution of values is a measurement of uncorrected filter transformations between ATOM measurements and the Bessel system used by Hamuy and Maza (1989), whereas the sharpness of the distribution shows the photometric accuracy (uncorrected effects for star color dependent atmospheric extinctions are also present in the sharpness of the distribution, but these are independent of the used photometric aperture and can therefore be neglected here).

[13] At time of writing still the most recent one

[14] Several requests by different people for more information about PSF fitting implemented in SExtractor have been placed in the SExtractor users web forum, but have always been denied by the author of SExtractor .

no.	photometric aperture type
1	fixed aperture with 2" diameter
2	fixed aperture with 4" diameter
3	fixed aperture with 6" diameter
4	fixed aperture with 8" diameter
5	fixed aperture with 10" diameter
6	fixed aperture with 15" diameter
7	fixed aperture with 20" diameter
8	variable aperture, SExtractor 's MAG_ISOCOR
9	variable aperture, SExtractor 's MAG_ISO
10	variable aperture, SExtractor 's MAG_AUTO

Table 5.1.: Different aperture types offered by SExtractor and used in this test. All apertures are automatically centered over the center-of-mass of the light distribution of each individual object.

All data shown here is taken using the R band filter. Data points which deviates more than 0.5 mag from the expected values are considered to come from mis-identifications of stars or other measurement errors and are omitted.

The summary results of this parameter study is shown in figures 5.2 and 5.3, where the sum of all $d_{i,j}$ for each aperture type is given. The individual $d_{i,j}$ have been shifted to mode=0 before summation. Graphs showing the individual $d_{i,j}$ for each i, j and every aperture type are given in the appendix (fig. G.1 to G.6).

Conclusion

No difference in RMS is seen for fixed aperture sizes between $2 \ldots 20$ arcsec. The RMS of all magnitude difference measurements is ± 0.02mag. Usage of SExtractor specific adaptive apertures leads to higher RMS values.

Given the average seeing of > 2 arcsec, an **aperture of 8 arcsec is chosen to be the default value for ADRAS**[15]. This is $> 3\times$ the average seeing, so assuming a Gaussian light distribution, we have 99% flux inside the aperture for point sources like stars (or AGN) and no aperture correction is necessary.

5.2.2. Further SExtractor parameter tuning

The behavior of SExtractor can be influenced via many parameters (see Bertin (2006)) and not only through the chosen aperture type (see previous section). Most parameters were left at their defaults and provided useful results. However, it was found that the default values do not lead to the best possible results if the images have problems based on a defocussed or badly tracking telescope as illustrated in fig. 5.4.

The photometric problem here is to convince SExtractor to treat donut-shaped or very elongated star projections as *one* object, and not split it into several objects like it happens using the default parameter values. The starting point to that problem lies

[15] all other apertures are still computed and stored in the database. Anyone interested can easily switch between them using command-line arguments or tuning the config file when running the analysis scripts.

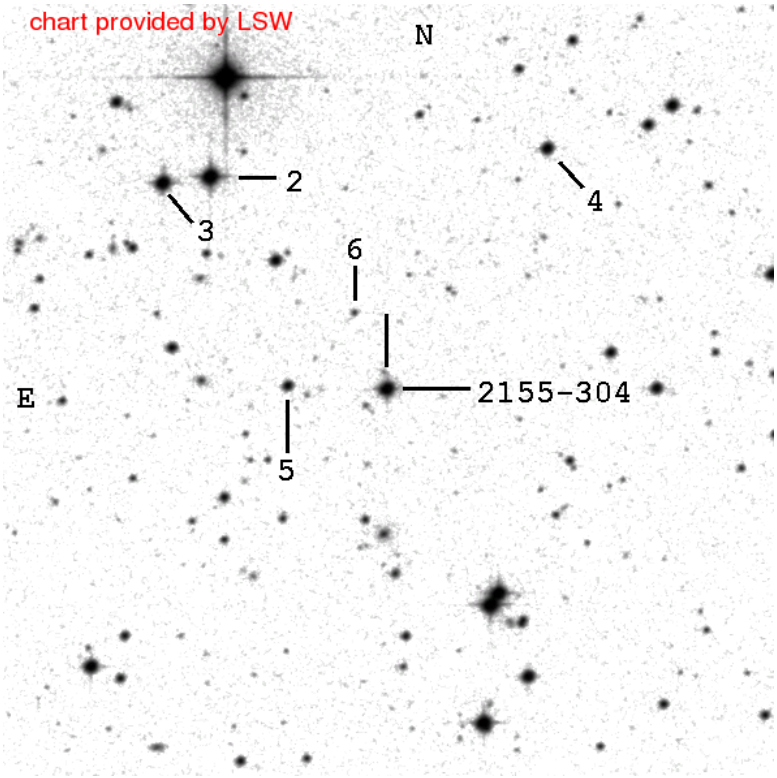

Figure 5.1.: PKS 2155-304 and comparison stars from Hamuy and Maza (1989) used in this test (taken from http://www.lsw.uni-heidelberg.de/projects/extragalactic/charts/2155-304.html)

in the SExtractor *deblending* routine, the procedure how SExtractor separates objects lying very near together. This is illustrated in figure 5.5: for each initial object detection (a set of connected pixels above the detection threshold), the area above the threshold flux level is spit into `DEBLENT_NTHRES` (a SExtractor parameter) equally spaced intensity levels, and the object splitting algorithm walks from top to bottom and checks at each junction if the contrast is larger than `DEBLEND_MINCONT` (another tuning parameter), in which case the detection is split into several objects, or it just continues its way down. So the way to convince the program to accept e.g. a defocussed star image (donut-shaped thing) to be one object is to lower the `DEBLEND_NTHRES` or increase `DEBLEND_MINCONT` or a combination of both.

A combination of parameters that work well for the vast majority of good images, as well as for problematic ones, is easier to find if the objects in the FoV are well separated. In crowded regions, like for example at low galactic latitudes, one has to pay attention that objects separated by a few arcsec only are not treated as one object. A quick parameter study showed that the number of intensity levels (`DEBLEND_NTHRES`) does not change the outcome of measurements significantly if it is not set too low (≤ 15). Thus this parameter was left at its default value of 32 for most objects and only the influence of `DEBLEND_MINCONT` was studied in greater detail in the next section.

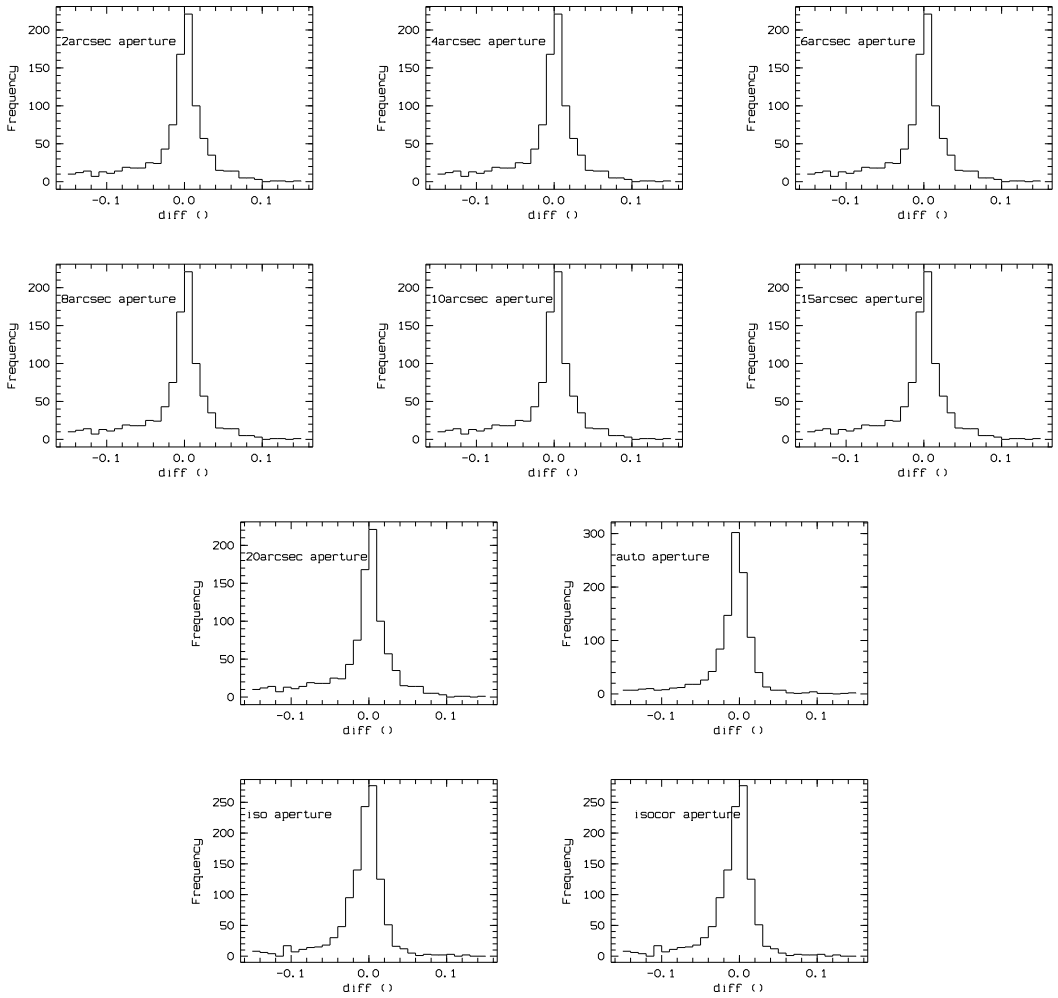

Figure 5.2.: difference of measured differential magnitudes $d_{i,j}$ vs. literature values (only R band). All combinations of (star$_i$ - star$_j$, $i \neq j$) have been summed-up. The individual distributions have been shifted to mode=0 before addition.
Individual (star$_i$ - star$_j$) combinations are shown in the appendix (figures G.1 to G.6), whereas mode and mean of individual combinations are given in fig. 5.3.

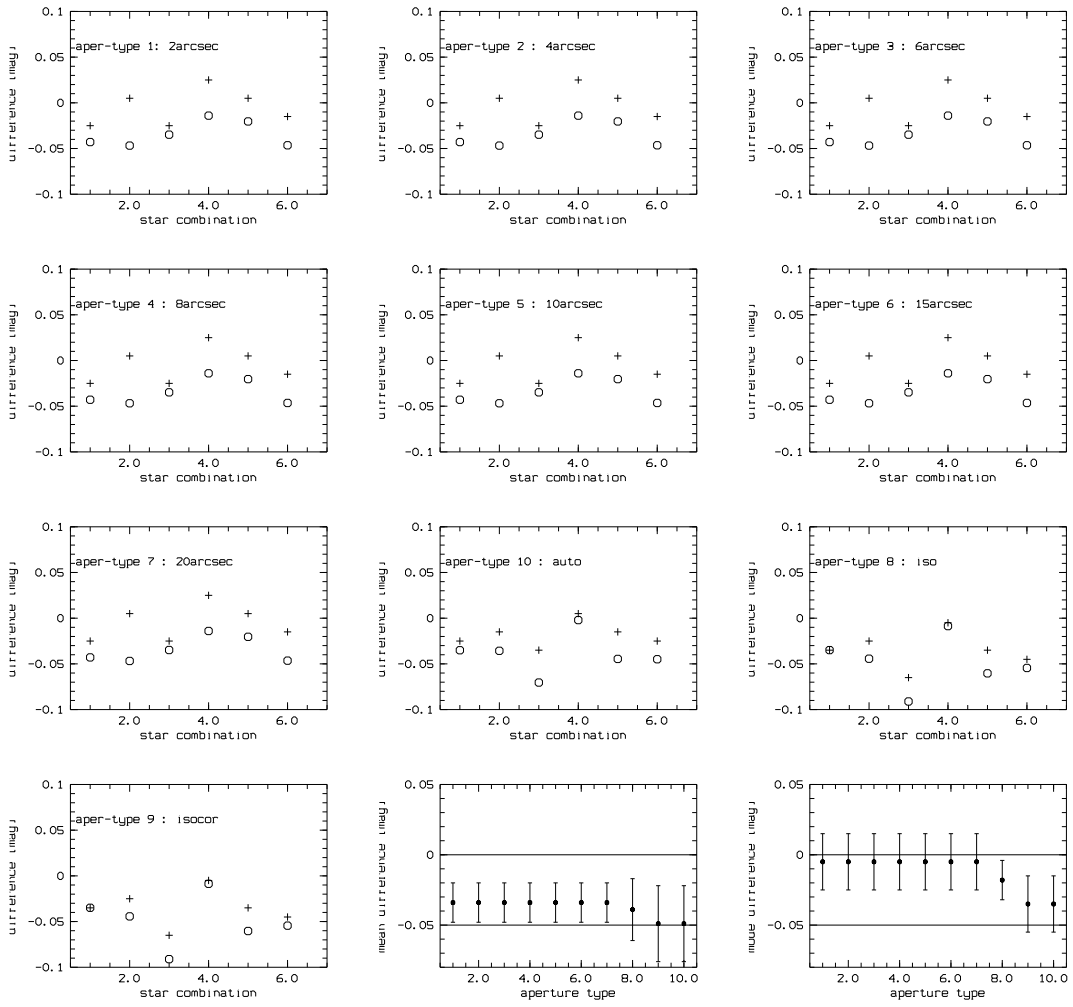

Figure 5.3.: mode (+) and mean (o) of distributions shown in figures G.1 to G.6 in the appendix (summary in fig. 5.2). The different star pairs are given as a sequence on the abscissa in the first plots. The last two plots show mean and RMS of the distributions shown in the first plots (second to last: mean, last: mode).

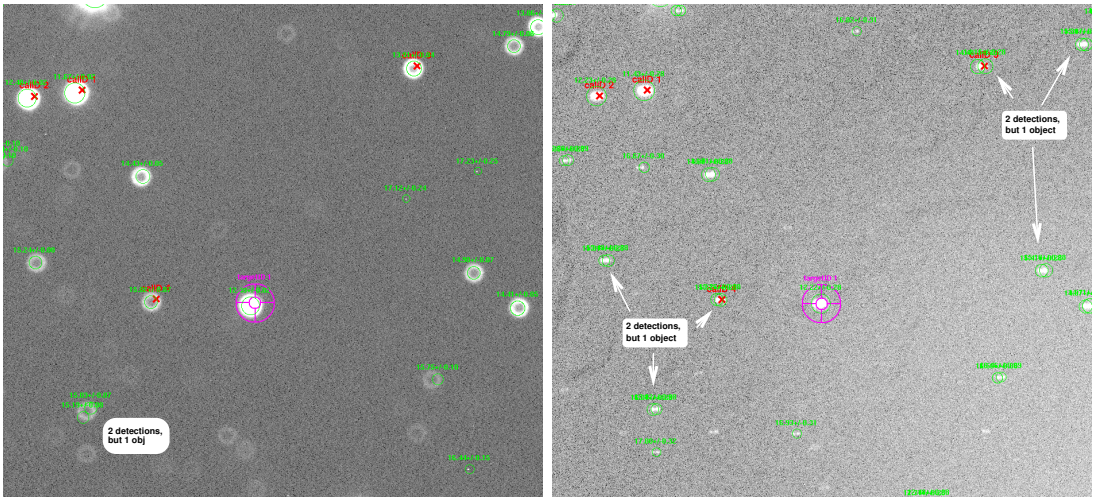

Figure 5.4.: Problems with defocussed (left) or badly tracked (right) images: the light distribution of one star is split into two (or even more) objects by the SExtractor software. This problem can be dealt with for most cases by choosing the parameters for SExtractor carefully. Of course, it is desirable to avoid getting this kind of images during observations. But dealing with this artefacts is definitely better than throwing away all these kind of images.

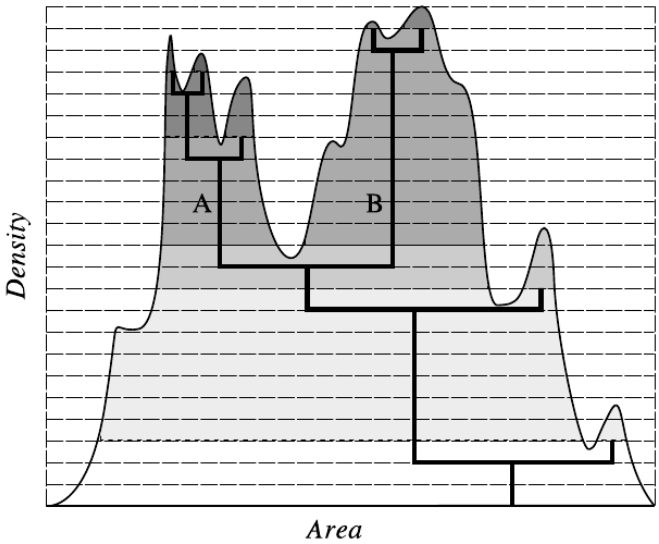

Figure 5.5.: Schematic overview on how SExtractor decides which image pixel belongs to which object. The tuning parameters for this are the number of intensity levels the area above the background is spit into (`DEBLENT_NTHRES`) and the minimum contrast necessary to split a branch into two sub-branches (`DEBLEND_MINCONT`). Default values are 32, resp. 0.005.
(Figure taken from Bertin (2006))

Finding the best `DEBLEND_MINCONT` value

The input for this parameter study are all images of PKS 2155-304 taken in August and September 2008 (140 frames). Only images taken with R band filer were used[16]. The sample was chosen to include several images with defocussed or badly guided exposures, as well as some taken during moon time. For each different value of `DEBLEND_MINCONT` shown in the following, the images in the sample interval were processed with the tailing part of the ADRAS pipeline (starting with the photometry and the following steps as described at the beginning of this chapter).

A set of photometry-related parameters is here considered to be *good* if a star (with assumed constant intrinsic brightness) is measured with always the same brightness within errors. Thus the RMS scatter of the magnitude of the different reference stars in the FoV around PKS 2155-304 is a good indicator for the best value of `DEBLEND_MINCONT`.

The graphs below are each showing the lightcurve of the AGN (shown here only for illustrative purpose) as well as the ones of the four reference stars 2...5 (numbers as in fig. 5.1) on the left-hand side. On the right, the histogram of the measured apparent magnitude of the reference stars is shown (binsize is always 0.01 mag). For better visibility, an arbitrary offset[17] was applied to the magnitude values before binning.

The width of the distributions is a measure for the quality of the photometric measurement. In an ideal world, one would always get the same value for a particular reference star and thus all histograms would show δ-functions. The resulting mean magnitude and the RMS of the distributions is given in the table following the graphs. All results are summarized in fig. 5.3.

[16] The selection of the filter does not influence the raw photometry, but of course one has to stick to one single filter to make the results comparable.

[17] The offset of course being constant for each individual star.

DEBLEND_MINCONT = **0.001**

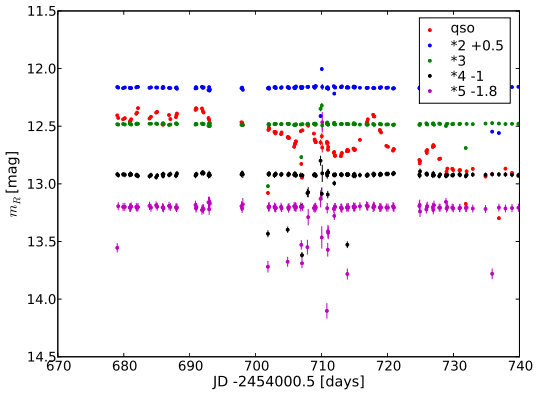

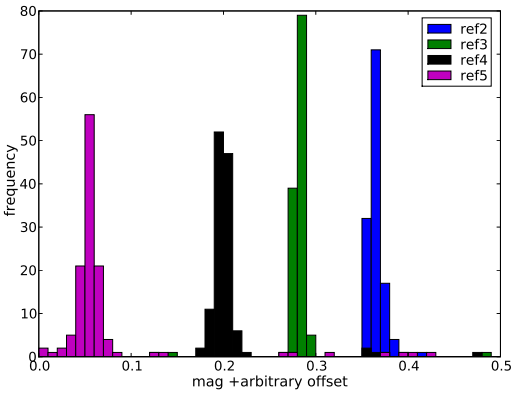

star	m_R[mag]	RMS[mag]
r2	11.672	0.055
r3	12.491	0.071
r4	13.944	0.107
r5	15.041	0.159

DEBLEND_MINCONT = **0.005 (default)**

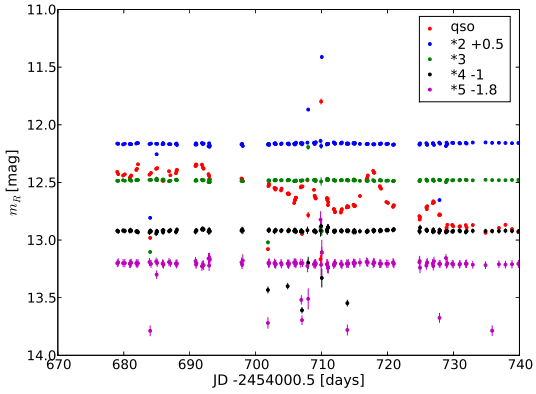

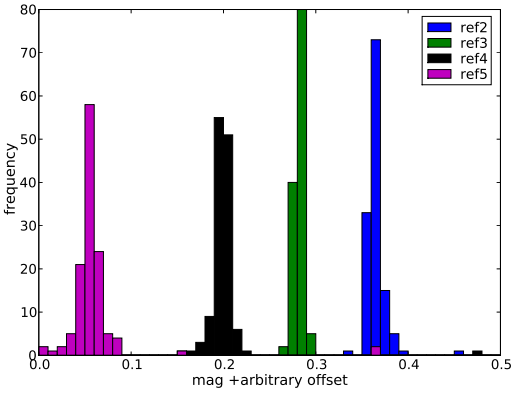

star	m_R[mag]	RMS[mag]
r2	11.666	0.100
r3	12.498	0.099
r4	13.942	0.108
r5	15.030	0.124

DEBLEND_MINCONT = **0.01**

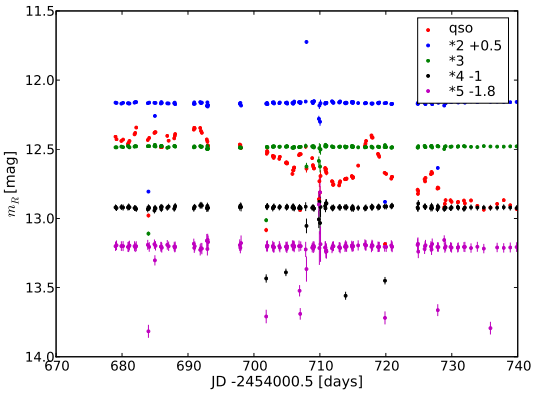

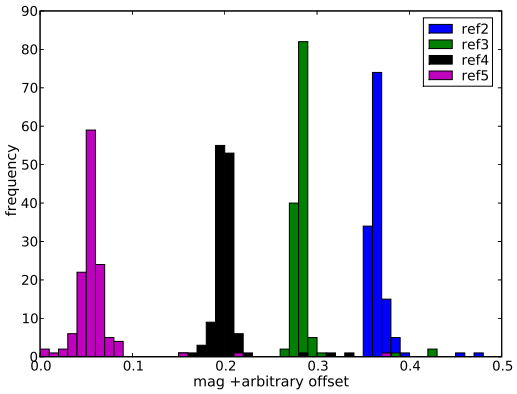

star	m_R[mag]	RMS[mag]
r2	11.678	0.100
r3	12.497	0.082
r4	13.938	0.094
r5	15.026	0.123

DEBLEND_MINCONT = **0.05**

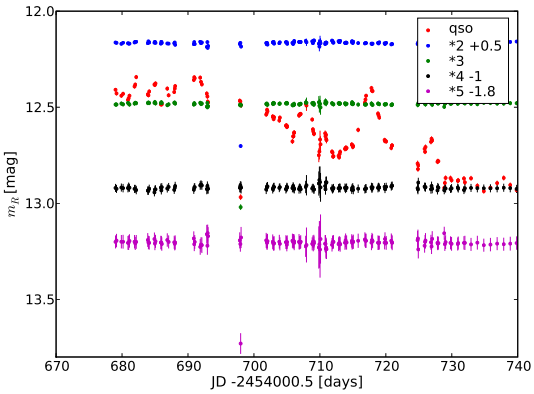

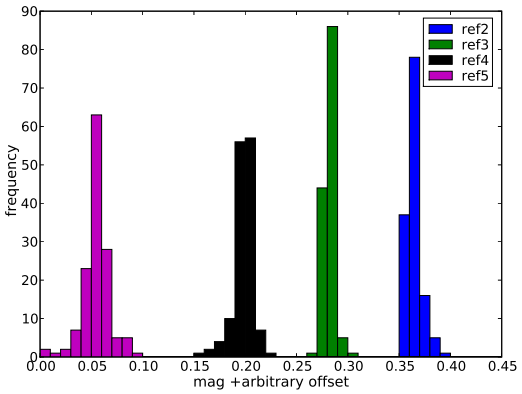

star	m_R[mag]	RMS[mag]
r2	11.668	0.046
r3	12.486	0.046
r4	13.919	0.009
r5	15.008	0.047

DEBLEND_MINCONT = **0.1**

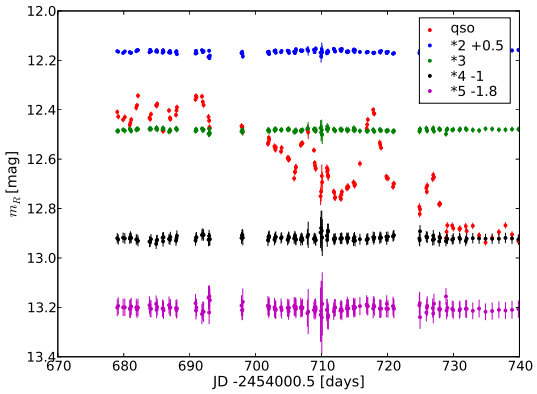

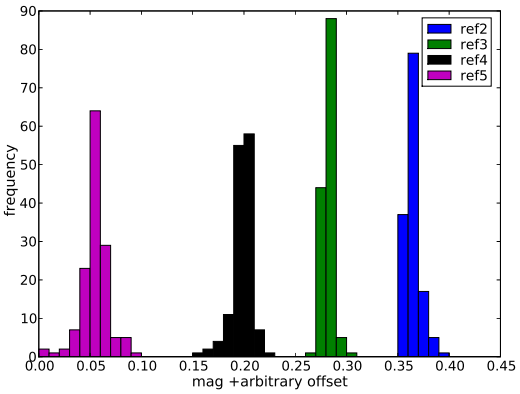

star	m_R[mag]	RMS[mag]
r2	11.665	0.007
r3	12.482	0.005
r4	13.919	0.009
r5	15.004	0.013

DEBLEND_MINCONT = **0.2**

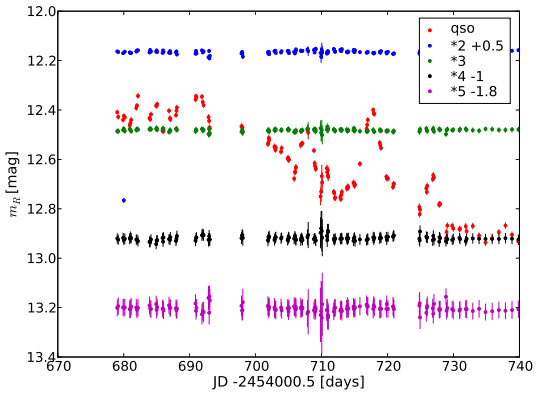

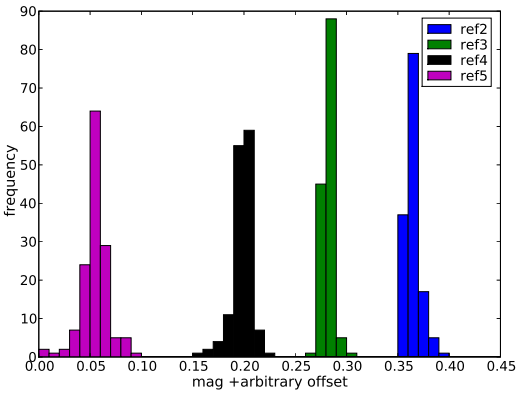

star	m_R[mag]	RMS[mag]
r2	11.669	0.051
r3	12.482	0.005
r4	13.919	0.009
r5	15.004	0.013

DEBLEND_MINCONT = **0.3**

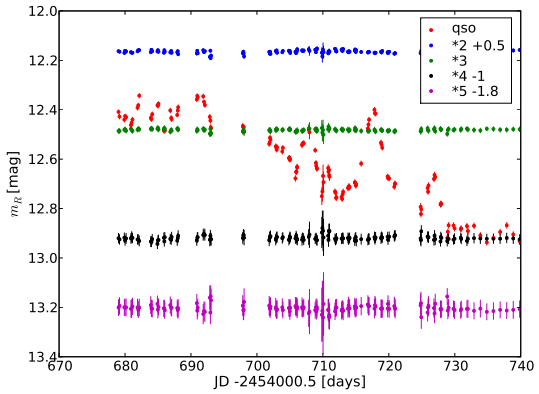

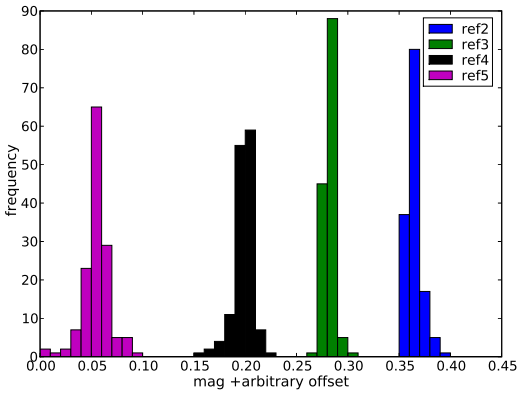

star	m_R[mag]	RMS[mag]
r2	11.665	0.007
r3	12.482	0.005
r4	13.919	0.009
r5	15.004	0.013

DEBLEND_MINCONT = **0.4**

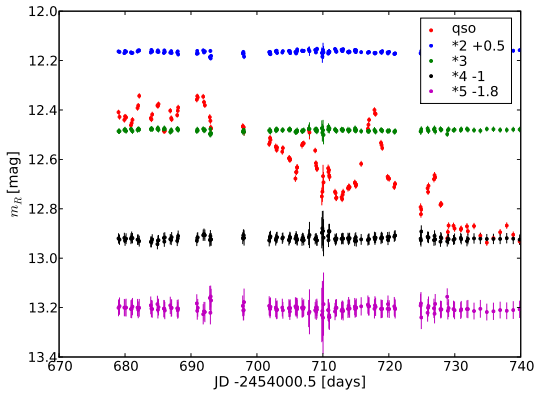

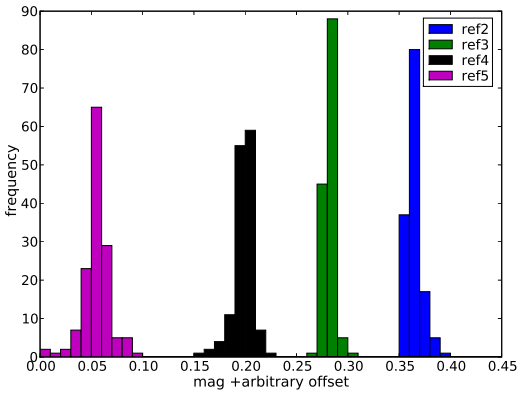

star	m_R[mag]	RMS[mag]
r2	11.665	0.007
r3	12.482	0.005
r4	13.919	0.009
r5	15.004	0.013

DEBLEND_MINCONT = **0.5**

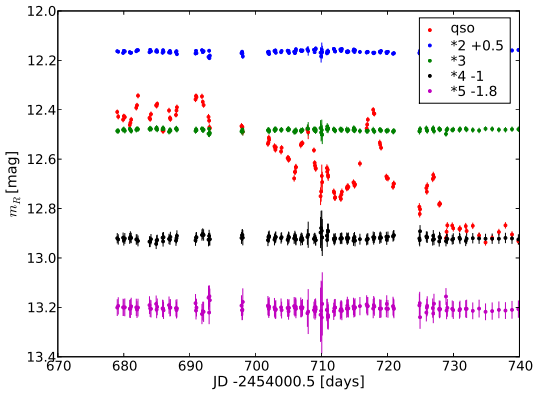

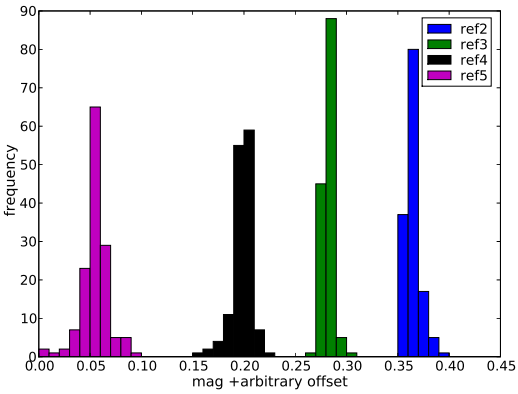

star	m_R[mag]	RMS[mag]
r2	11.665	0.007
r3	12.482	0.005
r4	13.919	0.009
r5	15.004	0.013

DEBLEND_MINCONT = **0.6**

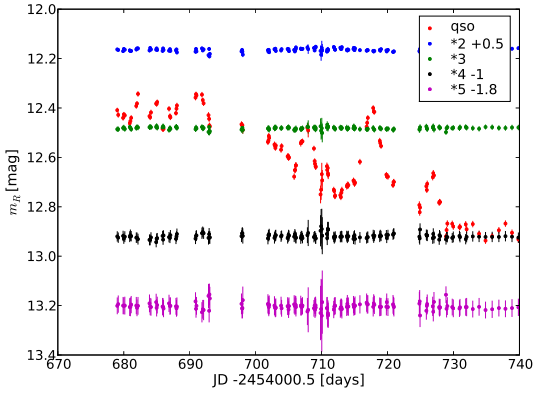

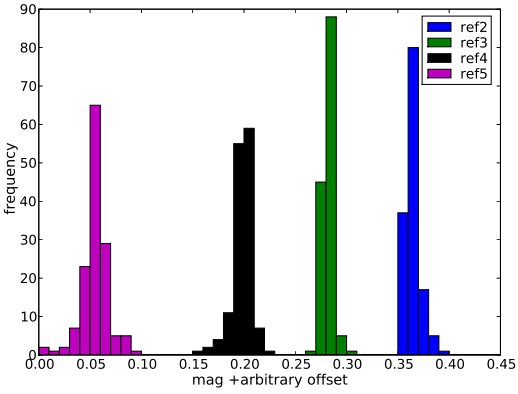

star	m_R[mag]	RMS[mag]
r2	11.665	0.007
r3	12.482	0.005
r4	13.919	0.009
r5	15.004	0.013

DEBLEND_MINCONT = **1.0**

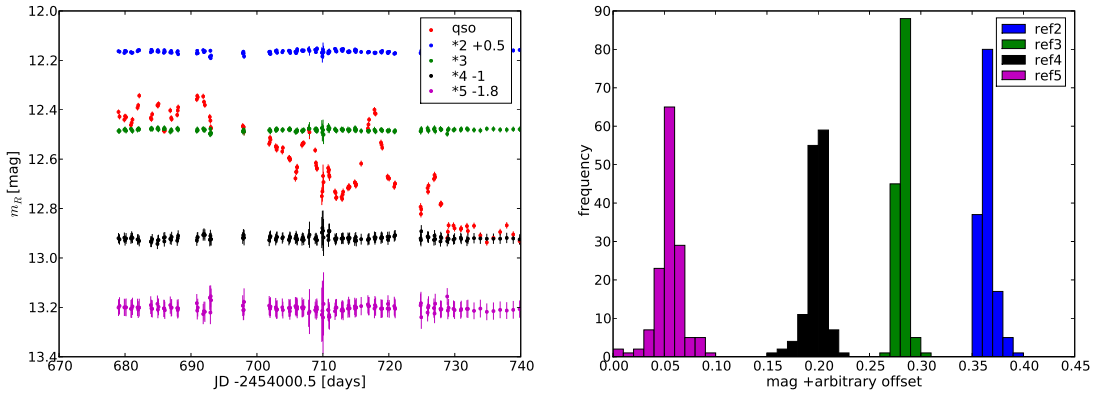

star	m_R[mag]	RMS[mag]
r2	11.665	0.007
r3	12.482	0.005
r4	13.919	0.009
r5	15.004	0.013

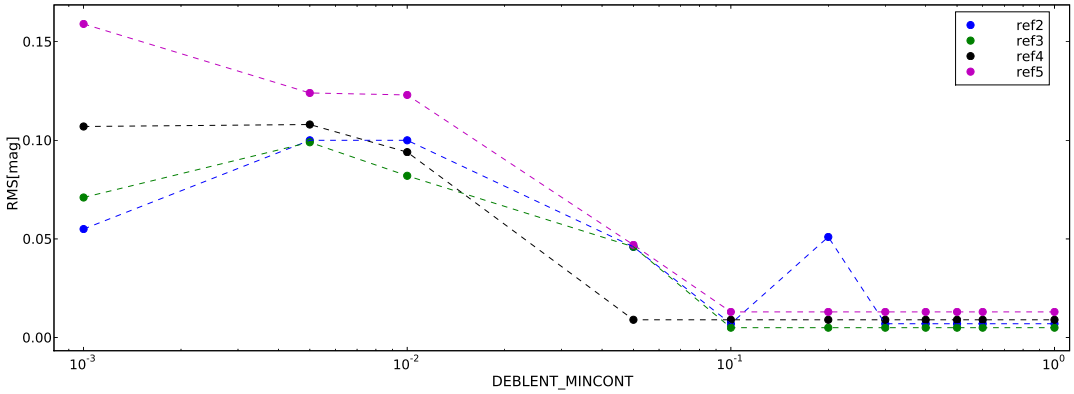

Figure 5.6.: Results of the parameter study on DEBLEND_MINCONT shown in section 5.2.2. The RMS of the measured magnitude of the reference stars is minimal for DEBLEND_MINCONT≥ 0.3, which is now choosen as the default value for ATOM data analysis via ADRAS.

Parameter conclusions Fig. 5.6 summarizes the results of the different values for DEBLEND_MINCONT. A value of ≥ 0.3 seems to be best suited for ATOM data of PKS 2155-304. This result is also valid for all other observing targets where the star density is not much higher than around PKS 2155-304, and so DEBLEND_MINCONT=**0.3 is now choosen to be the default value for ADRAS.**

Figure 5.7 shows the implication on the overall photometric values. *m(new)* refers to DEBLEND_MINCONT=0.3 and *m(old)* to the SExtractor default value of DEBLEND_MINCONT=0.005. The vast majority (the **not** defocussed or badly tracked images) are not affected by this change of parameters.

However, this high value for DEBLEND_MINCONT introduces problems at crowded fields, e.g. at objects with low galactic latitude. Or for objects like 3C 454.3, where one can

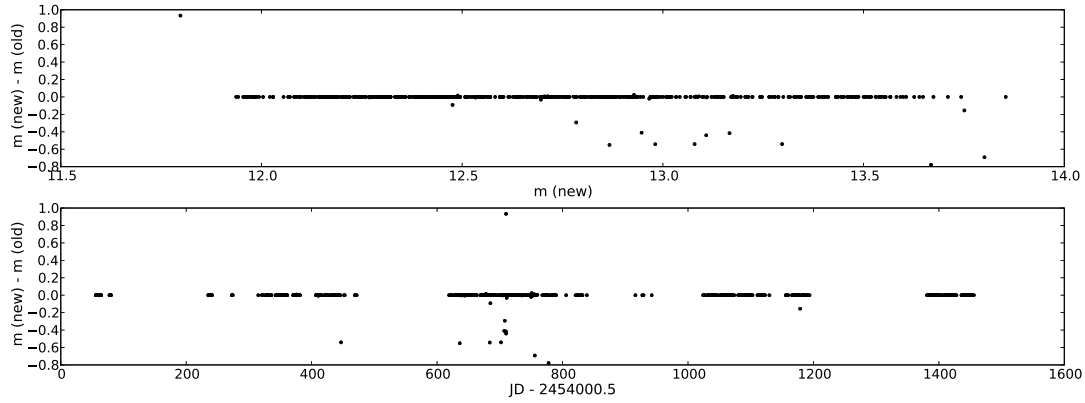

Figure 5.7.: Default vs. adapted SExtractor parameter `DEBLEND_MINCONT`. The default value distributed with SExtractor is `DEBLEND_MINCONT`=0.005 (the so calculated magnitudes are labels as m(old)), whilst it was found that `DEBLEND_MINCONT`=0.3 –labeled as m(new)– is much better suited for ATOM data.
Both panels are showing the magnitude difference of old/new parameter photometry on the y axis. The abscissa is the new magnitude for the upper panel; the lower panel is giving it as a function of time. The vast majority (read: the **not** defocussed / bad tracked images) are not affected by this change of parameters.

find a bright star right next to the AGN (15 arcsec away). Here the deblending does not work well with such a high value. Because of this, ADRAS has the capability to define a specific `DEBLEND_MINCONT` value for each observing target.

Running similar tests as shown above for these objects, it was found that a value of `DEBLEND_MINCONT`=0.06 is well suited for crowded fields. The drawback here is that defocussed or badly tracked images cannot be analyzed in an automatic fashion, but since the vast majority of all images do not have these problems, this is not a big issue.

5.2.3. Photometric calibration

The photometric package SExtractor does only measure the flux per object w.r.t. an unknown offset, the *instrumental zeropoint zp*. So the real apparent magnitude m of any object on the CCD frame is defined as

$$m = \underbrace{-2.5 \cdot \log(counts[ADU])}_{m_{\text{instrumental}}} + zp \tag{5.3}$$

There are two ways to determine zp: *absolute* and *differential* photometry. *Absolute photometry* is done by modelling the atmosphere above the telescope to be able to identify the amount of light that is absorbed and scattered away from the objects flux when it travels trough the atmosphere to the telescope. In addition to that, one has to consider the light loss inside the instrument and the detector efficiency. This requires observation of standard stars with different colors at different airmasses and the assumption that the atmospheric conditions do not change between the observations done to fix the model parameters and the observations of the object of interest. While this is the only way to achieve a photometric calibration for new, unknown objects, this effort

has already been done for many of the famous AGN and photometric data for stars in the neighborhood of these targets is available in the literature.

This allows us to use *differential photometry*. Here, one uses the known apparent magnitude m of some star and its measured flux $m_{\text{instrumental}}$ to determine zp according to eq. (5.6). ADRAS is using not only one, but several reference stars in the FoV of each target, zp is then defined by averaging over all the individual zp_i per frame. The RMS of this averaging is added to the resulting error on the final photometric measurement value of each object.

Tuning the reference stars

Unfortunately, not for all of the ATOM monitoring targets are well-calibrated reference stars published. Therefore, for all targets without published reference stars, stars from the USNO astrometric catalogs are used. At the beginning of this project, the reference stars were picked from the USNO-A catalog (Monet et al. (1998)). With the availability of the NOMAD catalog (Zacharias et al. (2004a)) via SIMBAD, I switched over to this newer catalog with improved photometry values for all new observing targets. Another improvement is the availability of V and I magnitudes in NOMAD, whereas USNO-A was only giving B and R filter bands.

The photometric quality of these catalogs is relatively poor[18] and so introduces a large systematic error on the photometric result.

ADRAS is computing the resulting error on any photometric point as the quadratic sum of the photometric error determined by SExtractor (σ_{sex}) and the scatter of the individual zeropoints measured from the reference stars ($\sigma_{\text{RMS,refstar}}$).

$$\sigma_{\text{total}} = \sqrt{\sigma_{\text{sex}}^2 + \sigma_{\text{RMS,refstar}}^2} \tag{5.4}$$

with the mean instrumental zeropoint per frame

$$\bar{zp} = \frac{1}{n} \sum_i zp_i \tag{5.5}$$

(zp_i instrumental zeropoint per reference star ($\log(ADU) - m_{catalog}$); n number of reference stars)
and the RMS of the individual zeropoints per star which here defines the statistical error on the photometric calibration

$$\sigma_{\text{RMS,refstar}} = \sqrt{\frac{1}{n(n-1)} \sum_i (zp_i - \bar{zp})^2} \tag{5.6}$$

The way chosen here to cope with that is to minimize $\sigma_{\text{RMS,refstar}}$ by a) removing stars from the sample of used reference stars if their measured zp_i differs significantly from the ones of the other reference stars and b) adding a constant offset o_i to the catalog magnitudes of the remaining used reference stars so that $\sigma_{\text{RMS,refstar}}$ gets minimal. This introduces a *constant* systematic error not visible in the resulting lightcurves, but any low-amplitude variations the AGN flux can now be clearly seen and is no longer hidden between large error bars. This is demonstrated in the following as an example for

[18] for USNO-A, the authors are stating "errors up to 0.3mag"

	offset in R [mag]	
star 1	−0.043	±0.034
star 2	0.115	±0.019
star 3	−0.132	±0.051
star 4	−0.179	±0.045
star 5	0.209	±0.022
star 6	0.036	±0.025

Table 5.2.: Mean and RMS values of distributions shown in figure 5.8, 2nd row. An additive offset of these values was applied to the catalog magnitudes of the reference stars to get the lightcurve in the bottom row of fig. 5.8.

PKS 2356-309 and PKS 2005-489, for which no published reference stars could be found in the literature and so USNO stars were used.

Examples Initially, 7 USNO stars in the vicinity of *PKS 2356-309* were used as photometric reference. Figure 5.8 (top row) is showing the resulting lightcurve and the distribution of difference between the mean instrumental zeropoint and the zeropoint using a single star. It is telling two things: a) the distributions of offsets of stars $1 \ldots 6$ looks reasonable, whereas star 7 may have some problems (significantly wider distribution and higher offset to the mean than the other stars) and b) it should be possible to reduce the error of the photometric zeropoint $\sigma_{\mathrm{RMS,refstar}}$ to something like 0.05 mag (average width of the distributions of star $1 \ldots 6$).

At first, star 7 is omitted from the sample. The resulting distribution is shown in the second row of figure 5.8. The next step is to minimize the deviation from the mean instrumental zeropoint. This is done by adding some correctional term (see table 5.2.3) to the catalog magnitudes of the reference stars. The resulting lightcurve is shown in the third row of fig. 5.8. It was possible to reduce the average total error on the resulting photometric points from ≈ 0.3mag down to ≈ 0.07mag.

Figure 5.9 is showing the same exercise for *PKS 2005-489*. Here, the difference before and after correction is even larger. For this source, there was also a non-suited star (number 2 in this case) in the sample of references, which was identified using this method and removed from the list of reference stars for PKS 2005-489.

A slightly different method to check for not suited reference stars is to have a closer look at the differences between the instrumental magnitudes of stars $d_{i,j}$ (similar to the procedure demonstrated in sec. 5.2.1). If e.g. one of the stars is a variable one, this would simply lead to broader distributions in the histograms shown in figures 5.8 and 5.9 without giving an indication *why* this happens. By looking at $d_{i,j}$ over time, a periodic change in e.g. star 2 would be clearly visible in all $d_{2,j}(\mathrm{t})$, whereas for all combinations with $i, j \neq 2$ no periodicity would show up. This is also tested within ADRAS. Fig. 5.10 is showing an excerpt of these studies for PKS 2005-489. Is is obvious that all $d_{2,j}(\mathrm{t})$ are showing a larger scatter (thus no periodicity as in the hypothetical example in the previous sentence) than the rest. This is a confirmation that the above mentioned removal of star 2 from the sample of reference stars was justified.

This correction procedure is applied to all ATOM observing targets at all filter bands as soon as there are enough observations taken (> 20 usually), so that one can get useful distributions. For many targets, this is repeated after some time (when more observations have been taken) to get even finer correction terms.

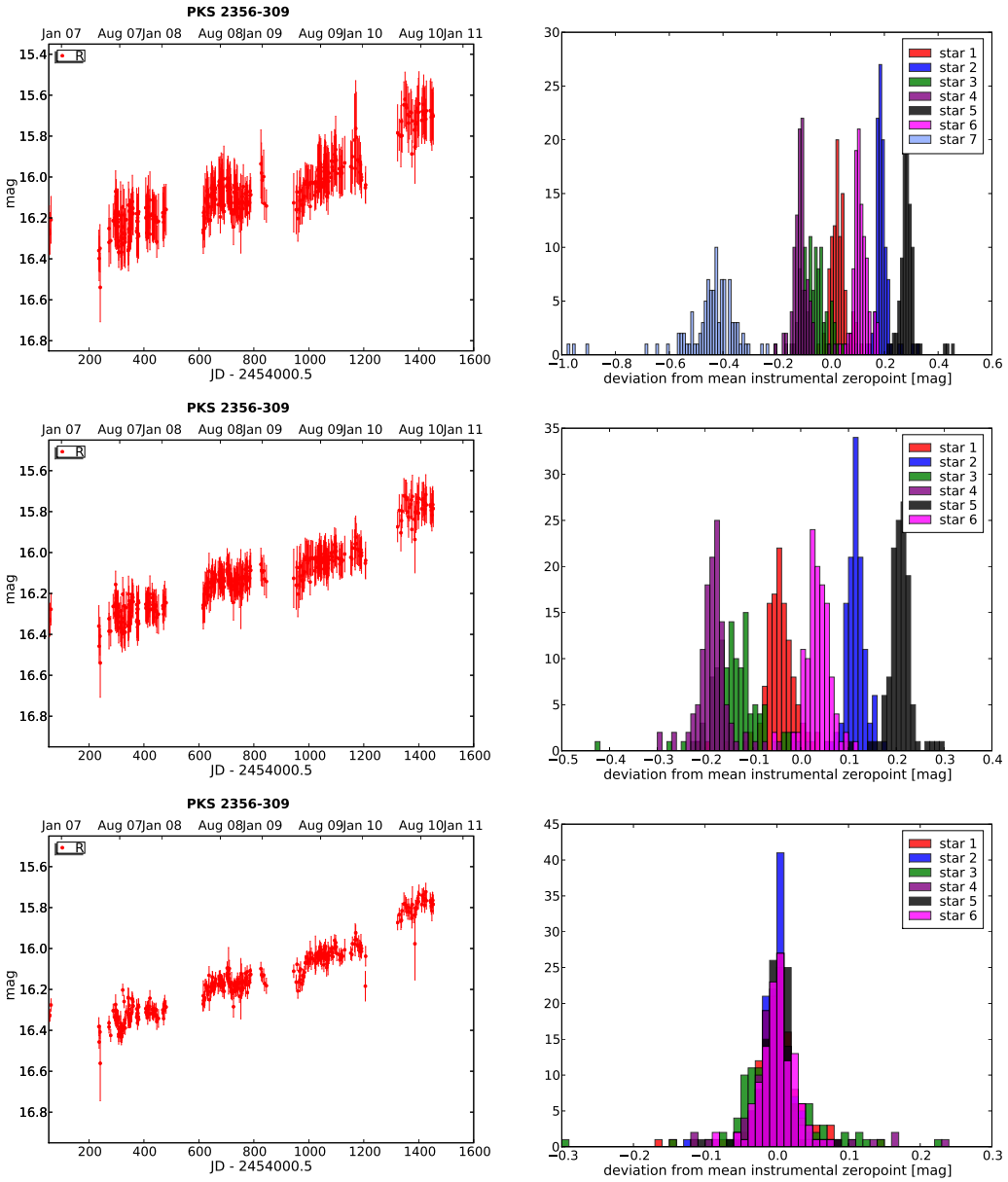

Figure 5.8.: *left column:* Resulting lightcurve of PKS 2356-309 using USNO stars as photometric reference. *right column:* distribution of difference between mean instrumental zeropoint and the zeropoint using a single star.
1st row: using 7 USNO stars located next to the AGN as reference. Star 7 has a much broader distribution than the other stars and is therefore omitted.
2nd row: as above, but without star 7.
3rd row: as above, but the catalog magnitude of each star shifted to the common mean.
The average error on each data point is reduced from ≈ 0.3mag down to ≈ 0.02mag using this approach (at the expense of an systematic error of the order of the correction terms). This allows now to see a finer modulation in the lightcurve, as well as to identify outlying points.

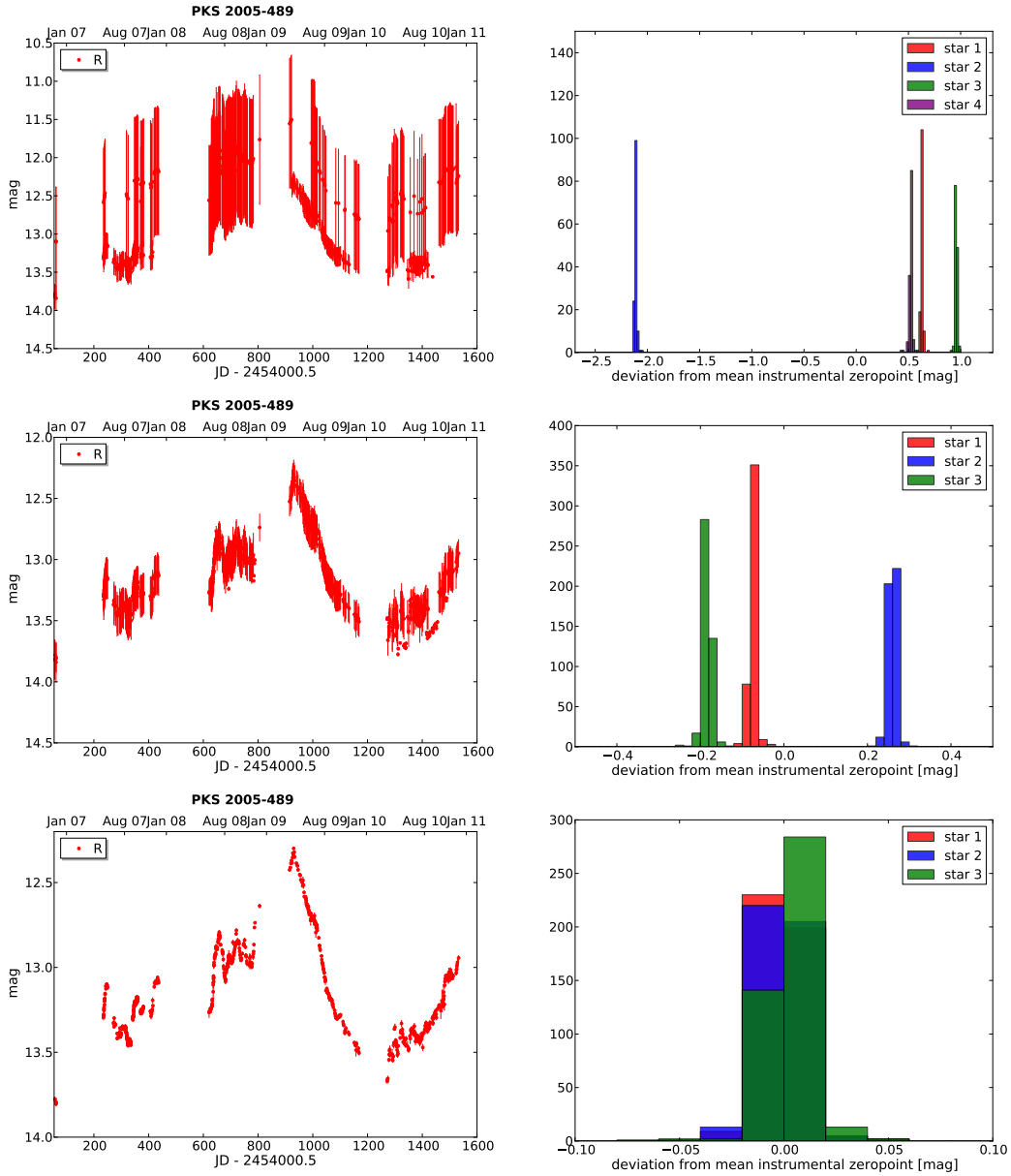

Figure 5.9.: Lightcurve and reference star scatter of PKS 2005-489, figure composition like fig. 5.8. Similar to the case of PKS 2656-309 in the previous figure, the lightcurve (left column) is showing an extremely large error and the histograms in the graph on the right-hand side show that the reference star no. 2 is off by more than 2mag w.r.t. to the other three stars. Star no. 2 was therefore excluded, results are shown in the second row. The third row shows the resulting lightcurve after a small additive correction was applied to the catalog magnitudes of the remaining 3 stars.
The lightcurves in the top and middle row are showing several points with considerably smaller errors than the remaining ones. The reason for that are telescope pointing offsets which caused star 2 to be outside the FoV (for the top row lightcurve). Similar for the middle panel: some exposures were taken with pointing offsets that large to move star 2 (star 3 in the consecutively numbering in the top panel) to be outside the FoV, thus reducing the error contribution of scatter between the reference stars according to eq. (5.6).

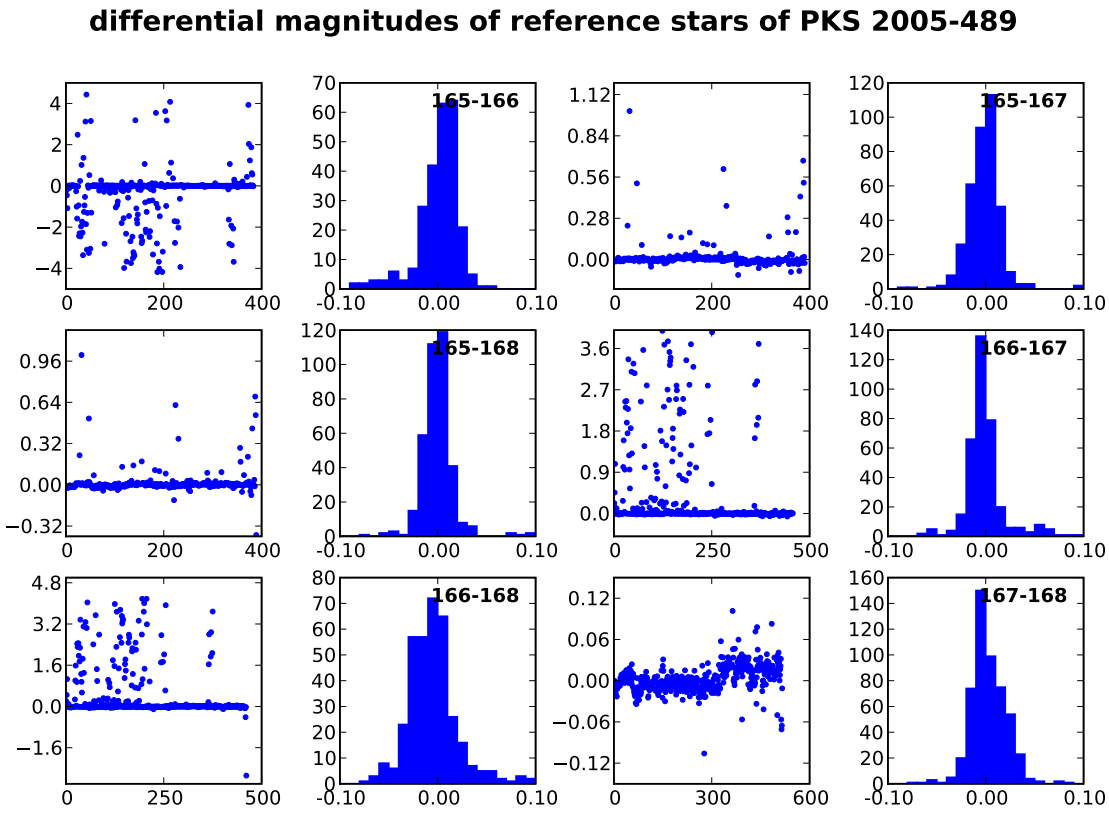

Figure 5.10.: Instrumental magnitude difference between the four reference stars of PKS 2005-489. It is evident that star no. 2 (in the text), resp. 166 (ADRAS internal numbering, shown in the graph) is not a suitable reference star for differential photometry.

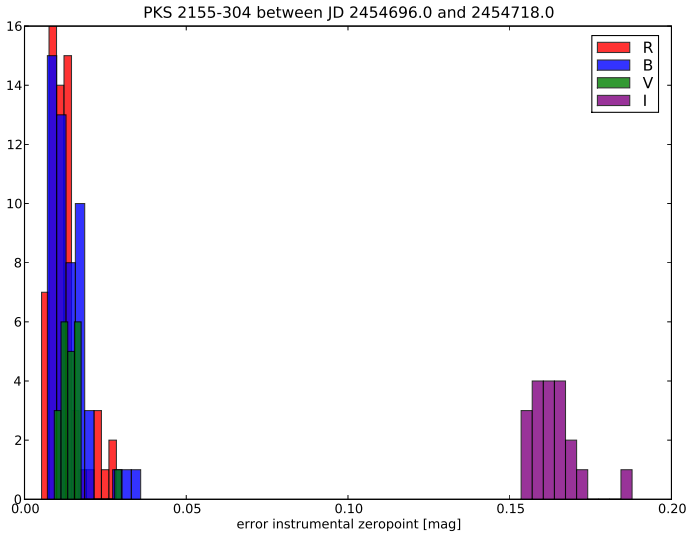

Figure 5.11.: Distribution of the error of the instrumental zeropoint per frame ($\sigma_{\mathrm{RMS,refstar}}$), separated by filter bands. The *I band* frames are significantly offset from all other filters (*B,V,R* band: mean=0.01 mag, *I* band: mean=0.16 mag).

Peculiarities in the I band observations of PKS 2155-304 ADRAS lightcurves of PKS 2155-304 in the *I* band are generally showing a significant larger error than all other bands. The question that arises immediately now: is this due to worser flatfielding in this band, or is the calibration of reference stars used for determining the photometric zeropoint per frame the reason? To have a homogeneous dataset for this study, the analysis here is restricted to the data taken on PKS 2155-304 during the H.E.S.S./*Fermi* campaign in August/September 2008 (Aharonian et al. (2009)).

Looking at figure 5.2.3, it is evident that the problem with the *I* band lightcurves originates (at least for the sample under investigation here) from the calibration of the individual instrumental photometric zeropoint of the frames, and is not a problem of standard reduction or flatfielding.

One explanation for that would be if one of the four used reference stars (see fig. 5.1) is listed with a wrong magnitude in the literature. This would increase the RMS of the zp_i in a systematic way. To test for this, the analysis that lead to figure 5.2.3 was repeated whilst excluding one of the four reference stars each time. Results are shown in figure 5.12.

It is obvious that star 4 introduces a highly significant offset in the *I* band. After omitting star 4 (*bottom-left* panel of fig. 5.12) a hidden issue becomes visible: the error in the *I* band is still a) larger and b) wider spread than in the other bands. This may point to flatfielding problems in the *I* band.

Another way of showing the behavior of reference stars than in figure 5.12 is given in figure 5.13, where –separated for filter bands– the deviation of the instrumental zeropoint per frame as measured using a single reference star from the frame instrumental zeropoint[19](eq. (5.5)) is shown. One sees that the given magnitude $m_I = 13.56\,\mathrm{mag}$ of star 4 is off by 0.35mag w.r.t. the other reference stars.

[19]given as the average of all the individual zeropoints

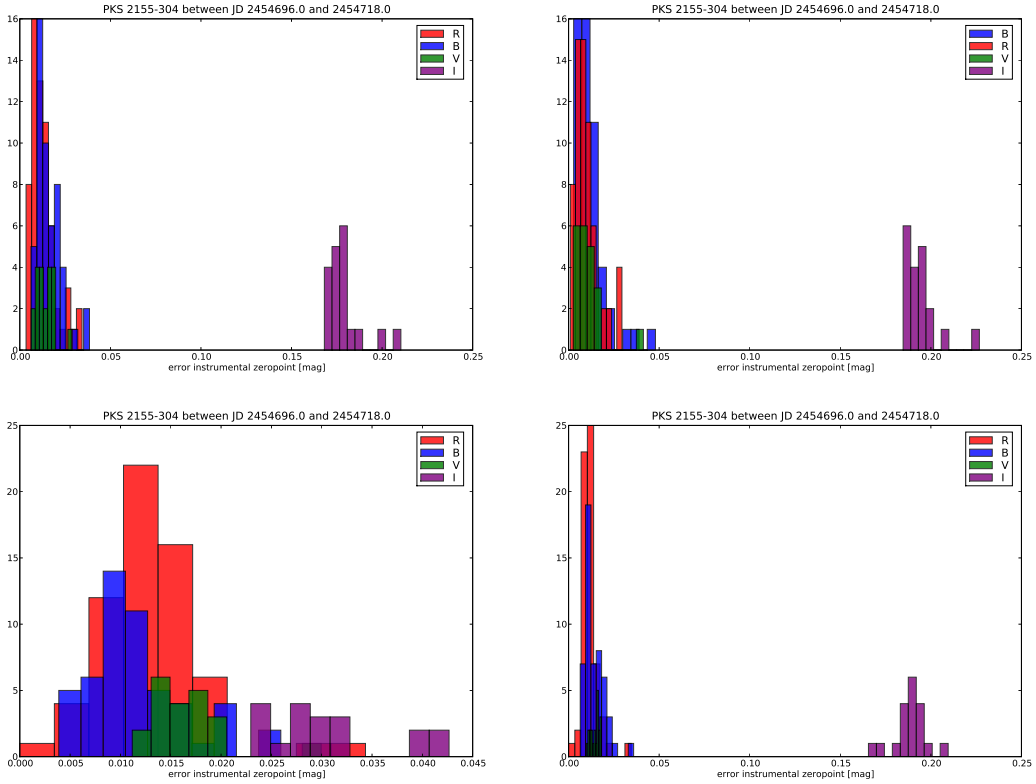

omitted reference star	band	$\sigma_{\mathrm{RMS,refstar}}$ [mag]	omitted reference star	band	$\sigma_{\mathrm{RMS,refstar}}$ [mag]
2	B	0.016 ± 0.007	4	B	0.012 ± 0.005
	V	0.014 ± 0.005		V	0.017 ± 0.004
	R	0.013 ± 0.007		R	0.013 ± 0.005
	I	$\mathbf{0.179} \pm 0.010$		I	$\mathbf{0.031} \pm 0.006$
3	B	0.012 ± 0.009	5	B	0.014 ± 0.005
	R	0.010 ± 0.007		V	0.015 ± 0.003
	V	0.011 ± 0.008		R	0.012 ± 0.004
	I	$\mathbf{0.194} \pm 0.010$		I	$\mathbf{0.189} \pm 0.010$

Figure 5.12.: Error distributions ($\sigma_{\mathrm{RMS,refstar}}$, defined in eq. 5.6) like in figure 5.2.3, but with one reference star omitted in each graph to check whether this star adds a significant number to the mean error value. The star numbering is the same as defined in fig. 5.8. *Top-left* to *bottom-right*: error distribution without stars 2...5. It is clearly visible that star 4 introduces a highly significant offset in the I band. After omitting star 4 a hidden issue becomes visible: the error in the I band is still a) larger and b) wider spread than in the other bands. This may point to flatfielding problems with the I band.

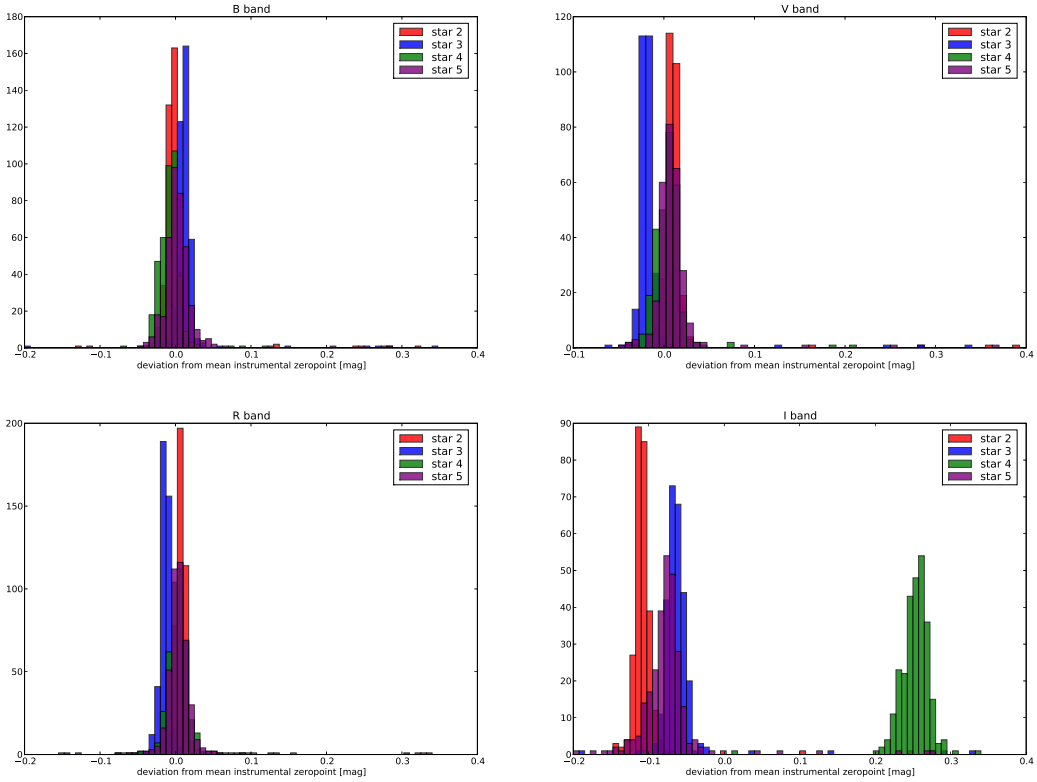

band	source	mean, RMS	band	source	mean, RMS
B	star 2	0.009 ± 0.096	R	star 2	0.014 ± 0.079
	star 3	0.023 ± 0.097		star 3	-0.006 ± 0.078
	star 4	-0.046 ± 0.279		star 4	-0.022 ± 0.228
	star 5	0.014 ± 0.101		star 5	0.014 ± 0.083
V	star 2	0.033 ± 0.145	I	star 2	-0.097 ± 0.085
	star 3	0.004 ± 0.142		star 3	-0.053 ± 0.084
	star 4	-0.053 ± 0.393		**star 4**	0.217 ± 0.252
	star 5	0.015 ± 0.202		star 5	-0.067 ± 0.090

Figure 5.13.: Deviation of instrumental zeropoint for each individual reference star from mean zeropoint per frame. This sample includes all data on PKS 2155-304 until Nov 8, 2008.

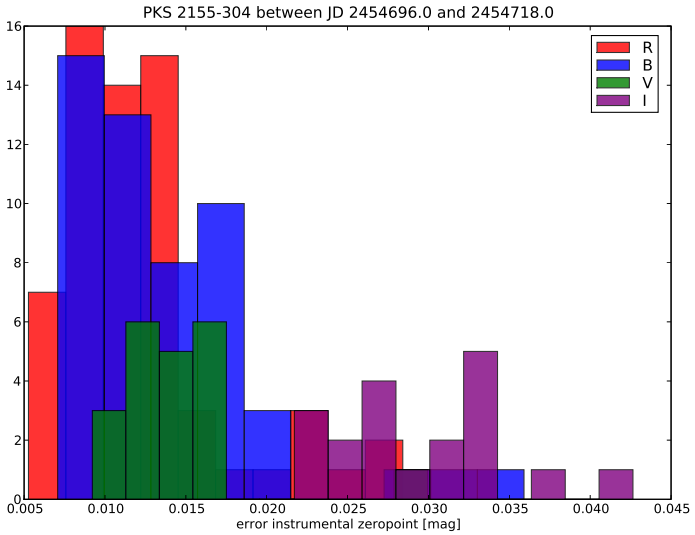

Figure 5.14.: Distribution of the error of instrumental zeropoint per frame ($\sigma_{\mathrm{RMS,refstar}}$), divided by filter bands. This is the same input data as in fig. 5.2.3, with the exception that the apparent I band magnitude of star 4 was assumed to be $m_I = 13.56 - 0.35 = 13.57$. This brings $\sigma_{\mathrm{RMS,refstar}}(I)$ down to 0.03mag (which is still 3x higher than for the other bands).

5.2.4. Lightcurves

The creation of lightcurves is straight-forward after all the calibration processes described above have been applied. ADRAS stores all photometric detections of all processed frames in a large single table[20], holding -beside other information- the different measured fluxes[21], position, target ID (a unique number assigned to each target object) and detection frame ID number. So all the system has to do is to select all detections at the target position and apply the instrumental zeropoint of the detection frame to get a list of fluxes vs. observation time (from the reference to the detection frame). To speed up the selection process, a pre-selection based on filter and target ID is applied before the positional search in RA and Dec (including some uncertainty) is done. To give some numbers, the query for all photometric points in all filter bands for our prime target, PKS 2155-304, takes 2.6 sec on my Desktop PC (2700 data points in total). A graphical representation is also implemented in ADRAS. For an example, please see any lightcurve presented within this thesis.

5.2.5. Automatic alarms

ADRAS can raise an alarm in case any source exceeds a pre-defined trigger level. This event is automatically distributed via mail, alerting the persons involved in the ATOM project about an optical flaring source.

[20] > 6 million rows up to now...
[21] different apertures are used, see sec. 5.2.1

6. Atmospheric extinction

Atmosphere – the burden of optical astronomy, part of the detector for IACTs and natural habitat for us humans. At least because of the first two of the before mentioned characteristics, it is necessary to characterize its influence on light crossing through it from outer space (or, in case of IACTs, from 10 km altitude) to telescope and detectors on the ground. In this chapter, I will present my approach to describe atmospheric extinction over Goellschau using observations with ATOM as well as the cloud monitor measurements (see sec. 2.5) and show the relation to the H.E.S.S. measurements.

6.1. Photometric parametrisation of extinction

Atmospheric extinction is usually modelled (in optical astronomy) by describing the light absorption in the atmosphere in *magnitudes per airmass*, k[1], and a color term γ, taking into account the wavelength dependence of extinction as well as the differences between the photometric reference system and the real photometric system at the telescope.

To connect now the measured quantity (which is flux on the detector per time interval) to the real apparent magnitude of a star, a third quantity, describing the sensitivity of the light collection system, is needed. This is usually called the *zeropoint zp*. A detailed description of this model can for example be found in Harris et al. (1981).

Taken this all together, the model for relating the true apparent magnitude of a star M with the measured flux m[2] and the true star color c can be written as

$$M = m + zp + (\gamma + \gamma\prime \cdot c) \cdot c - (k + k\prime \cdot c) \cdot z \tag{6.1}$$

For the sake of simplicity and inspired by *ESO Quality Control*, I am following their procedure[3] to describe the atmosphere over Paranal and the behavior of the two FORS instruments (see Appenzeller et al. (1998)) and neglect the first order airmass term and the second order color term ($\gamma\prime = k\prime = 0$) at first.

Thus, eq. (6.1) becomes

$$M = m + zp + \gamma \cdot c - k \cdot z \tag{6.2}$$

The observations used to determine the photometric coefficients were all targeted at well-defined *standard fields* (Landolt (1992)). In the beginning of ATOM operations, these fields were observed several times per night in case there was the chance that this

[1] Since magnitudes are a logarithmic scale, this linear ansatz is equivalent to an exponential absorption process. *Airmass* is a relative measurement of the amount of atmosphere the light has to traverse, i.e. it is equal unity for observations at zenith and increases with decreasing elevation like airmass $z = \sec(90^\circ - \text{elevation})$

[2] M, m being expressed in magnitudes, so $m = -2.5 \log(\text{counts/sec})$

[3] see Patat (2000) and http://www.eso.org/observing/dfo/quality/FORS2/qc/photcoeff/photcoeffs_fors2.html

Name	RA (J2000)	Dec (J2000)	2006	2007	2008	2009	2010	total
SA 92	+00:54:37	+00:38:57	4	177	56	36	19	292
PG 0231+051	+02:33:40	+05:18:38	11	51	28	22		112
SA 95	+03:53:19	+00:00:57		90	34	33	8	165
SA 98	+06:52:13	-00:19:40	79	38	3	22	7	149
Ru 149	+07:24:14	-00:33:04	48	46	8	8	5	115
Ru 152	+07:29:58	-02:06:39	80	41	11	18		150
PG 0942-029	+09:45:12	-03:08:03				5	6	11
PG 1047+003	+10:50:08	-00:01:04		10	37	39	5	91
PG 1323-086	+13:25:46	-08:49:34		64	70	73	10	217
SA 109	+17:44:13	-00:02:17		234	91	71	3	399
Mark A	+20:43:59	-10:47:42		13	77	10	4	104
SA 113	+21:41:06	+00:22:33		235	72	45	16	368
total			222	999	487	382	77	2167

Table 6.1.: Standard fields observed by ATOM. The table is giving the pointing position used by ATOM and the number of BVRI observation sets of this field per year as well as the total sum. The decreasing number of standard field observations is due to the increasing number of scientific monitoring targets, and thus less available telescope time per individual source.

night might be photometric (i.e. no clouds visible in the late afternoon and a positive weather forecast). The frequency of standard field observations decreased with more and more AGN monitoring targets entering the ATOM schedule, and thus less available observing time per target. Table 6.1 gives an overview of the used standard fields and the number of observations over the years.

Photometric coefficients have been computed on a night-by-night basis by using all observations of standard stars during that night and minimizing the function

$$\min\Big((M-m) - zp + \gamma \cdot c - k \cdot z\Big) \tag{6.3}$$

using `Minuit` (James (1998)) via its python wrapper `pyminuit`[4].

The results are shown in figure 6.1 with no cuts applied to the resulting parameters. The data of many nights leads to bad fits (red. $\chi^2 \gg 1$). This is most probably due to data being taken during non-photometric conditions. A result set with fit results leading to reduced χ^2 values > 2 omitted is shown in figure 6.2. This data can be used to draw some conclusions about the photometric quality of the telescope site. Please note that for the nightly parameters shown here most times only one or two high/low airmass observation pairs were used, thus leading to larger errors.

Table 6.2 is showing the resulting photometric parameters using a longer lasting data set, here covering the months May–August for the years 2007–2010, where we expect good weather in Namibia (September is known to have no cloud cover, but a dust layer in the lower atmosphere (also known to some people as the *Thomas-Lohse effect*).

From the resulting χ^2 values, it is clear that the resulting set of parameters is *not* a valid description of the atmosphere. This initiated further checking whether is was a good idea to neglect the first order airmass term and the second order color term as described before. Table 6.3 is giving the results of parameter fits to the full model of Harris et al. (1981) (eq. (6.1) and –since it did not lead to better fits (according to

[4] http://code.google.com/p/pyminuit/

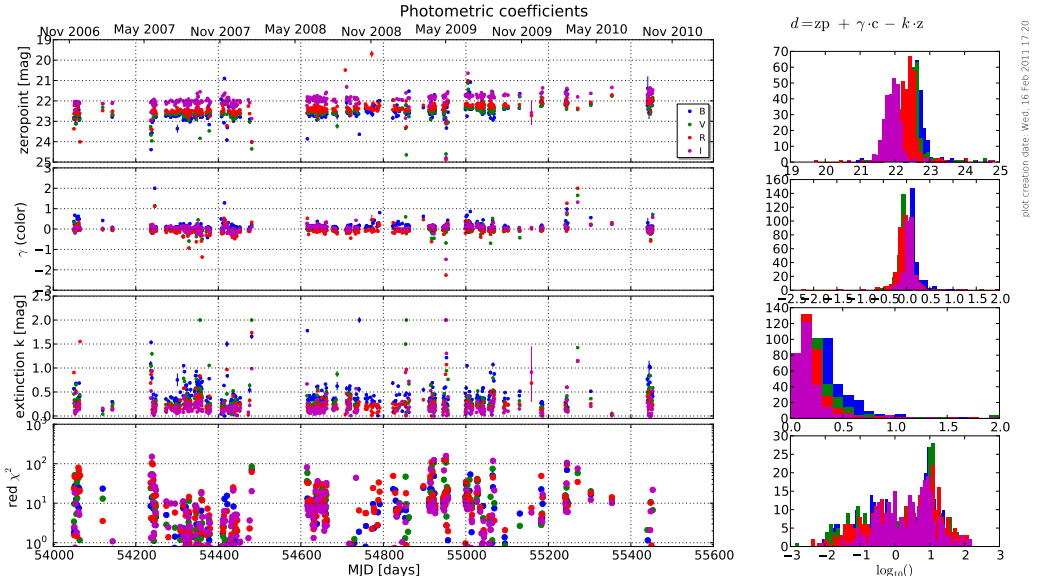

Figure 6.1.: Photometric parameters defined in eq. (6.2) per night. The different panels are showing (from top to bottom): the zeropoint zp, color term γ, the extinction coefficient k and the reduced χ^2 value of the fit. The histograms on the right-hand side are giving an overview of the distribution of the respective parameter. The colors denote which photometric filter band is shown. Note that for this exercise, no selection between photometric/non-photometric nights was done. So the nights resulting in bad fits (reduced $\chi^2 \gg 1$) can be attributed to be non-photometric. See figure 6.2 for the same presentation, but all night resulting in really bad fits (reduced $\chi^2 > 2$) omitted.

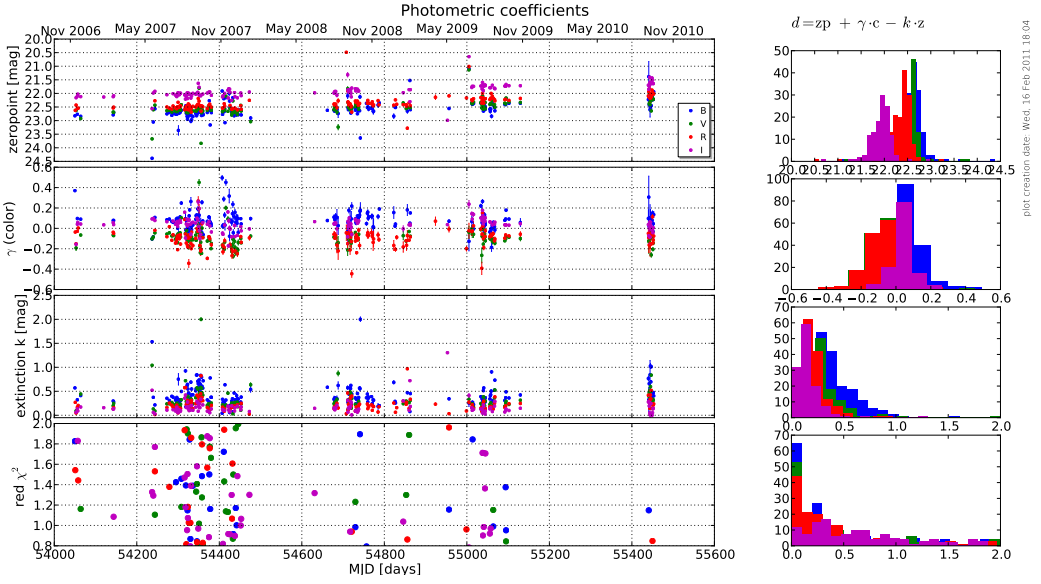

Figure 6.2.: Photometric parameters defined in eq. (6.2) on a nightly basis. Same presentation as in figure 6.1, but all nights resulting in bad parameter fits (reduced $\chi^2 > 2$) omitted.

band		2007	2008	2009	2010	Paranal
B	zp[mag]	22.01 ± 0.002	22.61 ± 0.002	22.32 ± 0.003	23.06 ± 0.072	28.0
	k	0.06 ± 0.001	0.35 ± 0.001	0.34 ± 0.002	0.98 ± 0.032	0.24
	γ	0.86 ± 0.001	0.13 ± 0.001	0.15 ± 0.003	0.07 ± 0.003	0.14
	red. χ^2	106	10.4	13.2	1.18	
V	zp[mag]	22.38 ± 0.001	22.38 ± 0.001	22.27 ± 0.002	22.48 ± 0.045	28.2
	k	0.14 ± 0.001	0.14 ± 0.001	0.23 ± 0.001	0.46 ± 0.019	0.15
	γ	0.16 ± 0.001	0.16 ± 0.001	-0.01 ± 0.002	-0.02 ± 0.002	+0.07
	red. χ^2	43.5	16.0	21.1	6.20	
R	zp[mag]	22.41 ± 0.002	22.41 ± 0.002	22.12 ± 0.002	22.62 ± 0.053	28.27
	k	0.14 ± 0.001	0.14 ± 0.001	0.17 ± 0.001	0.51 ± 0.023	0.09
	γ	0.02 ± 0.001	0.02 ± 0.001	0.02 ± 0.002	-0.25 ± 0.002	-0.01
	red. χ^2	16.5	17.0	24.9	8.59	
I	zp[mag]	22.03 ± 0.001	22.03 ± 0.001	21.71 ± 0.002	22.08 ± 0.030	27.6
	k	0.12 ± 0.001	0.12 ± 0.001	0.13 ± 0.001	0.39 ± 0.013	0.05
	γ	0.08 ± 0.001	0.08 ± 0.001	0.10 ± 0.001	-0.01 ± 0.014	-0.01
	red. χ^2	11.7	14.5	32.8	4.92	

Table 6.2.: Average photometric parameters over four month periods (May-August) in 2007–2010. Although the fitting program is able to find parameter values which describes the data best, the resulting χ^2 values clearly show that the atmosphere cannot be described with a single parameter set over a longer period in time (see also table 6.3 for parameters of other models). The last column is giving the atmospheric parameters published by ESO for Paranal in April–September 2010[5] as a comparison for typical values on a known good site (errors omitted).

the χ^2 values)– also to a very simplified model with no color term ($M = m + zp + k \cdot z$). No parameter set for any of these two models could be found that represent a valid (or just better) description of the atmospheric extinction.

Since this is true for all four years of data available, for all four filters and all three tested models, it seems to be fair to conclude that the atmosphere over Goellschau is not stable over a time span of month, and atmospheric extinction parameters are only valid for short time intervals like single nights (see figure 6.2).

Note that the possibility that I have made a mistake writing the fitting software seems to be tiny, since I have tested my software against the test data given in Patat (2000) and got the same results than the authors get.

6.1.1. Simpler approach to absolute photometry

The very simple approach to characterize the atmosphere without any color term (see previous section) will be investigated more deeply in the following. The used approach is to average over a longer period in time and select only "good" nights ("good" will be defined later).

The working model for the atmosphere here is

$$\begin{aligned} (m - M) = d &= zp - k \cdot z \\ zp &= d + k \cdot z \end{aligned} \tag{6.4}$$

, with the parameters being defined like in eq. 6.1. zp is determined here by differential photometry on standard fields using the default ADRAS procedures (see sec. 5.2.3),

[5] observing period P 85, measured with chip1 on FORS2; taken from http://www.eso.org/observing/dfo/quality/FORS2/qc/photcoeff/photcoeffs_fors2.html on Feb 16, 2011.

band		2007		2008		2009		2010	
B	zp[mag]	22.35 ± 0.00	22.92 ± 0.001	22.54 ± 0.003	22.63 ± 0.001	21.66 ± 0.004	22.24 ± 0.002	21.26 ± 0.017	22.14 ± 0.004
	k	0.17 ± 0.002	0.31 ± 0.001	0.31 ± 0.002	0.32 ± 0.001	0.22 ± 0.003	0.25 ± 0.001	0.03 ± 0.014	0.25 ± 0.003
	$k\prime$	-0.07 ± 0.003	-	0.02 ± 0.003	-	0.11 ± 0.004	-	0.30 ± 0.019	-
	γ	-0.14 ± 0.006	-	0.10 ± 0.004	-	1.21 ± 0.005	-	1.57 ± 0.023	-
	$\gamma\prime$	0.61 ± 0.002	-	0.05 ± 0.002	-	-0.36 ± 0.003	-	-0.45 ± 0.008	-
	red. χ^2	45.5	55.6	5.42	5.60	6.41	8.24	2.00	2.57
V	zp[mag]	22.38 ± 0.003	22.53 ± 0.001	22.54 ± 0.003	22.48 ± 0.001	22.12 ± 0.006	22.26 ± 0.002	22.25 ± 0.052	22.27 ± 0.013
	k	0.11 ± 0.002	0.18 ± 0.001	0.25 ± 0.002	0.23 ± 0.001	0.23 ± 0.003	0.23 ± 0.001	1.01 ± 0.044	0.38 ± 0.011
	$k\prime$	0.06 ± 0.002	-	-0.08 ± 0.004	-	0.00 ± 0.003	-	-0.80 ± 0.048	-
	γ	0.04 ± 0.005	-	-0.01 ± 0.001	-	0.38 ± 0.009	-	-0.98 ± 0.064	-
	$\gamma\prime$	0.11 ± 0.002	-	-0.01 ± 0.001	-	-0.24 ± 0.004	-	-1.12 ± 0.021	-
	red. χ^2	20.9	21.3	9.70	9.76	16.5	16.6	1.26	2.16
R	zp[mag]	22.65 ± 0.002	22.36 ± 0.001	22.57 ± 0.002	22.28 ± 0.001	22.61 ± 0.002	22.14 ± 0.001	22.40 ± 0.004	22.10 ± 0.003
	k	0.26 ± 0.001	0.12 ± 0.001	0.24 ± 0.001	0.15 ± 0.001	0.38 ± 0.001	0.21 ± 0.001	0.29 ± 0.003	0.24 ± 0.002
	$k\prime$	-0.22 ± 0.002	-	-0.19 ± 0.002	-	-0.41 ± 0.002	-	-0.12 ± 0.006	-
	γ	-0.36 ± 0.004	-	-0.58 ± 0.003	-	-1.04 ± 0.003	-	-0.70 ± 0.008	-
	$\gamma\prime$	-0.18 ± 0.002	-	0.02 ± 0.001	-	0.01 ± 0.001	-	0.04 ± 0.001	-
	red. χ^2	11.7	12.76	9.67	10.61	11.2	14.25	4.64	6.16
I	zp[mag]	21.92 ± 0.002	22.12 ± 0.001	21.87 ± 0.003	21.99 ± 0.001	21.50 ± 0.005	21.80 ± 0.001	21.59 ± 0.042	21.89 ± 0.009
	k	0.04 ± 0.001	0.13 ± 0.001	0.10 ± 0.002	0.12 ± 0.001	0.07 ± 0.003	0.12 ± 0.001	0.26 ± 0.029	0.28 ± 0.008
	$k\prime$	0.08 ± 0.001	-	0.02 ± 0.002	-	0.05 ± 0.002	-	0.03 ± 0.026	-
	γ	0.13 ± 0.003	-	0.13 ± 0.004	-	0.43 ± 0.008	-	0.54 ± 0.061	-
	$\gamma\prime$	0.03 ± 0.001	-	0.00 ± 0.001	-	-0.12 ± 0.003	-	-0.21 ± 0.024	-
	red. χ^2	8.29	8.69	12.1	12.58	25.2	25.7	0.79	0.81

Table 6.3.: Same as table 6.2, but using the full model as defined in eq. 6.1 and a even more simplified version of eq. (6.2) by setting the color term $\gamma = 0$. It is evident from the resulting red. χ^2 values $\gg 1$ (with the exception of I band in 2010) that none of this models can describe the atmospheric conditions over a 4 month period of mostly good weather.

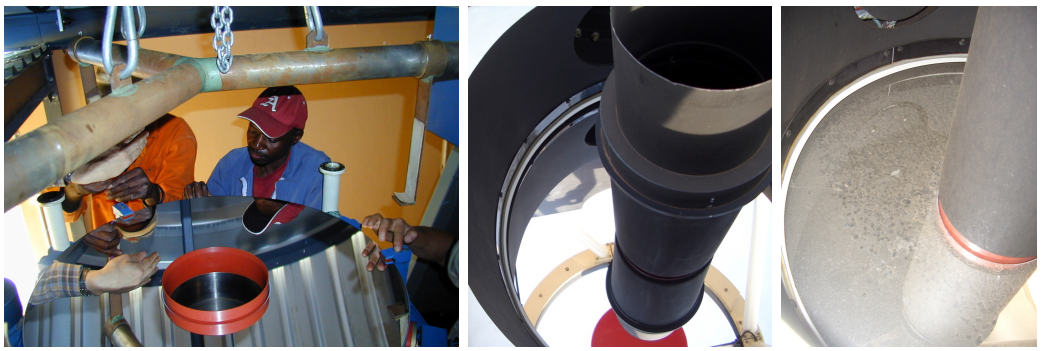

Figure 6.3.: A macroscopic view on the mirror degradation by dust. From left to right: during installation (Aug 2005), after a few month in Namibia in Nov 2005 and four years later in Nov 2009.

Band		all	2007	2008	2009	2010
B	zp	22.67 ± 0.04	22.76 ± 0.03	22.63 ± 0.04	22.46 ± 0.06	21.99 ± 0.10
	k	0.38 ± 0.03	0.36 ± 0.03	0.30 ± 0.04	0.34 ± 0.06	0.17 ± 0.10
	red. χ^2	0.11	0.17	0.17	0.06	0.16
V	zp	22.44 ± 0.08	22.76 ± 0.03	22.35 ± 0.04	22.25 ± 0.05	21.96 ± 0.10
	k	0.22 ± 0.02	0.21 ± 0.03	0.11 ± 0.04	0.21 ± 0.05	0.13 ± 0.10
	red. χ^2	0.71	0.11	0.11	0.25	0.10
R	zp	22.43 ± 0.03	22.45 ± 0.02	22.26 ± 0.03	22.16 ± 0.04	21.99 ± 0.07
	k	0.23 ± 0.02	0.18 ± 0.02	0.08 ± 0.03	0.17 ± 0.04	0.17 ± 0.07
	red. χ^2	0.44	0.07	0.04	0.12	0.11
I	zp	22.03 ± 0.02	22.14 ± 0.02	21.95 ± 0.03	21.87 ± 0.03	21.61 ± 0.05
	k	0.14 ± 0.02	0.15 ± 0.02	0.09 ± 0.03	0.15 ± 0.03	0.09 ± 0.05
	red. χ^2	0.36	0.05	0.20	0.053	0.15

Table 6.4.: Fitting results of data presented in figure 6.4 (column "all"). For the years 2007–2010, the same date intervals as in table 6.2 were chosen to allow comparing the two methods. The resulting graphs for the yearly data sets are given in appendix D.1 ff.

and a coarse cut is applied to remove obvious outliers (mostly weather affected) and define the "good" data sample. The remaining data points are binned into 5 intervals of increasing airmass (binwidth=0.2 airmasses). The resulting points are fitted with eq. (6.4). Figure 6.4 shows the data/fit curve and fitting results are given in table 6.4.

The resulting reduced χ^2 values are all $\ll 1$, which would normally mean that the measurement errors of the input data are overestimated, but here it is because of the input data being binned. The results are looking reasonable, plausibility checks are

- *decreasing extinction* coefficient k with *increasing wavelength*. This is expected, since the most relevant scattering process, *Rayleigh* scatter, is $\propto \lambda^{-4}$.

- *falling zeropoint zp over time* (51% in 3 years in B, 52% in V, 35% in R and 38% in I band), reflecting the degradation of the mirrors. See also figure 6.3 for photos of the mirror state.

The results here give better results than the fit results presented in the previous section, which were also not considering any color term ($\gamma = \gamma\prime = 0$, listed in table 6.3) and using the same data.

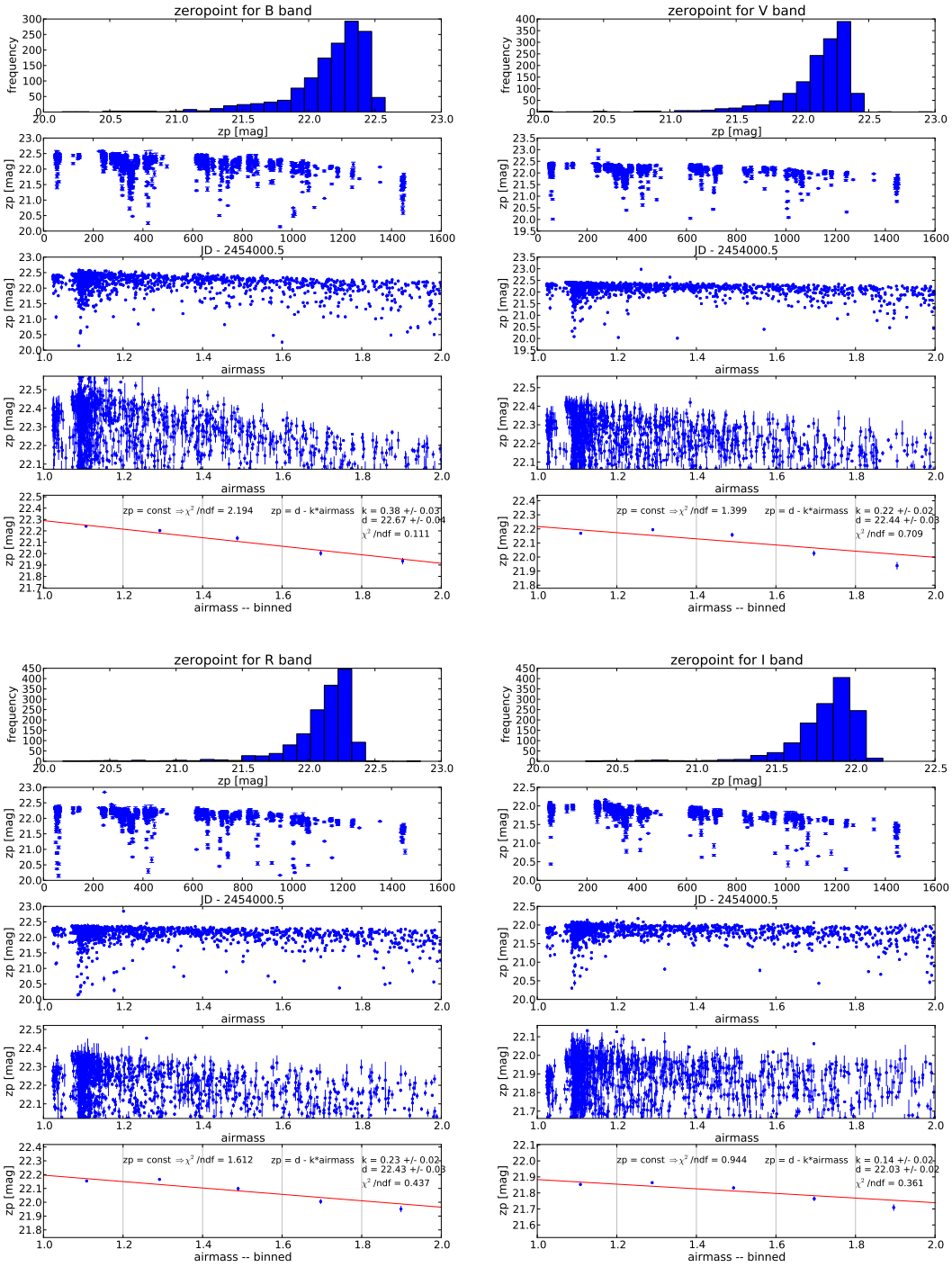

Figure 6.4.: Simple photometric model, just a linear dependence of absorption (expressed in logarithmic units, so an exponential damping in linear units) with airmass. The four filter bands are sorted by increasing wavelength. Each graph consists of five sub-panels. These are showing (top to bottom) the histogram of measured zeropoints, the zeropoint over time, the zeropoint vs. airmass, a blow-up of the previous one (showing only the data which was selected for binning), and on bottom the binned data and a linear fit to this. See table 6.4 for a summary of the fitting results. As a test, a constant value was also fitted to the data (meaning no extinction), yielding as expected always a worse χ^2 than the linear fit.

The difference between the approach in this section and the previous one is the binning of data here in several ways. In the previous section, each measured star flux was treated individually.

The following binning was applied:

1. only one common zeropoint per acquired frame was used, so this is an averaging over all detected standard stars in the image (numbers of stars depending on the standard field, something between 3 and 10).

2. averaging over airmass intervals like described before.

Binning seems to be necessary here to get useful results and to suppress the data taken during non-photometric conditions.

6.2. Atmospheric transparency as seen by the cloud monitor

One generic limitation of atmospheric transparency characterization via classical extinction measurements –like the ones presented in the previous section– is that one measures along a very narrow[6] line-of-sight and assumes that this describes the whole hemisphere. And typically not all (or even a major part) of the available telescope time is used for observations of standard fields, but one performs 1...3 observations of standards per night at most. This approach is valid in the cases where one has a homogeneous atmosphere and photometric conditions, but a continuous sampling of measurements of the whole sky would be an improvement.

ATOM offers a device with which this can be done: the cloud monitor, described in sec. 2.5 and 4.2.

As described before, this device is operating with an all-sky camera without any bandpass filter, so no color information is available. But it is offering all-sky images every few minutes, and the procedure of searching for clouds by determining which fraction of stars is visible at different parts of the sky is giving a number between 0 and 10, representing the sky transparency, averaged over the whole visible part of the spectrum. Thus it enables the creation of sky transparency curves with dense temporal sampling and spacial resolution.

6.2.1. Directional trends

Figure 6.5 is showing the sky quality at zenith as estimated by the cloud monitor. Note that moonlight has a negative influence on the quality measurement as can be seen by the overlaid green bars, showing only data with the moon below the horizon. An azimuthal trend is visible in fig. 6.6, where the sky quality away from the zenith is visualized. Also note that this data is restricted to measurements with perfect quality ("10") in the zenith.

The sky quality is worse towards south-east. This is the direction to the guest farm Weissenfels, but Weissenfels is 6.5 km away and consists of only a few buildings. There is no direct line-of-sight to them because of the local topology. In addition to that, they are usually switching off their electric power generator at 10 pm, so it seems unlikely

[6] In case of ATOM, the FoV is (7.8x7.6≈ 60) arcmin^2, thus only $\approx 10^{-7}$ of the total sky area.

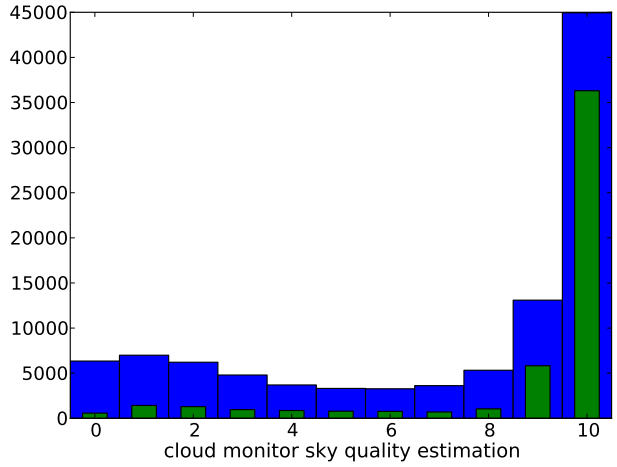

Figure 6.5.: Sky transparency at zenith, estimated by the cloud monitor (0: worst, 10:best). Shown is all available data (mid-2008 until end of 2010 without Dec'08 – Aug '09 were technical problems prevented the operation) in blue, while the green overlay is with data restricted to moonless time. Note that there is a bias in favor of good weather, since the cloud monitor does not operate during rain or 30 min afterwards.

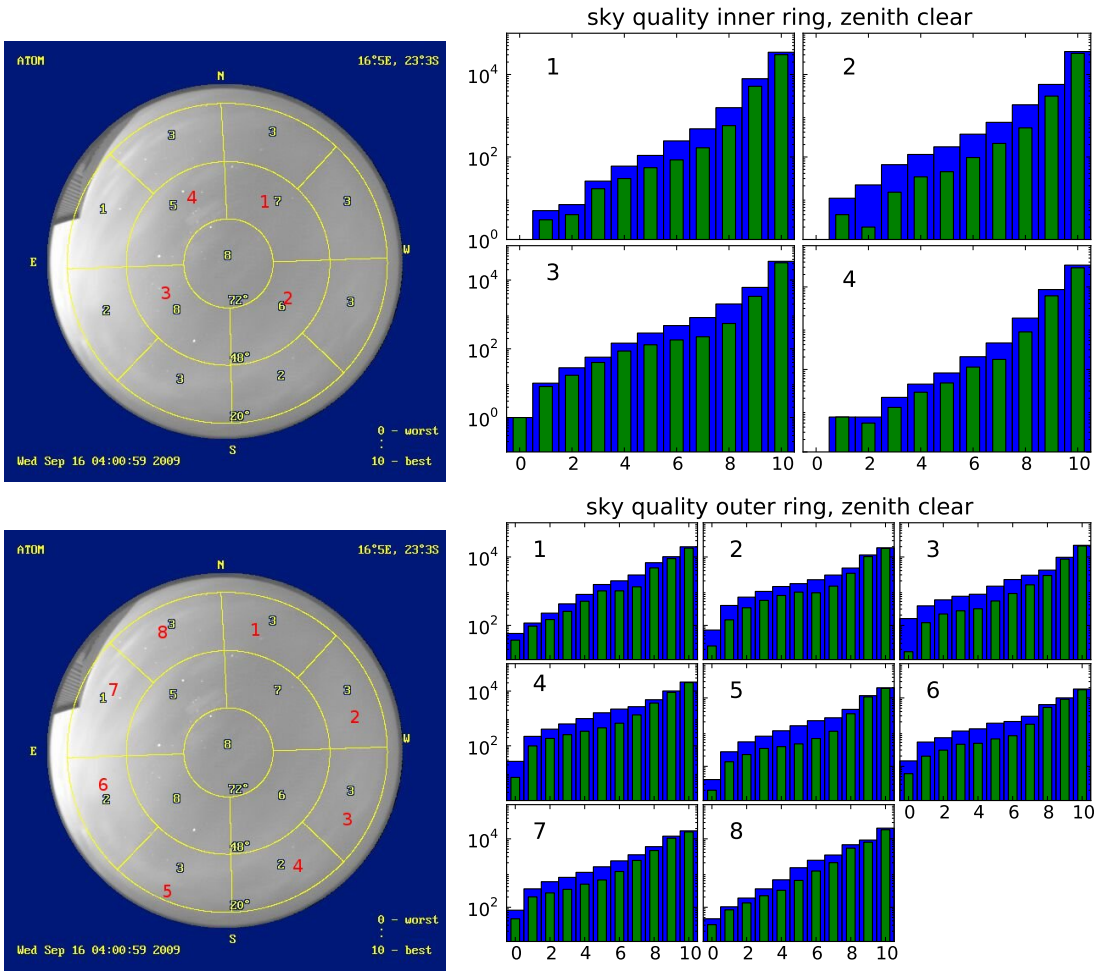

Figure 6.6.: Sky transparency at different azimuthal segments, restricted to measurements with perfect zenith sky quality. Data and color coding like in fig. 6.5 Top: inner ring, elevation between 45° and 72°; bottom: lower ring: elevation between 10° and 45°. Especially in the lower ring data, one can notice on average a worse sky quality towards south-east direction (segments 5+6).

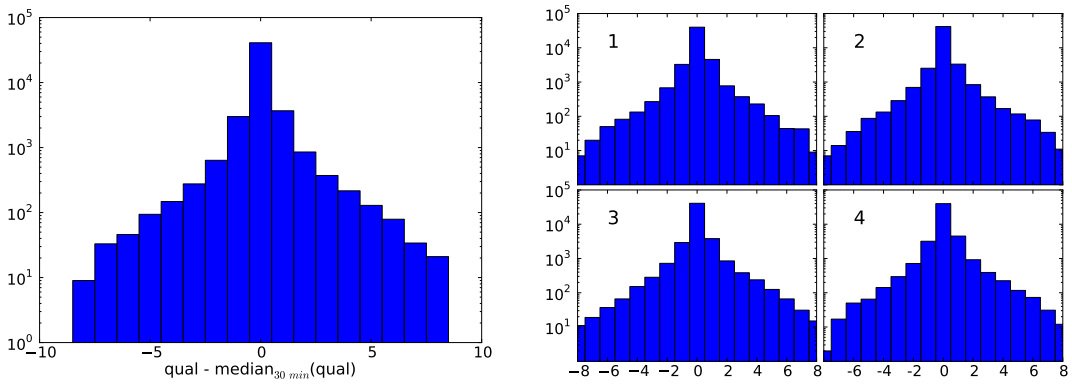

Figure 6.7.: Characteristic time scales of changing atmospheric conditions. *left:* zenith segment, *right*: inner ring, numbers like in fig. 6.6. There is a clear asymmetry visible: it is more likely that *worse* weather changes occur in a 30 min time window than clearing up.
(Note that these histograms are in log-scale.)

that this decrease of sky quality is based on light pollution by them. There is also no city in this direction before the land surface is falling down from 1800 m altitude to the *Namib-Naukluft National Park* at sea level and the Atlantic Ocean, so this lower sky quality in that direction is most probably not due to artificial light pollution, but meteorologically based.

6.2.2. Temporal trends

As mentioned earlier, one nice feature of the cloud monitor data is the fact that it delivers measurements every few minutes[7]. This allows to search for characteristic time scales, e.g. how fast the weather changes[8].

Fig. 6.7 is showing the deviation of a single measurement from the median value of all data within a 30 min time window (data again restricted to moonless times). It is evident that changes to worse atmospheric transparency in a 30 min interval happen more often than improvements.

Seasonal trends of transparency changes can be seen in fig. 6.8, which is a time resolved picture of the histograms shown in fig. 6.7 with the occurrence frequency being represented in color code.

6.3. Extinction vs. Cherenkov shower parameters

6.3.1. Cloud monitor

The simplest approach to compare two complex quantities (here: atmospheric transparency vs. Cherenkov shower parameters) is if the complex quantity can be reduced

[7] At present time, there is 1 image every 3 min acquired. At the beginning, it was 1 image per 5 min.
[8] This is quite important for the automatic operation of ATOM... do we have to close the roof immediately after the first clouds are coming in or can we continue observing for one hour and see how it evolves before risking rain on the telescope mirror?

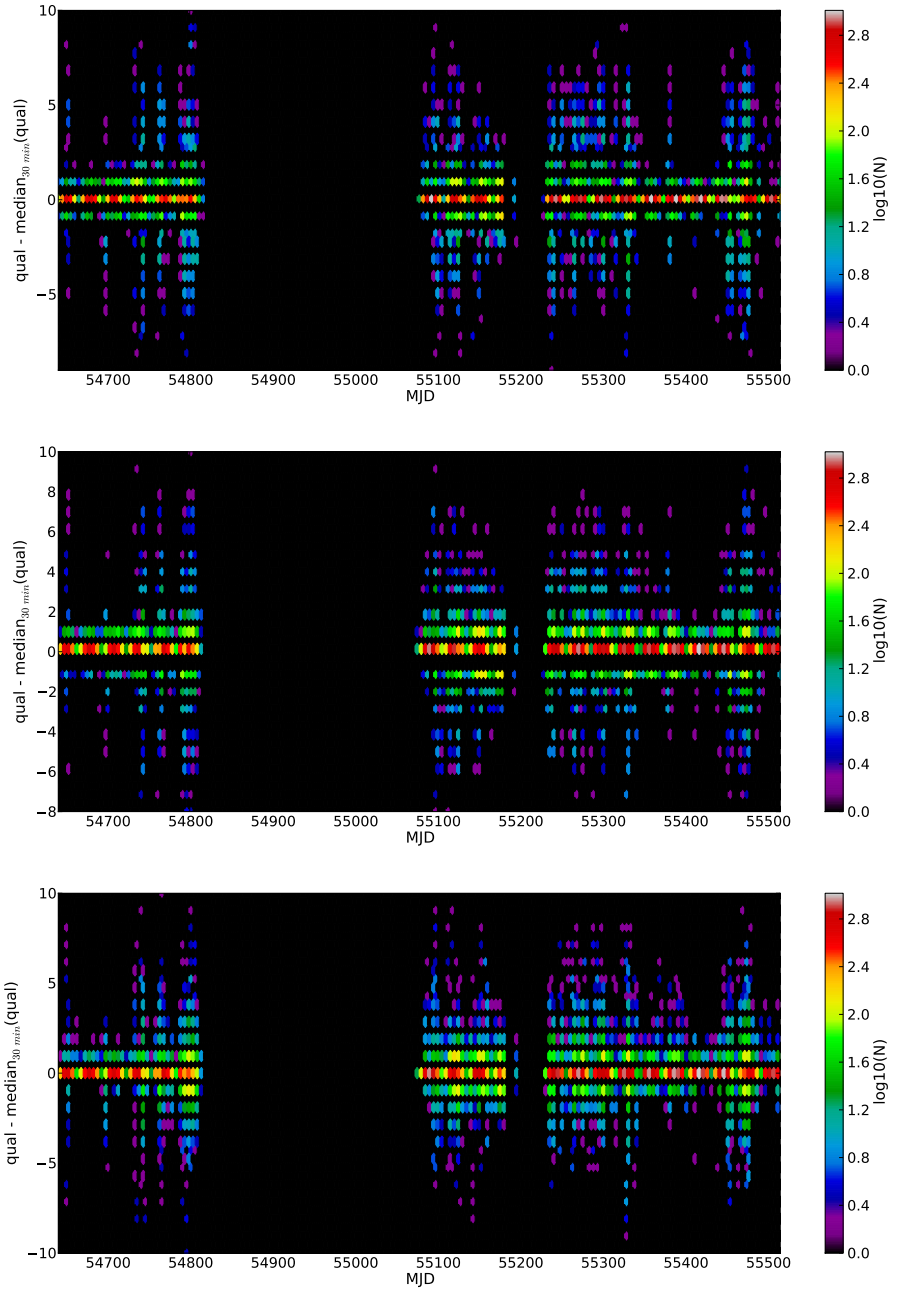

Figure 6.8.: Time-resolved seasonal changes of the cloud monitor determined sky transparency (only moonless times). The data has been binned in 5 day intervals. The 9 month gap starting December 2008 (MJD 548500) is due to technical problems with the cloud monitor device. *upper panel:* zenith segment; *central panel:* inner ring, north-west direction (segment 1 in fig. 6.6, upper panel); *lower panel:* south-east direction (segment 3).

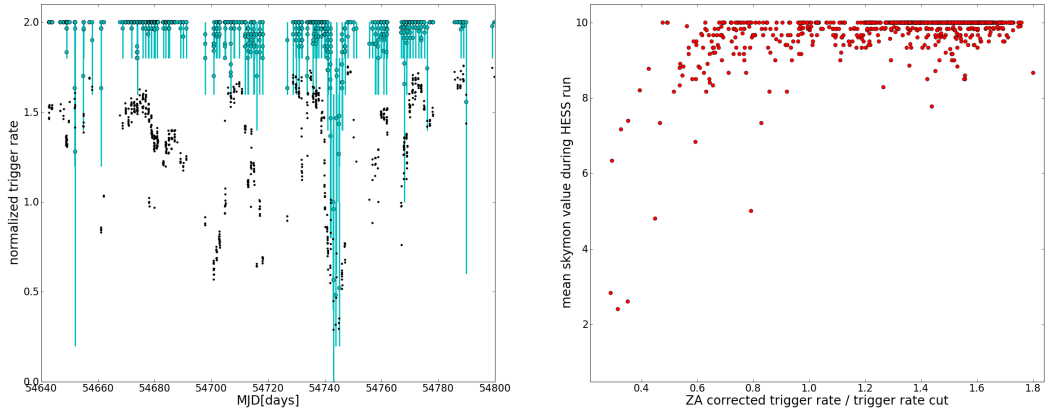

Figure 6.9.: H.E.S.S. trigger rate vs. sky monitor value. *left:* normalized H.E.S.S. trigger rate (black) and ATOM sky monitor values (turquoise), scaled from interval [0,10] to interval [0,2] for easier comparison, as a function of time. *right:* correlation plot of both numbers.
The right panel shows that nearly all of H.E.S.S. data is taken during conditions with sky monitor value ≥ 8, the vast majority at conditions ≥ 9. Thus it can be concluded that the H.E.S.S. trigger rate is much more sensitive to atmospheric transparency changes than the sky monitor in the way the all-sky images are analyzed at present time.

to a single number. Here, I adopt this approach by using the *sky quality number* determined by the ATOM cloud monitor (described in sec. 2.5 and 6.2) to compare the sky transparency to the normalized H.E.S.S. trigger rate[9], which is used by the H.E.S.S. analysis as quality criteria to cut-out weather affected data.

The idea behind this is to check if a) the trigger criteria is correlated (and how much) to the visual transparency of the sky and b) if the sky quality number may be another (better?) criteria for selecting H.E.S.S. runs affected by bad weather.

Figure 6.9 is showing the evolution of the normalized H.E.S.S. trigger rate and the sky monitor quality value over time (left panel) as well as a correlation plot of these two values (right panel).

The sky monitor numbers were spacially and temporally matched to the 28 min of a H.E.S.S. observation run; spacial match means picking the sky segment where H.E.S.S. was pointing at the middle of the run. The error bars of the sky monitor values represents the span of different measured values during a run, the point is the mean value. Since H.E.S.S. is only taking data during dark (moonless) nights, the contemporaneous sky monitor data is naturally also not affected by moonlight and hence the problems in false cloud detections mentioned in sec. 2.5 do not apply.

The right panel shows that nearly all of H.E.S.S. data is taken during conditions with sky monitor value ≥ 8, the vast majority at conditions ≥ 9. Thus it can be concluded that the H.E.S.S. trigger rate is much more sensitive to atmospheric transparency changes than the sky monitor in the way the all-sky images are analyzed at present time. However, one has to keep in mind that the ATOM sky monitor was never designed to help with the calibration of IACT data, but only to shut-down ATOM in

[9]The measured trigger rate is normalized to the expected trigger rate, taking into account the telescope elevation and the aging of the H.E.S.S. cameras and degradation of mirrors.

star	(B-R)	trig $= a \cdot (B-R) + b$			trig $= \exp(a + b \cdot (B-R))$		
	intrinsic	a	b	χ^2/ndf	a	b	χ^2/ndf
SA 113 / 239	0.8	-272	374	900/150 = 6.0	6.63	-2.01	844/150 = 5.63
SA 92 / 252	0.8	-189	306	916/117 = 7.83	6.08	-1.32	886/117 = 7.57
SA 113 / 233	0.9	-267	380	914/148 = 6.17	6.67	-1.96	865/148 = 5.85
SA 113 / 245	1.0	-275	444	875/148 = 5.92	7.09	-1.97	836/148 = 5.65
SA 92 / 249	1.1	-185	353	951/118 = 8.1	6.42	-1.31	918/118 = 7.77
SA 92 / 250	1.3	-190	382	961/118 = 8.1	6.49	-1.23	938/118 = 7.95
SA 109 / 956	2.01	-441	691	430/105 = 4.1	8.16	-2.58	453/105 = 4.32

Table 6.5.: The result of fitting a) a linear function and b) an exponential decay to the H.E.S.S. trigger rates vs. star color (B-R). Data and fit curves are shown in figure 6.10. The exponential fit is better than the linear one for all but one case. The stars are ordered by increasing color (i.e. from blue to red).

case of incoming clouds (a task that it handles perfectly).

6.3.2. Multi-color starlight

Another approach to check for correlations between the H.E.S.S. trigger rate and astronomical observables is to look for the atmospheric reddening of stars (extinction is stronger towards short wavelengths).

All optical starlight measurements shown here are from observations of photometric standard stars (Landolt (1992)). The images in B and R filters were taken right after one another, exposure times are of the order of minutes.

The measured B and R magnitudes were corrected to airmass=0 (equivalent to observations outside the atmosphere) by fitting a linear function (for each star in both colors) to the instrumental magnitude over airmass, while restricting the fit to data points not obviously affected by bad atmospheric conditions). The correlations found were used to normalize the measurements to airmass=0 (like in sec. 6.1.1).

The H.E.S.S. trigger rates, taken from the H.E.S.S.-Heidelberg database, are the averaged value over the 28 min long IACT observing run during which the optical observations were taken. The trigger rates are transformed to a virtual zenith angle of 0°. No further quality selection was applied to the trigger rates.

Positional consistency was not considered in this study. It may well be that e.g. the Cherenkov array was pointing to a clear patch of sky to the south whilst the optical telescope was affected by small clouds in the northern hemisphere. True spacial consistency is nearly impossible, since H.E.S.S. does not observe optical standard fields, and I am not aware of any TeV source in or next to any standard field.

The data shown here only represents large-scale atmospheric conditions (affecting the whole sky above the H.E.S.S. site), whereas isolated clouds on some parts of the sky add noise to the resulting correlation plots.

6.3.3. Conclusion on shower parameter correlations

Unfortunately, neither the cloud monitor measurements (sec. 6.3.1) nor the star reddening (sec. 6.3.2) can trace the normalized H.E.S.S. trigger rate. Since this trigger rate is being used as quality criteria for H.E.S.S. analysis since the beginning of this experiment, and H.E.S.S. data has gained quite some reputation in the VHE community, it is unlikely that it is a very bad quality criteria. Hence, any new number being proposed as quality check for H.E.S.S. needs to correlate with the trigger rate at least roughly (certainly, the correlation coefficient has to be <1, because if it would be ≈ 1, it would be the same and not possibly better).
So the two methods presented here are not suited for H.E.S.S. data quality control. Unfortunately, the other proposed method for H.E.S.S. quality control, LIDAR measurements of aerosol layers, do also not deliver promising results (and the devices are broken most time anyway).

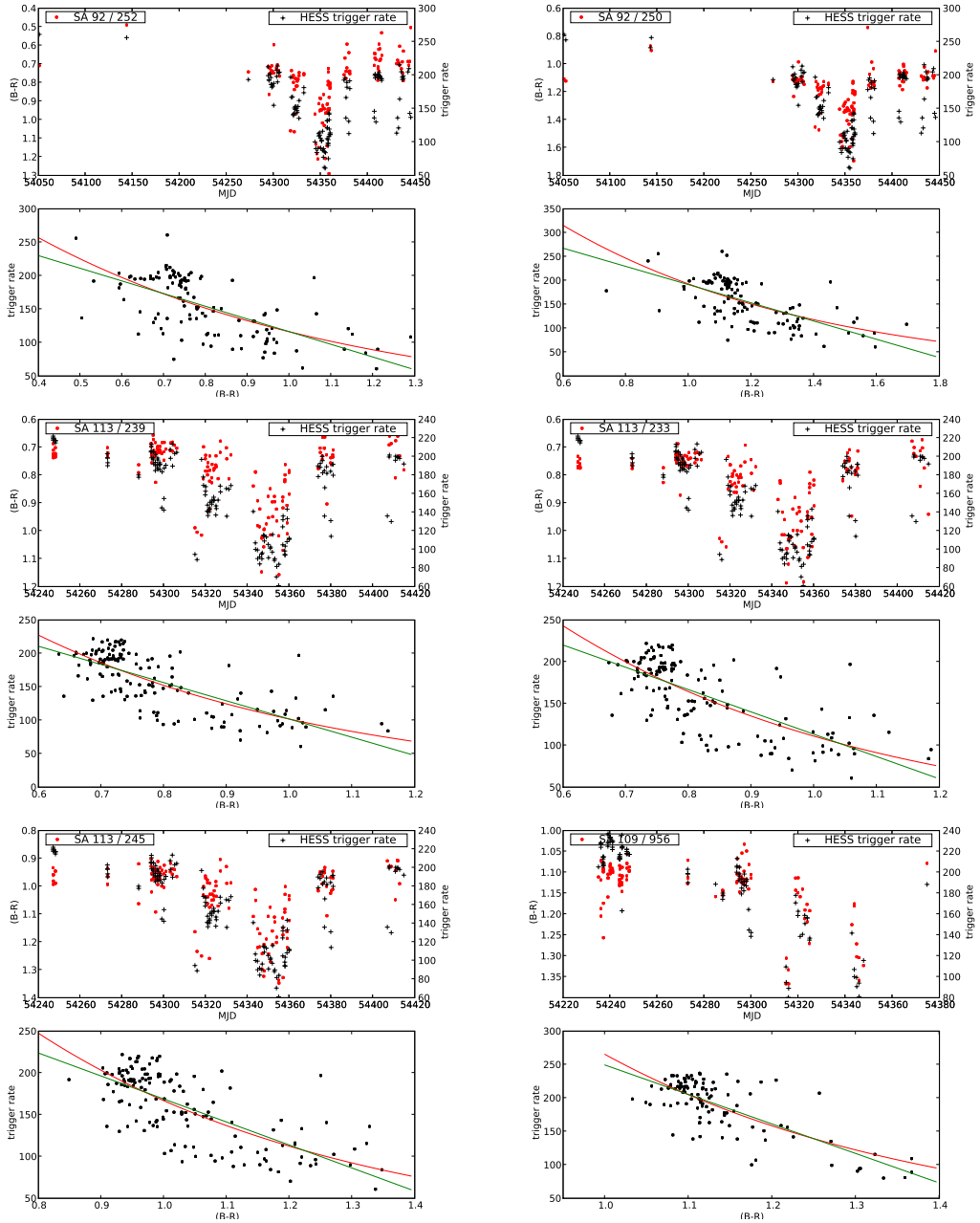

Figure 6.10.: Correlation between star color and the H.E.S.S. trigger rates for four different standard stars. Each box shows (B-R) color and H.E.S.S. trigger rate as a function of time in the upper panel and the correlation between color and trigger rate in the lower panel. The lines in the lower panels represent an exponential (red) and linear (green) functional fit to the data. The quality of the fit and the resulting fitting parameters are given in table 6.5. The error of the star color is ≈ 0.02 mag, error bars are omitted for clarity. All values are corrected to airmass=0.

7. Monitoring of Active Galactic Nuclei

In this chapter, I will present some of the results of ATOMs main mission: lightcurves from the optical monitoring of active galactic nuclei. As described earlier in sec. 4.1, the frequency of observations of a specific source is strongly depending on its importance. Some prominent AGN like PKS 2155-304 are supposed to be visited by the telescope every night, most every 3rd night and some only once per week or so (assuming perfect weather).

The ATOM measurements shown in refereed papers in the context of MWL campaigns are typically not the time-resolved lightcurves, but averages over the observing campaigns, mainly because the VHE experiments need to accumulate data for many nights to get a significant signal (see e.g. Aharonian et al. (2007) (1ES 10229+200), Aharonian et al. (2007) (1ES 0347-121), Aharonian et al. (2008) (RGB 0152+017), Aharonian et al. (2009) (PKS 2155-304) and HESS Collaboration et al. (2010) (PKS 2356-309))

A study on short-term variability of Mrk 421 is given in the first section of this chapter. Sec. 7.2 presents the lightcurves of all TeV-detected AGN observable by ATOM; prominent flares are shown in sec. 7.3. Color-magnitude diagrams of these AGN are discussed in sec. 7.4 as well as in appendix A, together with sources not detected in TeV, but for which at least 25 measurements in B+R were acquired. The whole archive of ATOM-lightcurves of more than 220 sources is only available online[1] due to space constrains in this thesis.

7.1. Investigation of possible short-term microvariability in Mrk 421

Alerted by an *Astronomers Telegram* about TeV flaring of Mrk 421 (Ong (2010)), H.E.S.S. committed ToO observations of this source in February 2010. Along with the observations by the IACT array, ATOM performed a dense monitoring of this source for 4 nights. This dense monitoring consists of a BVRI sequence at the beginning, followed by a 1..1.5 hour period during which only 1 minute R band exposures were taken one after another and ended typically with another BVRI sequence. The R band monitoring was contemporary to the IACT observations. Note that Mrk 421 is a northern source and not very well visible from Namibia (see fig. 7.1 for a visibility overview). The rapid R band observations in these days are covering the complete H.E.S.S. observation window plus some time buffer at the edges. This dataset allows to search for short term microvariability in Mrk 421

[1] http://atom.uni-hd.de/intern/Results/index.html

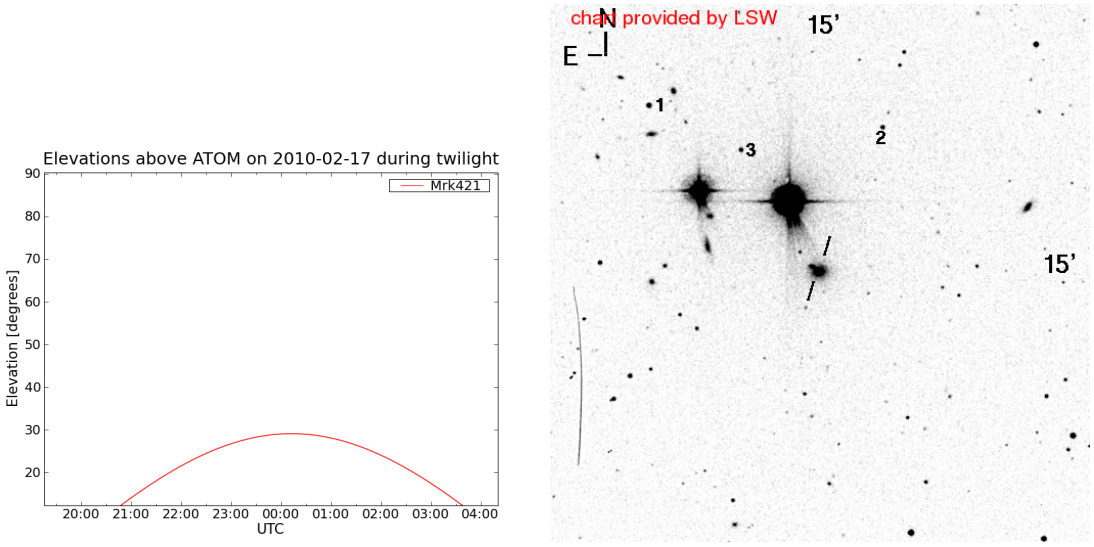

Figure 7.1.: *left:* visibility of Mrk412 from the H.E.S.S. site in February. *right:* FoV around Mrk 421 with the used reference stars indicated.

7.1.1. Photometric precision

Before putting effort in describing low amplitude variability in the AGN lightcurve, it is advisable to check for the achievable precision of the photometric measurements in this dataset. This was done by checking for star-to-star brightness variations.

If we assume the star brightness to be constant, the variation in $d_{ij} = m_i - m_j, i \neq j$ is giving a quantitative measurement of the precision of our instrumental photometry for this specific dataset. If $\sigma_{m_i - m_j} = \sigma_{d_{ij}}$ is describing the RMS of our sample, the error of the instrumental photometry $merr$ is given by

$$merr = \frac{1}{N} \sum_{i \neq j}^{N} \frac{\sigma_{d_{ij}}}{2} \tag{7.1}$$

(N number of reference stars; the factor 1/2 comes in since both measurements of m_i and m_j have errors of $merr$)

The reference stars for Mrk 421 were taken from Villata et al. (1998), and since these stars are used for differential photometry of this source since many years by many authors, the assumption of them being constant in flux seems to be justified. The position of these stars and of the AGN are shown in figure 7.1.

For easier visualization, all measurements $d_{ij} = m_i - m_j, i \neq j$ shown in figure 7.4 were shifted to $< d_{ij} >= 0$. The obvious outliers in d_{1j} can be explained by bad photometry of star 1 because of it being placed right at the edge of the CCD frame. The telescope pointing was correct after this being discovered and d_{1j} is behaving as expected in nights 3+4. The affected data was omitted from all further investigations. To get a quantitative number for the spread in d_{ij}, a Gaussian was fitted to the unbinned data (see figure 7.4) and the width of that Gaussian σ_d used to describe the limit of photometric precision. The results for different d_{ij} in different temporal intervals are given in table 7.1. It was found that $\sigma_d \leq 0.017$ mag for the whole dataset. So any detected variability in Mrk 421 of $\sigma_{Mrk} > 0.02$ mag cannot be explained by instrumental effects and thus has to be intrinsic.

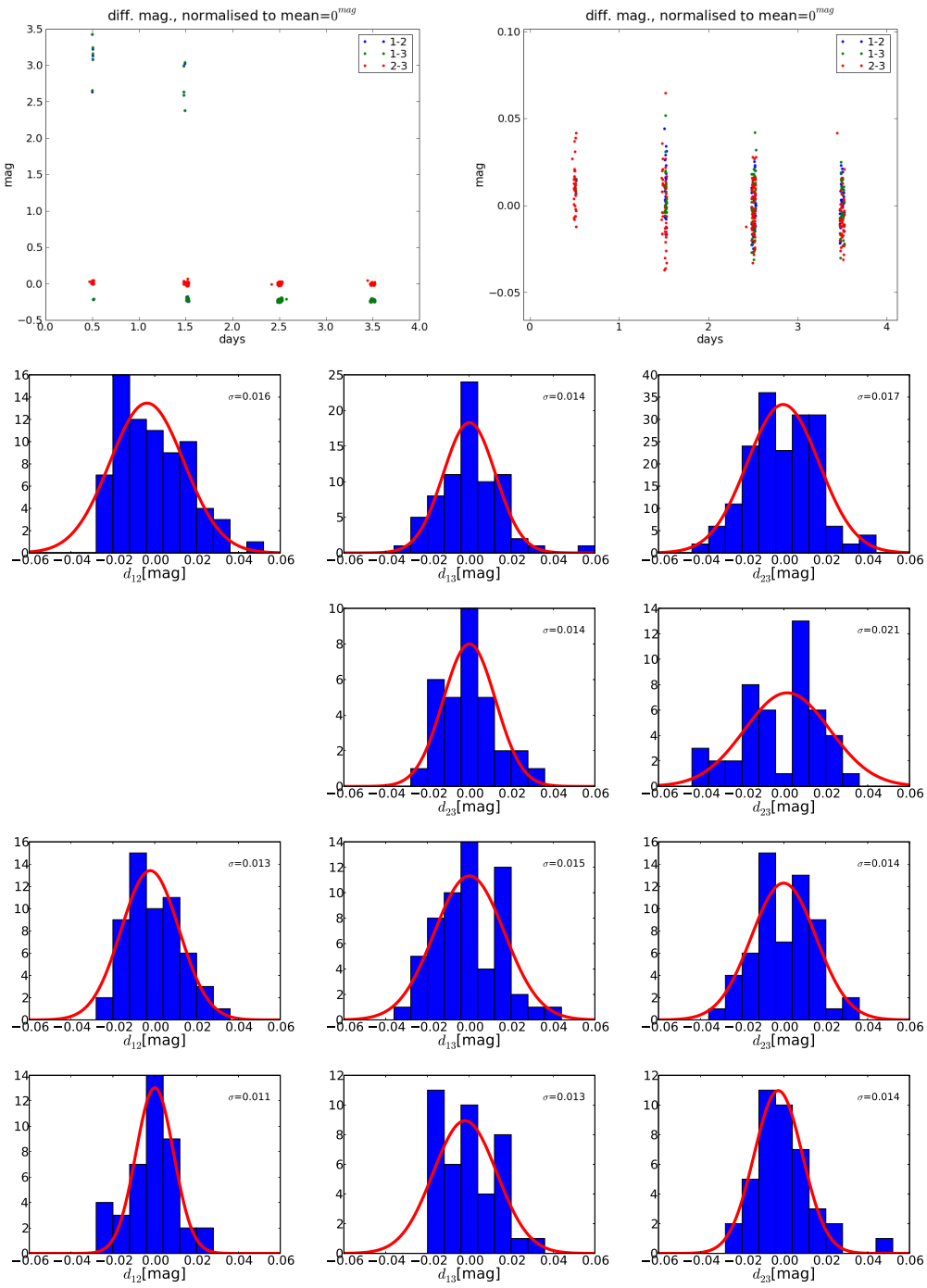

Figure 7.2.: Differential magnitudes $d_{ij} = m_i - m_j$ of reference stars $i, j = [1, 3]$ shifted to $< d_{ij} >= 0$.
***upper row**, left:* all data. It is obvious that here is some problem with star 1 in the first two nights, see text for more explanations. This affected data of star 1 was omitted from further investigations. The *right-hand* graph is showing the same relation with the affected data being removed.
***second row**:* distribution of d_{ij} for all three combinations (all 4 nights). The red line is showing a Gaussian fit to the data, the σ in the upper-right corner denotes the width of the Gaussian. The fit was done using the *unbinned* data.
***third row**:* as above, but only d_{23} for night one and two. The other four distribution for these two night contain too few data to conclude anything useful and are therefore not shown.
***row 4,5**:* as above, for night 3+4.

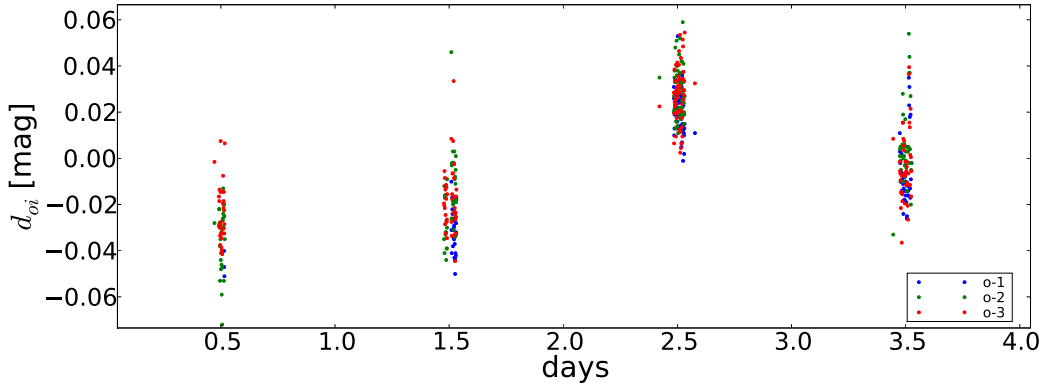

Figure 7.3.: Differential magnitudes of Mrk 421 - reference star $i = [1, 3]$ ($d_{oi} = m_o - m_i$) , shifted to $< d_{oi} >= 0$. The distributions of the individual d_{oi} are shown in figure 7.4

7.1.2. Variability measurements and results

The same exercise as for the reference stars in the previous section (7.1.1) is now applied to the magnitude difference between Mrk 421 (labeled *object* or index o in the following) and the reference stars.

As it is demonstrated in figure 7.4 and shown in table 7.1, *no evidence* for intra-night variability is found. Due to the short visibility of Mrk 421 from Namibia, *intra-night* here refers to a timescale of ≈ 2 hours.

The maximum amplitude in the nightly binned data is 0.06 mag.

night	$\sigma_{d_{12}}$	$\sigma_{d_{13}}$	$\sigma_{d_{23}}$	$\sigma_{d_{o1}}$	$\sigma_{d_{o2}}$	$\sigma_{d_{o3}}$
1	-[2]	-[2]	0.014	0.005[2]	0.013	0.013
2	- [2]	-[2]	0.021	0.010	0.016	0.014
3	0.013	0.015	0.014	0.009	0.011	0.012
4	0.011	0.013	0.014	0.014	0.017	0.015
all nights	0.016	0.014	0.017	0.024	0.028	0.025

Table 7.1.: Fitted width of distributions d_{ij} and d_{oi} shown in figures 7.2 and 7.4. All numbers are in units of magnitudes. For night 1+2, no fit could be obtained for samples d_{1j} (see text). In all individual nights $d_{oi} \leq d_{ij}$, which means that there is no indication for intra-night variability in Mrk 412 in this dataset (intra-night means in this sample a 2 hour timescale). However, $d_{oi} > d_{ij}$ for the complete four nights sample, meaning that there *is* variability on a night-by-night timescale. This is also visible in the lightcurve.

[1] There are only three events in this sample because of the mispointing issue described in the text. This number is therefore not significant.

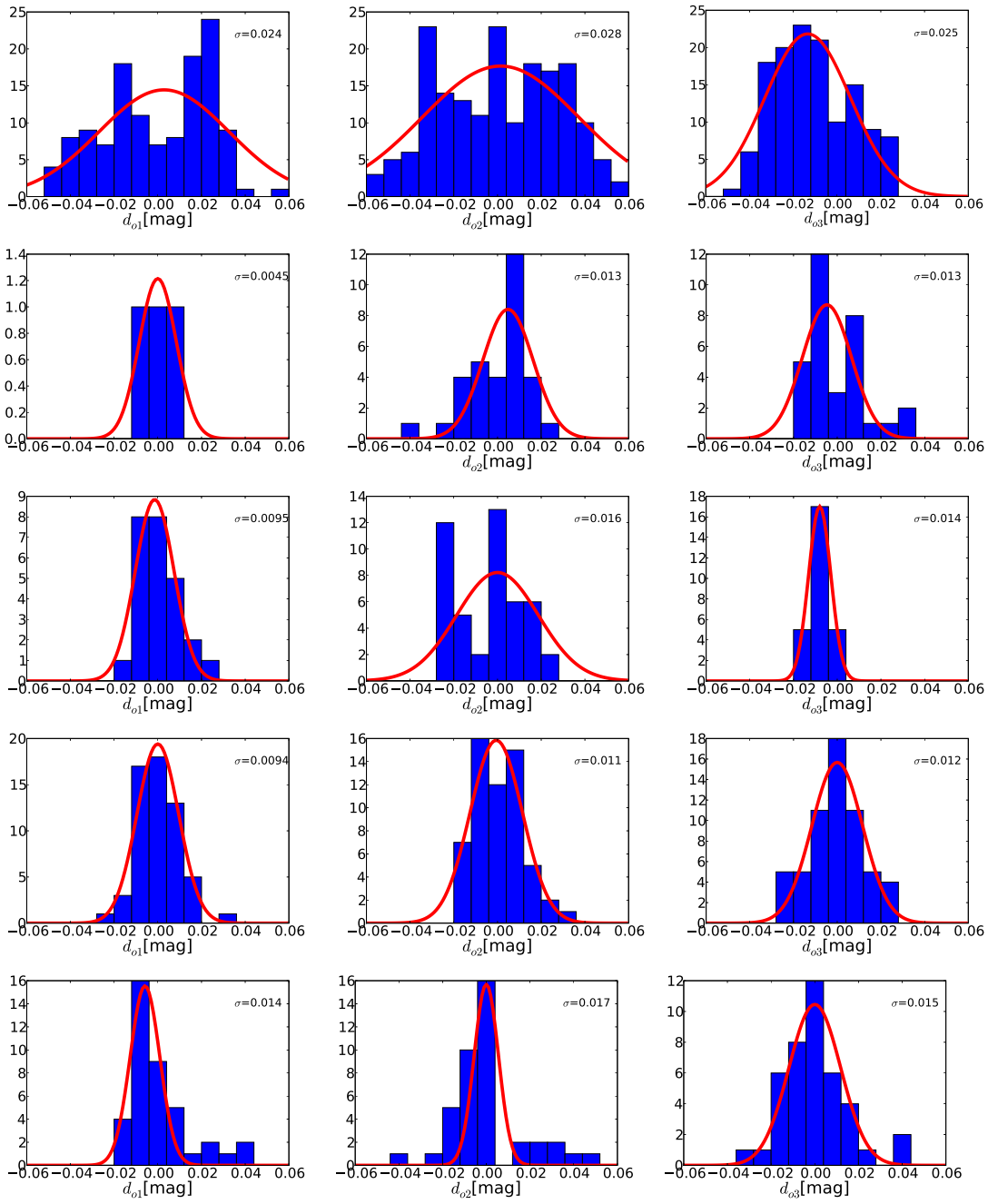

Figure 7.4.: Differential magnitudes of Mrk 421 - reference star $i = [1, 3]$ ($d_{oi} = m_o - m_i$) , shifted to $< d_{oi} >= 0$.
first row: distribution of d_{oi} for all three combinations (data from all 4 nights). The red line is showing a Gaussian fit to the data, the σ in the upper-right corner denotes the width of the Gaussian. The fit was done using the *unbinned* data.
row 2–4: as above, but night one, two and three separated. Note that d_{o1} contains only three entries for night 1, so this fit is meaningless.
The width of the different Gaussians are listed in table 7.1 for easier comparison.

Name	α_{2000}	δ_{2000}	Obs. since	freq.	number of observations				
					B	V	R	I	total
SHBL J001355.9-185406	$00^h13^m56.0^s$	$-18°54'06"$	Jun 08	0.30	119	2	173	2	**296**
RGB J0152+017	$01^h52^m39.6^s$	$+01°47'17"$	Nov 07	0.30	355	101	498	97	**1051**
1ES 0229+200	$02^h32^m48.6^s$	$+20°17'17"$	Nov 06	0.30	193	62	252	68	**575**
1ES 0347-121	$03^h49^m23.0^s$	$-11°59'26"$	Nov 06	0.30	229	70	314	97	**710**
1ES 0414+00.9	$04^h16^m52.5^s$	$+01°05'23"$	Nov 06	0.30	326	95	377	90	**888**
PKS 0447-439	$04^h49^m24.7^s$	$-43°50'08"$	Aug 09	0.30	51	0	109	0	**160**
VER J0521+211	$05^h21^m46.0^s$	$+21°12'51"$	Oct 09	0.30	38	0	47	0	**85**
PKS 0548-322	$05^h50^m40.6^s$	$-32°16'17"$	Nov 06	0.30	165	69	197	69	**500**
1ES 1101-232	$11^h03^m37.6^s$	$-23°29'30"$	Feb 07	0.20	294	153	327	116	**890**
Mrk 421	$11^h04^m27.5^s$	$+38°12'31"$	May 07	0.33	82	37	278	36	**433**
W Comae	$12^h21^m31.7^s$	$+28°13'58"$	Jun 08	0.30	73	9	103	8	**193**
1ES 1312-423	$13^h15^m3.4^s$	$-42°36'50"$	Mar 08	0.33	88	1	145	1	**235**
PKS 1424-418	$14^h27^m56.3^s$	$-42°06'19"$	Jul 08	0.30	173	3	246	24	**446**
1ES 1440+122	$14^h42^m48.3^s$	$+12°00'39"$	May 08	0.30	73	0	132	0	**205**
PKS 1510-089	$15^h12^m50.5^s$	$-09°05'58"$	May 07	0.30	285	84	518	112	**999**
PKS 1514-241	$15^h17^m41.8^s$	$-24°22'19"$	Jul 08	1.00	45	1	67	1	**114**
PG 1553+113	$15^h55^m43.0^s$	$+11°11'24"$	Aug 07	0.33	218	16	257	16	**507**
PKS 2005-489	$20^h09^m25.4^s$	$-48°49'53"$	Nov 06	1.00	865	477	922	483	**2747**
PKS 2155-304	$21^h58^m52.0^s$	$-30°13'32"$	Nov 06	1.00	959	485	1045	486	**2975**
PKS 2356-309	$23^h59^m8.0^s$	$-30°37'37"$	Nov 06	0.30	462	191	477	195	**1325**

Table 7.2.: The table is presenting the summarized properties of the TeV-detected ATOM monitoring targets as of February 2011. The lightcurves of these sources are shown in this section. The different columns are giving the name and position of the source, the date when the source entered the monitoring program, the desired observing frequency in days and the number of observations performed up to now (separated by filters and in total). A complete list of all monitoring targets is given in the appendix (tabl. E.1).

7.2. Lightcurves and structure functions

The TeV-detected sources out of the monitored AGN are presented in this section[3].

For the sources that were included in the monitoring program from the beginning, more than four years of data are available. Sources with a high monitoring frequency like PKS 2155-304 are coming up to 3000 measurements in all filters together. Table 7.2 is giving the properties of these sources with their monitoring frequency and number of observations, where as the full list of all ATOM monitoring sources is given in the appendix (tab. E.1).

Individually picked flux thresholds for each source are essential if one wants to identify flaring states of a source. Lightcurves, the flux vs. time representation, allows to find a trigger threshold for a source w.r.t. its historical context. This means that in an ideal case, one is able to to discriminate between quiescent and flaring states of an AGN. However, this is only true if the source is that nice to show these two discrete states. Figure 7.5 is giving an example of one ideal and two extreme cases: first, PKS 1510-089 is showing an quiescent state over 1.5 years, followed by a flaring state of some months (see also sec. 7.3.1), and then back to a quiescent flux level for one year now. On the other hand, 3C 454.3 is very variable, making it impossible to define a quiescent level (of

[3]Only a selection and not all because with 220+ sources being on the monitoring list, this would be too verbose for this thesis. All lightcurves are available online and up-to-date for the interested (and authorized –H.E.S.S. only, sorry!) reader at http://atom.uni-hd.de/intern/Results/index.html

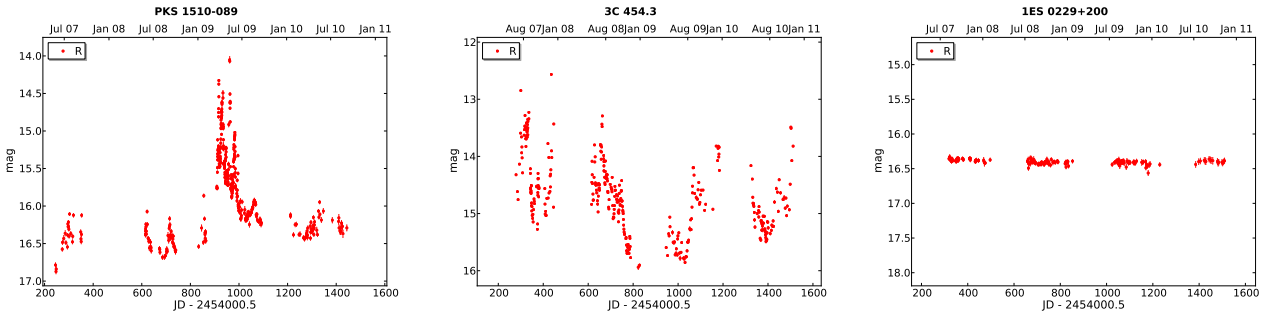

Figure 7.5.: Three AGN showing different behaviors. *Left:* PKS 1510-089 entered the monitoring program with a one year period without much variations, allowing to well define a quiescent level of R< 16mag, followed by a huge flaring time for some months (see also sec. 7.3.1), followed again by a quiescent state. *In the middle*, the lightcurve of 3C 454.3 is given. This AGN is behaving very variable, over a similar dynamic range than PKS 1510-089, but without any well-defined quiescent states. 1ES 0229+200 on the *right-hand side* is not showing any variability at all.

course, one can still define high and low flux states). And finally, 1ES 0229+200 which does not show any variability at all over many years. Some examples for definite flaring states of AGN detected by ATOM are given in section 7.3.

However, beside clear flares, there are other kinds of variability. One possibility to characterize this is the *structure function* (SF), which can reveal characteristic timescales in the AGN (see e.g. Simonetti et al. (1985)).

The SF is defined as the squared difference of a time-depended quantity $x(t)$ at two different times $t, t+\tau$. Applying this to photometric flux measurements of an AGN at different observing times, $f(t)$ and $f(t+\tau)$, averaged over all measurements N inside a certain time interval, the SF can be written as

$$\mathrm{SF}(\tau) = \left\langle \big(x(t) - x(t+\tau)\big)^2 \right\rangle = \frac{1}{N}\sum_{i=1}^{N}(x_i - x_{i+\tau})^2 \tag{7.2}$$

The here used procedure is to compute all possible flux differences[4]

$$d_{i,j} = f(t_i) - f(t_j), \quad (i > j) \wedge (i \in [1, N])$$

and apply a binning on the time scale τ in a second step. The time scale for all sources here is limited to $\tau \in [1, 600]$ days, following the canonical approach that SF are only reliable to $\tau < 1/2 \max(dt)$ in the data, and there are at most 4 years of monitoring data available. Bins are chosen here to be equally spaced in logarithmic scale, the SF data point per bin is computed using the error-weighed arithmetic mean of the individual $d_{i,j}$ points per bin.

For easier comparison of the SF of the different sources emitting at different flux levels, the flux of each object was normalized to $< f >= 1$ before computing the SF.

The behavior of these TeV-detected AGN as seen by the ATOM monitoring is described briefly in the following:

[4]algorithm implemented in the script `structure-function.py`.

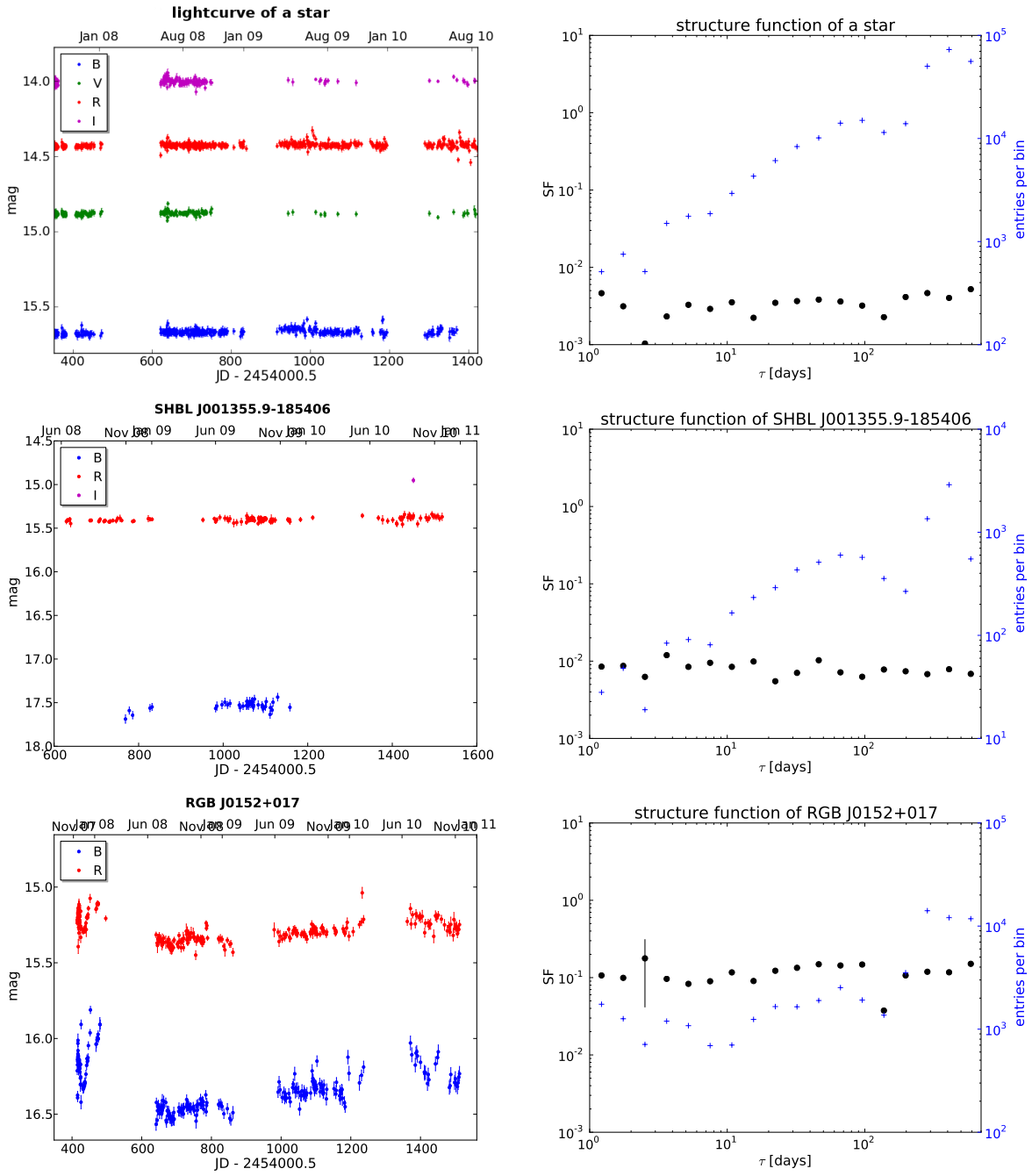

Figure 7.6.: Optical lightcurves and structure functions of VHE detected AGN, continued on next pages. *left:* lightcurves created as final product by ADRAS (see sec. 5.2.4). *right:* structure functions (black points), computed according to eq. (7.2), using *R band* data. The blue crosses give the number of d_{ij} data points per time bin $\Delta\tau$, out of which the black points were computed using a weighted arithmetic mean. This allows to estimate the significance of each SF data point. The scaling of SF graphs is fixed for all SF graphs to allow easier comparison of the different sources. The first shown object is a *star* in the FoV around PKS 2155-304 to demonstrate how a *constant source* looks in the graphs resulting from ADRAS. The following sequence of graphs is ordered by increasing RA.

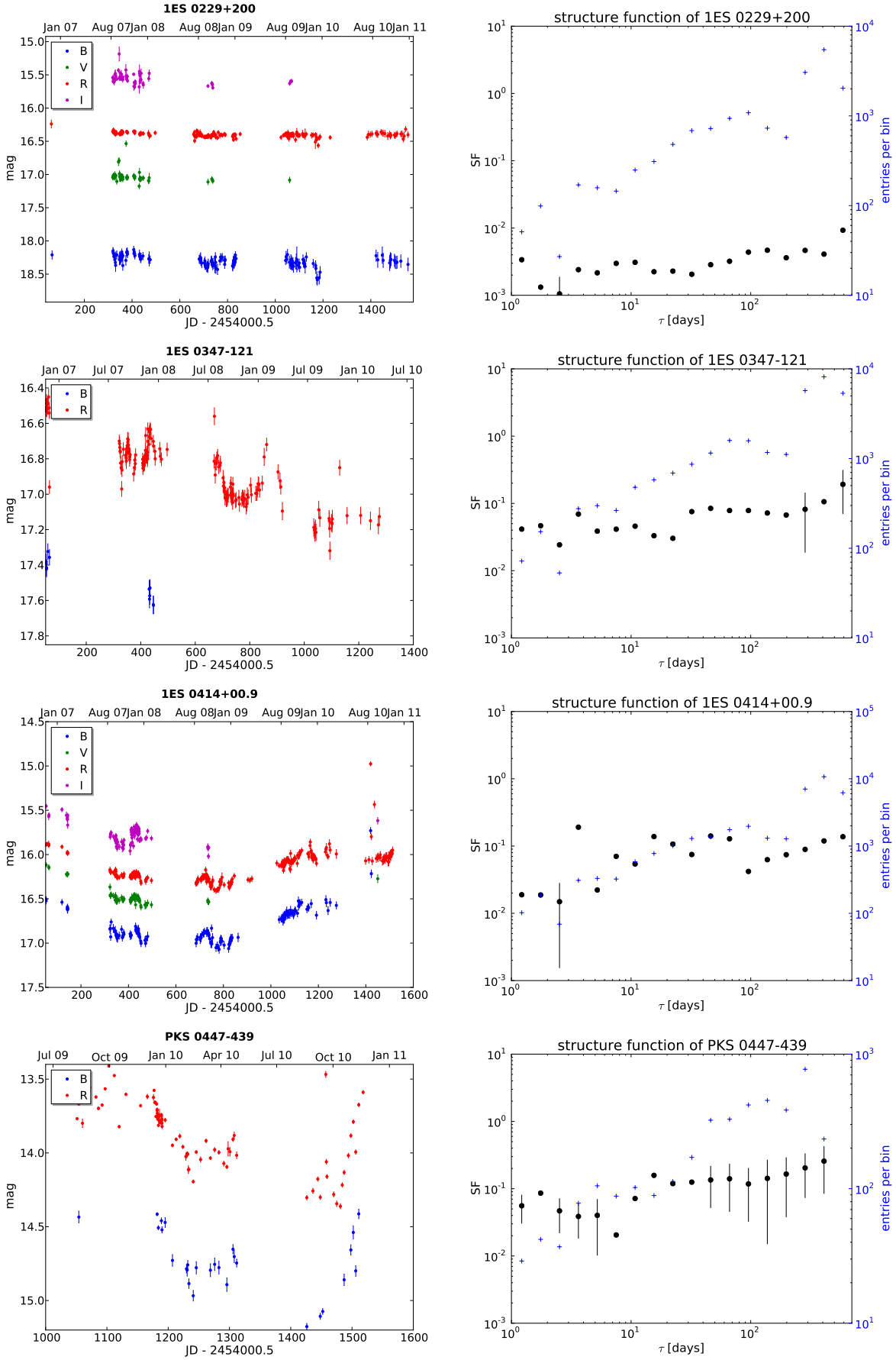

Figure 7.6 (continued)

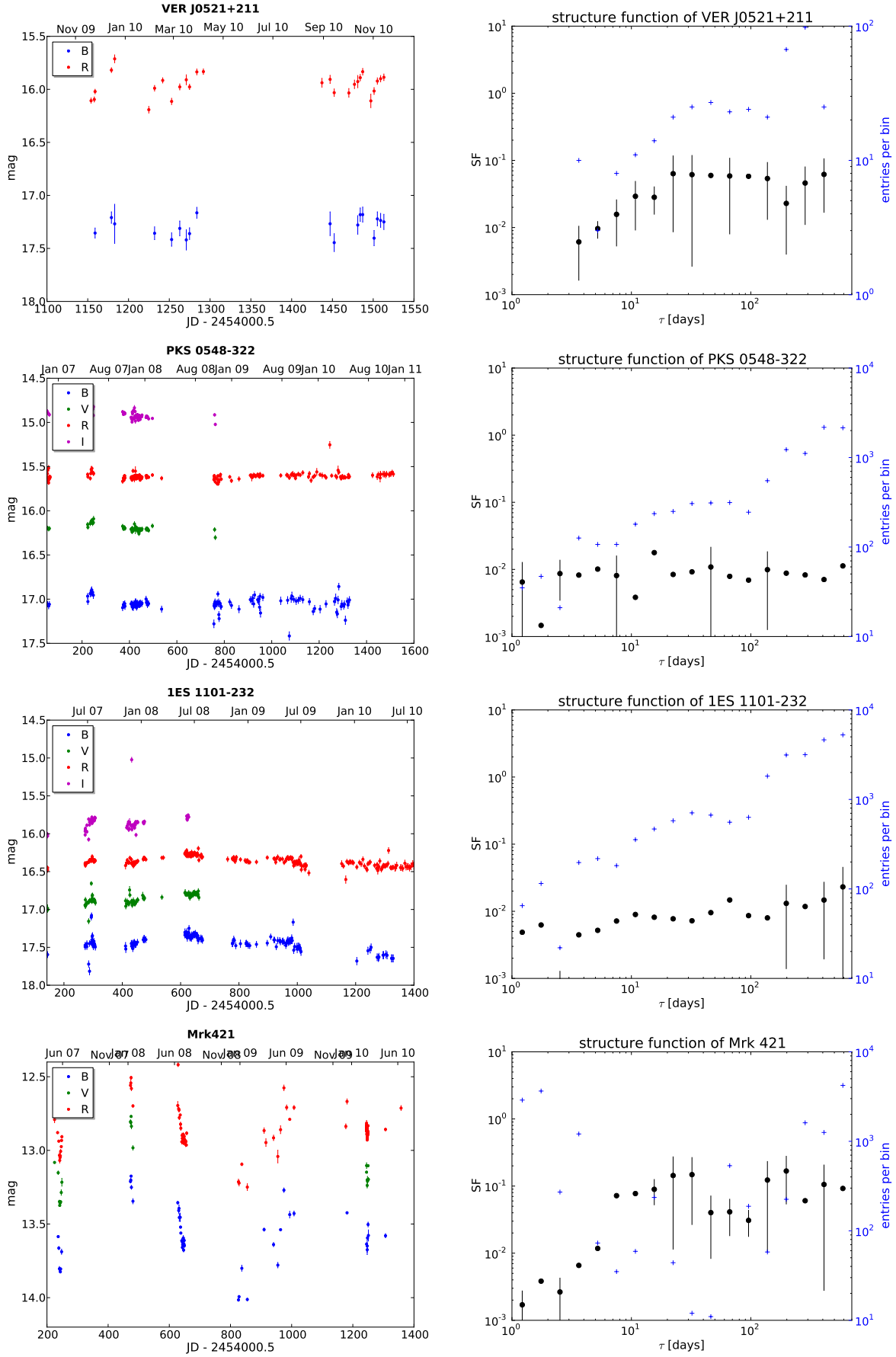

Figure 7.6 (continued)

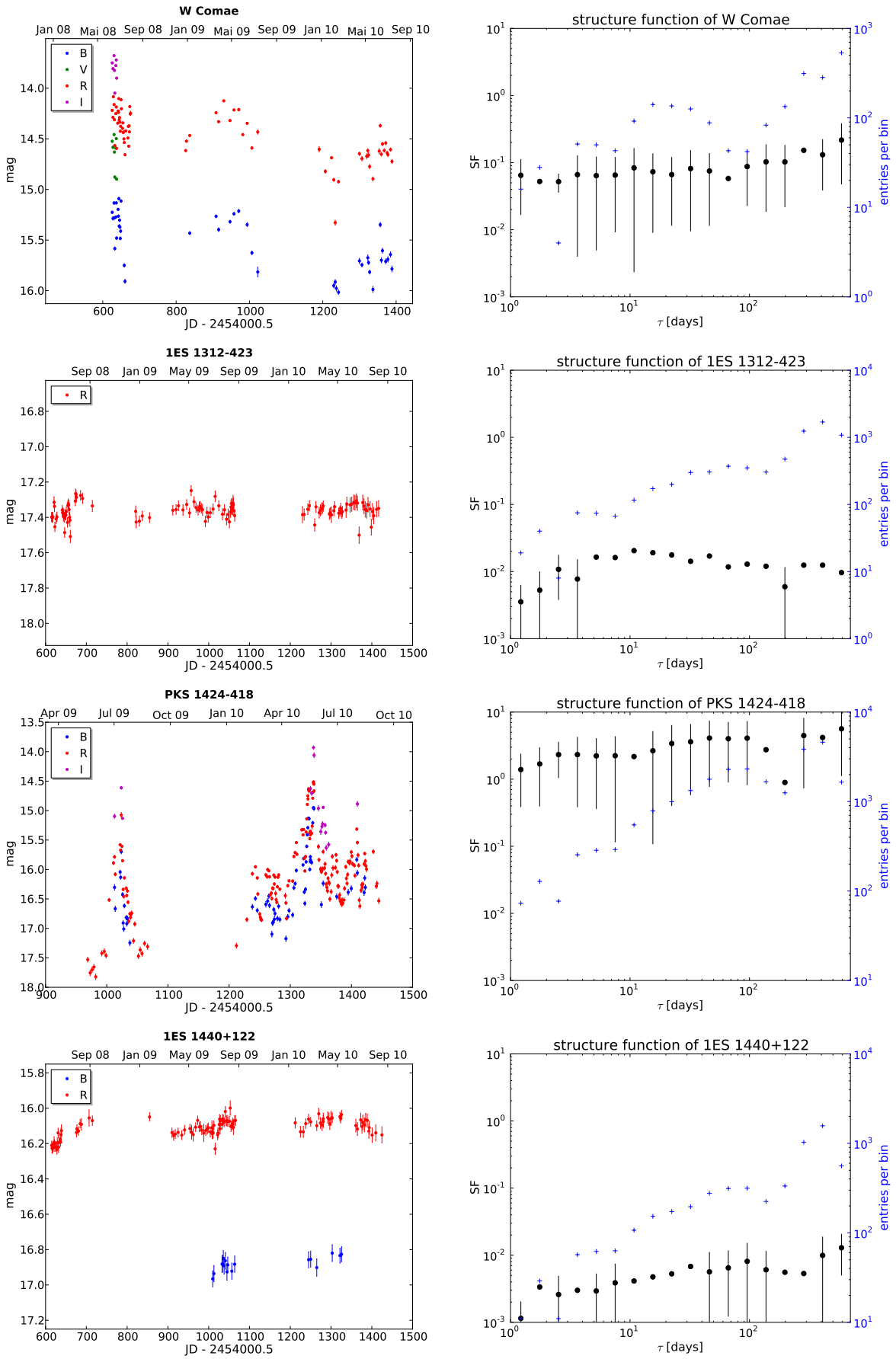

Figure 7.6 (continued)

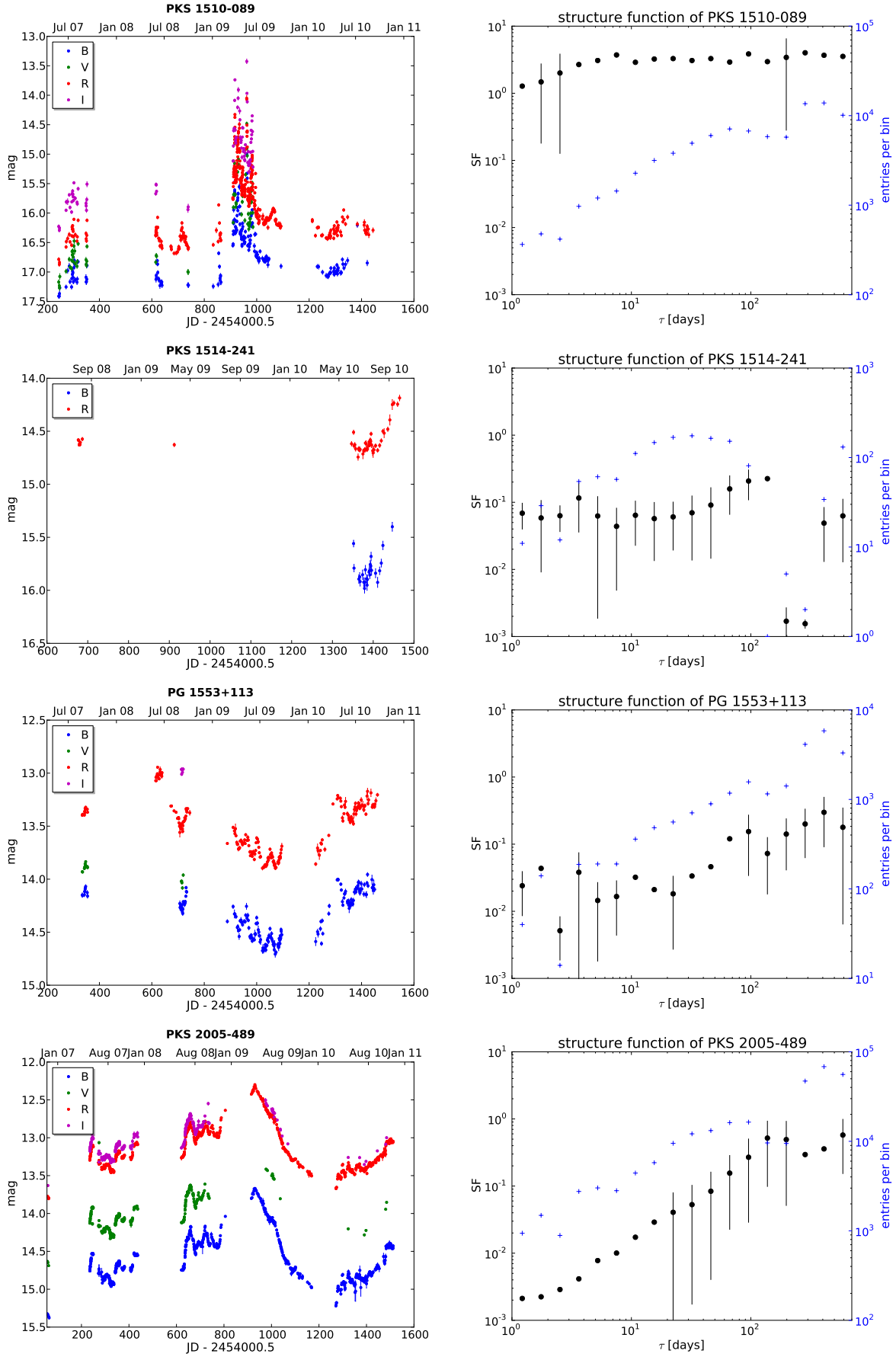

Figure 7.6 (continued)

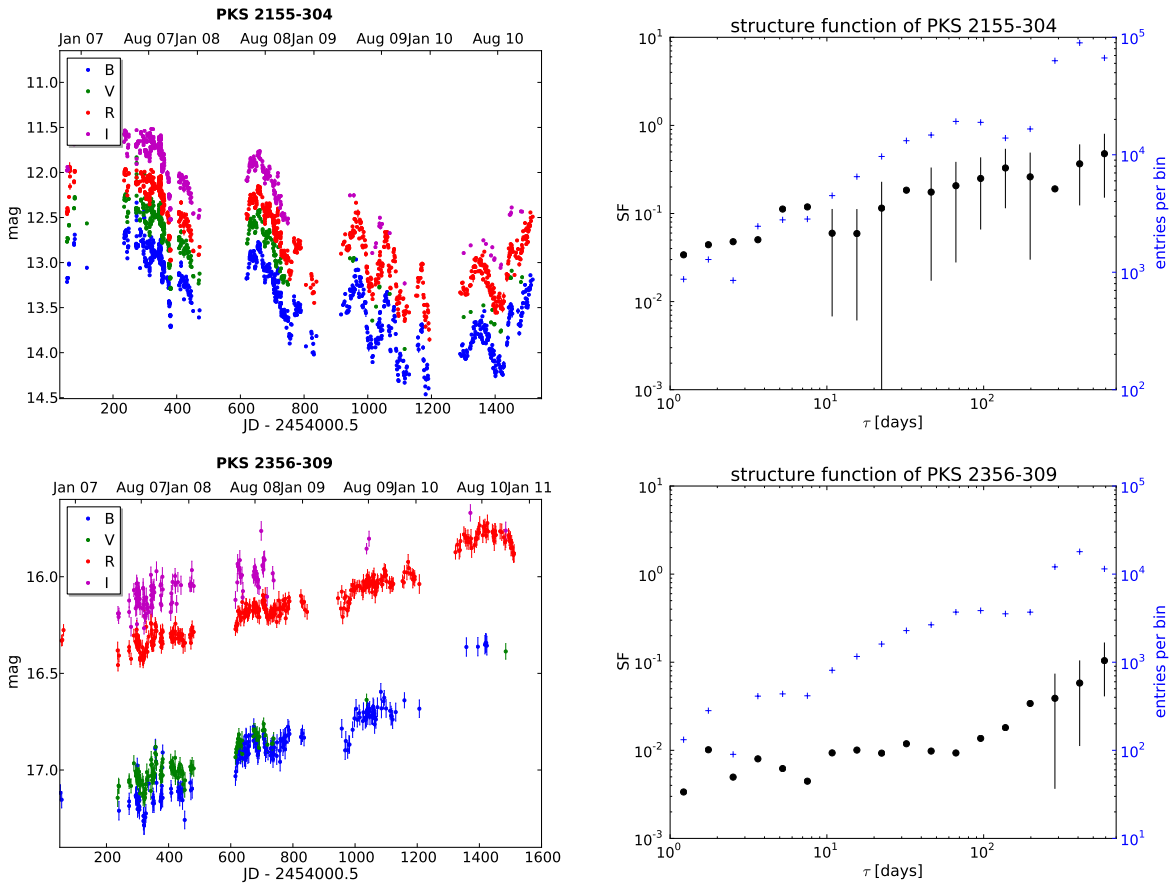

Figure 7.6 (continued)

SHBL J001355.9-185406 (shown on page 120) is a stable source, no significant variability detected.

RGB J0152+017 did only vary by 0.4 mag over the observed time span. Most variability was observed during its detection in TeV energies at the beginning of its monitoring (see Aharonian et al. (2008).

1ES 0229+200: stable source, shown on page 121.

1ES 0347-121 has faded by 0.6 mag over the monitoring period.

1ES 0414+00.9 has dropped its brightness by 0.5 mag and re-gained to the initial value of $m_R = 15.8$ mag over 3 years. A short ($\approx$ days) flare of about $\Delta m_R \approx 1$mag was detected in August 2010.

PKS 0447-439 is a variable source with a $\Delta m \approx 1$ mag over one year. However, there was a flare (only one measurement) in Sep 2010, followed by a drop to the lowest measured flux, which was again followed by a steep increase until the end of its visibility at the end of 2010.

VER J0521+211 (on page 122) was showing some variability of 0.5 mag over one year of monitoring up to now. The SF shows a plateau starting at a timescale of 200 days.

PKS 0548-322 : stable source.

1ES 1101-232 is a very stable source.

Mrk 421 is very variable with an amplitude of < 0.8 mag. Its monitoring by ATOM suffers from the northern position of this source.

W Comae : variable on a scale of 0.5 mag (shown on page 123)

1ES 1312-423 quite stable source, no significant variability.

PKS 1424-418 was showing a very variable behavior during two prominent flares (Hauser et al. (2010a)), with m_R between 18 and 14.5 mag. See also the details about the two flaring states of this source in sec. 7.4.2 (color changes) and sec. 7.5.1 (comparison with *Fermi* measurements).

1ES 1440+122 : not very variable, amplitudes are $\Delta m_R < 0.2$mag.

PKS 1510-089 (page 124) is showing several small flares and a big one in summer 2009. The SF enters its plateau state at a timescale of ≈ 8 days.

PKS 1514-241 , also known as AP Lib, increased its brightness by 0.5 mag towards the end of its last observable period. No significant variability detected before, but –due to a mistake in scheduling– only very few observations were acquired.

PG 1553+113 variable on a timescale of ≈ 0.8 mag / year with overlaid smaller variations on a weekly scale.

PKS 2005-489 showed an magnitude increase of about 1 mag up to $m_R = 12.2$ mag in summer 2009. This was serendipitously during an H.E.S.S.-organized MWL campaign, the results will be described in an upcoming paper (joint publication by the H.E.S.S. and *Fermi* collaborations, accepted by *A&A*). The SF shows the generally expected monotonic increase with the plateau probably starting at ≈ 150 days (timescale uncertain because of a too short monitoring time span).

PKS 2155-304 (page 125) was varying between $m_R = 12.0 \ldots 13.5$ mag over 4 years, showing at least one significant peak per year. Its multi-wavelength characteristics (including TeV energies) are described in Aharonian et al. (2009).

PKS 2356-309 was continuously brightening from $m_R = 16.4$ mag to 15.6 mag over 4 years with overlaid small amplitude variations. See also HESS Collaboration et al. (2010) for the TeV aspect of this source.

7.3. Flares of AGN

The detection of an AGN in a flaring state is one of the primary missions of ATOM. If an AGN out of the TeV-candidate group is found in an optical flaring state, there is the chance that this flare in the synchrotron regime probed by ATOM is reflected by an increase in the inverse Compton branch and thus in an increase in the H.E.S.S.-accessible energy range (assuming an SSC scenario).

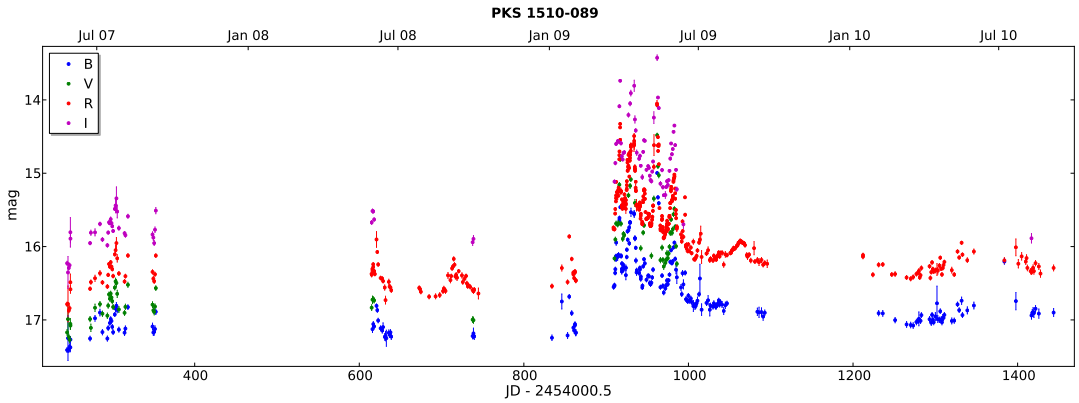

Figure 7.7.: Lightcurve of PKS 1510-089. During the big flare in March 2009 (accompanied by a flare in GeV and a detection in TeV energies), the flux of this source had risen by 2.8 mag.

When such a flare is detected and the source is observable by the H.E.S.S. array (i.e. outside moon-affected time and not too low above the horizon), a *target-of-opportunity* (ToO) observing request is planned to be issued to the *H.E.S.S. observing committee*(OC).

The most impressive flares are described in the following:

7.3.1. March 2009: PKS 1510-089

PKS 1510-089 is a TeV detected FSRQ at a redshift of z=0.36. Its detection by H.E.S.S. was during a flaring state in optical (see Wagner and HESS collaboration (2010) and fig. 7.7) and GeV (D'Ammando et al. (2009)) energies.

The base line of this source was $m_R \approx 16.5$ mag in the 2 years before, and $m_R \approx 16.2$ mag after the flare. The highest flux measured during the flare was $m_R = 13.74 \pm 0.03$ mag on March 27, 2009. Taken the flare and the four years of multi-color monitoring data surrounding it into account, this source is clearly showing a *bluer-when-brighter* behavior (see section 7.4 and figure 7.15).

7.3.2. April 2009: PKS 2005-489

PKS 2005-489 is a BL Lac object, which was already detected in VHE in 2005 (Aharonian et al. (2005)). Right before the start of a long planned multiwavelength campaign on this source in May, ATOM measured with $m_R = 12.30 \pm 0.01$ the highest flux it has ever measured on this object (see fig. 7.8). The multiwavelength campaign in May and June 2009 probed the electromagnetic spectrum emitted by PKS 2005-489 from eV up to TeV energies, the results are published in HESS Collaboration et al. (2011).

7.3.3. February 2010: PKS 1222+216

PKS 1222+216 is a quasar at a redshift of z=0.432 (Osterbrock and Pogge (1987)). When ATOM started to monitor this source in July 2008, it had was of $m_R \approx 16$ mag bright (see lightcurve in fig. 7.9). After a small flare up to $m_R = 15.5$ mag in May 2009, ATOM monitoring of this source was intensified. When it became visible again

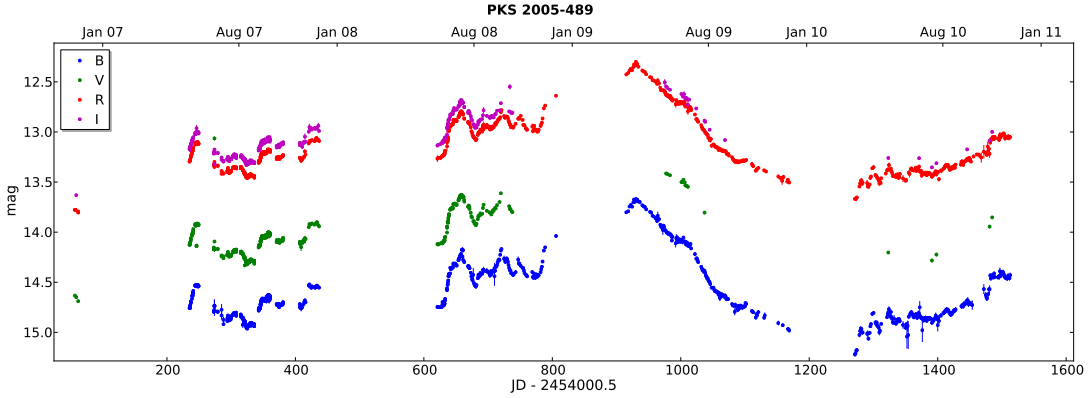

Figure 7.8.: Lightcurve of PKS 2005-489. The highest flux measured by ATOM of this source was $m_R = 12.30 \pm 0.01$ mag on April 9, 2009; right before the start of a planned multiwavelength campaign on it.

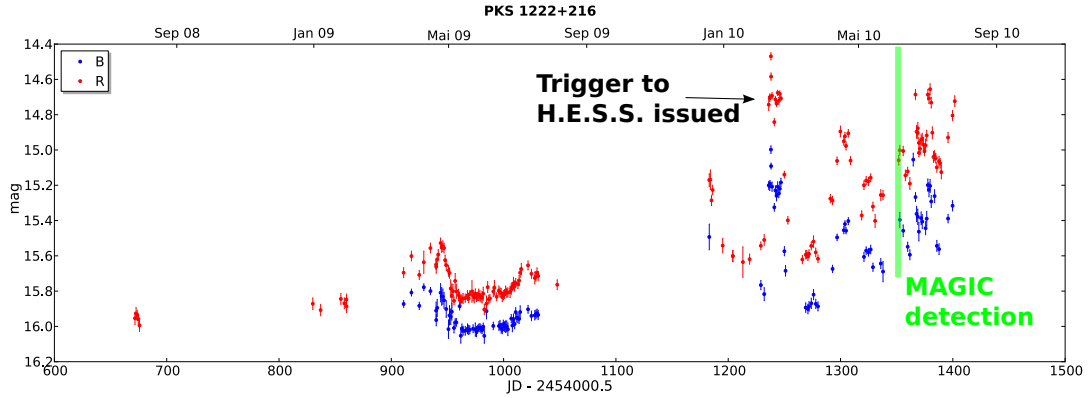

Figure 7.9.: Lightcurve of PKS 1222+216. Because of a significant flare detected in February 2010, a trigger was issued to the H.E.S.S. array. This trigger was not followed. A few month later, the MAGIC collaboration reported the detection of this source in the VHE regime during a time where the optical flux was lower.

end of 2009, its brightness had again increased to nearly 15 mag, but dropped shortly after this. In February 2010, this source was undergoing a huge flare. After a flux increase of more than 1 mag, a request for ToO observations of this source was issued to the H.E.S.S.-OC. Unfortunately, this request was declined and no observations by the IACT array were conducted. The flare went on for ≈ 10 days, the maximum apparent magnitude measured was $m_R = 14.47 \pm 0.04$ mag on February 11, 2010.

On June 17, 2010 this source was detected for the first time in VHE regime (Mose Mariotti (2010)). The MAGIC collaboration reported a $> 8\sigma$ above background detection in 30 min, corresponding to a flux level of $\approx 30\%$ of the Crab flux. The optical flux measured by ATOM at this point in time was $m_R = 15.1$ mag, about 0.5 mag *less* than during the flare in February. Assuming a connection between TeV and eV energy bands as in SSC models, it seems as if H.E.S.S. missed a clear chance to detect a (for VHE astronomy) high redshift source here.

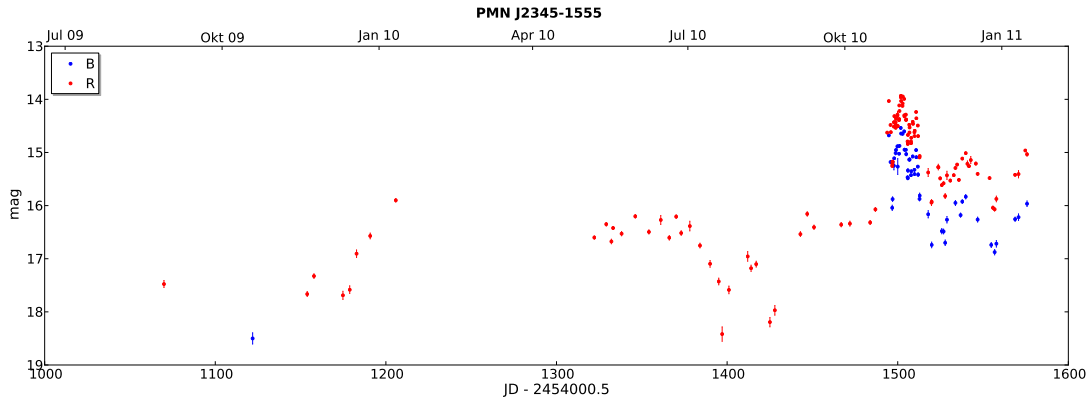

Figure 7.10.: Lightcurve of PMN J2345-1555

7.3.4. October 2010: PMN J2345-1555

In October 2010, the FSRQ PMN J2345-1555 at a redshift of z=0.621 (Healey et al. (2008)) was flaring.

The source had brightened by 2 mag in one week and by > 4 mag (approximately a factor 50 in linear flux scale) compared to its faintest state ever measured by ATOM 3 month before. The H.E.S.S. array took some data on this source during bad weather conditions (≈ 6 hours livetime), but no signal was detected (the online analysis gave a detection significance of 1.39σ in total).

Figure 7.11.: Color composite of 1ES 0414+00.9 and PKS 1510-089. Many single frames per color were co-added using `SWarp` , color images were created using `STIFF` (Bertin et al. (2002))

7.4. Colors of AGN

As described in the introduction (sec. 1.1.2), the emission of AGN at optical wavelengths is –in the absence of a host galaxy– dominated by synchrotron emission. The color of the object is then of course determined by the position of the observing window on the synchrotron hump (which itself is mainly a function of magnetic field strength B and charge distribution n_{e^-}). If the synchrotron emission peak is in or near the optical wavelength regime, any change in peak position (hinting to changes in B or n_{e^-}) should be visible as changes of the observed color. This is illustrated in figure 7.12.

Possible color changes of the more prominent and most observed AGN are investigated in the following. Only a few AGN are presented here as an example, the graphs of the remaining ATOM monitored and TeV-detected sources are given in appendix A.1.

Figures 7.14 to 7.17 and the ones in appendix A are all composed of two sub-panels: in the *upper panel*, the R-band light curve is shown in red, the corresponding scale is on the left hand side. The (B-R) color is overlaid in blue with the corresponding scale on the right hand side. The *lower panel* presents the color-magnitude diagram of this source for the time span given in the light curve above. For better orientation, the year of observation is color-coded (the few observations of Nov and Dec 2006 are attributed to the year 2007). Error bars are omitted here for better visibility, but can be deduced from the (color) lightcurve in the upper panel.

To characterize the behavior of the AGN w.r.t its color changes, a linear fit was applied to the (B-R) vs. R data. The resulting slope is shown in table 7.3, together with the correlation coefficient (Pearsons r) of these two data sets.

Correlation coefficients found range from -0.77 in PKS 1510-089 to 0.75 in PKS 2005-489, so both appearances, *redder-when-brighter* as well as *bluer-when-brighter* are found. Correlation coefficients of ≈ 0.7 are typically not accepted as tight correlations, and no further tests about the statistical probability of such a correlation coefficient was done here. But Böttcher et al. (2010) did such a study in their work about the correla-

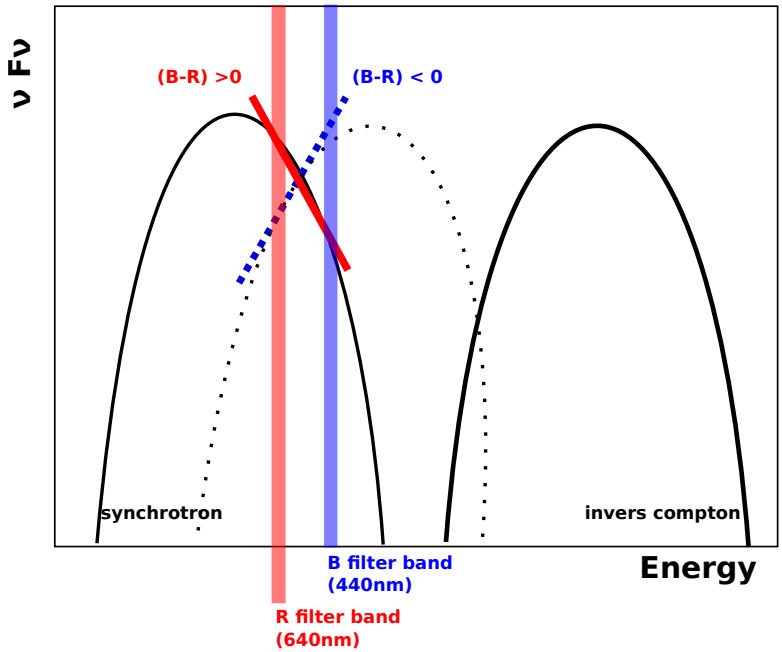

Figure 7.12.: The meaning of measured (B-R) color in an SED: If the peak of the synchrotron hump of an AGN changes its energy, this is reflected in changes of the color. For example, if it changes from lower (solid line) to higher energy (dottet line), the flux ratio between B and R filter band (also known as *(B-R) color*) changes. The given numbers (*(B-R)>0*, *(B-R)<0*) should be only taken as an indication, since magnitude (and thus color) are *flux* quantities, wheras the SED here is plotted in *frequency multipied flux* scale.

tion between (B-R) color and R magnitude in the VHE-detected blazar 1ES 1011+496, where they have shown via Monte-Carlo tests that a correlation coefficient of $r = 0.57$ corresponds to a probability of non-correlation $P(> r) \approx 4 \cdot 10^9$, and $r = 0.78$ to a probability for non-correlation of $P(> r) \approx 10^{15}$ for their data, thus giving at least a strong indication that the correlation coefficients found here are significant.

The slope and correlation coefficients were computed for all 74 ATOM monitored targets that were observed in B+R more than 25 times ((color)lightcurves given in appendix A). The distributions of these two quantities are shown in fig. 7.13. Both states, *bluer-when-brighter* and *redder-when-brighter* are approximately equally present.

Name	slope	corr. coeff.
SHBL J001355.9-185406	-0.18	-0.17
RGB J0152+017	0.13	0.11
1ES 0229+200	0.88	0.42
1ES 0347-121	0.90	0.67
1ES 0414+00.9	0.05	0.13
PKS 0447-439	0.11	0.19
VER J0521+211	-0.24	-0.42
PKS 0548-322	0.00	0.00 [sic!]
1ES 1101-232	0.32	0.22
Mrk 421	0.20	0.34
W Comae	-0.05	-0.11
1ES 1312-423	-0.23	-0.17
PKS 1424-418	0.06	0.44
1ES 1440+122	-0.18	-0.15
PKS 1510-089	-0.17	-0.77
PKS 1514-241	-0.19	-0.23
PG 1553+113	-0.02	-0.11
PKS 2005-489	0.11	0.75
PKS 2155-304	-0.01	-0.15
PKS 2356-309	0.38	0.62

Table 7.3.: Slope of a linear fit to the (B-R) vs. R data of VHE detected sources shown in figures 7.14 to 7.17 and in appendix A.1. A slope > 0 corresponds to a *redder-when-brighter* characteristic, indicating that the synchrotron peak of the source moves to lower energies with increasing flux; a slope of < 0 means the opposite. The distribution of these quantities of all 74 ATOM monitored AGN targets that were observed in B+R more than 25 times are listed in tab. A.1 and shown in fig. 7.13.

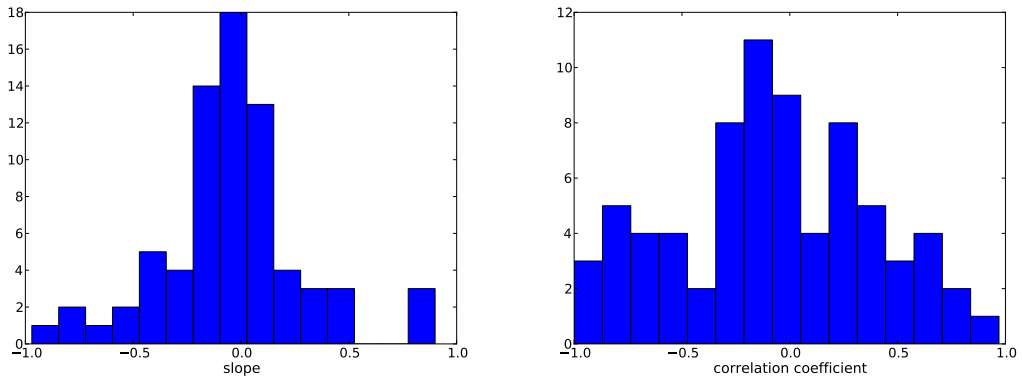

Figure 7.13.: Histograms of the slope of a linear fit to (B-R) over R *(left)* and the corresponding correlation coefficient *(right)* for *all 74 ATOM monitored AGN* that were observed more than 25 times in B and R colors each. The numerical values are listed in table A.1 in the appendix.

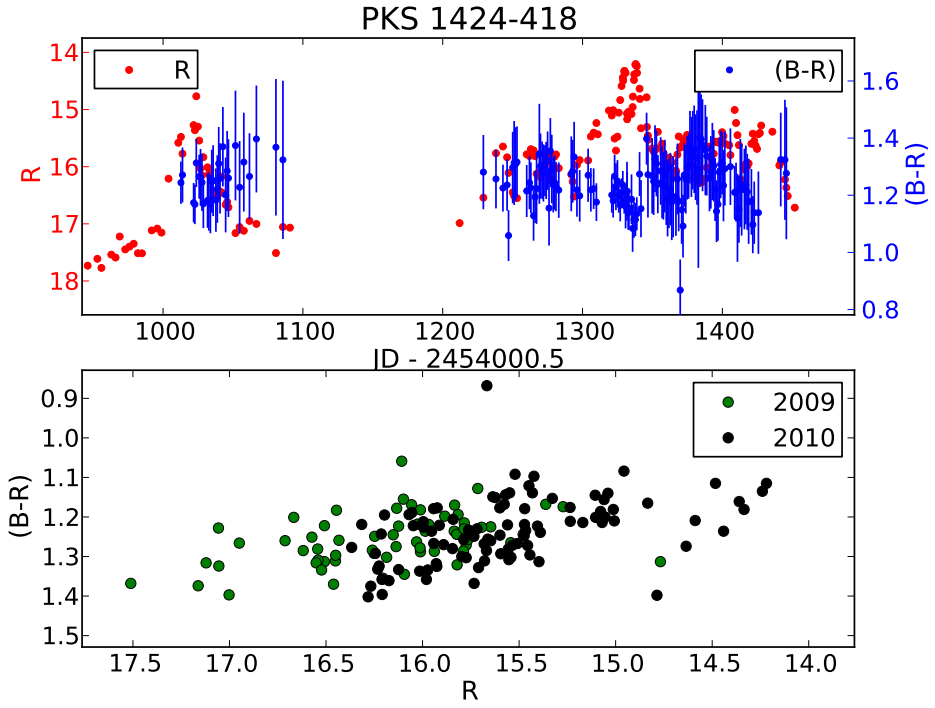

Figure 7.14.: Lightcurve and color-magnitude diagram of PKS 1424-418. See also sec. 7.4.2 for more details.

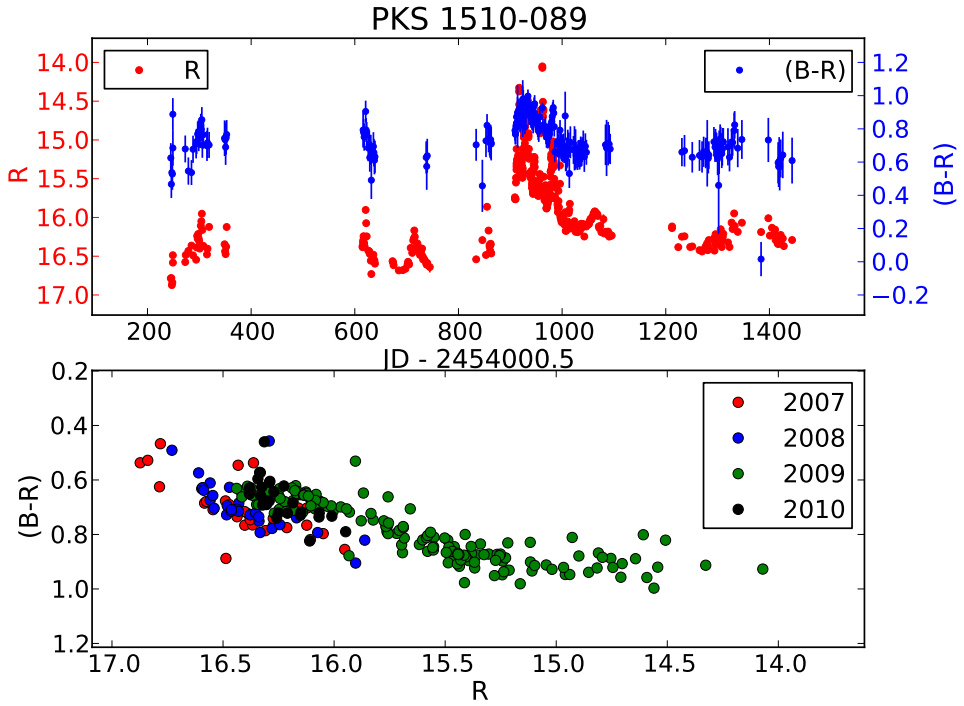

Figure 7.15.: Lightcurve and color-magnitude diagram of PKS 1510-089.

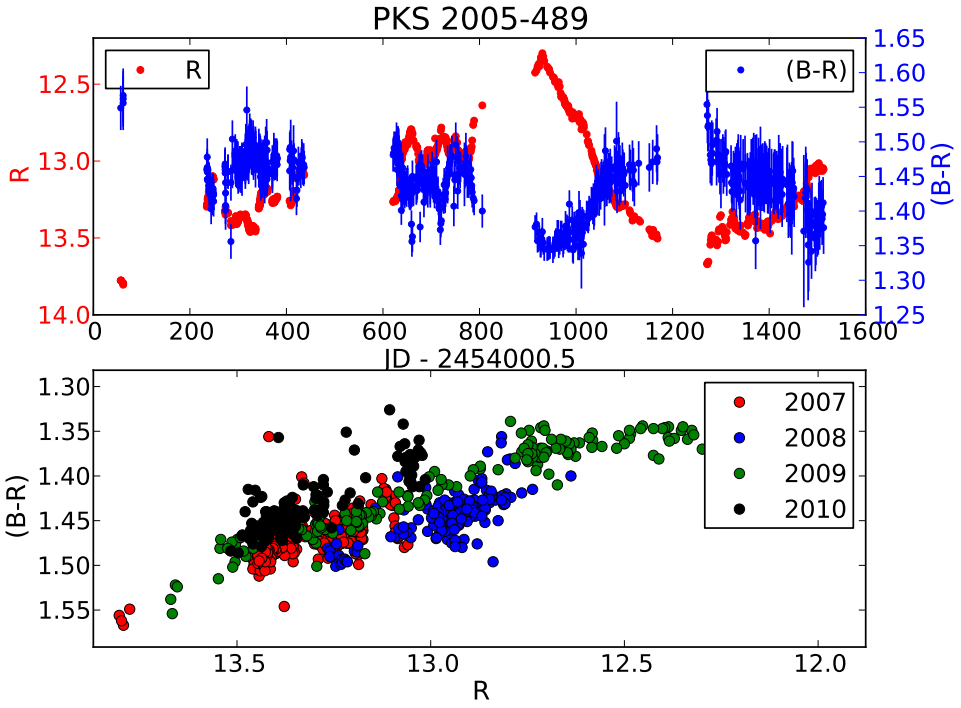

Figure 7.16.: Lightcurve and color-magnitude diagram of PKS 2005-489.

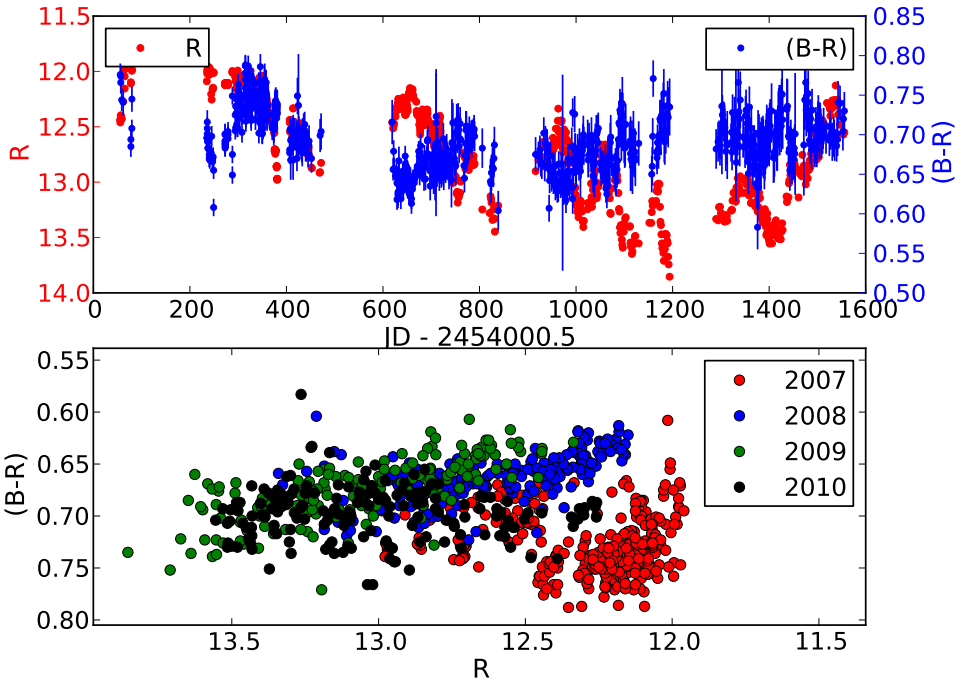

Figure 7.17.: Lightcurve and color-magnitude diagram of PKS 2155-304. See also sec. 7.4.1 for some details.

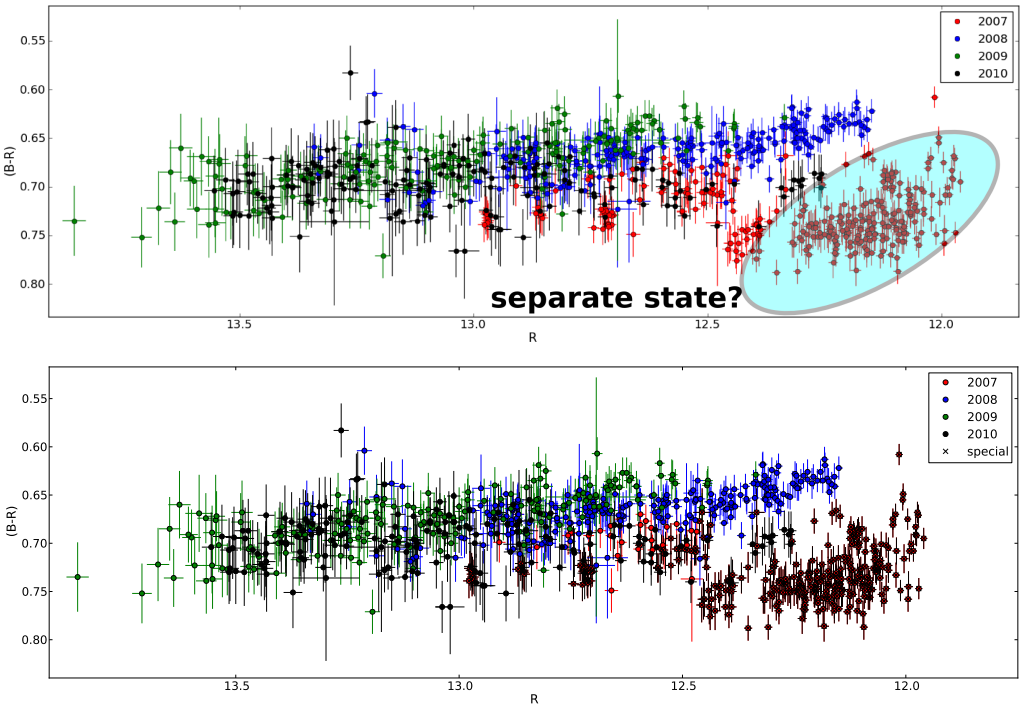

Figure 7.18.: Same graph as lower panel of fig. 7.17, but this time including error bars. A dichotomy is visible in the color-magnitude space of PKS 2155-304 (blue overlay). This may be a hint to a separate spectral state of this source. In the lower panel, all data points taken before Nov 2007 (JD $<$ 2454420) are marked with an "**X**". It stands out that most -but not all- observations taken before that point in time belong to the separate state. The ≈ 20 points being recorded before Nov 2007, but not belonging to the apparent special spectral state, are not from the beginning of ATOM observations (so that the special state would be from one continuous time period), but from Oct 2007.

7.4.1. Peculiar spectral state of PKS 2155-304

The color-magnitude diagram of PKS 2155-304 (fig. 7.17) reveals a dichotomy between most observations done before Nov 2007 and the remaining ones. These data points are especially marked in figure 7.18.

It was found that nearly all data points recorded between the start of ATOM operation in Nov 2006 and Nov 2007 do belong to this special branch (312 R/(B-R) points in total).

In this first year data, there are about 20 points at $m_R < 12.5$ mag around JD$=2454379 \pm 2$ days (first week of Oct 2007) which do *not* belong to the special branch. However, there *are* 12 points after that time span which *do* still belong to the special branch.

To test for any possible instrumental or atmospheric effect, the color-magnitude diagram of a star 1 arcmin away from PKS 2155-304 (and always in the FoV around the AGN) was computed and is shown in fig. 7.19. No extra spectral state is visible here. Also, several other AGN have been observed in the very same nights, right before and after PKS 2155-304, and none of them is showing a special branch in the color-magnitude diagram (see e.g. PKS 2005-408 in fig. 7.16 and PKS 2356-309 in fig. A.15). Thus it can

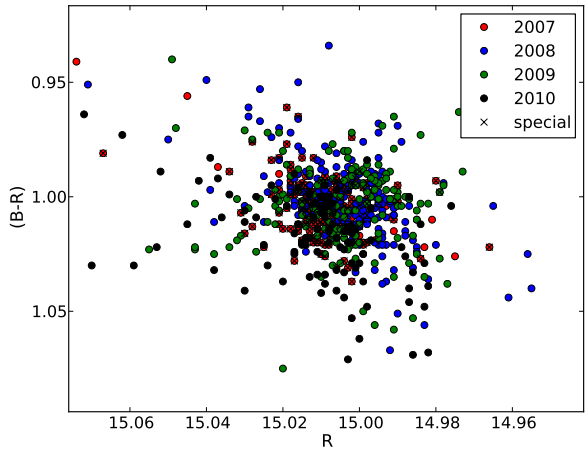

Figure 7.19.: Color-magnitude diagram of a star 1 arcmin away from PKS 2155-304. The color coding is the same as in fig. 7.18 or any of the previous color-magnitude diagrams of this section. No separate branch could be detected, the stellar data is showing a constant source with the usual scatter (error bars omitted).

be concluded that this effect is real and not an instrumental or atmospheric artefact.

7.4.2. The two flares of PKS 1424-418

Two flares in optical and GeV energies have been observed by ATOM and *Fermi* in this source. An interesting relation between the optical and GeV energies measured by *Fermi* has been found and will be presented at the upcoming *2011 Fermi Symposium*, a first look at the GeV data is given in section 7.5.1.

Here, I will describe the properties of the two flares at eV energies. The R band and (B-R) color lightcurves are shown again in fig. 7.20, including a zoom-in on the two flares. Please see fig. 7.14 in the overview section 7.4 for the (R, (B-R)) correlation plot.

Flare 1, occurring around JD 2455020, raised the flux in R band by nearly 3.5 mag. Alerted by our report about the optical flare (Hauser et al. (2009b))), this source was investigated by the *Fermi* team, and they found a contemporaneous flaring in GeV energies (Longo et al. (2009)). During the flare, ATOM started taking B band observations[5]. No significant color changes have been observed during that flare. The two isolated (B-R) points with outstanding blue color during that flare were both taken during non-clear weather conditions and may be affected by uncorrected extinction. However, even *including* these points, a fit of a constant value to this data between JD=2455000 and JD=2455060 gives a red. χ^2 value of 1.14. Excluding these two points is giving a $\chi^2/(24\,\text{d.o.f.}) = 0.6$

Flare 2, about one year later, is showing a double-peak in optical wavelength. The maximum brightness was 0.6 mag higher than during flare 1. Here again, no significant color change was detected. A fit of a constant to the color data between JD 2455320 and JD 2455360 resulted in a red. χ^2 of 0.8. A linear fit to the data resulted in the same red. χ^2 value.

Fitting the whole data set with a constant gave also a red. χ^2 of 0.83. So all observed

[5]Previously, there were only R band observation because of scheduling constraints. B band observation of such a (at that time) faint source would have blown up the schedule

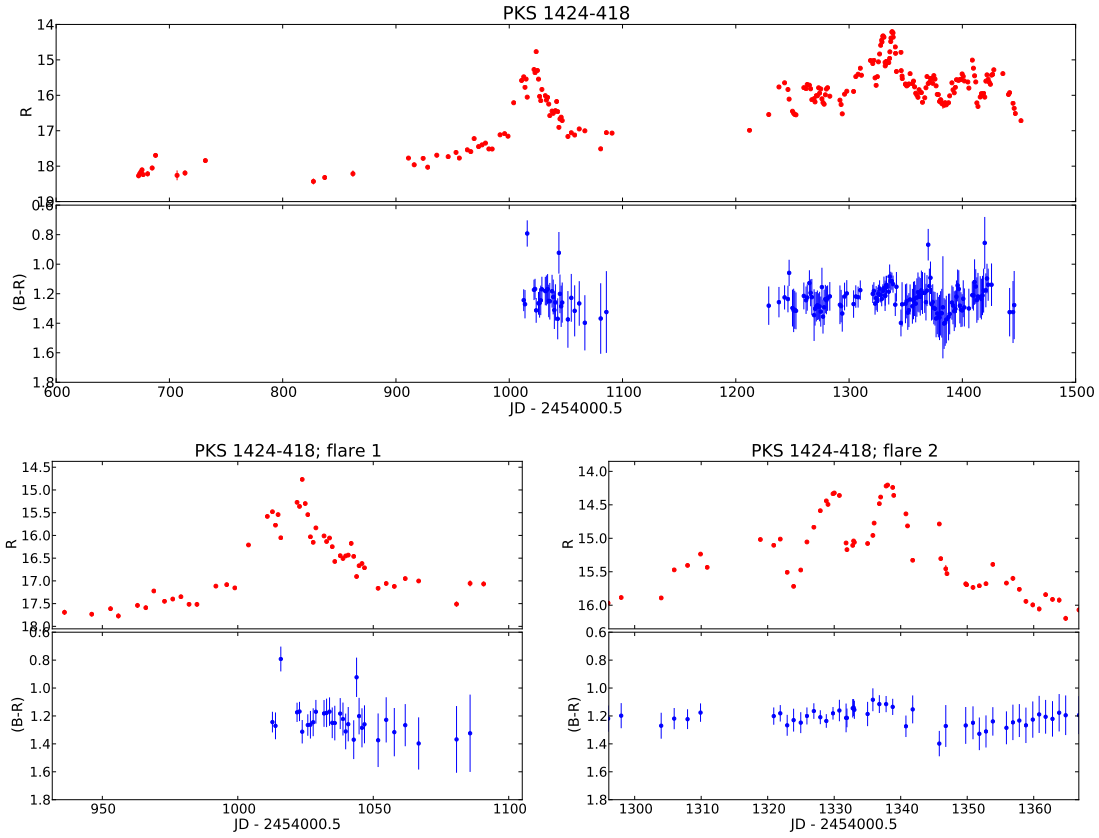

Figure 7.20.: Color evolvement of PKS 1424-418. *top panel*: whole data set, *bottom:* zoom into flare 1 and flare 2. The B band observations were only started after the R band observations showed a flare. The 2 (B-R) points with outstanding blue color index during *flare 1* were taken during non-clear weather. No significant color changes were observed.

flares of this source do not show a significant change in (B-R) color.

Note that the resulting reduced χ^2 values < 1 are a clear indication that the errors are overestimated. To get the expected red. χ^2 value of ≈ 1.00, the errors on the whole sample of (B-R) points of PKS 1424-418 would need to be shortened to 83.5% of their current value. This over-estimation of photometric errors in the ATOM data has been observed for some objects (but not all). A global solution/explanation for this problem is still missing.

7.5. Correlation studies between γ-ray and optical fluxes

Having homogeneous, multi-year lasting optical lightcurves available by ATOM, which are dense sampled for several AGN, allows to study possible correlations with γ-ray lightcurves. These type of correlations are expected in the view of SSC models, since with optical wavelength, one probes the synchrotron-emitting electron distributions that are also responsible for the comptonised part of the SED, visible in γ rays.

These kind of studies have already been done in the era of EGRET (see for example Wagner (1996)). A more recent study was done by Behera (2010), using a limited data sample of contemporal ATOM/*Fermi* data. He found a clear dichotomy in a flux-flux representation for a limited sample of 10 sources, using data from one year of observations.

Here, this study is extended using more data (all data available by *Fermi* from the start of its mission in August 2008 until the end of 2010; ATOM data surpasses this time span) and looking into more sources. The γ-ray data used here is taken from the public *LAT Monitored source list*, where the LAT team provides daily flux points[6] in the energy ranges 0.1-1 GeV, 1-300 GeV and 0.1-300 GeV. Used here are the daily bins in the 0.1-300 GeV energy band; days where only upper limits are available are omitted.

Optical data entering this study are the ATOM data points in the R band (640 nm). Days with more than one data point per source are averaged using a simple error-weighted average to get one optical point per *Fermi* temporal bin.

The dichotomy found by Behera (2010) is still visible using more than one year of additional data (see figure 7.21). His sample of 10 sources is extended to all sources from the *LAT Monitored source list* which have contemporal ATOM data points, leading to a sample of 17 sources with eight or more data points in the flux-flux plane. Behera (2010) noted that the redshift of the sources is following this dichotomy. Using the surpassing dataset here, this cannot be confirmed (see table 7.4 for numerical values and figure 7.24 for a graphical representation of this). All sources with more than 20 datapoints are showing a positive correlation (higher optical flux comes together with higher γ-ray flux). Besides that, no other relation between the correlation coefficient[7] and redshift can be deduced.

However, the dichotomy is still visible in the flux-flux plane when using the additional 7 sources now available. But it is not that significant like with the reduced number of sources, so this may very well be a selection effect. This is shown in figure 7.22.

Figure 7.23 is showing the optical/γ-ray lightcurves and correlation plots for PKS 2155-304 and 3C 454.3, two of the best sampled sources here, in more detail. A study on PKS 1424-418 using non-public *Fermi* data is given in sec. 7.5.1.

The resulting correlation coefficients of the different sources are given in table 7.4, the corresponding graphs are shown in the appendix (B). Only sources with more than 8 matching ATOM/*Fermi* data points are used here. The source names are the same as in the *Fermi* Monitoring List. Note that a subset of this study was already presented at the 38th COSPAR Scientific Assembly (Wagner and Hauser (2010)).

A quick check for any relation between redshift and the optical/γ correlation is shown in fig. 7.24: no obvious trend with redshift is visible, but it is notable that all sources

[6] The data was taken from http://heasarc.gsfc.nasa.gov/db-perl/W3Browse/w3query.pl.

[7] as always in this thesis, the term *correlation coefficient* refers to the definition of Pearsons r.

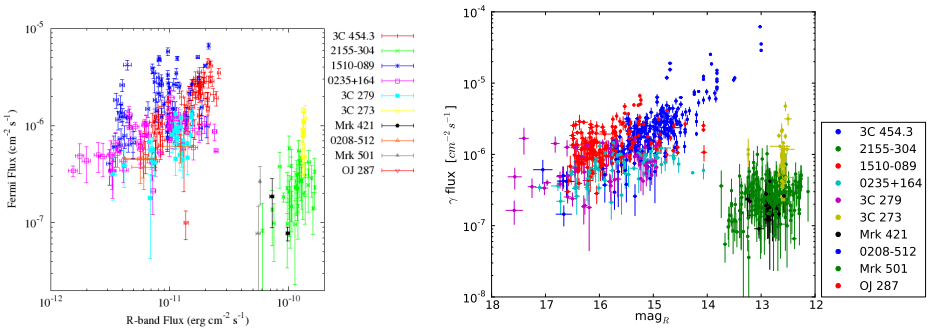

Figure 7.21.: γ-ray vs. optical flux. *left:* taken from Behera (2010), figure 3.5. *right:* this study, using the same source sample, but with all available data until end of 2010. The dichotomy is still there, with the sources PKS 2155-304, 3C 273, Mrk 421 and Mrk 501 in the optical-bright, γ low corner. See figure 7.22 for a version with more sources included.

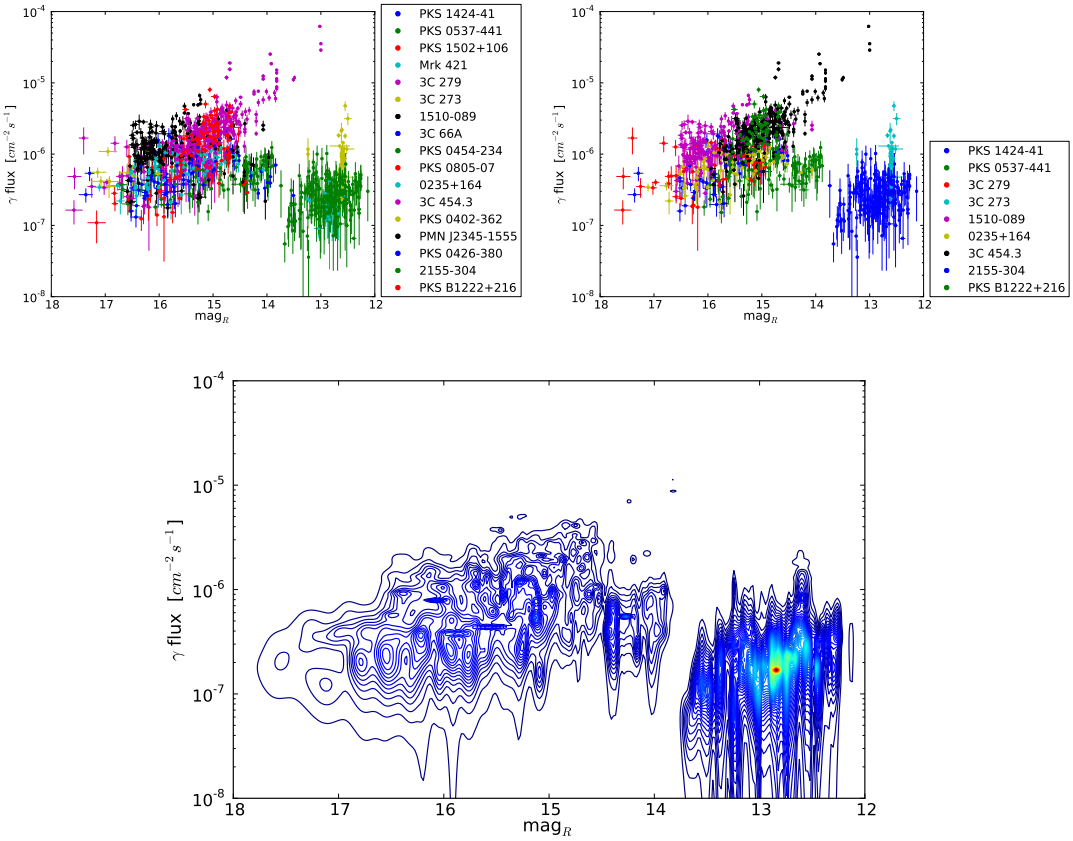

Figure 7.22.: γ-ray vs. optical flux (same as fig. 7.21, but including more sources). The *left graph* is showing all sources with more than eight data points, whereas the *right* one is restricted to sources providing more than 30 data points to make the graph less crowded. The lower graph is showing all data points converted into a symmetric Gaussian and summed up.

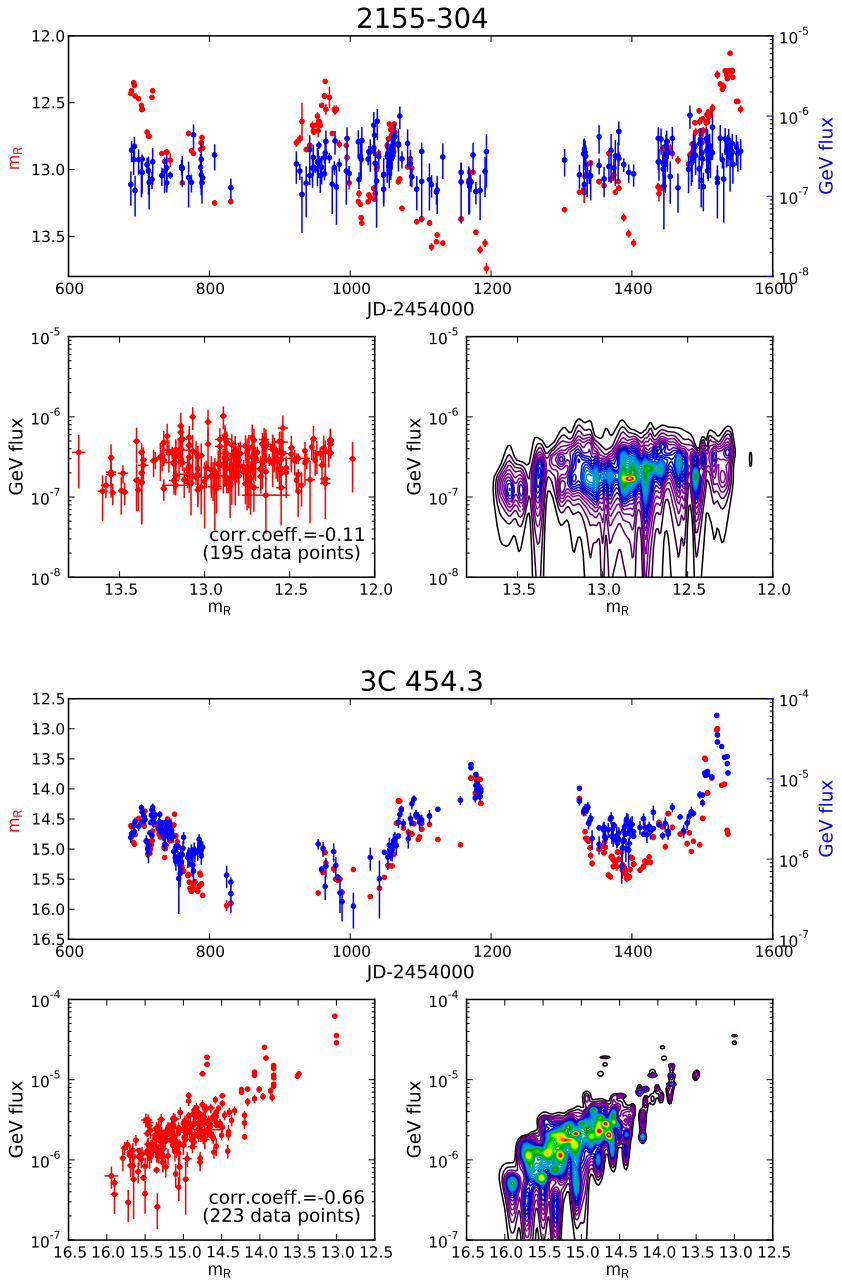

Figure 7.23.: γ-ray vs. optical flux for PKS 2155-304 (left) and 3C 454.3 (right) in detail. The upper panel is showing the lightcurve (daily bins) in both wavelength bands, the lower panels the optical vs. γ-ray flux in log-log scale. In the lower-left panels, each data point is plotted including its 1σ error bars. Since this leads to a very crowed plot with suboptimal informative value, each data point is converted into a 2dim Gaussian. All Gaussians are then summed up and visualized in the lower-right panels.
The two sources are showing a different behavior: whereas PKS 2155-304 does not show a significant correlation (variability in optical data, but nearly constant flux in γ rays), the optical and γ ray fluxes in 3C 454.3 are following each other.
The corresponding graphs for all the other sources under investigation are shown in appendix B.

source	z	N_data	corr. coefficient
3C 66A	0.44	9	+0.17
PKS 0235+16	0.524	65	-0.46
PKS 0402-362	1.42	8	+0.06
PKS 0426-380	1.1	21	-0.69
PKS 0454-234	1.00	15	-0.57
PKS 0537-441	0.896	78	-0.58
PKS 0805-07	1.837	26	-0.29
Mrk 421	0.031	15	+0.11
3C 273	0.158	36	-0.07
3C 279	0.536	63	-0.23
PKS 1424-41	1.522	54	-0.54
PKS 1502+106	1.839	10	-0.57
PKS B1222+216	0.435	80	-0.28
PKS 1510-089	0.36	173	-0.39
PKS 2155-304	0.117	195	-0.11
3C 454.3	0.859	173	-0.39
PMN J2345-1555	0.621	19	-0.67

Table 7.4.: Correlation coefficients between optical and γ-ray fluxes for different sources. The corresponding correlation graphs (like fig. 7.23) are listed in appendix B. The relation redshift vs. corr.coefficient is shown in figure 7.24.

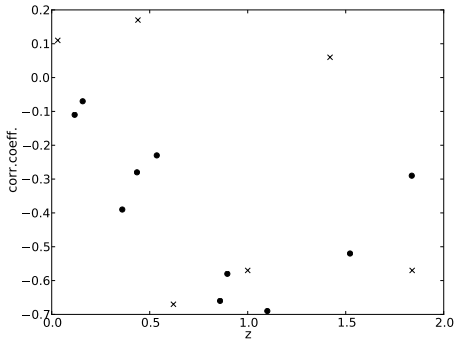

Figure 7.24.: Correlation coefficients vs. redshift. Sources with more than 20 data points are marked with filled circles, the remaining sources with X-crosses. It is notable that all points with *positive* correlation (***less** optical flux belonging to **more** γ-flux*, remember the magnitude scale for the optical points) are all coming from sources with few data. So this unexpected behavior may very well be a problem of low numbers. Otherwise, no relation between the correlation coefficient and redshift can be deduced.

for which a *less optical flux belonging to more γ-flux* behavior was found were entering this study with only a few data points, so this unexpected behavior may very well be a problem of low numbers.

7.5.1. Comparison between public and non-public *Fermi* data of PKS 1424-418

In the context of the two flaring periods of PKS 1424-418 presented in sec. 7.4.2, I started collaborating with members of the *Fermi* collaboration to investigate these two flares in a multiwavelength context. First results of this ongoing study will be presented at the *2011 Fermi Symposium* in Rome. This cooperation allows me to compare the public available daily *Fermi* fluxes (which were used for the studies in the previous section; the correlation graph for PKS 1424-418 is given on page 168) with fluxes derived from a dedicated analysis of this source by *Fermi* members. They introduced a time-adaptive analysis technique, which is adapting the duration of each time bin to gather enough flux so that the data point in each bin has a detection significance of *TS=50*, corresponding

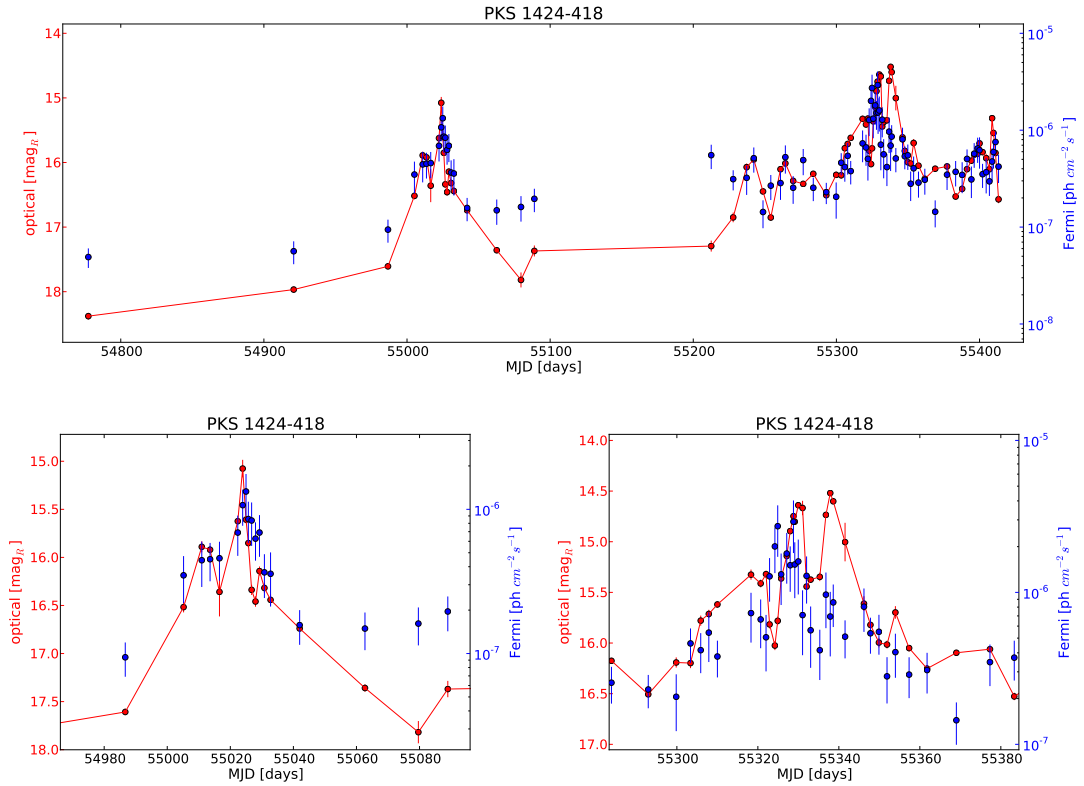

Figure 7.25.: ATOM and *Fermi* lightcurve of PKS 1424-418, using the time-adaptive binning described in the text. The upper panel is showing the complete time span holding *Fermi* data from this study, the lower panel are zoom-ins of the flaring periods. The optical R band measurements (shown in red) are connected with a line to make the tend in optical better visible under the forest of the error bars of the *Fermi* points shown in blue. It is especially noteworthy that the 2nd flare is clearly double-peaked in optical, whereas the flare in the GeV band is only single peaked.

to $\approx 7\sigma$ above background (*D. Thompson, priv.comm.*).

For correlation studies, the ATOM R band data was binned using the same time binning intervals that were used for the *Fermi* data; every single optical point inside one time bin was combined to one optical point virtually simultaneous to the GeV point using an error-weighted average. The resulting lightcurves are given in fig. 7.25.

During the first flaring period, the optical and the GeV flare are more or less simultaneous. In contrast to the second flare, where the GeV increase is preceding the first peak of the *double-peaked optical flare*. The second peak –being slightly brighter than the first one– is *not* accompanied by a GeV event. This may be a hint that ATOM was probing two different electron distributions in the source. As it was demonstrated in sec. 7.4.2, no significant color change was detected during both flares.

In figure 7.26, the proprietary *Fermi* data set using the adaptive binning is compared with the public available daily binned data set during both flaring periods. While the adaptive binning is obviously giving a higher time resolution during high flux periods, the daily binned data can trace the flaring state also very well. So it is not clear that a

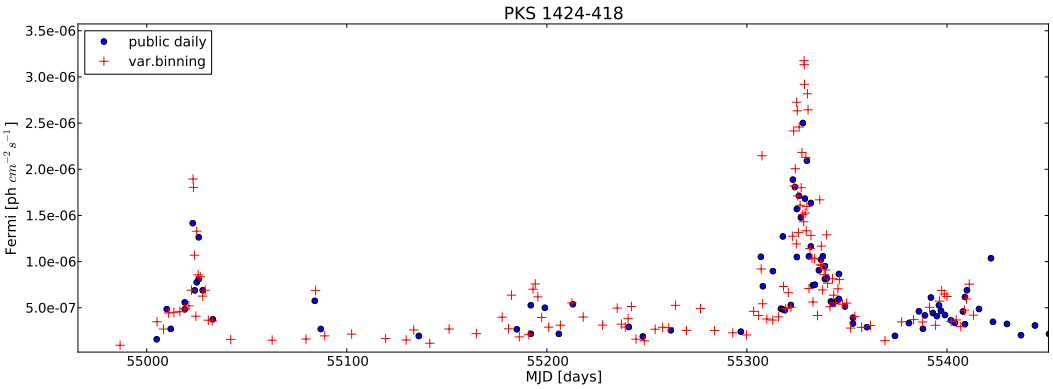

Figure 7.26.: Comparison of the two used *Fermi* data sets (linear scale). The proprietary data set with the time-adaptive binning (red crosses) has obviously a higher time resolution during the flares, but the public daily binning (blue dots) can trace the flaring state also very well.

specific *Fermi* analysis is better suited for these kind of studies.

For correlation studies, the picture is different. The correlation between *Fermi* and ATOM data for the different binning is compared in figure 7.27. Using the whole data set, the resulting correlation coefficient does not change significantly between the daily and the adaptive binning. When restricting the analysis to the flaring periods (middle and right column), the picture changes. During flare 1, where the optical and GeV fluxes behave similar, the adaptive binning is leading to tighter correlations. During flare 2, with its different behavior in optical and GeV, the correlation coefficient is decreasing to much lower values for the adaptive binning than for the daily bins (which is also lower than compared to flare 1) – as expected. But one has to conclude that the adaptive binning is giving better results than the public daily binning, if one defines *better* as giving the correlation coefficient relations one expects after looking at figure 7.25.

One problem with daily binning here is that there are less simultaneous optical/GeV points than with adaptive binning. To test if one can overcome this problem with a wider time bin, a 48 hour binning[8] was tested and is shown in the 3rd row of fig. 7.27: For flare 1, this is resulting in a tighter correlation than using the daily binning (but worse than with adaptive binning), but the correlation coefficient is also increasing for flare 2. There, this can be explained with the smearing over the double-peak structure using the two day binning function.

So the adaptive binning introduced by the *Fermi* team seems to be better suited to trace flaring periods, and the so-determined values are probably also better suited for any models trying to reproduce the lightcurves.

I thank D. Thompson and L. Escande for providing me with the time-adaptive binned *Fermi* data of this source.

[8] *48 hour binning* is defined here as averaging over all ATOM data points within a ±24 hour period around each *Fermi* data point to get corresponding optical points to nearly every available *Fermi* point.

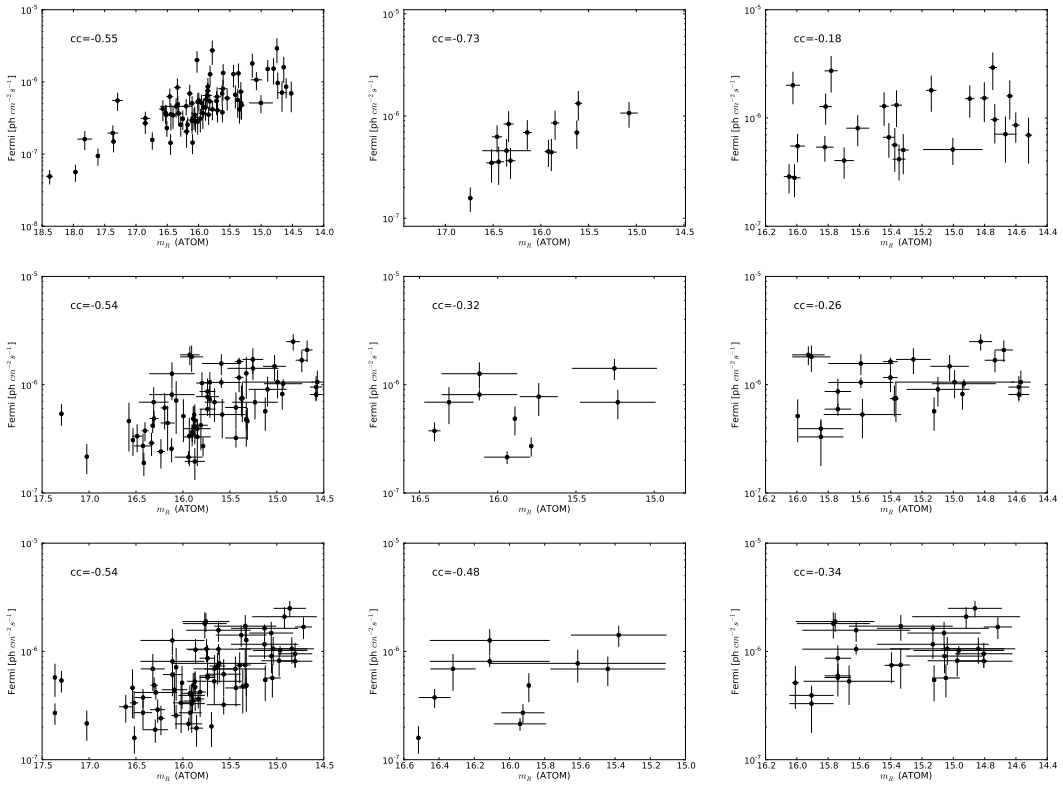

Figure 7.27.: Correlation between *Fermi* and ATOM data. *upper row*: time-adaptive binning, *middle row:* daily binning, *bottom row:* 48 hour binning. *left to right:* all data, first and second flare. The corresponding correlation coefficient is given in the graph. The correlation of the second flare is always worse than for the first one which is not surprising because of its double peak structure in the optical band vs. a single peak in GeV.

8. Summary and outlook

8.1. Technical and operational summary

This thesis is presenting the incarnation of the *Automated Telescope for Optical Monitoring*. I have described in detail the selection and testing procedures of different CCD camera systems, the modifications applied on the old *Zeiss* telescope of LSW and its relocation to Namibia. The automatic operation of ATOM in the context of the H.E.S.S. experiment was also presented. The different steps, quality control and outcome of the *automated data reduction and analysis system* ADRAS have been shown in chapter 5.

ATOM is now a very successful automatic telescope system and is operating since four years without severe problems.

Of course, it is not perfect, and several improvements could be applied. The most promising improvement of ATOM operations would probably be the implementation of an automatic scheduling system. It would not only eliminate the necessity of daily human activity (namely to create an observing schedule *every* day), but would allow to dynamically adapt the nightly schedule to unstable weather conditions, e.g. allow an instantaneous start of observations after clouds have vanished, omitting the compulsory break after a re-start during the night to get back on the pre-defined observing schedule (see sec. 4.2). Or even prefer observation on one part of the sky if the other part of the sky is affected by clouds (the input data for such decisions is already provided by the cloud monitor).

The second (and last) need of human interaction with daily operation is the start-up at sunset (sec. 4). Up to now, there is no automatism available to check for good weather before the cloud monitor starts its operation at nautical twilight (this is too late for twilight flats). Therefore, the human operator has to check for good weather at -or shortly before- sunset and approve system start-up to allow for taking twilight flats (this is usually done by checking a webcam on site). A possibility for automation of this task would e.g. be an upgrade of the cloud monitor that would enable this device to take images during daytime. The latest model of H.-J. Hagens cloud monitor series in 2011 is equipped with a grey filter position in the protection cover over the entry lens of the optical system and is thus able to image the sky even in direct sunlight. A hardware upgrade of ATOMs cloud monitor to this latest version and the enhancement of the software to e.g. being able to track the sun or any other algorithm to determine the cloud cover during daytime would allow for a complete automatic start-up of the system.

The implementation of these two suggested upgrades would allow to operate ATOM in a complete robotic way.

8.2. Scientific summary and outlook

The first presented scope of scientific outcome was about the atmospheric conditions over Goellschau, the location of ATOM and the H.E.S.S. experiment, in chapter 6. I have shown that one can draw plausible conclusions about atmospheric conditions over longer timescales like months and years, but that the atmosphere is very variable over shorter timescales like nights and hours, and that a single set of parameters cannot describe the nightly atmospheric conditions in the majority of nights. The approach to use the extinction parameters as a quality control tool for atmospheric influences on H.E.S.S. measurements did not lead to promising results, nor can the all sky cloud monitor results in the present form be used to draw conclusions about H.E.S.S. measurements.

A deeper study of the relation between atmospheric extinction coefficients and H.E.S.S. shower parameters done in sec. 6.3 would be possible if much more observing time would be spend on truely simultaneous observations between H.E.S.S. and ATOM. I.e. if H.E.S.S. is observing one target for e.g. 6 runs (2.5 hours), ATOM would have to observe this target also for 2.5 hours, split in many much shorter exposures. This would allow to compare H.E.S.S. trigger rates with raw detected star light fluxes and color changes on comparable time scales (note that for a complete set of extinction parameters one needs observations at different airmasses). The drawback of this procedure would be a drastically reduced number of monitored (AGN) targets. Because where H.E.S.S. needs to observe a source for many hours (often many nights) to get a significant detection, these sources are often so bright in optical that ATOM can get a solid 2-color measurement in typically 10-30 min.

Another possibility would be to look into the cloud monitor sky quality estimation algorithm. The now implemented algorithm to characterize sky transparency by counting stars is not necessarily the best approach to this problem (it *is* very well suited for stopping/re-starting ATOM during the night because of cloud cover, the task it is designed for). Another approach, e.g. by analyzing the signal intensity distribution over the sky, would maybe correlate better with the H.E.S.S. trigger rate.

The large number of > 200 regularly monitored AGN is offering a lot of opportunities for further investigations. This thesis is providing a multi-year, multi-color data set for many of the monitored sources, which should allow for a much deeper timing analysis than what was presented in this work (e.g. like the time series study done by Emmanoulopoulos (2007), mainly on x-ray data). Or extending the investigation of color changes presented in sec. 7.4 to all of the monitored sources and use this results as input for SED modeling.

The ongoing *Fermi* satellite mission is expected to release more data in the future, allowing to extend the correlation study presented in section 7.5 to a) more sources spanning b) a longer time interval. It will be interesting to see if the dichotomy first found by Behera (2010) and being less significant after adding 7 additional sources (and more data for all sources) in this thesis will still be valid if one adds more data and sources to the sample.

And finally, I am waiting for the big flare of an AGN which is not yet detected in VHE, but will be after H.E.S.S. was triggered by ATOM. Some triggers to H.E.S.S. were described in sec. 7.3, but none led to a VHE detection. I was able to detect several more flares of AGN, all being uninteresting for H.E.S.S. because of their redshift. To allow the astronomical community to take advantage of this knowledge, these incidents were published promptly via Astronomer's Telegrams (Hauser et al. (2009b) (leading to a *Fermi* detection (Longo et al. (2009))), Hauser et al. (2009a), Hauser et al. (2010b), Hauser et al. (2010a)) to allow other systems to react to it.

A. Lightcurves and color-magnitude diagrams

In the following, the remaining lightcurves (LC) and color-magnitude diagrams (CMD) of a selection of ATOM monitoring sources not shown in the main text (section 7.4) are given.

The figures are all composed of two sub-panels: in the *upper panel*, the R-band light curve is shown in red, the corresponding scale is on the left hand side. The (B-R) color is overlaid in blue with the corresponding scale on the right hand side. The *lower panel* presents the color-magnitude diagram of this source for the time span given in the light curve above. For better orientation, the year of observation is color-coded (the few observations of Nov and Dec 2006 are attributed to the year 2007). Error bars are omitted here for better visibility, but can be deduced from the (color) lightcurve in the upper panel.

A.1. TeV detected sources

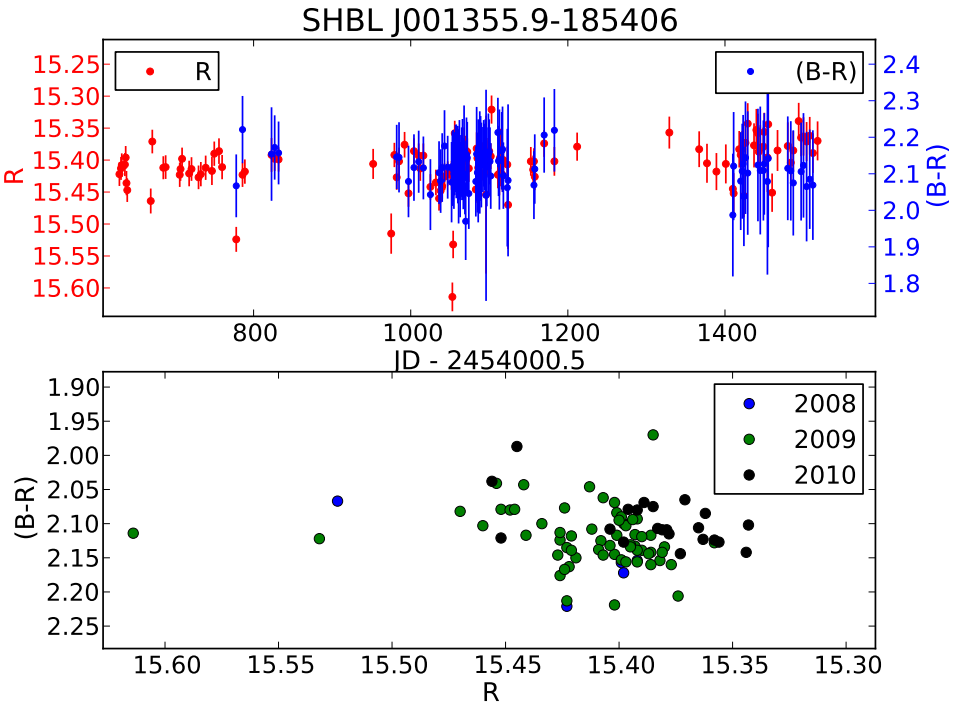

Figure A.1.: LC and CMD of SHBL J001355.9-185406.

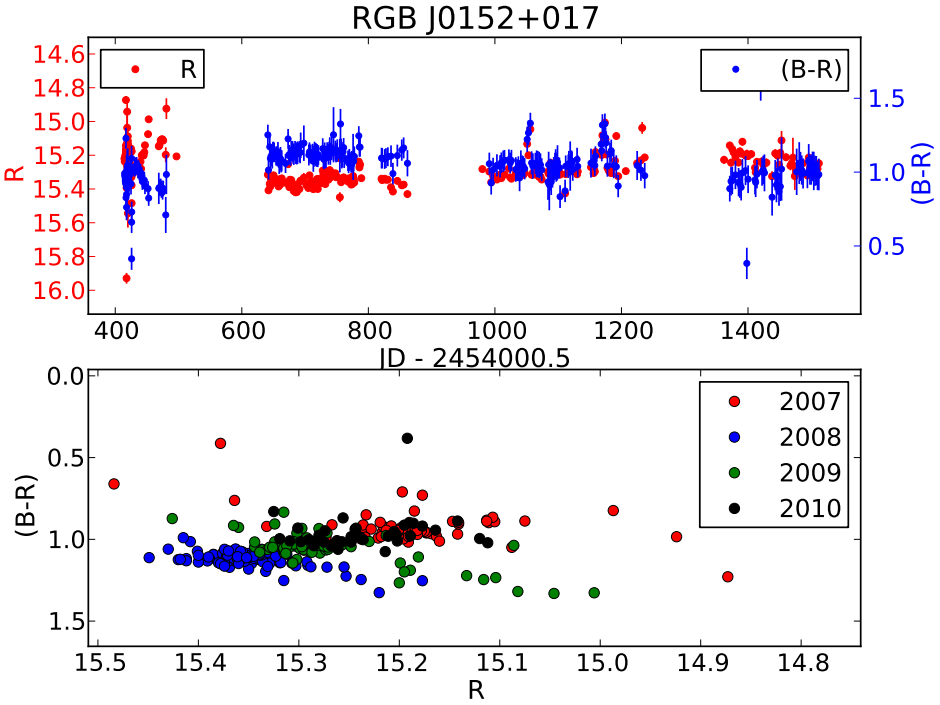

Figure A.2.: LC and CMD of RGB J0152+017

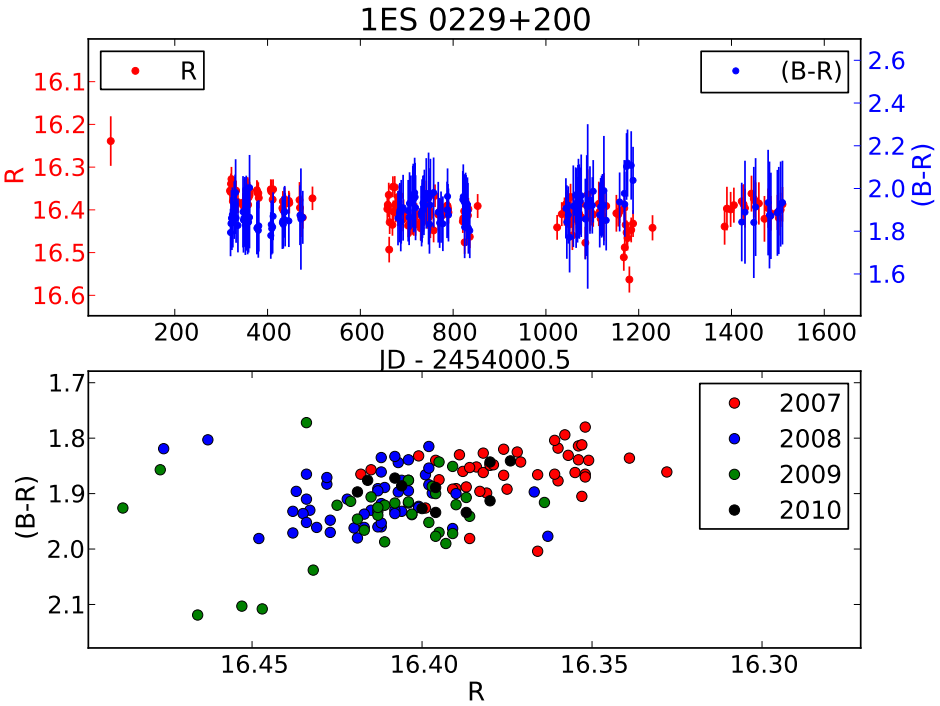

Figure A.3.: LC and CMD of 1ES 0229+200.

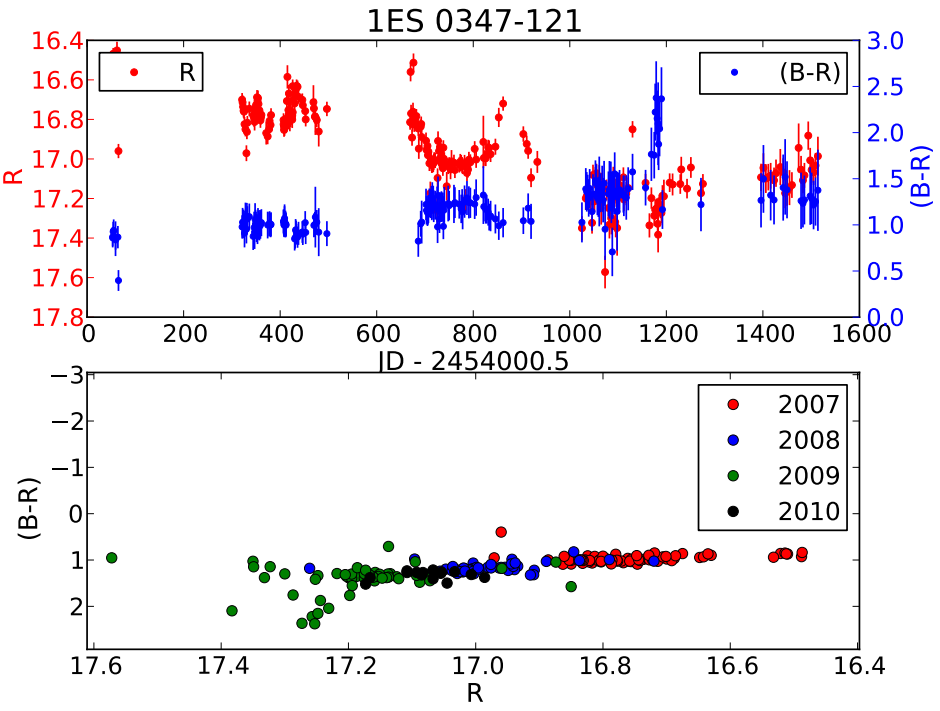

Figure A.4.: LC and CMD of 1ES 0347-121.

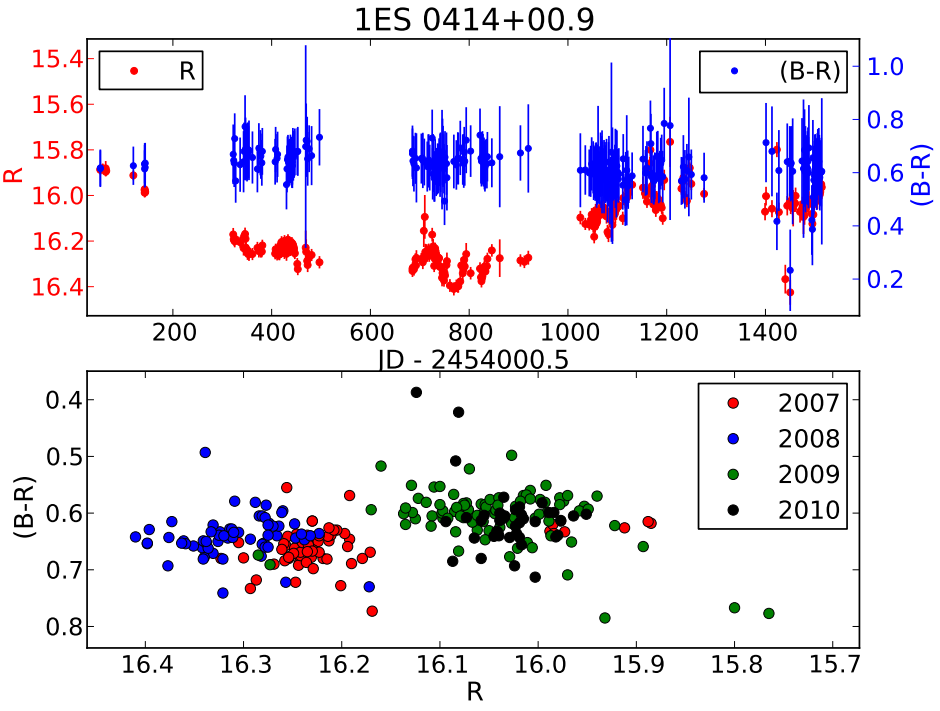

Figure A.5.: LC and CMD of 1ES 0414+00.9.

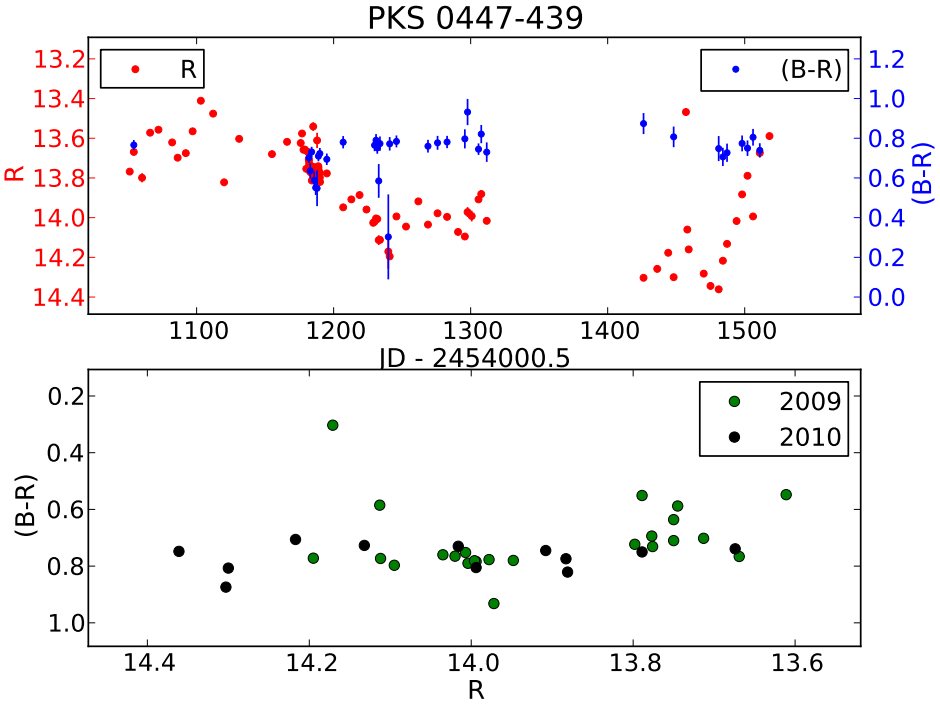

Figure A.6.: LC and CMD of PKS 0447-439.

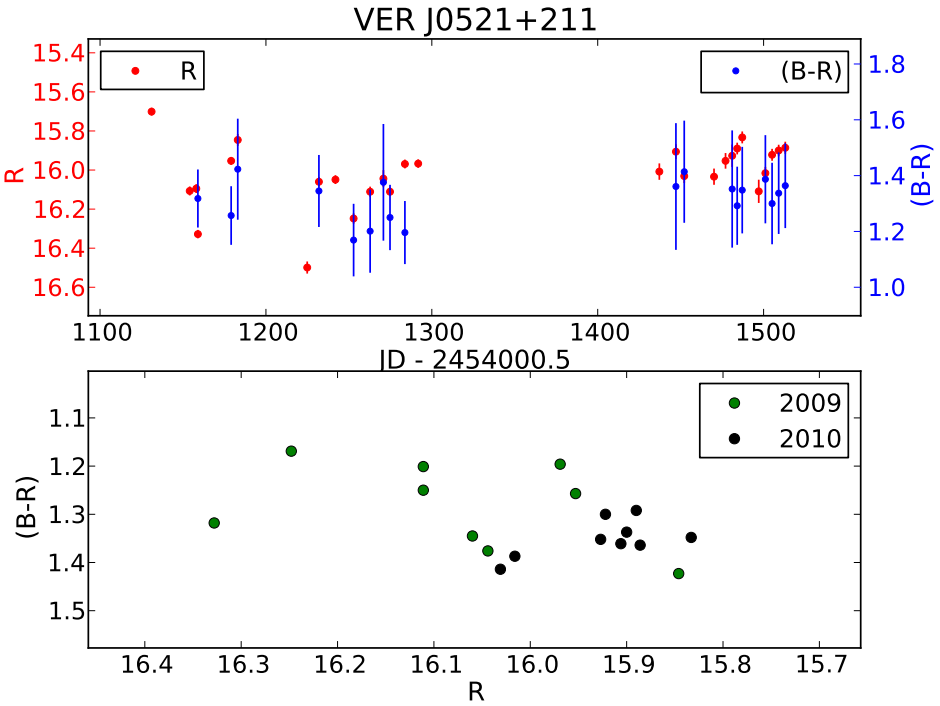

Figure A.7.: LC and CMD of VER J0521+211.

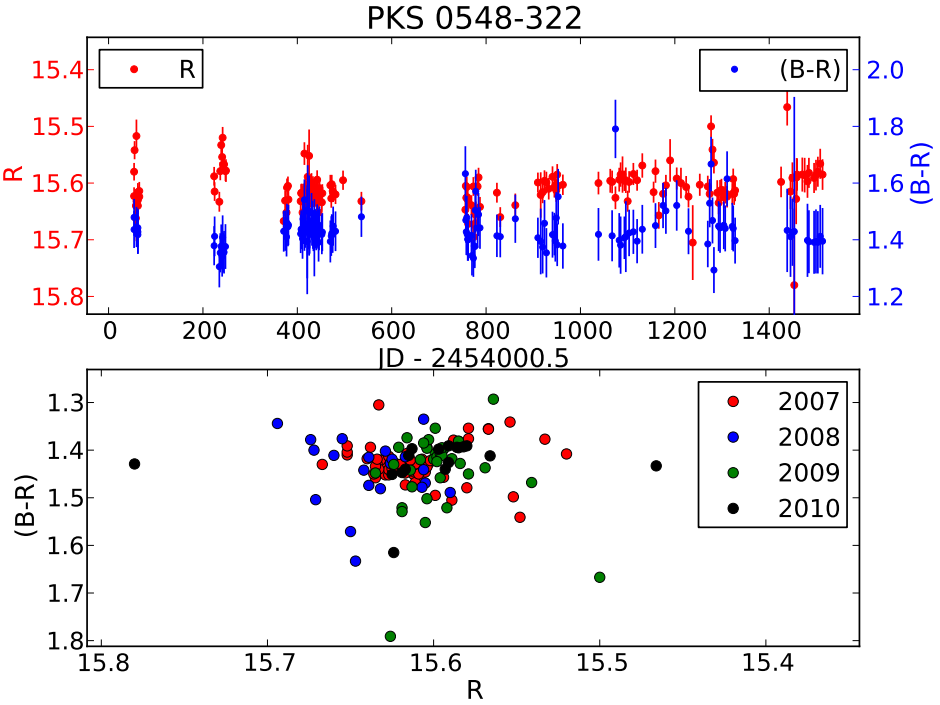

Figure A.8.: LC and CMD of PKS 0548-322.

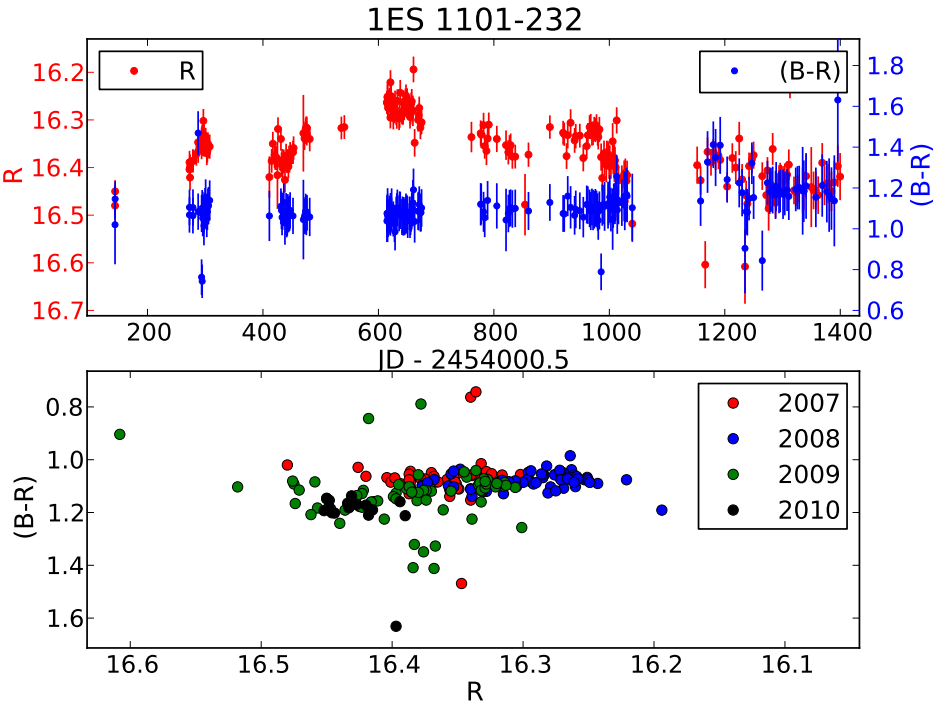

Figure A.9.: LC and CMD of 1ES 1101-232

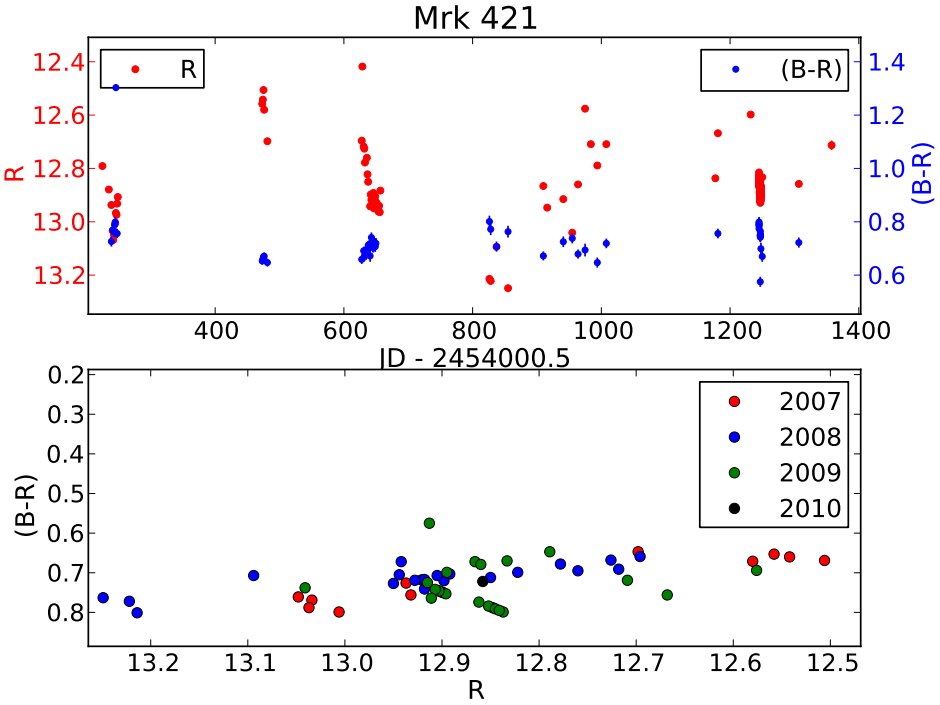

Figure A.10.: LC and CMD of Mrk 421.

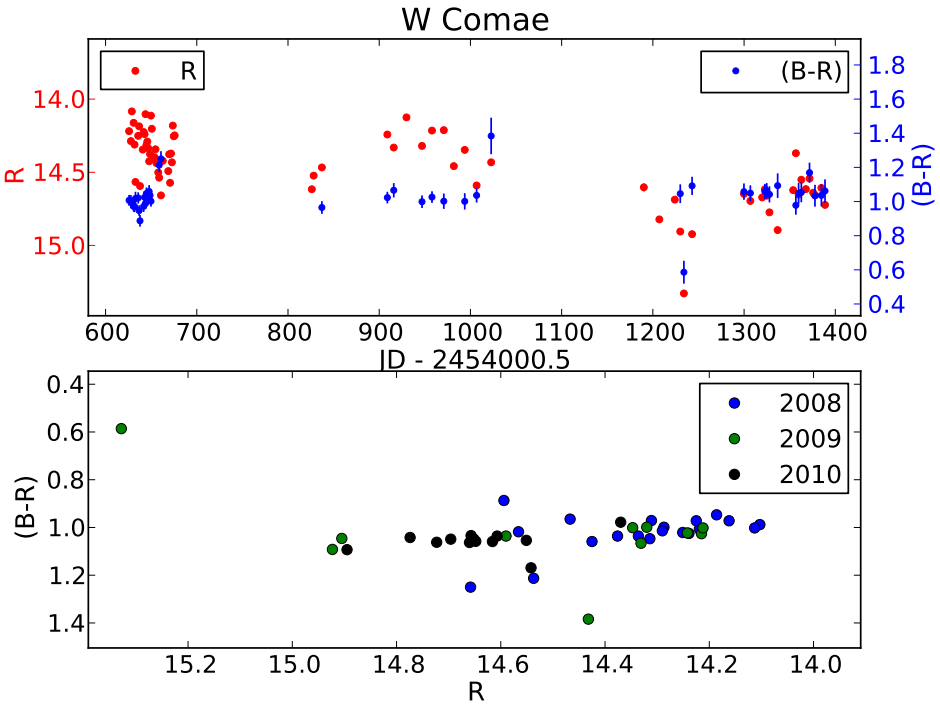

Figure A.11.: LC and CMD of W Comae.

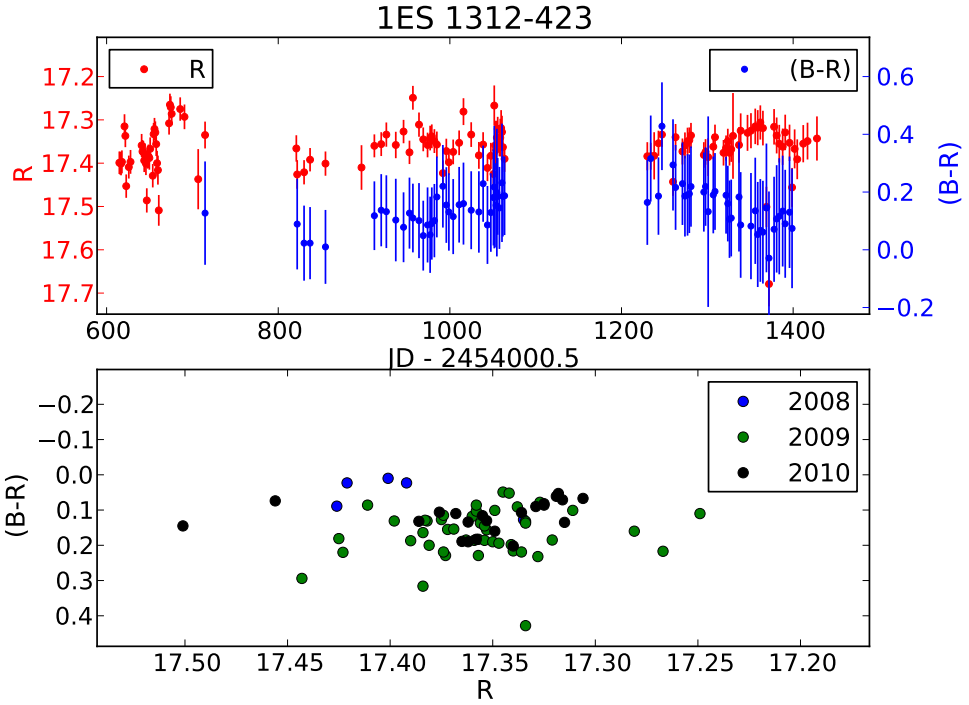

Figure A.12.: LC and CMD of 1ES 1312-423.

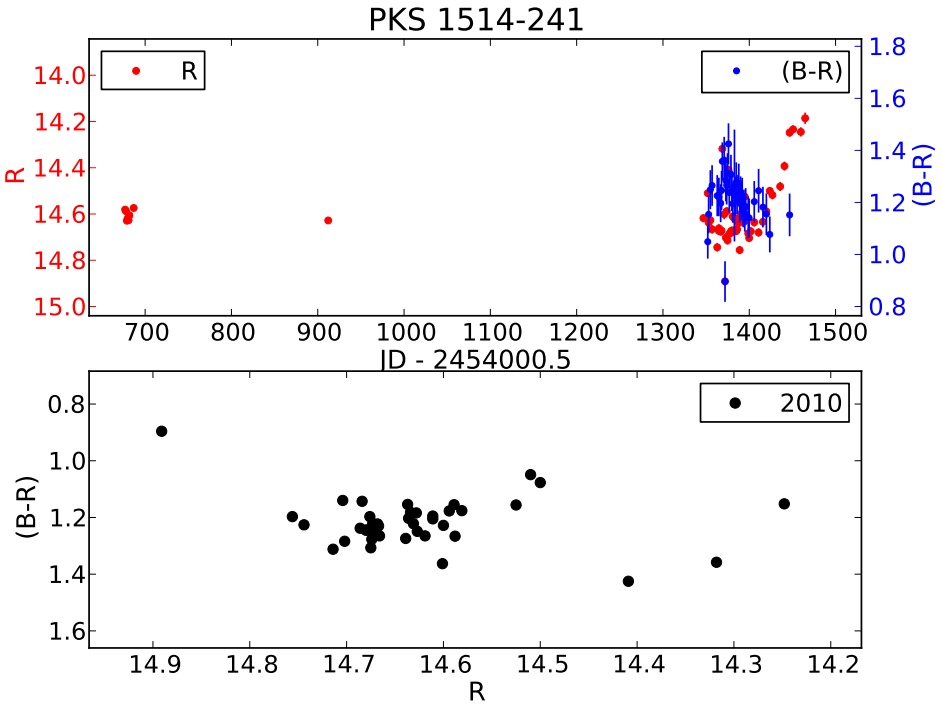

Figure A.13.: LC and CMD of PKS 1514-241.

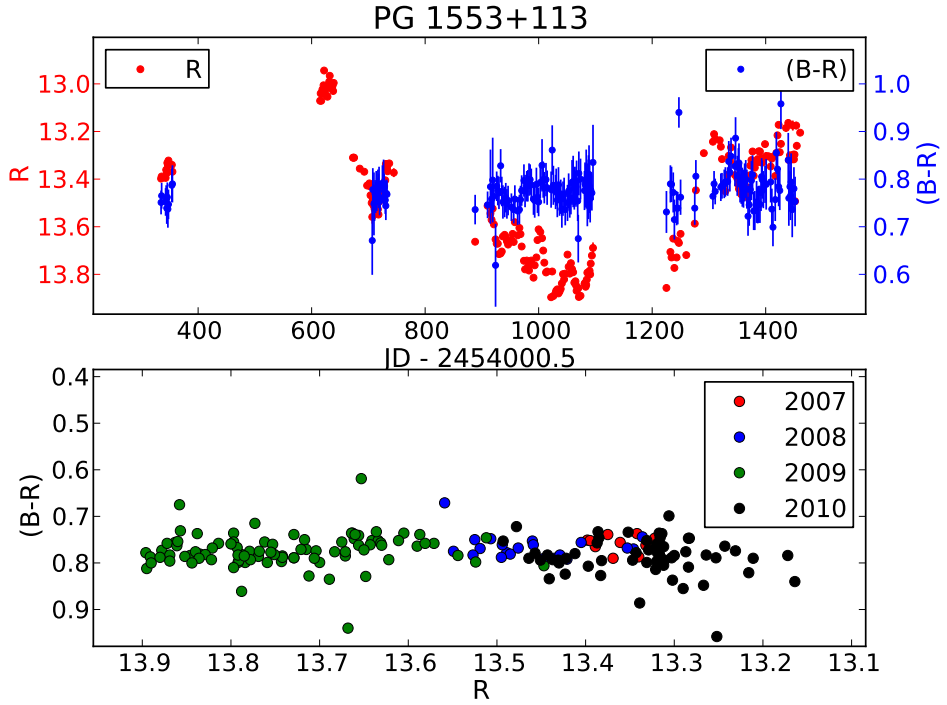

Figure A.14.: LC and CMD of PG 1553+113.

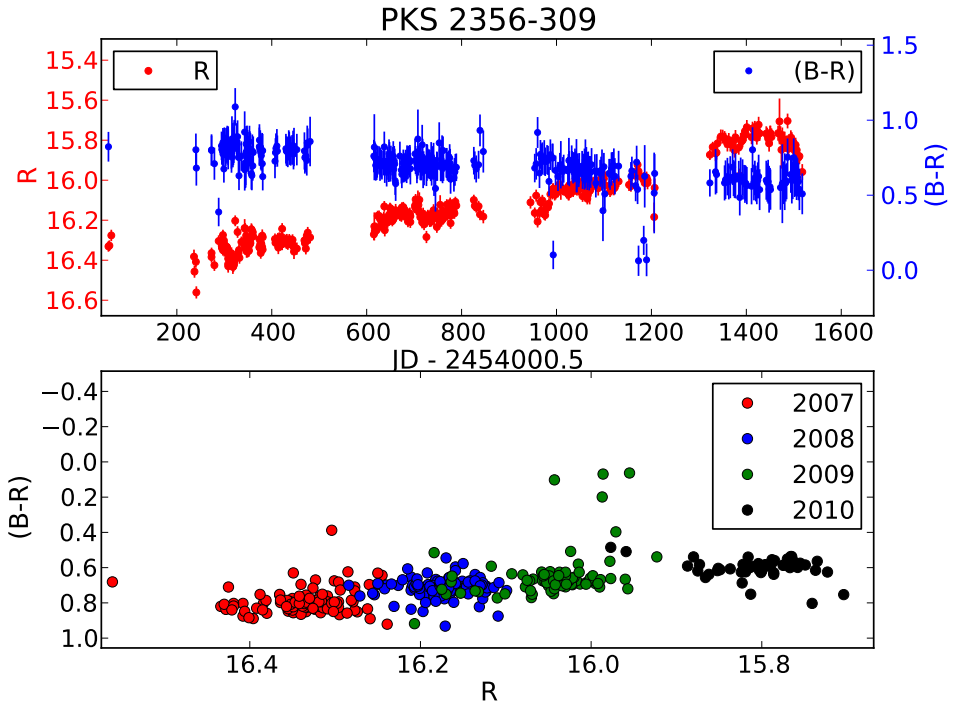

Figure A.15.: LC and CMD of PKS 2356-309

A.2. Sources not detected in TeV

These are all ATOM monitored sources from which more than 25 (B-R) color measurements exists.

Name	slope	cc.
QSO B0007+106	0.25	0.47
SHBL J001355.9-185406	-0.19	-0.18
3C 15	0.42	0.33
PKS 0048-097	-0.00	-0.00
4C 31.03	-0.97	-1.00
RGB J0152+017	0.13	0.11
PKS 0208-512	-0.06	-0.22
3C 66A	0.06	0.19
1ES 0229+200	0.88	0.42
AO 0235+16	0.00	0.02
PKS 0301-243	-0.35	-0.02
SHBL J030330.2+055430	-0.43	-0.13
SHBL J031951.9+184534	-0.12	-0.14
SHBL J032541.0-164618	0.13	0.24
1ES 0323+022	0.36	0.38
1ES 0347-121	0.90	0.67
PKS 0352-686	2.50	0.71
1ES 0414+00.9	0.09	0.22
3C 120	0.45	0.97
PKS 0447-439	0.11	0.19
PKS 0454-234	-0.12	-0.27
PKS 0521-365	0.18	0.43
PKS 0537-441	0.00	0.02
PKS 0735+178	-0.00	-0.01
PKS 0805-077	0.04	0.31
3EG J0829+2413	-0.60	-0.72
PKS 0829+046	-0.48	-0.79
RGB J0847+115	-0.19	-0.20
3EG J0852-1216	-0.09	-0.34
OJ 287	0.01	0.06
PMN J0948+0022	-0.34	-0.54
SHBL J101015.9-311908	0.84	0.55
1ES 1101-232	0.32	0.22
Mrk 421	0.20	0.34
PKS 1215+303	0.07	0.02
1ES 1218+304	0.21	0.79
W Comae	-0.05	-0.11
PKS 1222+216	-0.31	-0.96
3C 273	-0.49	-0.47
RGB J1230+253	0.02	0.06
3EG J1236+0457	-0.08	-0.64
PKS 1244-255	-0.35	-0.57
3C 279	0.03	0.13
1ES 1312-423	-0.23	-0.17
PKS 1334-127	-0.11	-0.24
PKS 1406-076	-0.19	-0.31
PKS 1424+240	-0.16	-0.34
PKS 1424-418	0.05	0.30
1ES 1440+122	-0.18	-0.15
PKS 1454-354	-0.18	-0.48
PKS 1510-089	-0.17	-0.77
PKS 1514-241	-0.19	-0.23
PG 1553+113	-0.02	-0.11
PKS 1622-297	-0.45	-0.74
3C 345	-0.19	-0.68
Mrk 501	0.44	0.51
RGB J1725+118	-0.44	-0.76
PKS 1725+044	-0.73	-0.86
PKS 1749+096	-0.00	-0.02
3EG J1911-2000	-0.06	-0.30
3EG J1921-2015	-0.16	-0.60
PKS 2004-447	-0.14	-0.13
PKS 2005-489	0.11	0.75
PKS 2052-474	-0.01	-0.07
SHBL J213135.4-091523	-0.80	-0.87
PKS 2155-304	-0.01	-0.15
BL Lacertae	0.12	0.62
PMN J2250-2806	-0.03	-0.09
3EG J2255+1943	0.14	0.31
3C 454.3	-0.09	-0.64
PMN J2345-1555	0.12	0.64
PKS 2356-309	0.38	0.62

Table A.1.: Complete version of table 7.3, showing the slope and correlation coefficient for all ATOM monitored targets for which more than 25 (B-R) points were available. The corresponding graphs are shown on the following pages, if they have not already been shown before in sec. 7.4 or sec. A.1.

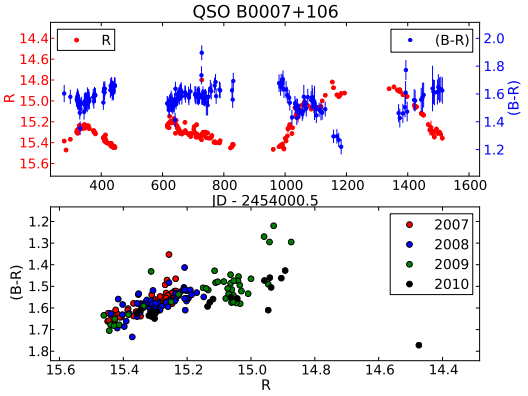

Figure A.16.: LC and CMD of QSO B0007+106.

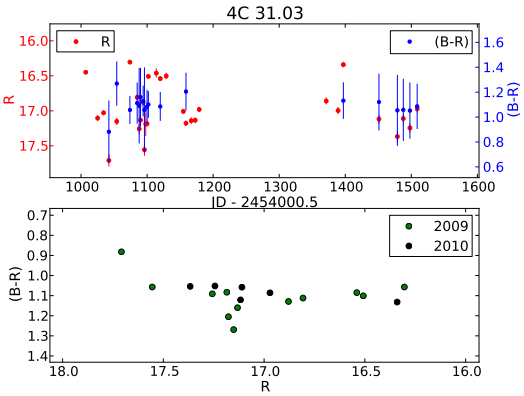

Figure A.19.: LC and CMD of 4C 31.03.

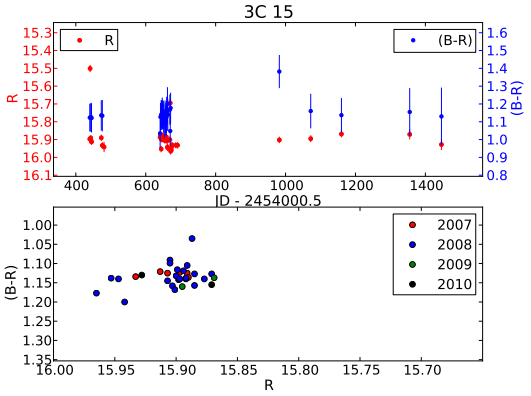

Figure A.17.: LC and CMD of 3C 15.

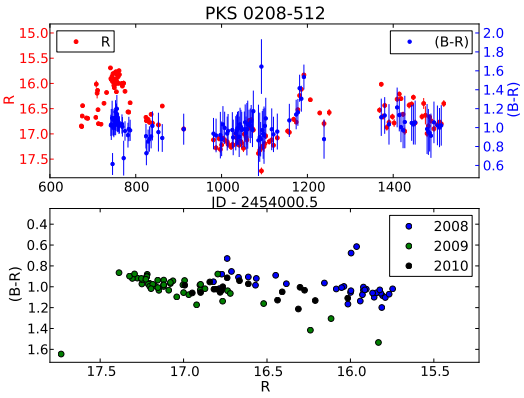

Figure A.20.: LC and CMD of PKS 0208-512.

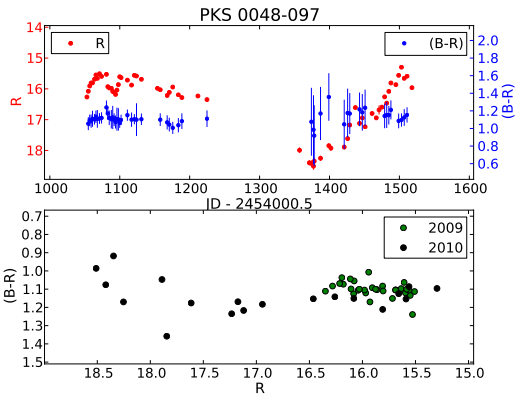

Figure A.18.: LC and CMD of PKS 0048-097.

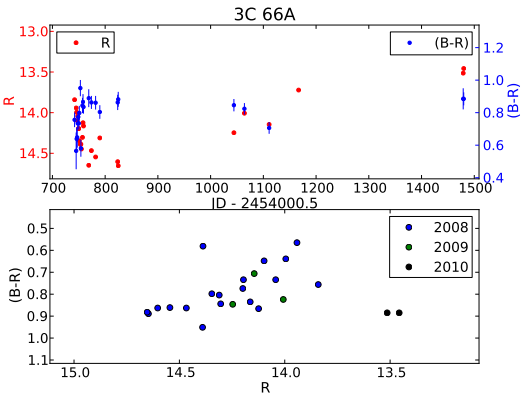

Figure A.21.: LC and CMD of 3C 66A.

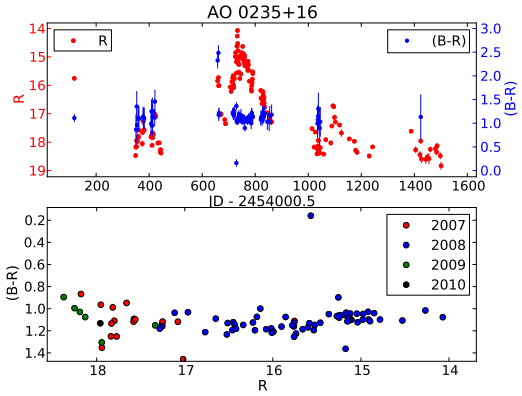

Figure A.22.: LC and CMD of AO 0235+16.

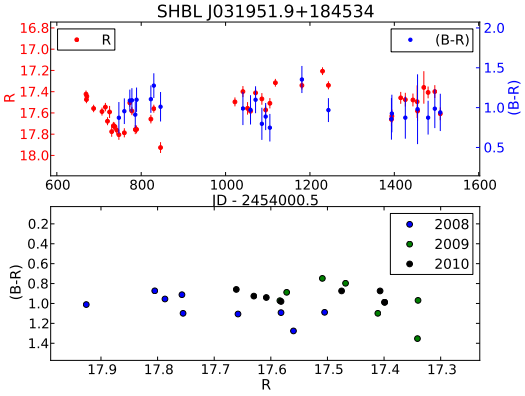

Figure A.25.: LC and CMD of SHBL J031951.9+184534.

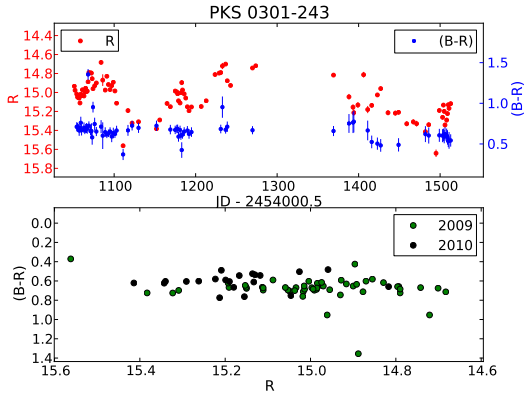

Figure A.23.: LC and CMD of PKS 0301-243.

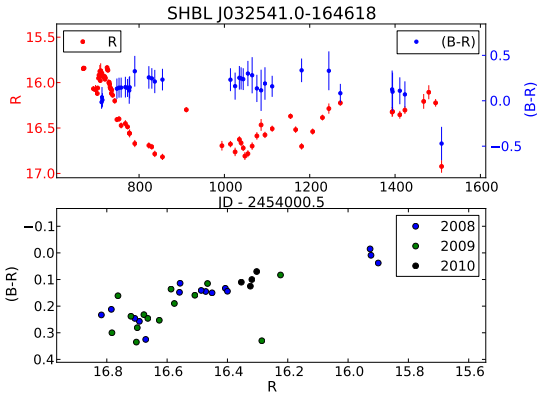

Figure A.26.: LC and CMD of SHBL J032541.0-164618.

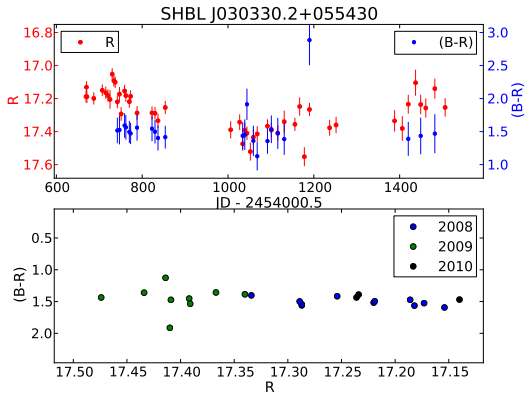

Figure A.24.: LC and CMD of SHBL J030330.2+055430.

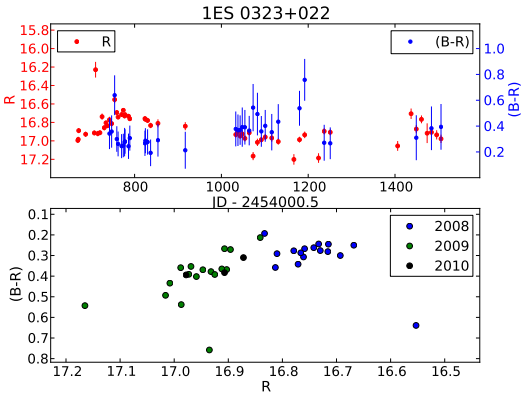

Figure A.27.: LC and CMD of 1ES 0323+022.

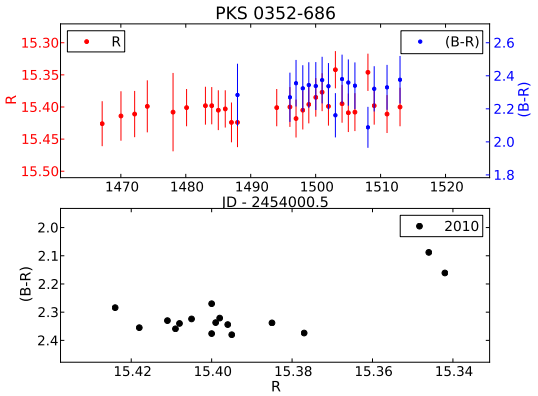

Figure A.28.: LC and CMD of PKS 0352-686.

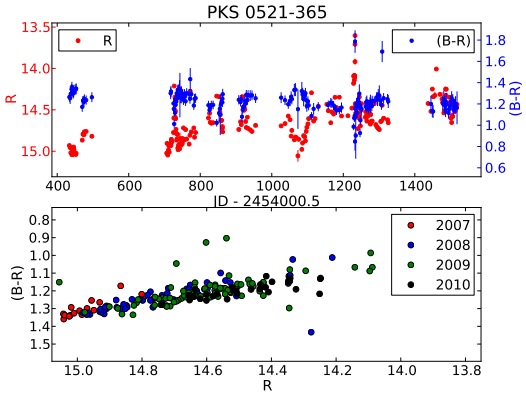

Figure A.31.: LC and CMD of PKS 0521-365.

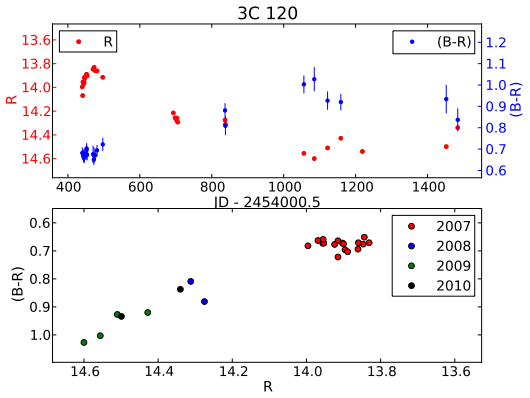

Figure A.29.: LC and CMD of 3C 120.

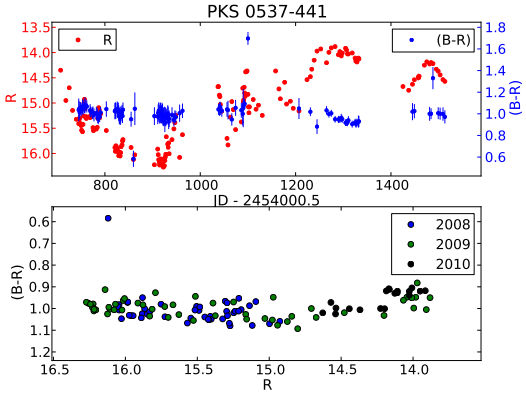

Figure A.32.: LC and CMD of PKS 0537-441.

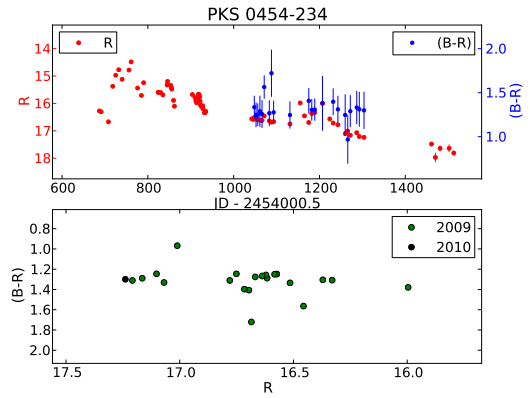

Figure A.30.: LC and CMD of PKS 0454-234.

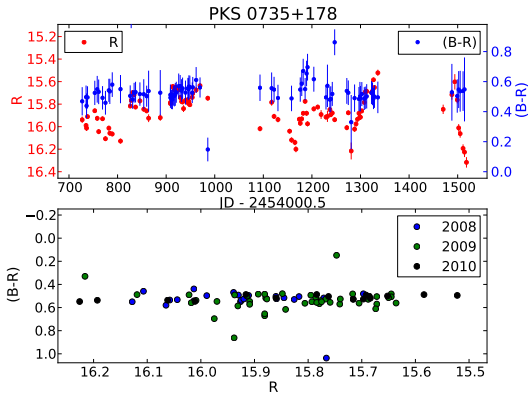

Figure A.33.: LC and CMD of PKS 0735+178.

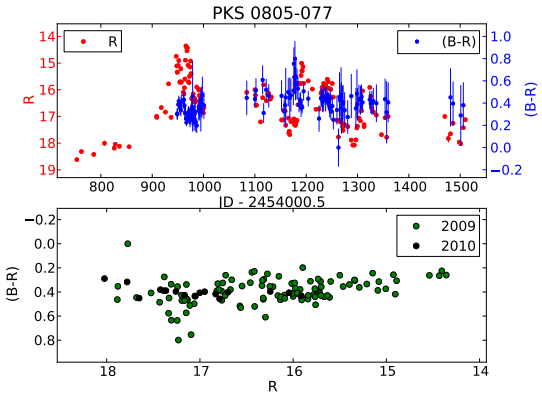

Figure A.34.: LC and CMD of PKS 0805-077.

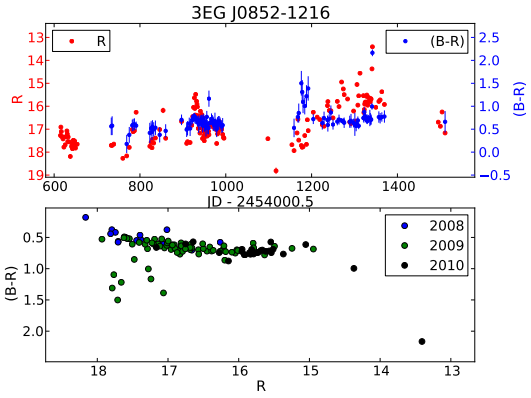

Figure A.37.: LC and CMD of 3EG J0852-1216.

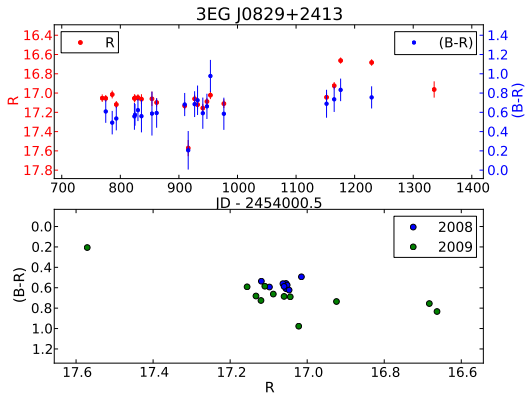

Figure A.35.: LC and CMD of 3EG J0829+2413.

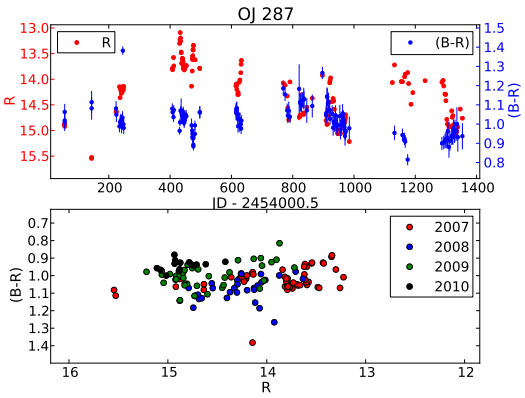

Figure A.38.: LC and CMD of OJ 287.

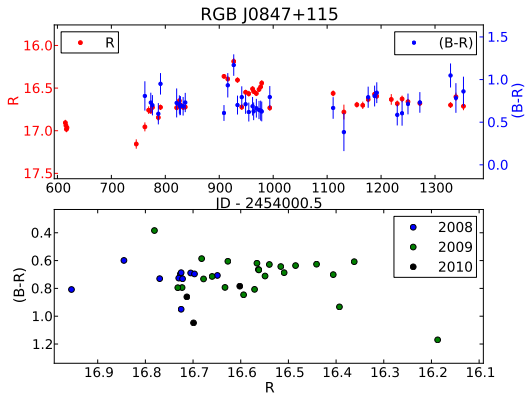

Figure A.36.: LC and CMD of RGB J0847+115.

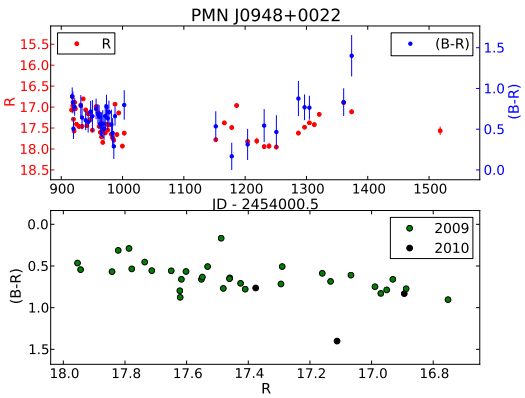

Figure A.39.: LC and CMD of PMN J0948+0022.

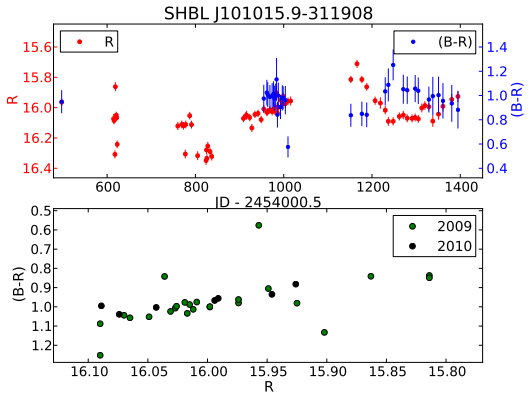

Figure A.40.: LC and CMD of SHBL J101015.9-311908.

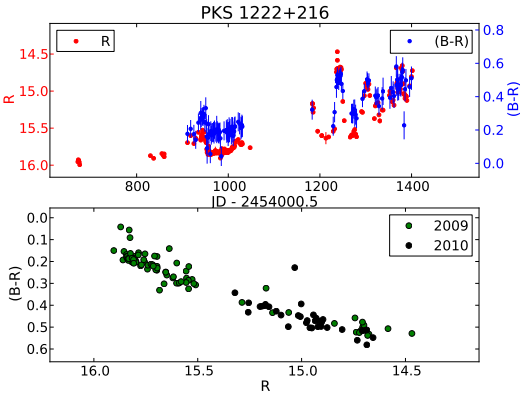

Figure A.43.: LC and CMD of PKS 1222+216.

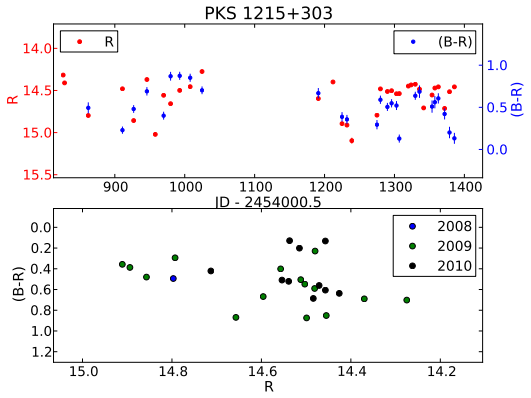

Figure A.41.: LC and CMD of PKS 1215+303.

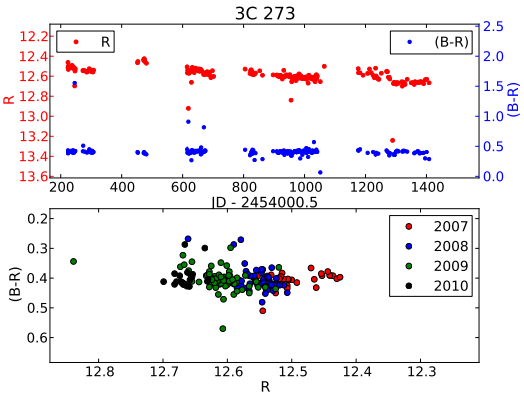

Figure A.44.: LC and CMD of 3C 273

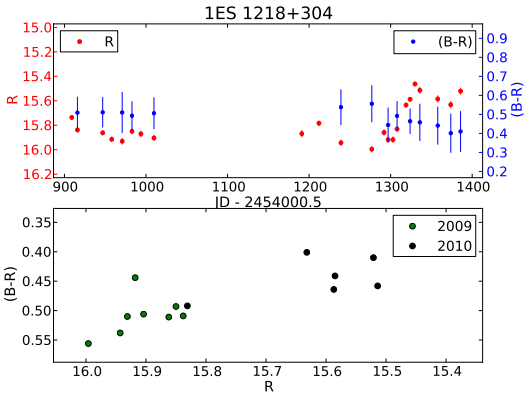

Figure A.42.: LC and CMD of 1ES 1218+304.

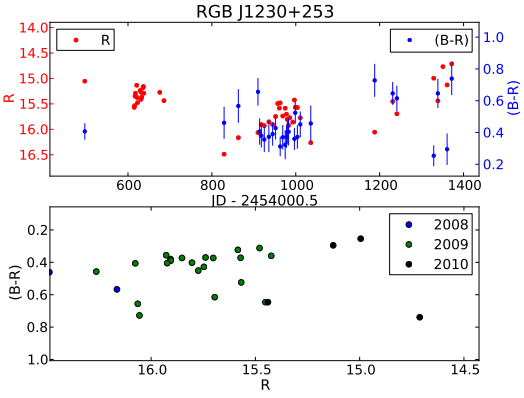

Figure A.45.: LC and CMD of RGB J1230+253.

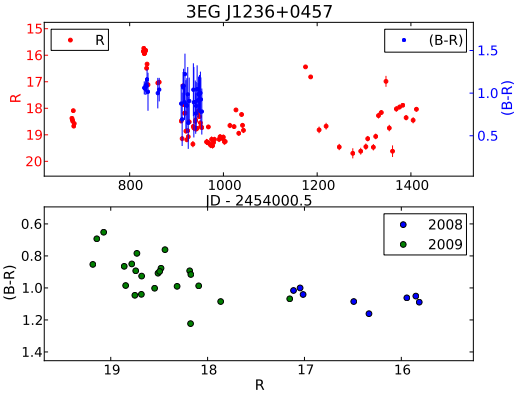

Figure A.46.: LC and CMD of 3EG J1236+0457.

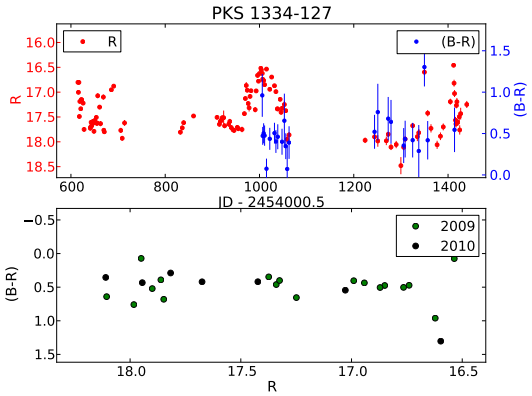

Figure A.49.: LC and CMD of PKS 1334-127.

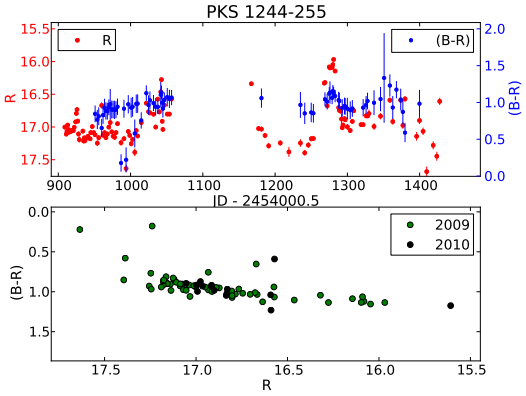

Figure A.47.: LC and CMD of PKS1244-255.

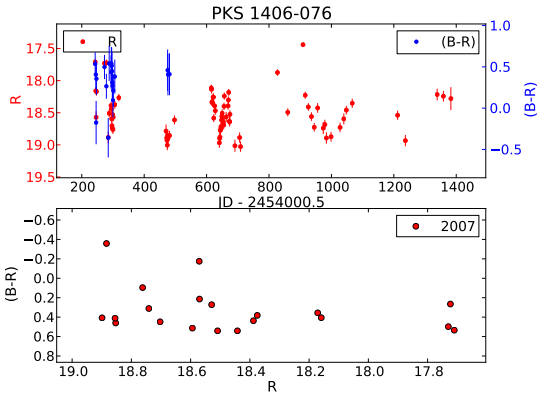

Figure A.50.: LC and CMD of PKS1406-076.

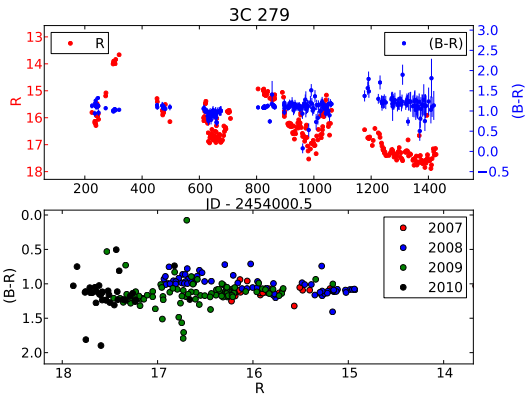

Figure A.48.: LC and CMD of 3C 279

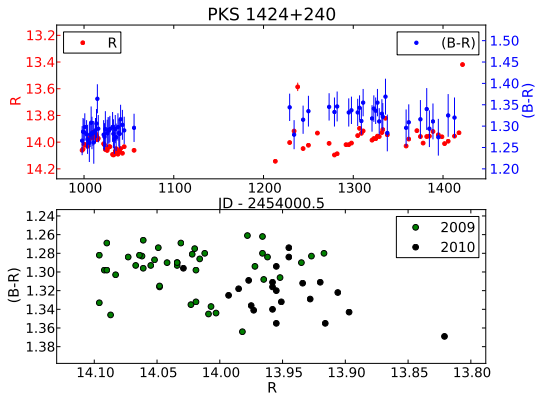

Figure A.51.: LC and CMD of PKS1424+240.

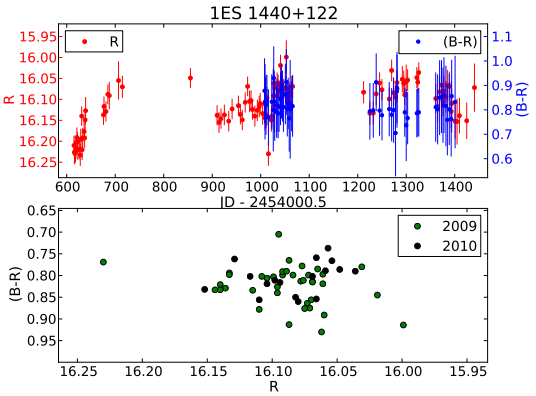

Figure A.52.: LC and CMD of 1ES 1440+122.

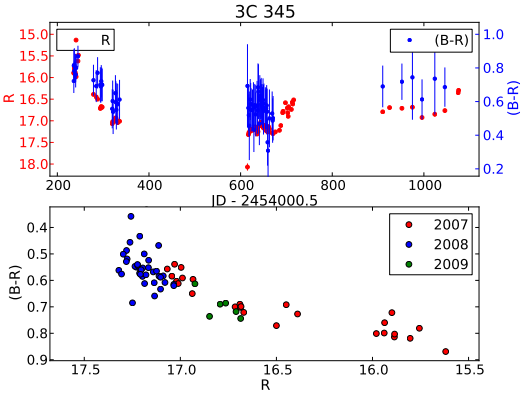

Figure A.55.: LC and CMD of 3C 345.

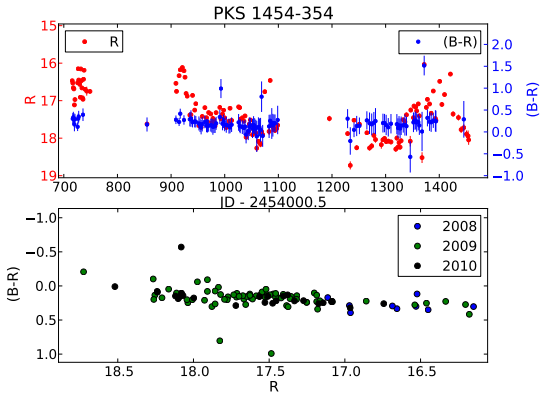

Figure A.53.: LC and CMD of PKS 1454-354.

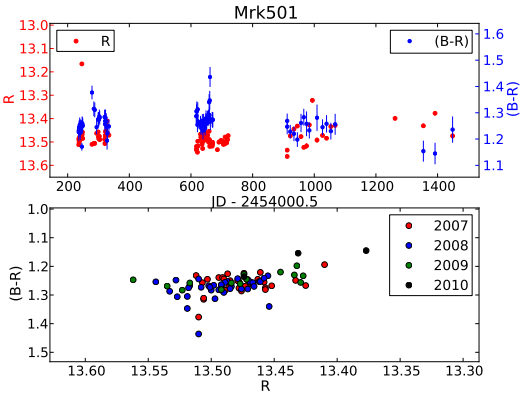

Figure A.56.: LC and CMD of Mrk 501.

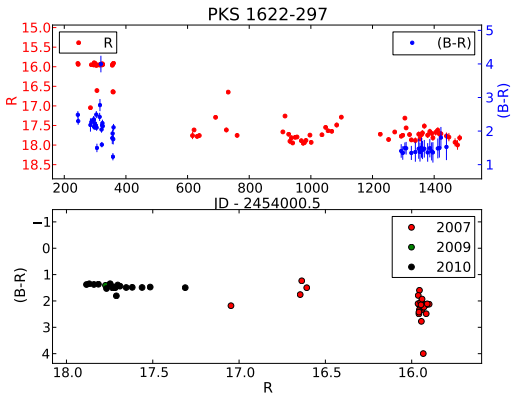

Figure A.54.: LC and CMD of PKS 1622-297.

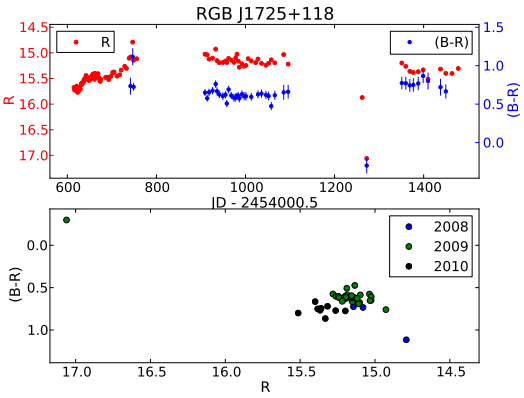

Figure A.57.: LC and CMD of RGB J1725+118.

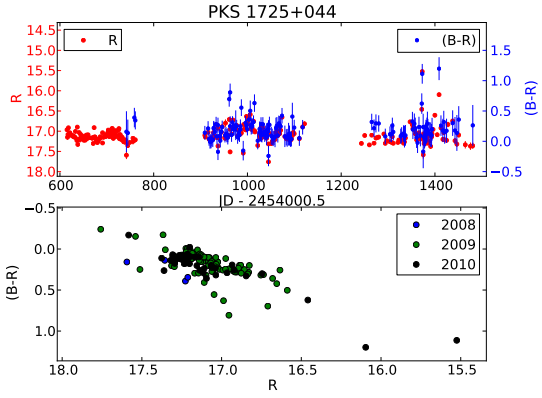

Figure A.58.: LC and CMD of PKS 1725+044.

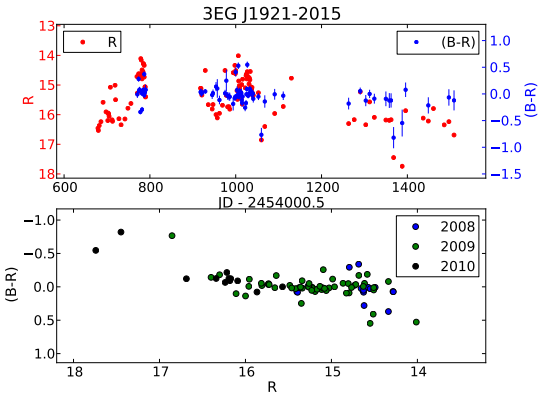

Figure A.61.: LC and CMD of 3EG J1921-2015.

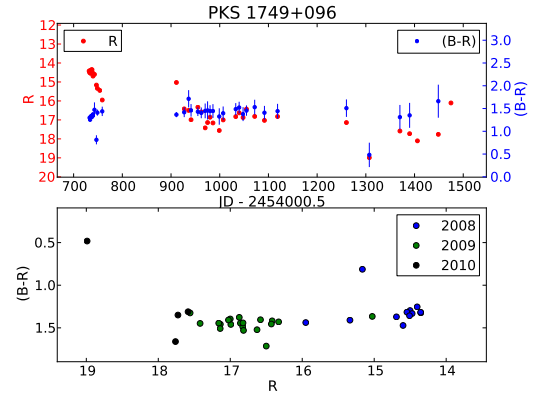

Figure A.59.: LC and CMD of PKS 1749+096.

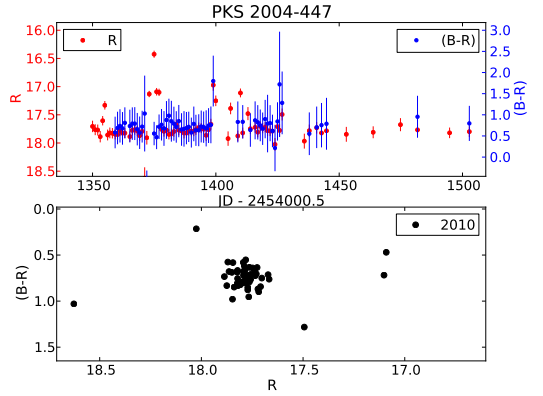

Figure A.62.: LC and CMD of PKS 2004-447.

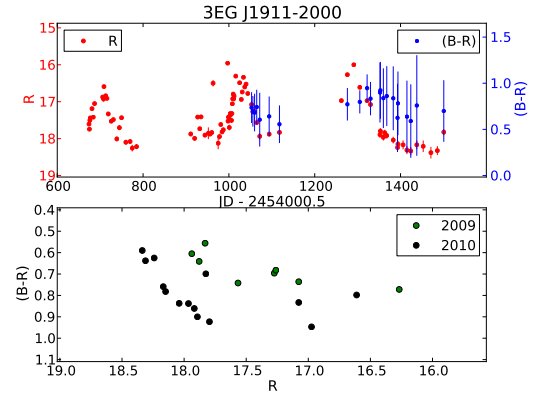

Figure A.60.: LC and CMD of 3EG J1911-2000.

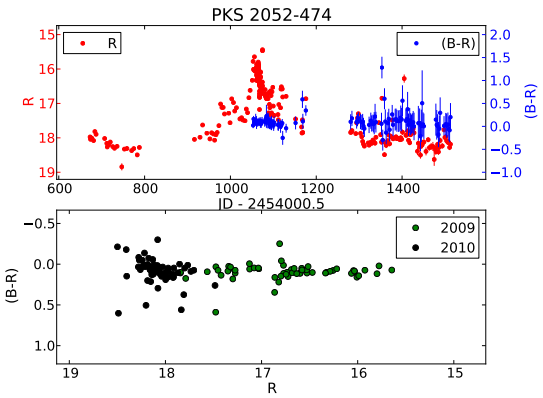

Figure A.63.: LC and CMD of PKS 2052-474.

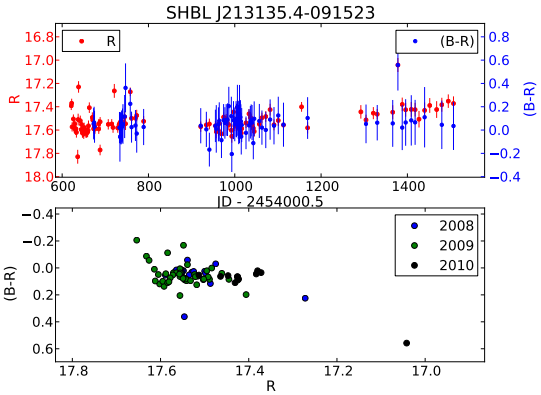

Figure A.64.: LC and CMD of SHBL J213135.4-091523.

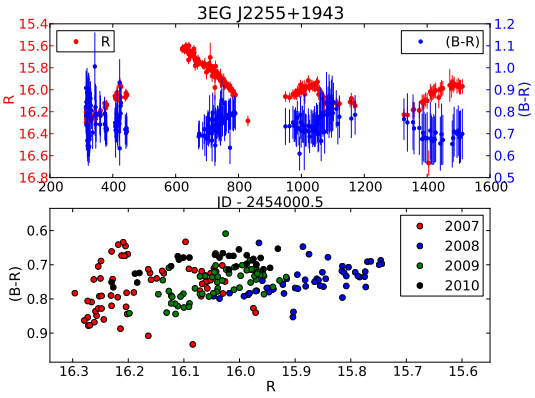

Figure A.67.: LC and CMD of 3EG 2255+1943.

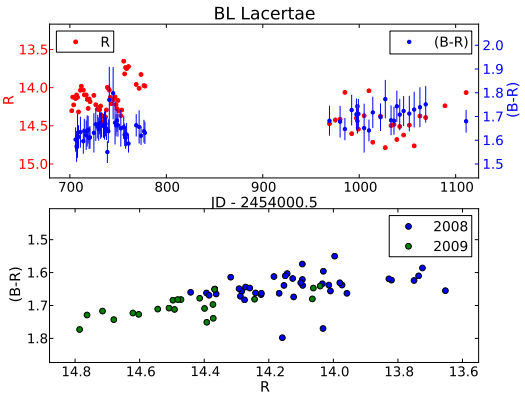

Figure A.65.: LC and CMD of BL Lac.

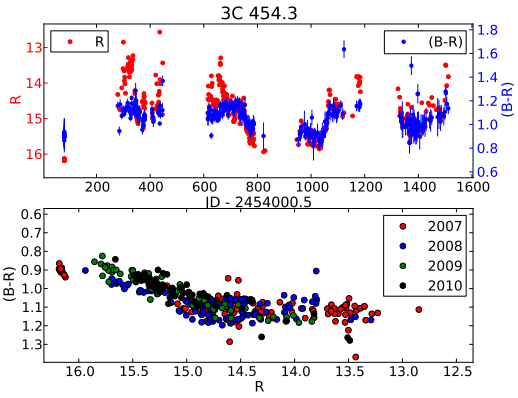

Figure A.68.: LC and CMD of 3C 454.3

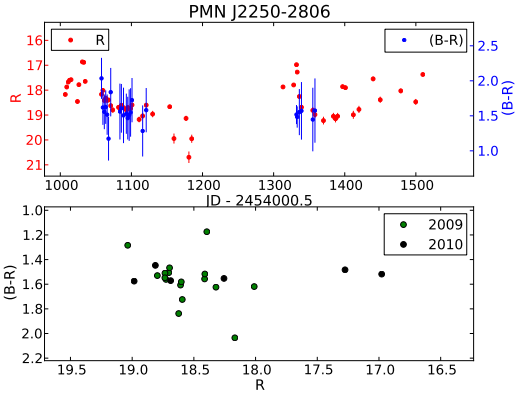

Figure A.66.: LC and CMD of PMN J2250-2806.

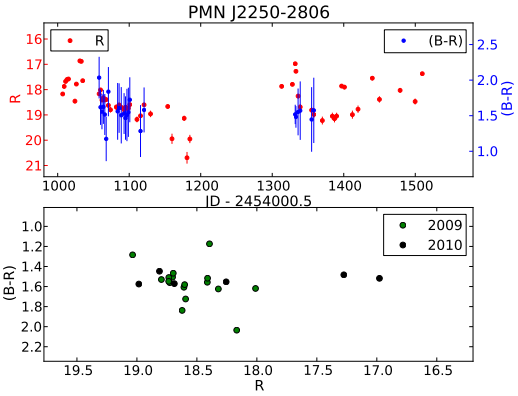

Figure A.69.: LC and CMD of PMN J2345-1555.

B. Correlation plots between optical and γ-ray fluxes

Supplement to sec. 7.5: γ-ray vs. optical flux for all sources on the *LAT monitored source list* for which simultaneous ATOM data exist (except PKS 2155-304 and 3C 454.3, which are shown in the main text).

The upper panel is showing the lightcurve (daily bins) in both wavelength bands, the lower panels the optical vs. γ-ray flux in log-log scale. In the lower-left panels, each data point is plotted including its 1σ error bars. Since this leads to a very crowed plot with suboptimal informative value, each data point is converted into a 2dim Gaussian. All Gaussians are then summed up and visualized in the lower-right panels.

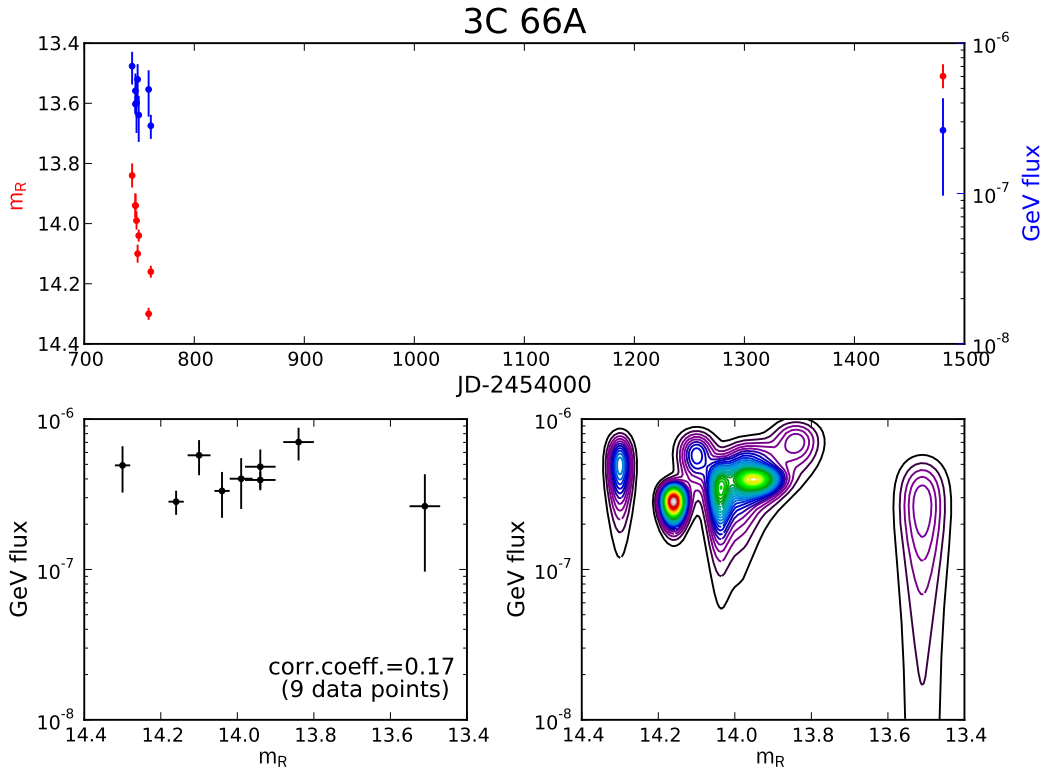

Figure B.1.: Correlation between optical and γ-ray flux: 3C 66a

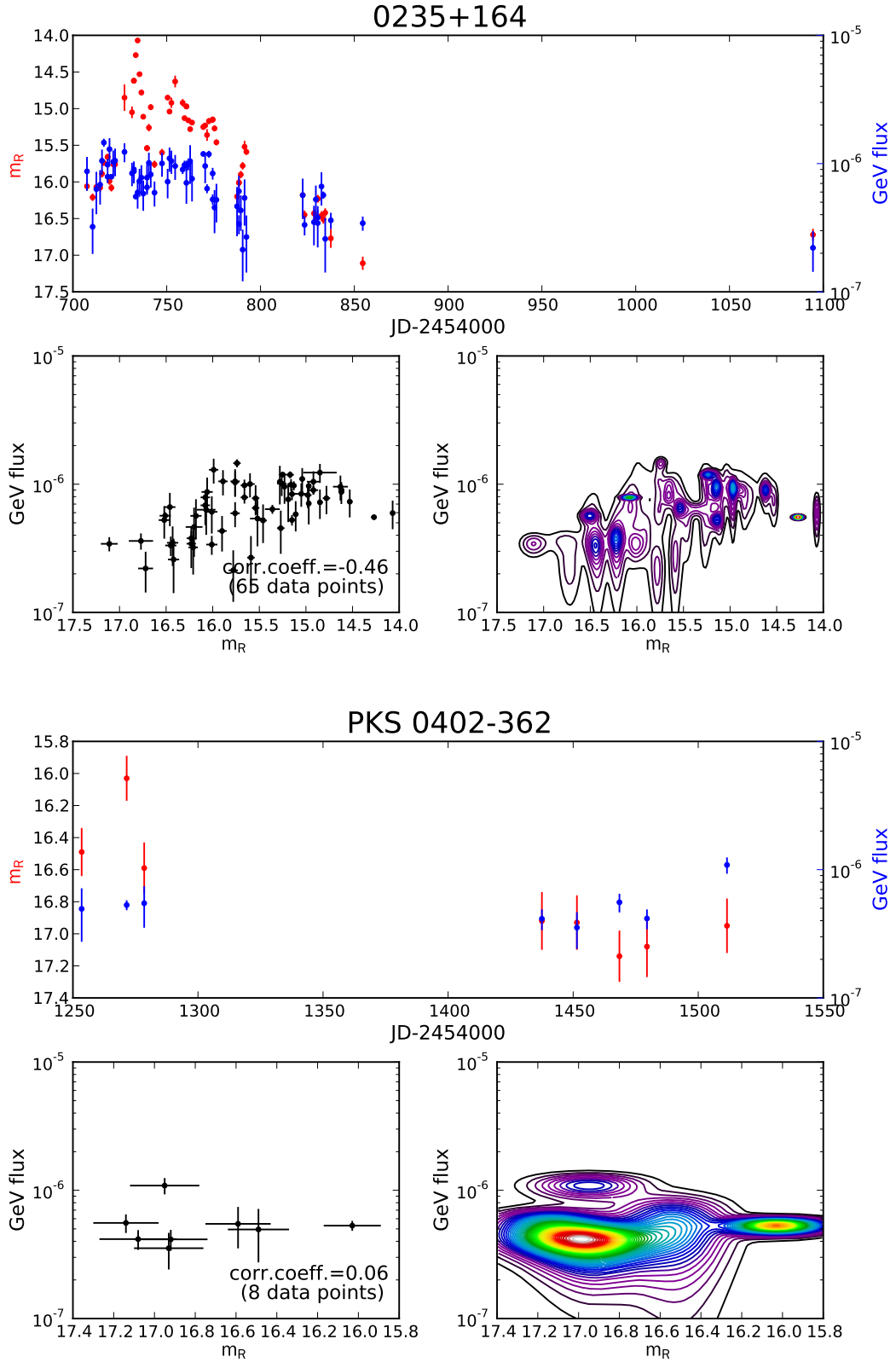

Figure B.2.: Corr. optical / γ-ray flux: 0235+164 and PKS 0402-362

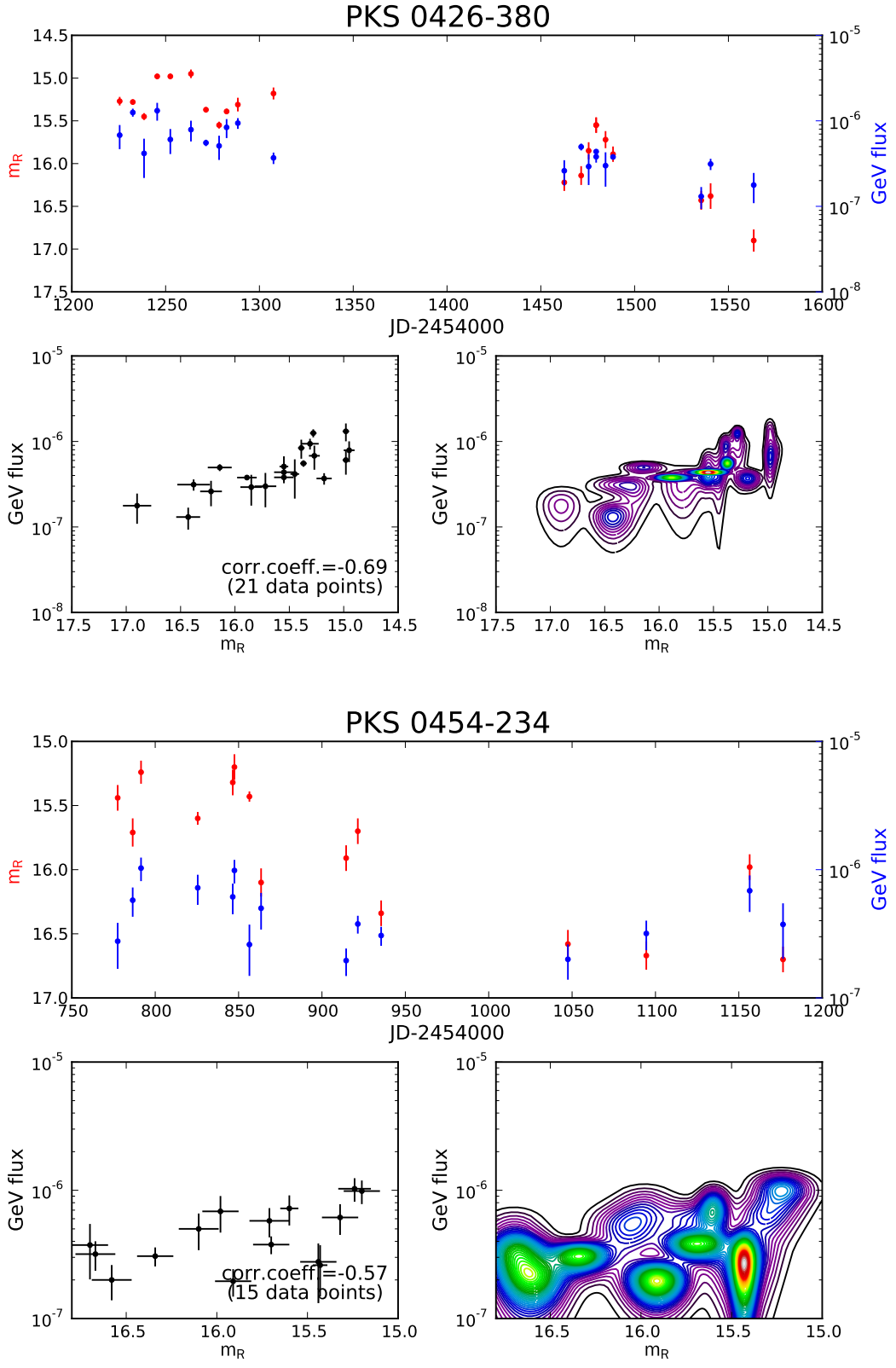

Figure B.3.: Corr. optical / γ-ray flux: PKS 0426-380 and PKS 0454-234

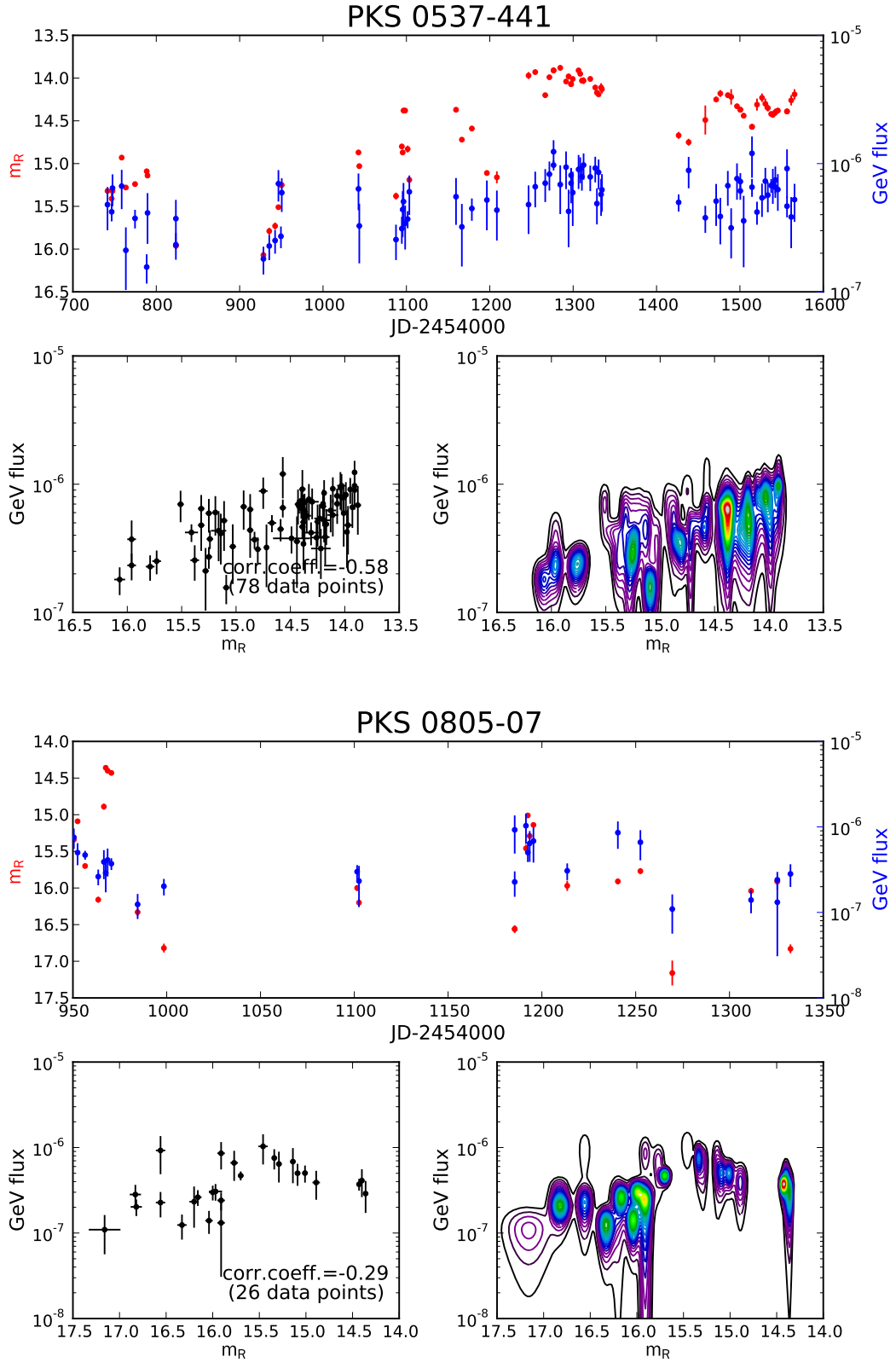

Figure B.4.: Corr. optical / γ-ray flux: PKS 0537-441 and PKS 0805-07

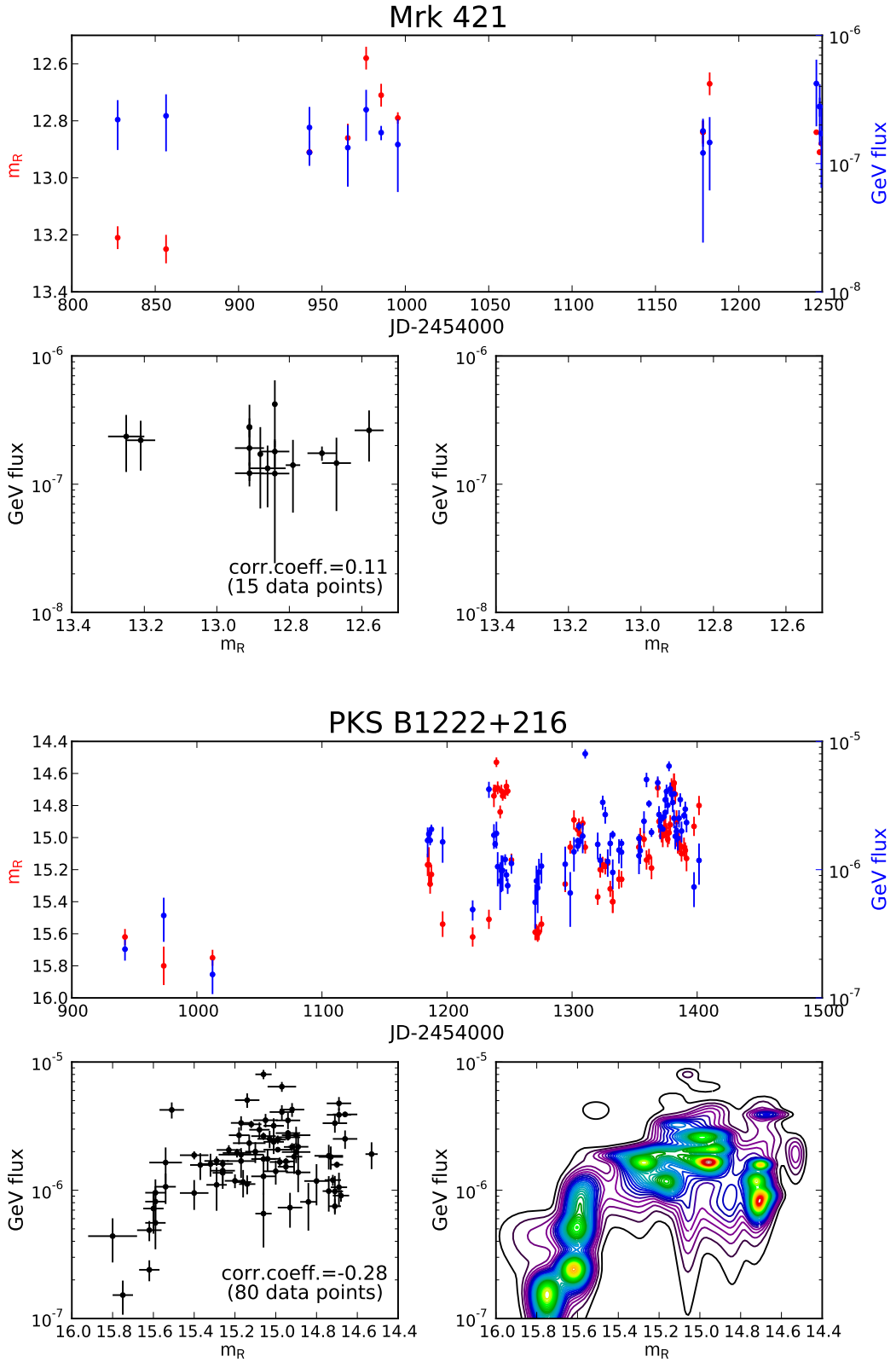

Figure B.5.: Corr. optical / γ-ray flux: Mrk 421 and PKS 1222+216

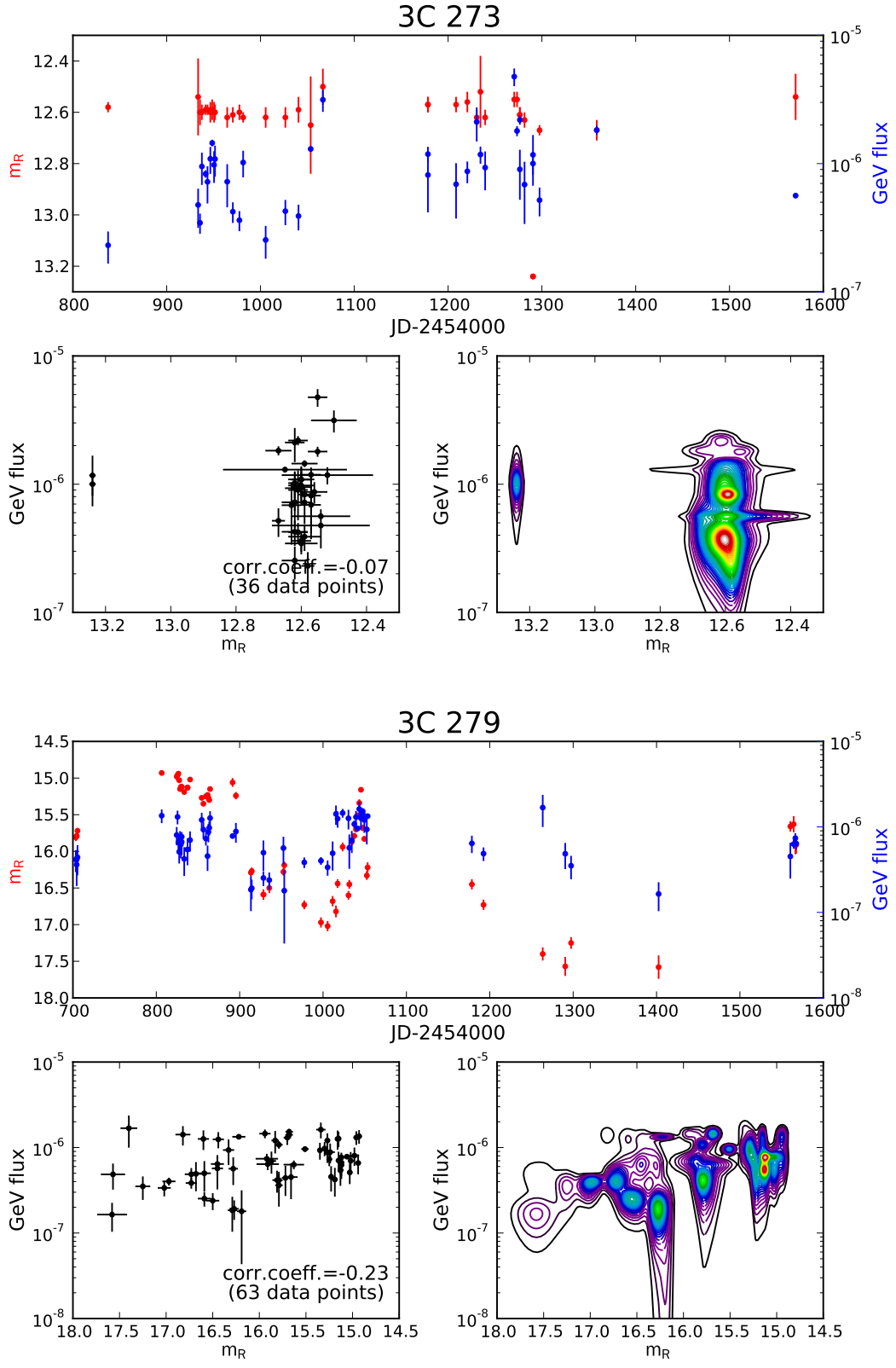

Figure B.6.: Corr. optical / γ-ray flux: 3C 273 and 3C 279

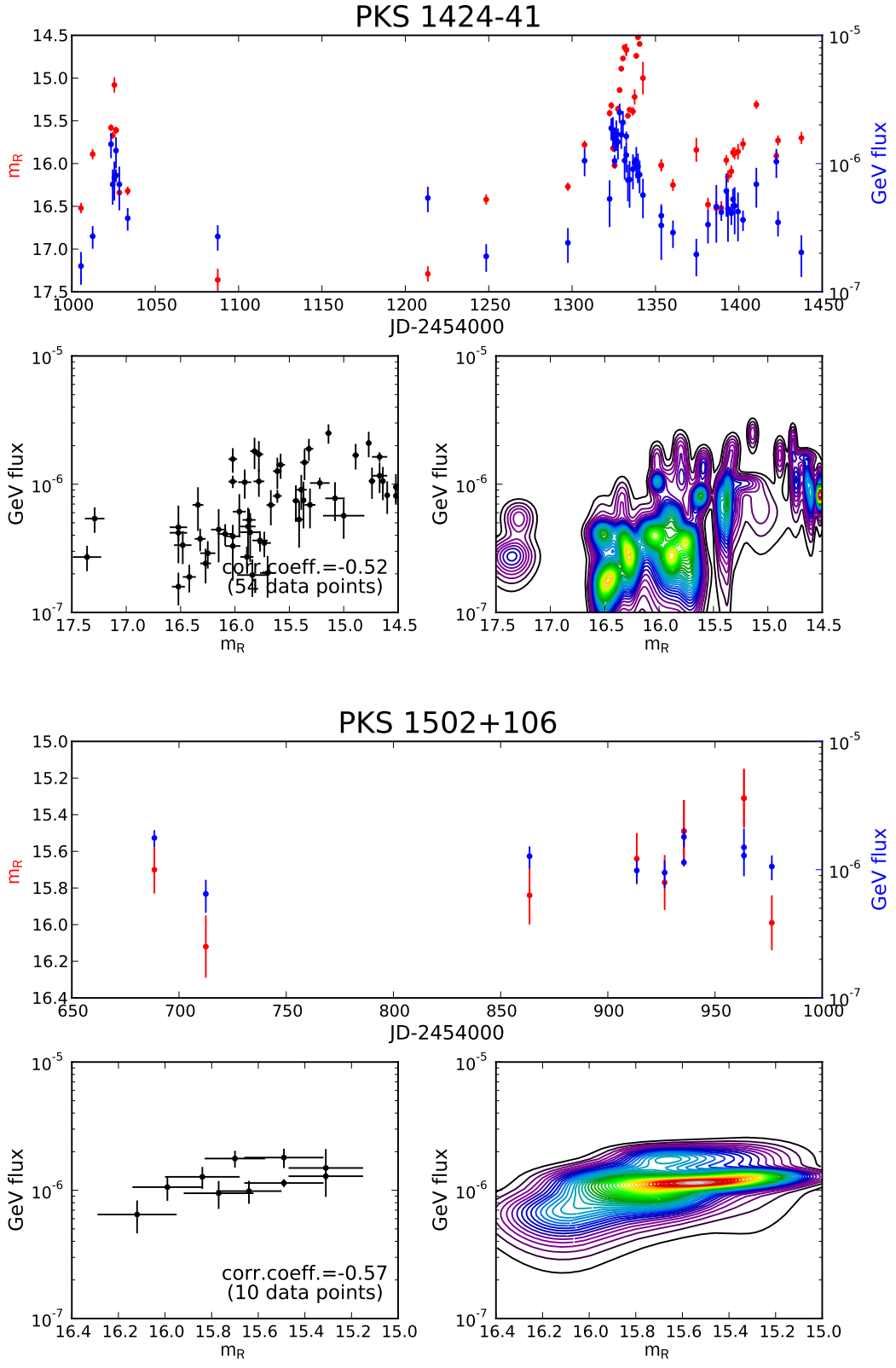

Figure B.7.: Corr. optical / γ-ray flux: PKS 1424-41 and PKS 1502+106

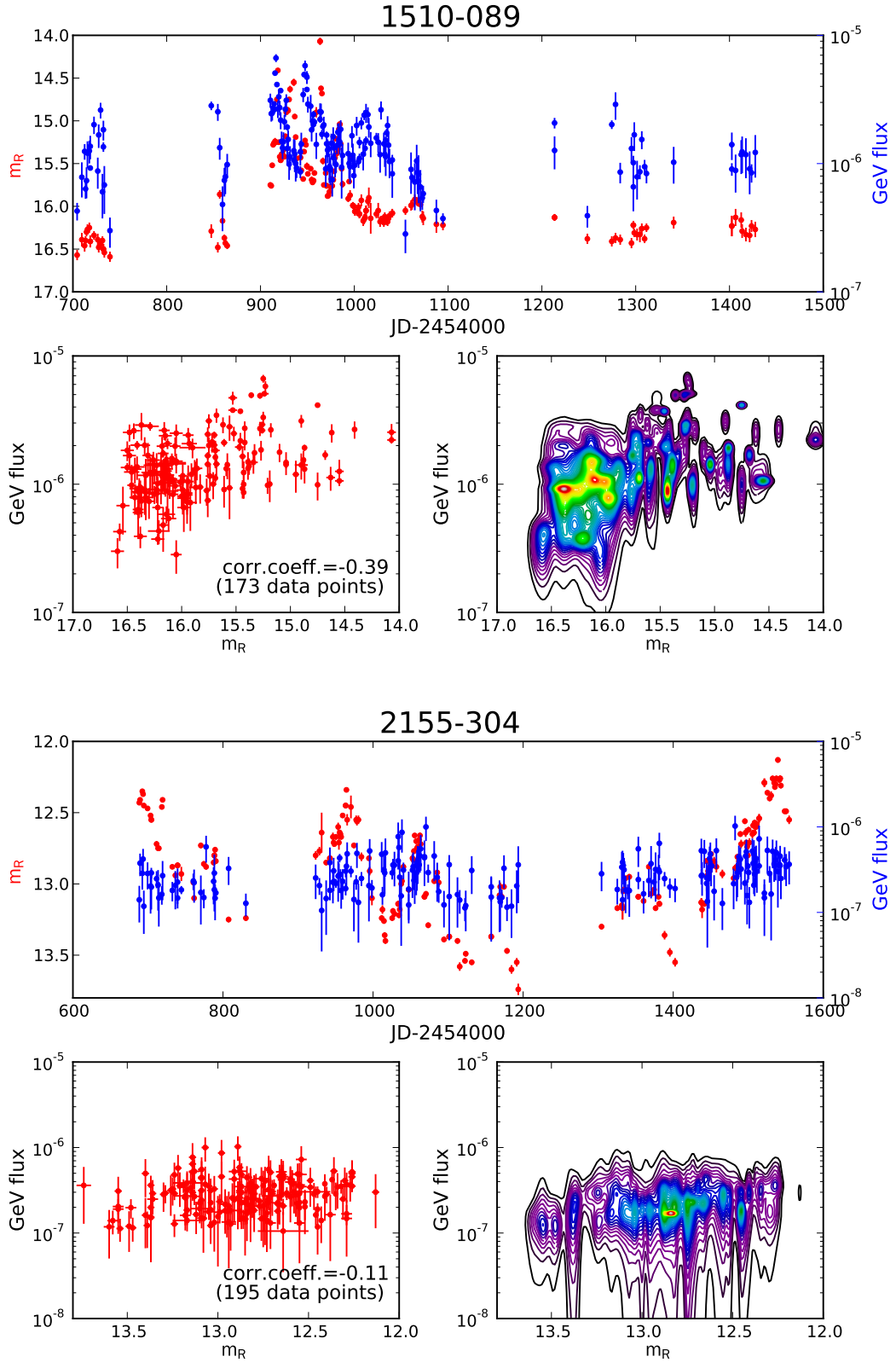

Figure B.8.: Corr. optical / γ-ray flux: PKS 1510-089 and PKS 2155-304

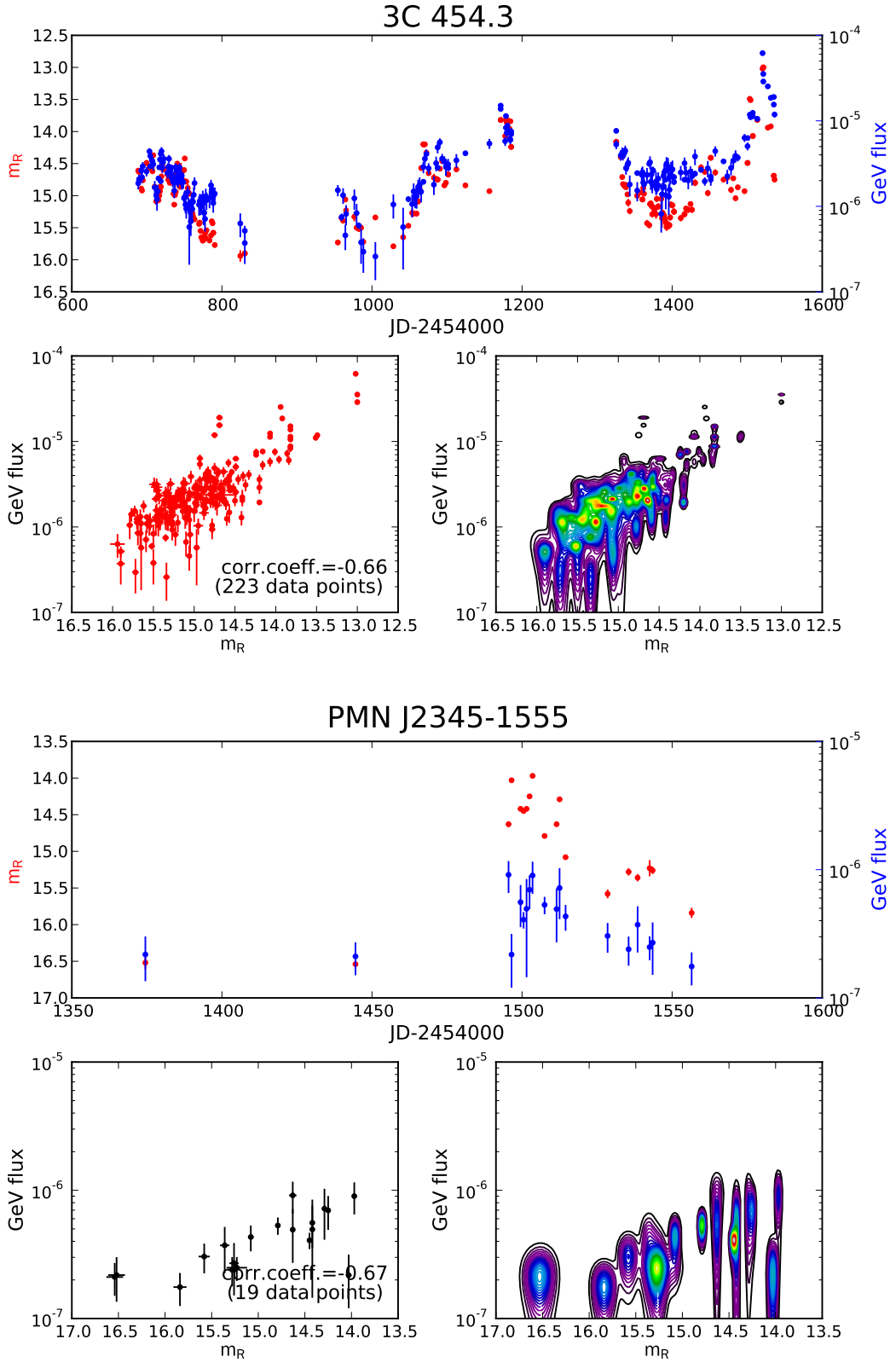

Figure B.9.: Corr. optical / γ-ray flux: 3C 454.3 and PMN J2345-1555

C. Monitoring of planetary occultations with ATOM/ external usage

Besides AGN monitoring, there were several occasions where ATOM was used to observe transients of *Trans-Neptunian Objects* (TNO), small objects orbiting the Sun around or behind the orbit of Neptune (at distances of $\gtrapprox 30$ AU). The method used for this kind of studies is to observe the occultation of a star by a TNO crossing the line of sight to it. Time-resolved observation of such an occultation allows to put really tight constrains on the orbital parameters of that TNO (the shadow of the occultation on earth is only a few 10 km wide), provide measurements of the radius on km accuracy as well as on its shape (spherically symmetric or not) and to detect a possible faint atmosphere around that object.

None of these investigations were part of this thesis, my contribution was to perform and analyze the observations which were done using the full ATOM equipment (kind of *service mode* operation) and provide a lightcurve for further analysis by the experts on TNO science. But it was a nice prove that ATOM has evolved to a stable and user-friendly system which can be used without expert knowledge.

In the two cases where ATOM was made available for external observers coming to the site and mounting their own camera (kind of extended *visitor mode* operation), my contribution was limited to technical support via telephone and email.

ATOM did observe four of these events, which will be briefly presented in the following:

C.1. Varuna stellar occultation in December 2008

A request for observations of a stellar occultation of the TNO *Varuna* in December 2008 was submitted by Bruno Sicardy (Observatoire de Paris) to the ATOM team. Since the request was to increase the time resolution as much as possible, only a small read-out window of 200x200 pixels (corresponding to 1.5x1.5 arcmin on the sky) was chosen for the CCD to minimize dead-time between the exposures[1].
Unfortunately, no observations were possible due to heavy rain on site.

C.2. Pluto stellar occultation in April 2009

In April 2009, the telescope was provided to A. Gulbis (MIT) for occultation observations of Pluto. Since they were going to be on site, operating the telescope on their own and using their own high-speed camera (Andor iXon, the same device we had tested for

[1] The dead-time for camera read-out is 8.5 s for 1000x1000 pixels and 2.3 s for 200x200. Reducing the read-out window more does not reduce the dead time significantly: for 100x100 it is still 2.3 s and goes down to 1.8 s for only 1 pixel read-out.

ATOM (sec. 3.2)), this was a good test to see if ATOM is a) stable and user-friendly enough and b) documented well enough to be used by non-experts of this facility.

No technical problems occurred, but clouds came in shortly before the predicted occultation, so no usable observations could be taken.

C.3. Varuna stellar occultation in February 2010

A similar request for observations of Varuna as in December 2008 was issued again by B. Sicary for the predicted occultation of star `UCAC2 410140042` by Varuna on Feb, 19 2010 around 23:05 UTC. A setup similar to the Dec '08 attempt was chosen for ATOM (small CCD read-out region, no filter in light path). The removal of the filter glass from the light path alters of course the optical light path of the telescope, moving the focal plane further down.

Having the instrumental setup of ATOM as described in sec. 2.3 in mind, it is clear that a) the autoguider camera is now completely out of focus and thus not usable and b) therefore also the automatic focussing as described in sec. 4.4 does not work. Because of that, I controlled the telescope remotely from Heidelberg for this observing run, taking care of re-focussing the telescope and correcting the telescope tracking manually.

Unlike last time, the weather permitted observations. The requested start of observations 15 min before the predicted occultation could not be achieved because of a power-cut on site shortly before the observing window. ATOM could be brought back into operation 7 min before the predicted occultation time, and observation went flawless.

No occultation was detected in the ATOM data. Also the observations being performed at Hakos (about 50 km away from the H.E.S.S. site) did not reveal any occultation. The event was detected by 2 stations in Brazil on the predicted shadow path. One reported an occultation duration of 52.5 ± 0.5 s which corresponds to a chord length of 1003 ± 9 km projected on the plane of the sky. The non-detection of Varuna by ATOM and the other stations in Namibia and South Africa requires a significantly elongated shape for this TNO (Sicardy et al. (2010)).

C.4. Pluto stellar occultation in July 2010

In July 2010, ATOM was again used by external observers with an own camera. No technical problems occurred, and the weather was fine as expected for July in Namibia. Our guests did gather useful data which is published in Person et al. (2010).

D. Extinction

Supplement to sec. 6.1.1, result summary in tab. 6.4.

D.1. Data from 2007

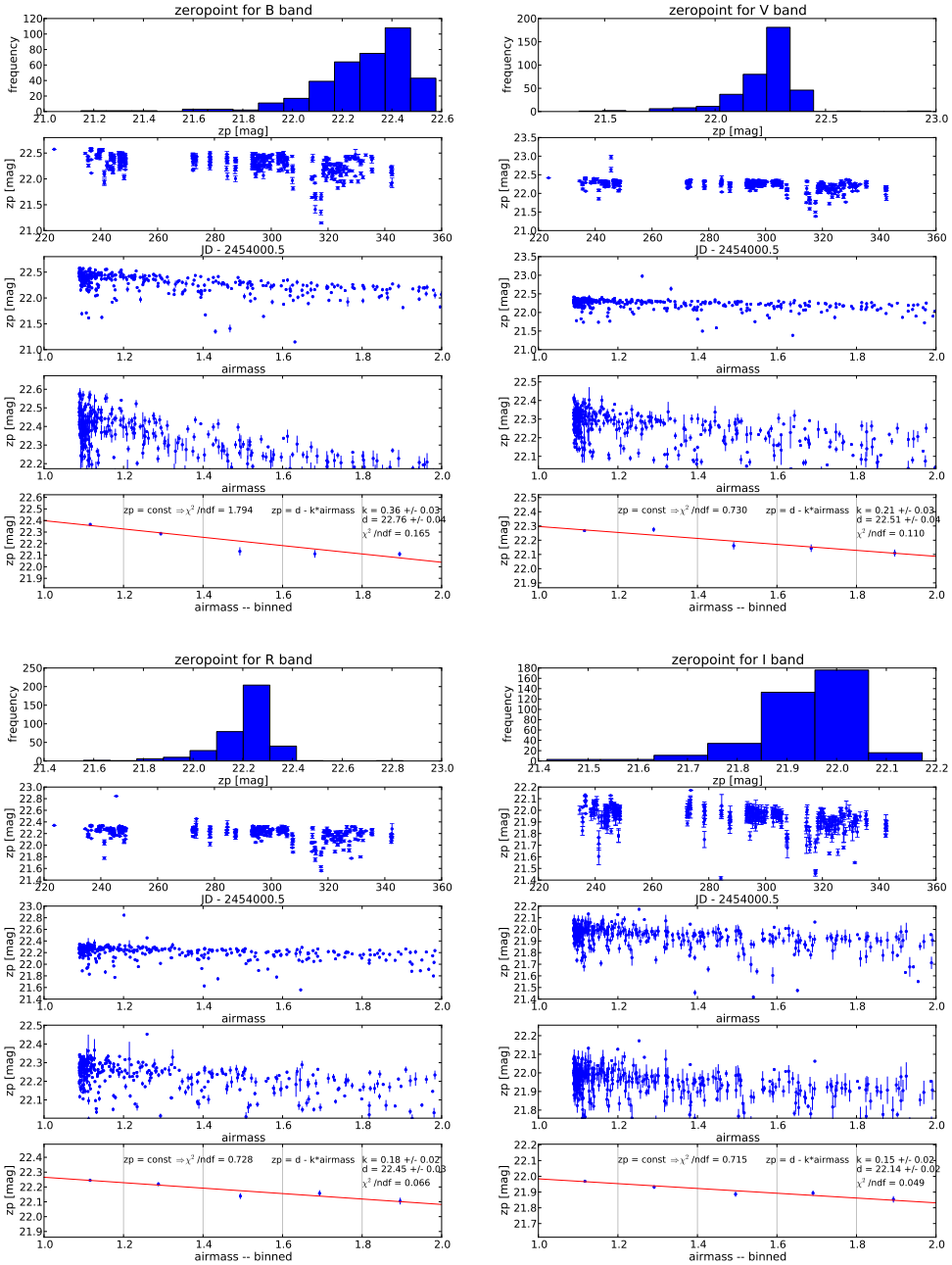

Figure D.1.: Instrumental zeropoints in 2007

D.2. Data from 2008

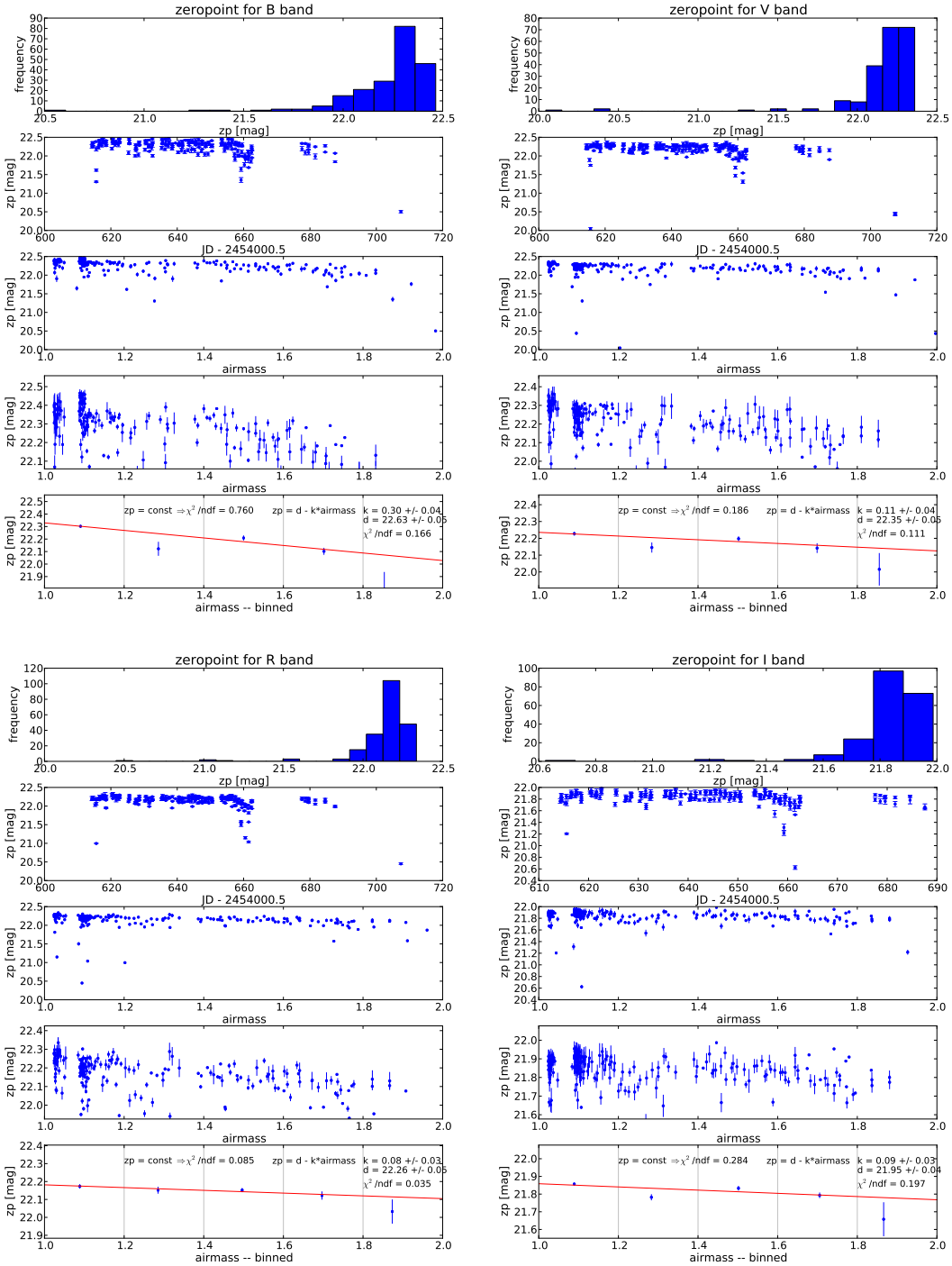

Figure D.2.: Instrumental zeropoints in 2008

D.3. Data from 2009

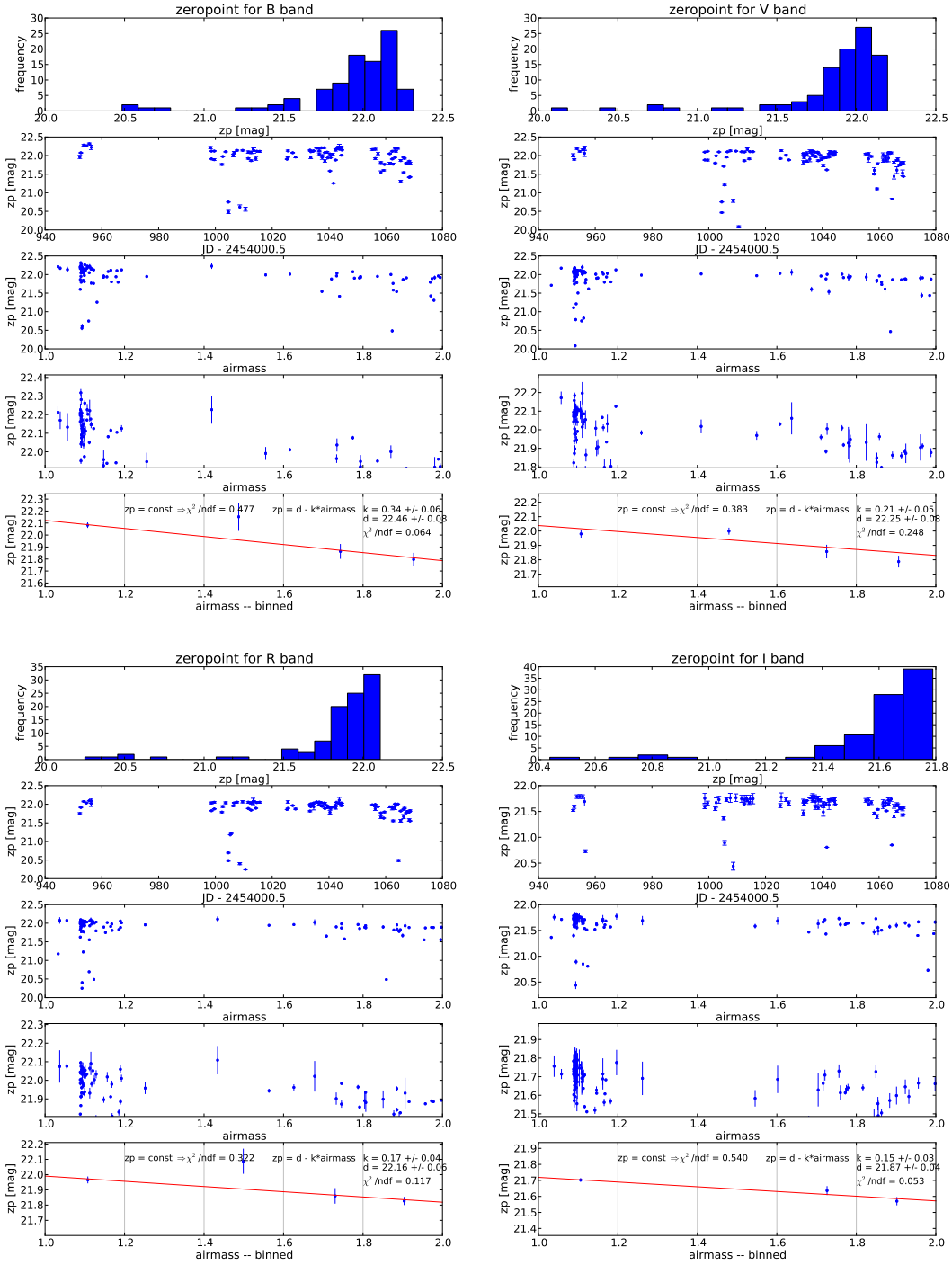

Figure D.3.: Instrumental zeropoints in 2009

D.4. Data from 2010

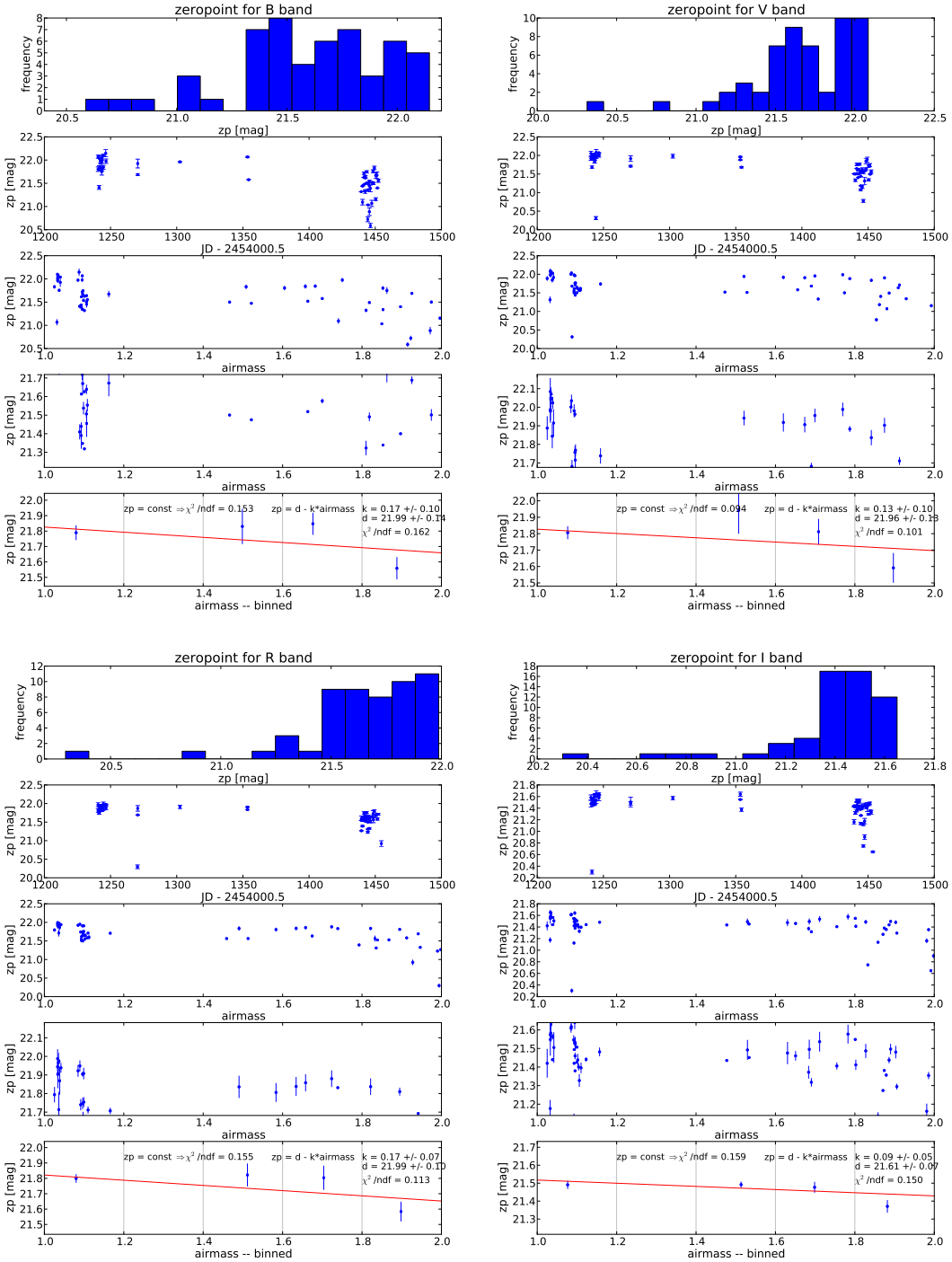

Figure D.4.: Instrumental zeropoints in 2010

E. List of monitored targets

Table E.1 presents all monitoring targets of ATOM as of February 2011. The different columns are giving the name, position of the source, the date when the source entered the monitoring program, the desired observing frequency in days and the number of observations perforemed up to now (separated by filters and in total).
The list is ordered by Right Ascention.

Name	α_{2000}	δ_{2000}	Obs. since	freq.	number of observations				
					B	V	R	I	total
QSO B0007+106	$00^h10^m31.0^s$	$+10°58'29"$	Jun 07	0.30	245	79	305	87	**716**
SHBL J001355.9-185406	$00^h13^m56.0^s$	$-18°54'06"$	Jun 08	0.30	119	2	173	2	**296**
SHBL J001827.8+294729	$00^h18^m27.9^s$	$+29°47'29"$	Jun 08	0.33	0	0	80	0	**80**
SHBL J003334.2-192133	$00^h33^m34.3^s$	$-19°21'33"$	Jan 08	0.30	8	0	104	0	**112**
3C 15	$00^h37^m4.1^s$	$-01°09'07"$	Dec 07	0.10	38	6	43	6	**93**
PKS 0048-097	$00^h50^m41.3^s$	$-09°29'04"$	Aug 09	0.30	65	0	86	0	**151**
PKS 0048-071	$00^h51^m8.2^s$	$-06°50'02"$	Aug 09	0.10	2	0	30	0	**32**
NGC 315	$00^h57^m49.0^s$	$+30°21'08"$	None	0.03	0	0	0	0	**0**
RGB J0109+182	$01^h09^m8.2^s$	$+18°16'08"$	Sep 09	0.30	0	0	73	0	**73**
SHBL J011050.0-125502	$01^h10^m50.0^s$	$-12°55'01"$	Sep 08	0.20	0	0	92	0	**92**
S2 0109+22	$01^h12^m5.8^s$	$+22°44'38"$	Aug 09	0.30	2	0	51	0	**53**
4C 31.03	$01^h12^m50.3^s$	$+32°08'17"$	Jun 09	0.10	25	0	41	0	**66**
PKS 0116-219	$01^h18^m57.3^s$	$-21°41'30"$	Aug 09	0.01	0	0	4	0	**4**
PKS 0118-272	$01^h20^m31.7^s$	$-27°01'24"$	Aug 09	0.30	1	0	58	0	**59**
3EG J0118+0248	$01^h21^m56.9^s$	$+04°22'24"$	Jul 08	0.10	0	0	15	0	**15**
3EG J0130-1758	$01^h32^m43.5^s$	$-16°54'48"$	Aug 08	0.10	2	0	51	0	**53**
TXS 0141+268	$01^h44^m33.0^s$	$+27°05'30"$	Aug 09	0.05	0	0	8	0	**8**
PKS 0142-278	$01^h45^m3.3^s$	$-27°33'34"$	Aug 09	0.30	0	0	62	0	**62**
RGB J0152+017	$01^h52^m39.6^s$	$+01°47'17"$	Nov 07	0.30	355	101	498	97	**1051**
PKS 0202+149	$02^h04^m50.4^s$	$+15°14'11"$	Jul 08	0.02	0	0	29	0	**29**
PKS 0202-17	$02^h04^m57.7^s$	$-17°01'19"$	Aug 09	0.30	2	0	62	0	**64**
PKS 0208-512	$02^h10^m46.2^s$	$-51°01'01"$	Jul 08	0.30	131	2	167	2	**302**
SHBL J021630.9+231513	$02^h16^m31.0^s$	$+23°15'12"$	Jul 08	0.33	0	0	58	0	**58**
PKS 0215+015	$02^h17^m48.9^s$	$+01°44'49"$	Aug 09	0.20	0	0	52	0	**52**
3C 66A	$02^h22^m39.6^s$	$+43°02'07"$	Oct 08	0.50	29	0	30	0	**59**
SHBL J022716.6+020158	$02^h27^m16.7^s$	$+02°01'58"$	Jul 08	0.33	0	0	77	0	**77**
PKS 0227-369	$02^h29^m28.5^s$	$-36°43'56"$	Aug 09	0.20	0	0	50	0	**50**
NVSS J023031+211411	$02^h30^m29.5^s$	$+21°12'44"$	Aug 08	0.08	0	0	21	0	**21**
1ES 0229+200	$02^h32^m48.6^s$	$+20°17'17"$	Nov 06	0.30	193	62	252	68	**575**
PKS 0235-618	$02^h36^m53.2^s$	$-61°36'15"$	Jun 10	0.20	0	0	40	0	**40**
3EG J0239+2815	$02^h37^m52.4^s$	$+28°48'08"$	Jul 08	0.10	0	0	21	0	**21**
AO 0235+16	$02^h38^m38.9^s$	$+16°36'59"$	Jan 07	0.20	153	68	231	68	**520**
PKS 0244-470	$02^h46^m0.0^s$	$-46°51'17"$	Aug 09	0.20	0	0	59	0	**59**
PKS 0250-225	$02^h52^m47.9^s$	$-22°19'25"$	Aug 09	0.10	7	0	19	0	**26**
PKS 0301-243	$03^h03^m26.5^s$	$-24°07'11"$	Aug 09	0.30	89	0	117	0	**206**
SHBL J030330.2+055430	$03^h03^m30.3^s$	$+05°54'29"$	Jul 08	0.33	37	0	61	0	**98**
NGC 1218	$03^h08^m26.0^s$	$+04°06'38"$	None	0.03	0	0	0	0	**0**
RBS 413	$03^h19^m51.8^s$	$+18°45'33"$	Sep 10	0.25	0	0	23	0	**23**
SHBL J031951.9+184534	$03^h19^m51.8^s$	$+18°45'34"$	Jul 08	0.33	32	0	52	0	**84**

Name	α_{2000}	δ_{2000}	Obs. since	freq.	number of observations				
					B	V	R	I	total
Fornax A	$03^h22^m41.0^s$	$-37°12'29"$	None	0.03	0	0	0	0	**0**
SHBL J032541.0-164618	$03^h25^m41.1^s$	$-16°46'18"$	Jul 08	0.30	40	2	86	2	**130**
1ES 0323+022	$03^h26^m14.0^s$	$+02°25'14"$	Jul 08	0.33	42	0	65	0	**107**
PKS 0332-403	$03^h34^m13.6^s$	$-40°08'25"$	Aug 09	0.30	2	0	60	0	**62**
3EG J0340-0201	$03^h39^m30.9^s$	$-01°46'35"$	Jul 08	0.14	0	0	56	0	**56**
1ES 0347-121	$03^h49^m23.0^s$	$-11°59'26"$	Nov 06	0.30	229	70	314	97	**710**
PKS 0347-211	$03^h49^m57.8^s$	$-21°02'47"$	Aug 09	0.10	0	0	25	0	**25**
PKS 0352-686	$03^h52^m57.6^s$	$-68°31'16"$	Sep 10	0.30	36	0	54	0	**90**
3C 98	$03^h58^m54.4^s$	$+10°26'03"$	Aug 08	0.20	6	0	18	0	**24**
PKS 0402-362	$04^h03^m53.7^s$	$-36°05'01"$	Feb 10	0.30	24	0	47	0	**71**
PKS 0405-385	$04^h06^m59.0^s$	$-38°26'28"$	Aug 09	0.30	1	0	64	0	**65**
PKS 0414-189	$04^h16^m36.5^s$	$-18°51'08"$	Mar 10	0.20	0	0	20	0	**20**
1ES 0414+00.9	$04^h16^m52.5^s$	$+01°05'23"$	Nov 06	1.00	326	95	377	90	**888**
3EG J0416+3650	$04^h18^m21.3^s$	$+38°01'35"$	Aug 08	0.30	0	0	11	0	**11**
PKS 0420-014	$04^h23^m15.8^s$	$-01°20'33"$	Jul 08	0.30	0	0	64	0	**64**
PKS 0426-380	$04^h28^m40.4^s$	$-37°56'19"$	Aug 09	0.30	2	0	64	0	**66**
3C 120	$04^h33^m11.1^s$	$+05°21'15"$	Dec 07	0.10	30	17	37	17	**101**
3EG J0433+2908	$04^h33^m37.8^s$	$+29°05'55"$	Sep 08	0.14	0	0	27	0	**27**
SHBL J044127.4+150456	$04^h41^m27.5^s$	$+15°04'55"$	Mar 08	0.10	0	0	49	0	**49**
PKS 0440-003	$04^h42^m38.7^s$	$-00°17'43"$	Jul 08	0.30	0	0	98	0	**98**
3EG J0450+1105	$04^h49^m7.7^s$	$+11°21'28"$	Jul 08	0.20	0	0	28	0	**28**
PKS 0447-439	$04^h49^m24.7^s$	$-43°50'08"$	Aug 09	0.30	51	0	109	0	**160**
3EG J0458-4635	$04^h55^m50.8^s$	$-46°15'58"$	Aug 08	0.30	9	0	23	0	**32**
PKS 0454-234	$04^h57^m3.2^s$	$-23°24'52"$	Aug 08	0.25	33	0	110	0	**143**
3EG J0500-0159	$05^h01^m12.8^s$	$-01°59'14"$	Aug 08	0.14	0	0	49	0	**49**
3EG J0459+0544	$05^h02^m15.5^s$	$+06°09'07"$	Aug 08	0.10	0	0	31	0	**31**
SHBL J050939.0-040036	$05^h09^m38.2^s$	$-04°00'46"$	Mar 08	0.33	0	0	58	0	**58**
3EG J0512-6150	$05^h16^m44.9^s$	$-62°07'05"$	Aug 08	0.10	0	0	4	0	**4**
Pic A	$05^h19^m50.0^s$	$-45°46'44"$	Nov 06	0.03	7	7	8	7	**29**
VER J0521+211	$05^h21^m46.0^s$	$+21°12'51"$	Oct 09	0.30	38	0	47	0	**85**
PKS 0521-365	$05^h22^m58.0^s$	$-36°27'30"$	Nov 07	1.00	229	23	265	23	**540**
PKS 0528+134	$05^h30^m56.4^s$	$+13°31'55"$	Aug 08	0.20	0	0	8	49	**57**
CRATES J0531-4927	$05^h31^m59.7^s$	$-48°27'19"$	Oct 10	0.30	0	0	21	0	**21**
PKS 0537-441	$05^h38^m50.4^s$	$-44°05'08"$	Aug 08	0.30	164	0	193	0	**357**
3EG J0531-2940	$05^h39^m54.3^s$	$-28°39'55"$	Aug 08	0.10	0	0	41	0	**41**
3EG J0542-0655	$05^h41^m38.1^s$	$-05°41'49"$	Aug 08	0.10	0	0	37	0	**37**
PKS 0548-322	$05^h50^m40.6^s$	$-32°16'17"$	Nov 06	0.30	165	69	197	69	**500**
PKS 0558-504	$05^h59^m46.6^s$	$-50°26'36"$	May 07	0.10	52	52	225	52	**381**
3EG J0616-3310	$06^h16^m36.0^s$	$-33°10'12"$	Jan 09	0.10	12	0	23	0	**35**
3EG J0622-1139	$06^h19^m3.7^s$	$-11°40'50"$	Aug 08	0.05	0	0	31	0	**31**
RGB J0648+152	$06^h48^m47.6^s$	$+15°16'24"$	Mar 10	0.30	0	0	14	0	**14**
PKS 0700-661	$07^h00^m31.2^s$	$-66°10'45"$	Aug 09	0.30	2	0	77	0	**79**
MG2 J071354+1934	$07^h13^m55.7^s$	$+19°34'59"$	Sep 09	0.05	0	0	16	0	**16**
PKS 0727-115	$07^h30^m19.1^s$	$-11°41'12"$	Jul 08	0.14	0	0	41	0	**41**
PKS 0735+178	$07^h38^m7.4^s$	$+17°42'19"$	Jan 08	0.33	114	2	133	2	**251**
PKS 0805-077	$08^h08^m15.5^s$	$-07°51'09"$	Sep 08	0.30	131	0	194	0	**325**
PKS 0823-223	$08^h26^m1.6^s$	$-22°30'27"$	Sep 09	0.01	0	0	9	0	**9**
3EG J0829+2413	$08^h30^m52.1^s$	$+24°10'59"$	Oct 08	0.14	27	0	39	0	**66**
PKS 0829+046	$08^h31^m48.9^s$	$+04°29'39"$	Mar 08	0.33	140	1	172	1	**314**
RGB J0847+115	$08^h47^m12.9^s$	$+11°33'50"$	Mar 08	0.20	51	0	69	0	**120**
3EG J0852-1216	$08^h50^m9.6^s$	$-12°13'35"$	Mar 08	0.30	148	0	208	0	**356**
OJ 287	$08^h54^m49.0^s$	$+20°06'30"$	Nov 06	0.33	195	68	205	62	**530**
3EG J0903-3531	$09^h05^m0.0^s$	$-35°27'00"$	Sep 08	0.10	2	1	12	1	**16**
PKS 0907+022	$09^h09^m39.9^s$	$+02°00'05"$	Oct 09	0.01	1	0	6	0	**7**

Name	α_{2000}	δ_{2000}	Obs. since	freq.	number of observations				
					B	V	R	I	total
0FGL J0910-5041	$09^h10^m45.6^s$	$-50°44'24"$	Oct 08	0.10	1	0	7	0	**8**
3C 218	$09^h18^m5.7^s$	$-12°05'44"$	Dec 07	0.10	24	18	62	18	**122**
PMN J0948+0022	$09^h48^m57.3^s$	$+00°22'26"$	Mar 09	0.30	47	0	69	0	**116**
SHBL J101015.9-311908	$10^h10^m16.0^s$	$-31°19'08"$	Feb 08	0.33	39	1	83	1	**124**
0FGL J1012.9+2435	$10^h12^m40.3^s$	$+24°39'03"$	Nov 09	0.01	0	0	6	0	**6**
PMN J1016+05	$10^h16^m3.1^s$	$+05°13'02"$	Nov 09	0.01	0	0	6	0	**6**
0FGL J1054.5+2212	$10^h54^m30.4^s$	$+22°10'54"$	Nov 09	0.01	0	0	6	0	**6**
FGST J1057-6027	$10^h57^m13.9^s$	$-60°27'28"$	Jun 09	0.20	0	0	12	0	**12**
PKS 1055+018	$10^h58^m29.6^s$	$+01°33'58"$	Nov 09	0.01	0	0	5	0	**5**
PKS 1057-79	$10^h58^m43.3^s$	$-80°03'54"$	Aug 09	0.30	0	0	69	0	**69**
1ES 1101-232	$11^h03^m37.6^s$	$-23°29'30"$	Feb 07	0.20	294	153	327	116	**890**
Mrk 421	$11^h04^m27.5^s$	$+38°12'31"$	May 07	0.33	82	37	278	36	**433**
PKS 1118-056	$11^h21^m25.1^s$	$-05°53'56"$	Mar 09	0.14	24	0	54	0	**78**
PKS 1127-14	$11^h30^m7.1^s$	$-14°49'27"$	Nov 09	0.01	0	0	5	0	**5**
PKS 1144-379	$11^h47^m1.4^s$	$-38°12'11"$	Nov 09	0.01	0	0	5	0	**5**
3EG J1200+2847	$11^h59^m31.8^s$	$+29°14'43"$	Dec 08	0.14	0	0	22	0	**22**
PKS 1215+303	$12^h17^m52.1^s$	$+30°07'00"$	Dec 08	0.10	40	0	44	0	**84**
3C 270	$12^h19^m23.0^s$	$+05°49'31"$	Dec 08	0.10	6	0	147	0	**153**
1ES 1218+304	$12^h21^m21.9^s$	$+30°10'36"$	Mar 09	0.30	30	0	40	0	**70**
W Comae	$12^h21^m31.7^s$	$+28°13'58"$	Jun 08	0.30	73	9	103	8	**193**
PKS 1222+216	$12^h24^m54.5^s$	$+21°22'45"$	Jul 08	0.30	150	0	190	0	**340**
M84	$12^h25^m3.0^s$	$+12°53'12"$	Feb 08	0.03	1	1	1	1	**4**
3C 273	$12^h29^m6.7^s$	$+02°03'08"$	Jan 07	0.20	248	62	273	61	**644**
RGB J1230+253	$12^h30^m14.1^s$	$+25°18'06"$	Feb 08	0.33	45	1	67	1	**114**
M87	$12^h30^m49.0^s$	$+12°23'27"$	None	0.03	0	0	0	0	**0**
3EG J1230-0247	$12^h32^m0.0^s$	$-02°24'04"$	Jul 08	0.10	0	0	51	0	**51**
3EG J1236+0457	$12^h39^m32.8^s$	$+04°43'05"$	Jul 08	0.20	46	1	121	1	**169**
3EG J1246-0651	$12^h46^m4.2^s$	$-07°30'46"$	Jul 08	0.10	0	0	50	0	**50**
PKS 1244-255	$12^h46^m46.8^s$	$-25°47'48"$	Jan 09	0.30	89	0	151	0	**240**
SHBL J125341.1-393159	$12^h53^m41.2^s$	$-39°31'59"$	Mar 08	0.33	0	0	84	0	**84**
3C 278	$12^h54^m36.0^s$	$-12°33'47"$	Feb 08	0.10	8	1	8	1	**18**
3C 279	$12^h56^m11.2^s$	$-05°47'21"$	May 07	0.30	277	54	320	41	**692**
SHBL J125731.9+241240	$12^h57^m32.0^s$	$+24°12'39"$	Mar 08	0.33	0	0	70	0	**70**
NGC 4874	$12^h59^m36.0^s$	$+27°57'33"$	None	0.03	0	0	0	0	**0**
B2 1308+32	$13^h10^m28.7^s$	$+32°20'43"$	Jan 10	0.10	0	0	10	0	**10**
1ES 1312-423	$13^h15^m3.4^s$	$-42°36'50"$	Mar 08	0.33	88	1	145	1	**235**
3EG J1314-3431	$13^h16^m8.0^s$	$-33°38'59"$	Jul 08	0.10	0	0	51	0	**51**
Cen A	$13^h25^m27.6^s$	$-43°01'08"$	May 07	0.33	8	8	8	8	**32**
3EG J1323+2200	$13^h27^m0.9^s$	$+22°10'50"$	Jul 08	0.10	0	0	35	0	**35**
PKS 1329-049	$13^h32^m4.4^s$	$-05°09'43"$	Aug 09	0.30	0	0	68	0	**68**
3EG J1329+1708	$13^h33^m35.8^s$	$+16°49'04"$	Jul 08	0.10	0	0	10	0	**10**
PKS 1334-127	$13^h37^m39.8^s$	$-12°57'24"$	Mar 08	0.25	34	0	182	0	**216**
PKS 1352-104	$13^h54^m46.5^s$	$-10°41'02"$	Aug 09	0.30	0	0	57	0	**57**
PKS 1406-076	$14^h08^m56.5^s$	$-07°52'26"$	May 07	0.14	25	26	97	26	**174**
3C 296	$14^h16^m52.0^s$	$+10°48'25"$	None	0.03	0	0	0	0	**0**
PKS 1424+240	$14^h27^m0.4^s$	$+23°48'00"$	Jun 09	0.30	84	0	91	0	**175**
PKS 1424-418	$14^h27^m56.3^s$	$-42°06'19"$	Jul 08	0.30	173	3	246	24	**446**
H 1426+428	$14^h28^m32.6^s$	$+42°40'20"$	Aug 09	0.30	0	0	4	0	**4**
SHBL J143917.4+393243	$14^h39^m17.5^s$	$+39°32'43"$	Jun 08	0.33	0	0	29	0	**29**
1ES 1440+122	$14^h42^m48.3^s$	$+12°00'39"$	May 08	0.30	73	0	132	0	**205**
PKS 1454-354	$14^h57^m26.7^s$	$-35°39'09"$	Sep 08	0.30	126	0	168	1	**295**
PKS 1502+106	$15^h04^m25.0^s$	$+10°29'39"$	Aug 08	0.30	19	0	24	0	**43**
PKS 1508-05	$15^h10^m53.6^s$	$-05°43'07"$	Aug 09	0.30	0	0	61	0	**61**
PKS 1510-089	$15^h12^m50.5^s$	$-09°05'58"$	May 07	0.30	285	84	518	112	**999**

Name	α_{2000}	δ_{2000}	Obs. since	freq.	number of observations				
					B	V	R	I	total
PKS 1510-319	$15^h13^m21.8^s$	$-32°09'33"$	Apr 10	0.30	10	0	19	0	**29**
PKS 1514-241	$15^h17^m41.8^s$	$-24°22'19"$	Jul 08	1.00	45	1	67	1	**114**
B2 1520+31	$15^h22^m10.0^s$	$+31°44'14"$	Apr 09	0.10	0	0	39	0	**39**
SHBL J153311.3+185428	$15^h33^m11.2^s$	$+18°54'28"$	May 08	0.33	0	0	97	0	**97**
PKS 1551+130	$15^h53^m32.7^s$	$+12°56'51"$	Aug 09	0.30	0	0	60	0	**60**
PG 1553+113	$15^h55^m43.0^s$	$+11°11'24"$	Aug 07	0.33	218	16	257	16	**507**
0FGL J1604.0-4904	$16^h04^m3.6^s$	$-49°04'47"$	Aug 09	0.05	0	0	19	0	**19**
PKS 1604+159	$16^h07^m6.6^s$	$+15°51'33"$	May 08	0.33	0	0	209	0	**209**
3EG J1608+1055	$16^h08^m46.2^s$	$+10°29'07"$	Jul 08	0.14	20	0	67	0	**87**
3EG J1614+3424	$16^h13^m41.1^s$	$+34°12'47"$	Jul 08	0.14	0	0	34	0	**34**
PKS 1622-253	$16^h25^m46.9^s$	$-25°27'38"$	May 07	0.08	21	21	115	22	**179**
PKS 1622-297	$16^h26^m6.0^s$	$-29°51'26"$	May 07	0.30	55	34	151	34	**274**
0FGL J1634.9-4737	$16^h34^m55.4^s$	$-47°37'48"$	Aug 09	0.30	0	0	71	0	**71**
3EG J1635+3813	$16^h35^m15.5^s$	$+38°08'04"$	Jul 08	0.30	0	0	13	0	**13**
3C 345	$16^h42^m58.8^s$	$+39°48'36"$	May 07	0.30	81	35	97	27	**240**
Mrk501	$16^h53^m52.1^s$	$+39°45'36"$	May 07	0.33	93	37	109	36	**275**
PKS 1717+177	$17^h19^m13.0^s$	$+17°45'06"$	Aug 09	0.30	0	0	64	0	**64**
3C 353	$17^h20^m28.2^s$	$-00°58'46"$	Jun 08	0.10	12	0	44	0	**56**
3EG J1720-7820	$17^h23^m55.7^s$	$-77°14'13"$	Jul 08	0.06	0	0	27	0	**27**
RGB J1725+118	$17^h25^m4.4^s$	$+11°52'14"$	May 08	0.30	52	0	116	0	**168**
PKS 1725+044	$17^h28^m24.9^s$	$+04°27'05"$	May 08	0.30	153	0	297	0	**450**
PKS 1730-130	$17^h33^m2.7^s$	$-13°04'49"$	Jul 08	0.14	0	0	84	0	**84**
1ES 1741+196	$17^h43^m58.0^s$	$+19°35'08"$	May 08	0.33	17	2	123	2	**144**
PKS 1741-038	$17^h43^m58.9^s$	$-03°50'04"$	Jul 08	0.14	0	0	89	0	**89**
0FGL J1746.0-2900	$17^h46^m1.4^s$	$-29°00'36"$	Aug 09	0.02	0	0	7	0	**7**
PKS 1749+096	$17^h51^m32.8^s$	$+09°39'00"$	Sep 08	0.14	44	1	48	1	**94**
3EG J1800-3955	$18^h02^m42.7^s$	$-39°40'07"$	Jul 08	0.10	0	0	14	0	**14**
3EG J1806-5005	$18^h08^m13.9^s$	$-50°11'53"$	Jul 08	0.15	0	0	90	0	**90**
3EG J1832-2110	$18^h33^m39.9^s$	$-21°03'39"$	Jul 08	0.30	2	0	52	0	**54**
TXS 1846+322	$18^h48^m22.1^s$	$+32°19'02"$	Aug 09	0.10	0	0	24	0	**24**
3EG J1911-2000	$19^h11^m9.6^s$	$-20°06'55"$	Jul 08	0.14	25	0	102	0	**127**
PKS 1915-458	$19^h19^m16.7^s$	$-45°43'38"$	Jun 10	0.20	0	0	41	0	**41**
3EG J1921-2015	$19^h23^m32.2^s$	$-21°04'33"$	Jul 08	0.30	94	3	131	3	**231**
3EG J1935-4022	$19^h37^m16.2^s$	$-39°58'01"$	Jul 08	0.10	0	0	14	0	**14**
PKS 1936-155	$19^h39^m26.7^s$	$-15°25'43"$	Jul 08	0.10	0	0	18	26	**44**
HESS J1943+213	$19^h43^m56.4^s$	$+21°18'18"$	Aug 10	0.25	0	0	9	1	**10**
PKS 2004-447	$20^h07^m57.2^s$	$-44°34'46"$	Jun 10	0.25	71	0	91	1	**163**
PKS 2005-489	$20^h09^m25.4^s$	$-48°49'53"$	Nov 06	1.00	865	477	922	483	**2747**
PKS 2022-077	$20^h25^m40.7^s$	$-07°35'52"$	Jul 08	0.30	20	0	44	0	**64**
PKS 2052-474	$20^h56^m16.4^s$	$-47°14'47"$	Jul 08	0.30	134	0	310	0	**444**
SHBL J213135.4-091523	$21^h31^m35.5^s$	$-09°15'23"$	Jun 08	0.30	91	3	151	3	**248**
SHBL J213852.5-205348	$21^h38^m52.6^s$	$-20°53'48"$	Jun 08	0.33	0	0	130	0	**130**
MH 2136-428	$21^h39^m24.1^s$	$-42°35'21"$	Aug 09	0.30	1	0	85	0	**86**
OX 169	$21^h43^m35.5^s$	$+17°43'48"$	Aug 09	0.30	1	0	67	0	**68**
PKS 2144+092	$21^h47^m10.2^s$	$+09°29'46"$	Aug 09	0.30	1	0	68	0	**69**
PKS 2142-758	$21^h47^m12.7^s$	$-75°36'13"$	Apr 10	0.30	0	0	64	0	**64**
PKS 2155-304	$21^h58^m52.0^s$	$-30°13'32"$	Nov 06	1.00	959	485	1045	486	**2975**
PKS 2155-83	$22^h02^m19.0^s$	$-83°38'12"$	Jan 10	0.20	0	0	22	0	**22**
BL Lacertae	$22^h02^m43.3^s$	$+42°16'39"$	Aug 08	0.30	77	2	87	2	**168**
PKS 2201+171	$22^h03^m26.9^s$	$+17°25'48"$	Aug 09	0.30	2	0	60	0	**62**
PKS 2204-54	$22^h07^m43.7^s$	$-53°46'33"$	Aug 09	0.30	1	0	73	0	**74**
3EG J2209+2401	$22^h12^m6.0^s$	$+23°55'40"$	Jul 08	0.10	0	0	78	0	**78**
3C 445	$22^h23^m49.5^s$	$-02°06'12"$	Jun 08	0.10	17	0	59	0	**76**
PHL 5225	$22^h29^m40.1^s$	$-08°32'54"$	Aug 09	0.30	0	0	65	0	**65**

Name	α_{2000}	δ_{2000}	Obs. since	freq.	number of observations				
					B	V	R	I	total
3EG J2232+1147	$22^h32^m36.4^s$	$+11°43'50"$	Jul 08	0.14	0	0	89	0	**89**
PKS 2233-148	$22^h36^m34.1^s$	$-14°33'22"$	May 10	0.30	0	0	54	0	**54**
3EG J2248+1745	$22^h48^m57.6^s$	$+17°46'11"$	Jun 09	0.10	0	0	3	0	**3**
PMN J2250-2806	$22^h50^m44.4^s$	$-28°06'39"$	Jun 09	0.10	32	0	76	0	**108**
3EG J2255+1943	$22^h53^m7.4^s$	$+19°42'34"$	Nov 06	0.30	298	127	351	125	**901**
3C 454.3	$22^h53^m57.8^s$	$+16°08'53"$	Dec 06	0.30	372	158	416	117	**1063**
B2 2308+34	$23^h11^m5.3^s$	$+34°25'10"$	Aug 10	0.30	0	0	19	0	**19**
3EG J2321-0328	$23^h23^m31.9^s$	$-03°17'05"$	Jul 08	0.10	0	0	16	0	**16**
PKS 2325+093	$23^h27^m33.6^s$	$+09°40'09"$	Aug 09	0.20	1	0	59	0	**60**
PKS 2326-502	$23^h29^m20.9^s$	$-49°55'40"$	Aug 10	0.30	0	0	32	0	**32**
PMN J2331-2148	$23^h31^m4.0^s$	$-21°48'15"$	Jun 09	0.30	0	0	35	0	**35**
SHBL J234333.8+344004	$23^h43^m33.9^s$	$+34°40'04"$	Jun 08	0.30	0	0	74	0	**74**
PMN J2345-1555	$23^h45^m12.5^s$	$-15°55'07"$	Aug 09	1.00	57	0	137	0	**194**
3EG J2352+3752	$23^h49^m20.8^s$	$+38°49'17"$	Jul 08	0.10	0	0	18	0	**18**
PKS 2356-309	$23^h59^m8.0^s$	$-30°37'37"$	Nov 06	0.30	466	192	478	197	**1333**

Table E.1.: All monitoring targets of ATOM (February 2011)

F. Overview of software developed during this thesis

The following tables are giving a short overview over all software developed during this thesis.

At the time of writing, this software is installed not only in Namibia, but also on host `lx26.lsw` and can be used and tested there.

name	purpose	detailed description
`readSensors.py`	read-out hardware sensors (temperature, system load, ...) and stores to database	
`atomPlots`	tool to create different graphs visualizing the data collected via `readSensors.py`	
`readAPCstatus.py`	stores status of UPS in database	
`mispointing.py`	visualize telescope mispointing	2.2.2
`mispointing2.py`	create (shaft encoder value, true AzAlt) coordinate pairs to be used for computing pointing model parameters	2.2.2

Table F.1.: miscellaneus software that does not match more specific categories

name	purpose	described in sec.
`instops`	master process for instrument control (cameras and filter wheel)	2.3.4
`instops_on | _off`	start and stop `instops` server process. Must be run as `root`	
`libEPOS`	C library to control EPOS motor control	2.3.2
`filterwheel`	stand-alone program for low level filterwheel control and diagnostics	
`precipitation`	monitors rain sensor device and communicates to the outside word.	2.4.2
`rainsensor_on | _off`	start and stop `precipitation` server process. Must be run as `root`	

Table F.2.: software used for hardware control

name	purpose	detailed description
`scheduling_info.py`	computes target priorities based on individual target weights, demanded frequency and observing history.	4.1
`targetStatistics.py`	derives statistical information about targets out of database	4.2
`obs_report.py`	list observations of a single night (give date as argument)	
`createComSet`	creates the input file for the robot process	4.1
`skyqual.py`	queries cloud monitor, visualises measurement history and -based on that- stops or restarts observations.	
`startTelescope.py`	opens the enclosure and starts up the telescope.py	
`stopTelescope.py`	kills any ongoing observation and brings ATOM to safe state	
`automaticFlats`	acquire twilight flat field calibration frames	
`exposureStatistics.py`	creates statistics about night sky and dark frames	

Table F.3.: software related to observing

name	purpose	detailed description
`registerFrame.py`	put FITS file under `ADRAS` control	5
`standardRed.py`	make standard image reduction and astrometric calibration	5.1
`photometry.py`	run photometric process and store results in database	5.2
`calibrate.py`	compute photometric zeropoint per frame	5.2.3.
`lightcurve.py`	create lightcurve plots, ASCII tables and issue trigger alerts	5.2.4
`extinction.py`	compute atmospheric extinction parameters	6.1
`structure-function.py`	compute the structure function for a given data set	7.2
`check_reference_star.py`	show histograms of differential photometry of reference stars for one specific target	5.2.3
`create_result_website.py`	creates webpage showing ATOM results	
`deleteFrame.py`	removes FITS file from `ADRAS` .	
`describeFrame.py`	Well. . . , what do you guess?	
`farben.py`	computes star colors as function of airmass	
`getSeeing.py`	visualizes FWHM as function of time	
`getZeropoint.py`	statistics and visualization of photometric zeropoint over different frames	
`showDetections.py`	plot photometric measuremenst over FITS image	
`correlate_HESS_ATOM.py`	compute and show correlations between atmospheric extinction parameters and H.E.S.S. trigger rates	6.3

Table F.4.: software used for data reduction and analysis

G. Test of different aperture types

This is a supplement to the test results shown in section 5.2.1, where the different aperture types of SExtractor are investigated. The histograms in the following are the bases of the summary graphs shown in figures 5.2 and 5.3. The star labels refer to the labels of stars in the vinciny of PKS 2155-304 as indicated in figure 5.1.

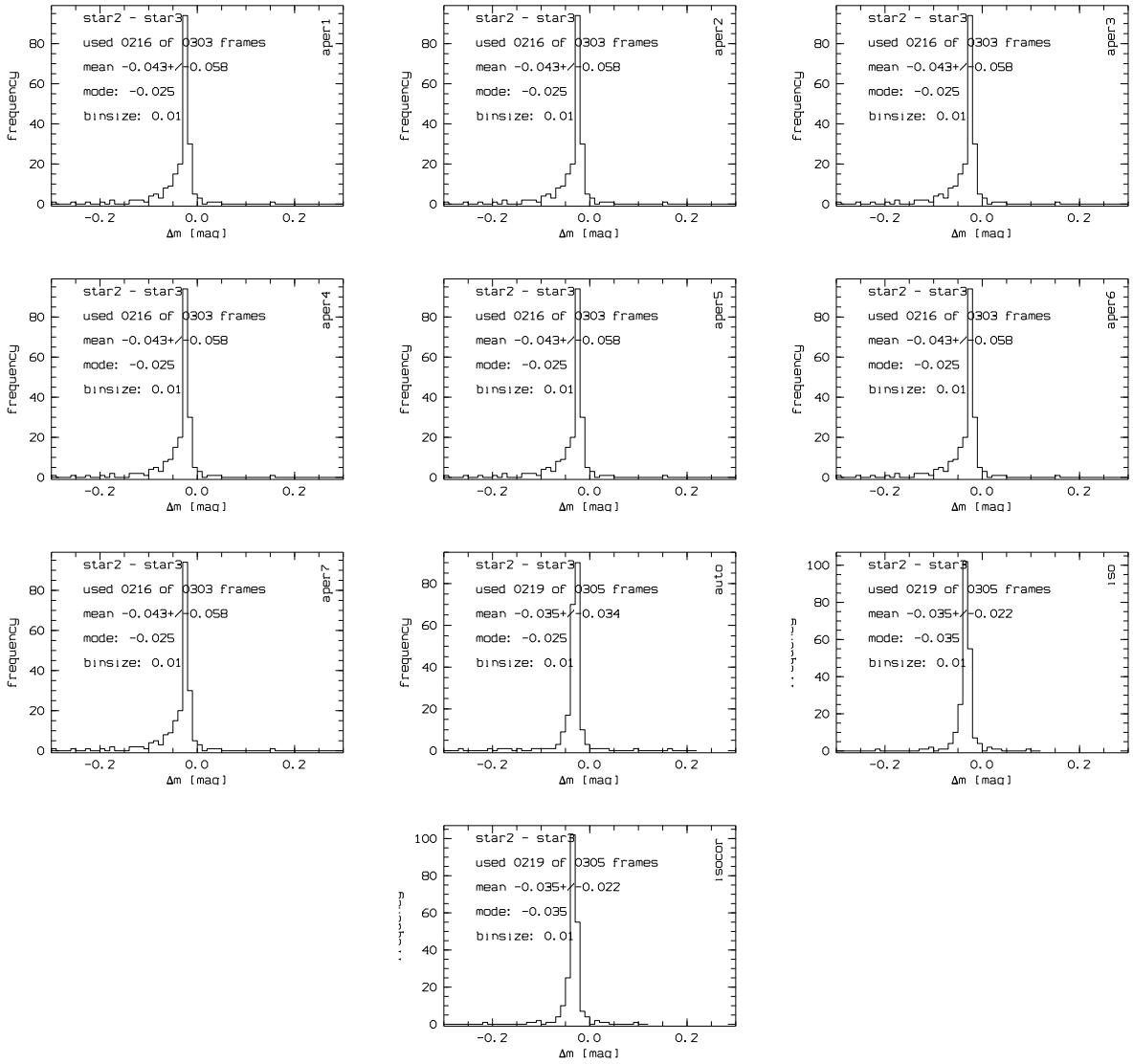

Figure G.1.: star 2 minus star 3 in R band: aperture sizes of 2”, 4”, 6”, 8”, 10”, 15”, 20” fixed diameter and SExtractor specific `auto`, `iso`, and `isocor` variable size apertures.

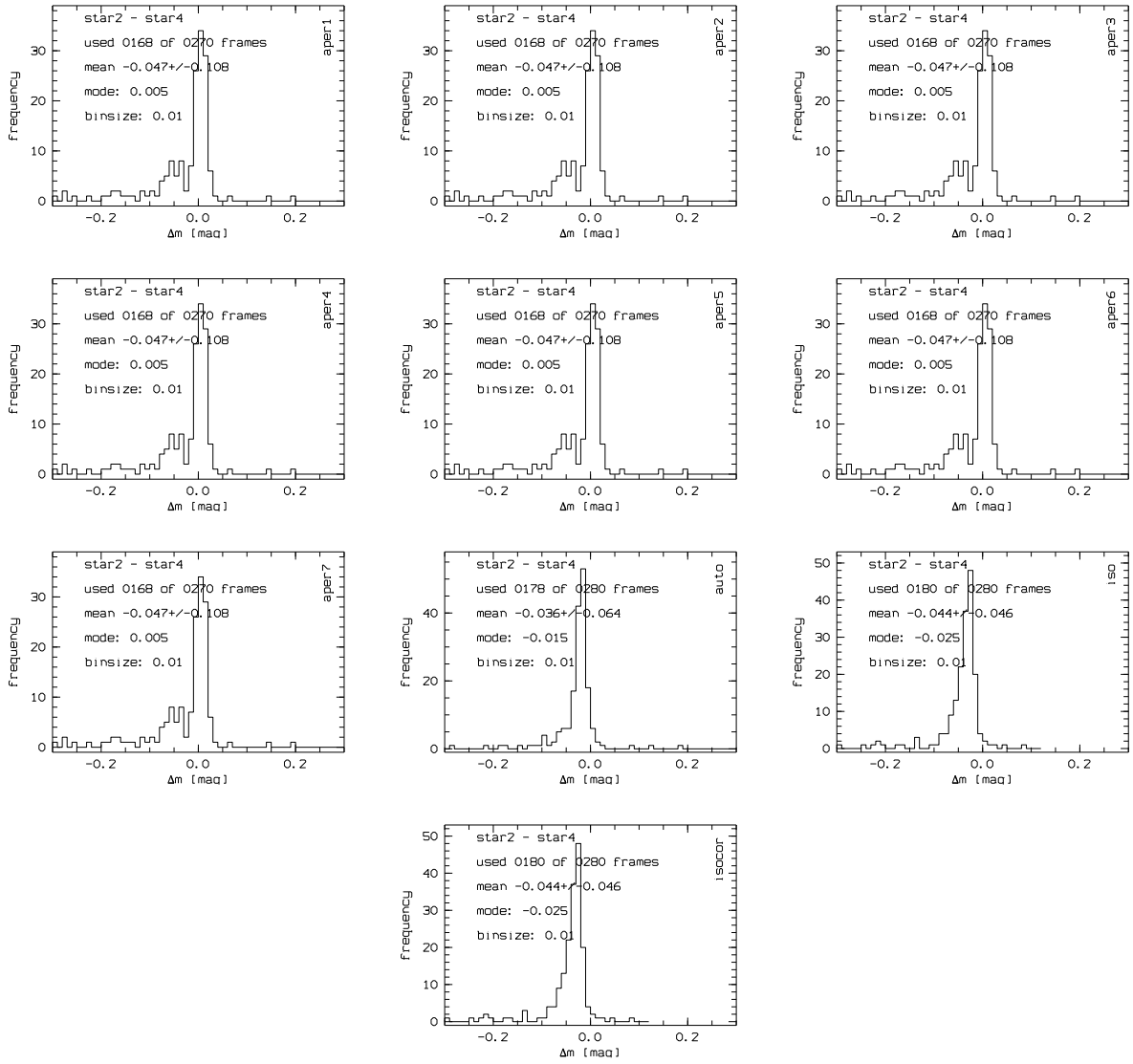

Figure G.2.: Star 2 minus star 4 in R band: aperture sizes of 2”, 4”, 6”, 8”, 10”, 15”, 20” fixed diameter and SExtractor specific `auto`, `iso`, and `isocor` variable size apertures.

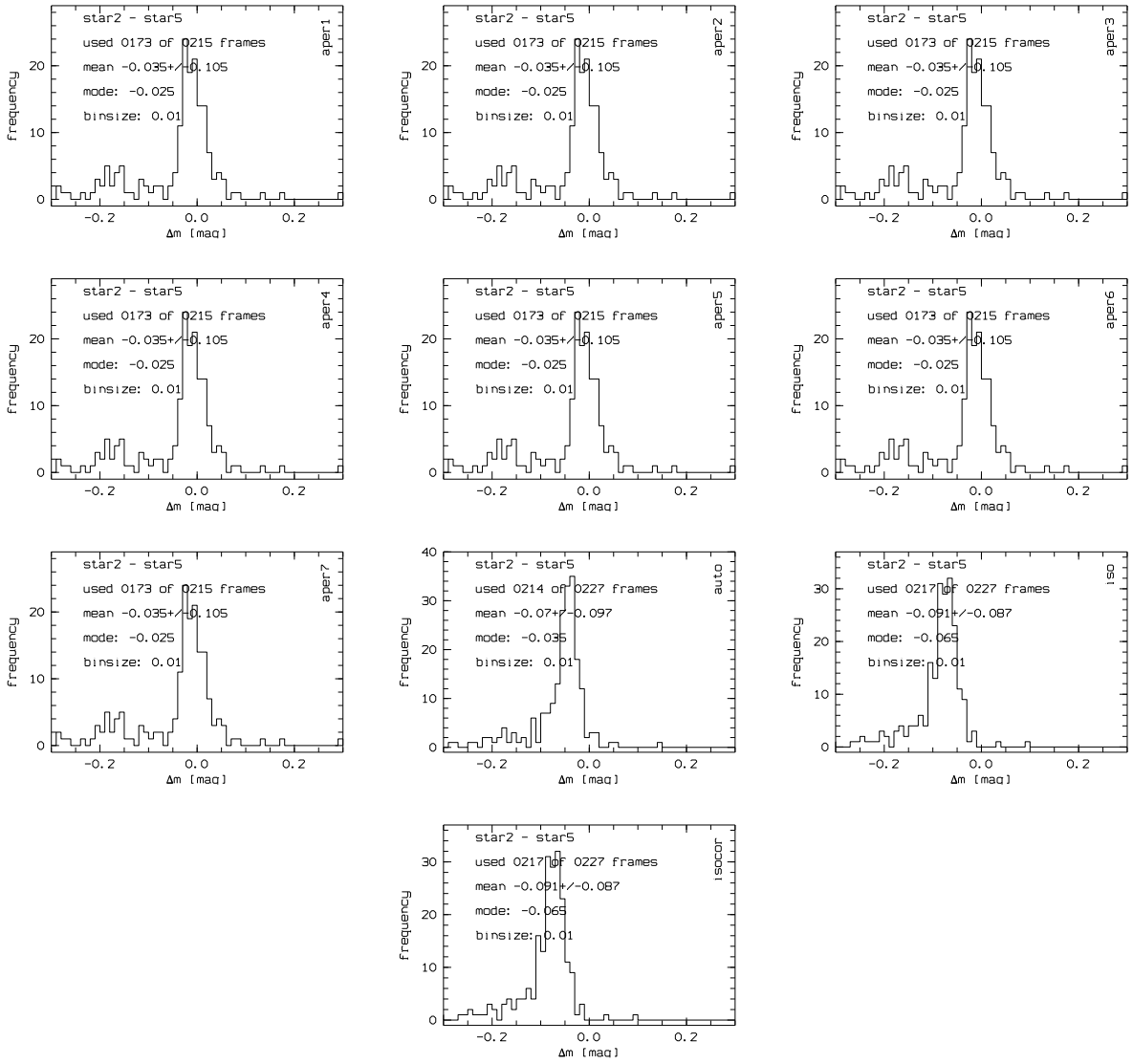

Figure G.3.: star 2 minus star 5 in R band: aperture sizes of 2”, 4”, 6”, 8”, 10”, 15”, 20” fixed diameter and SExtractor specific `auto`, `iso`, and `isocor` variable size apertures.

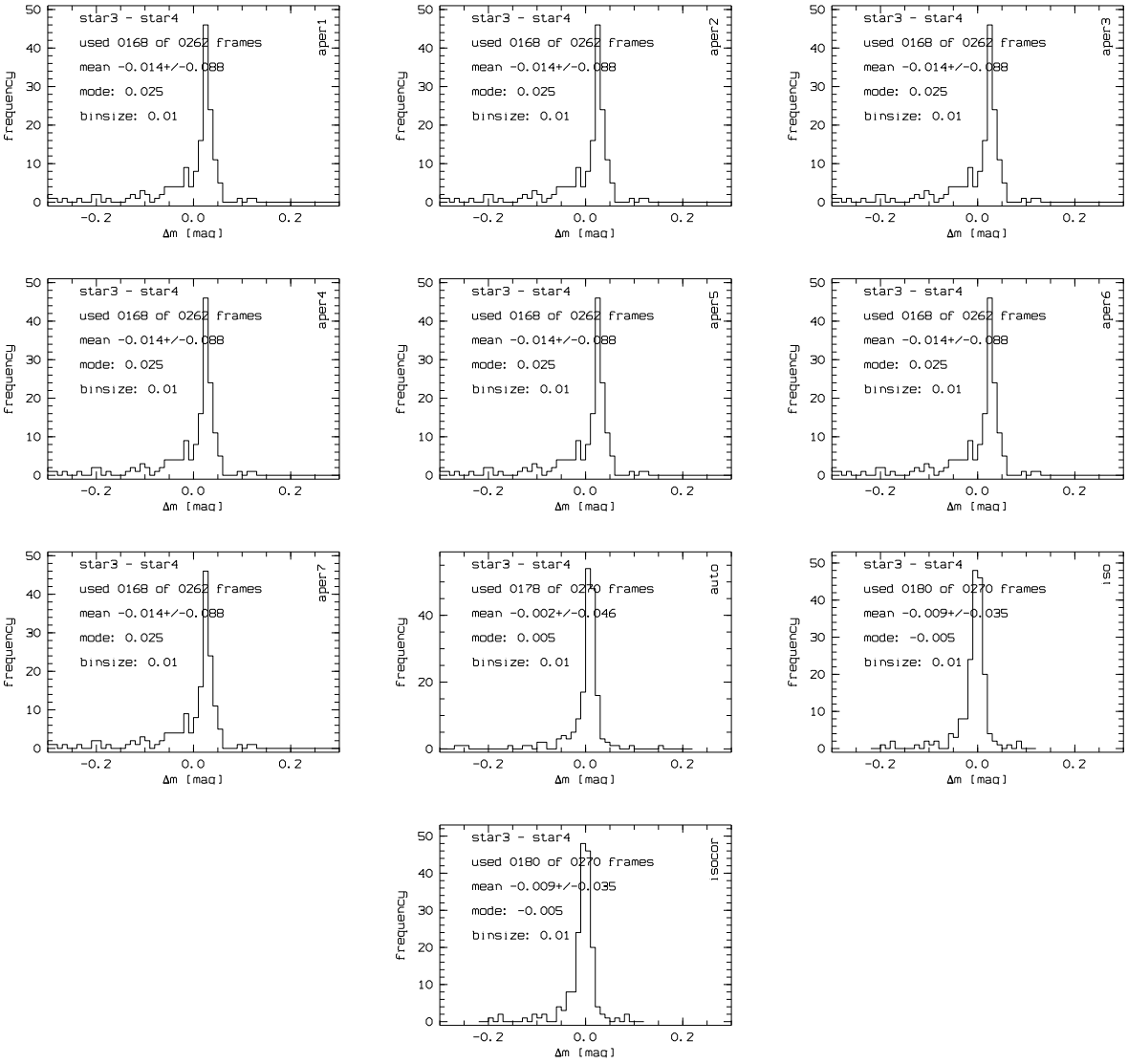

Figure G.4.: star 3 minus star 4 in R band: aperture sizes of 2”, 4”, 6”, 8”, 10”, 15”, 20” fixed diameter and SExtractor specific `auto`, `iso`, and `isocor` variable size apertures.

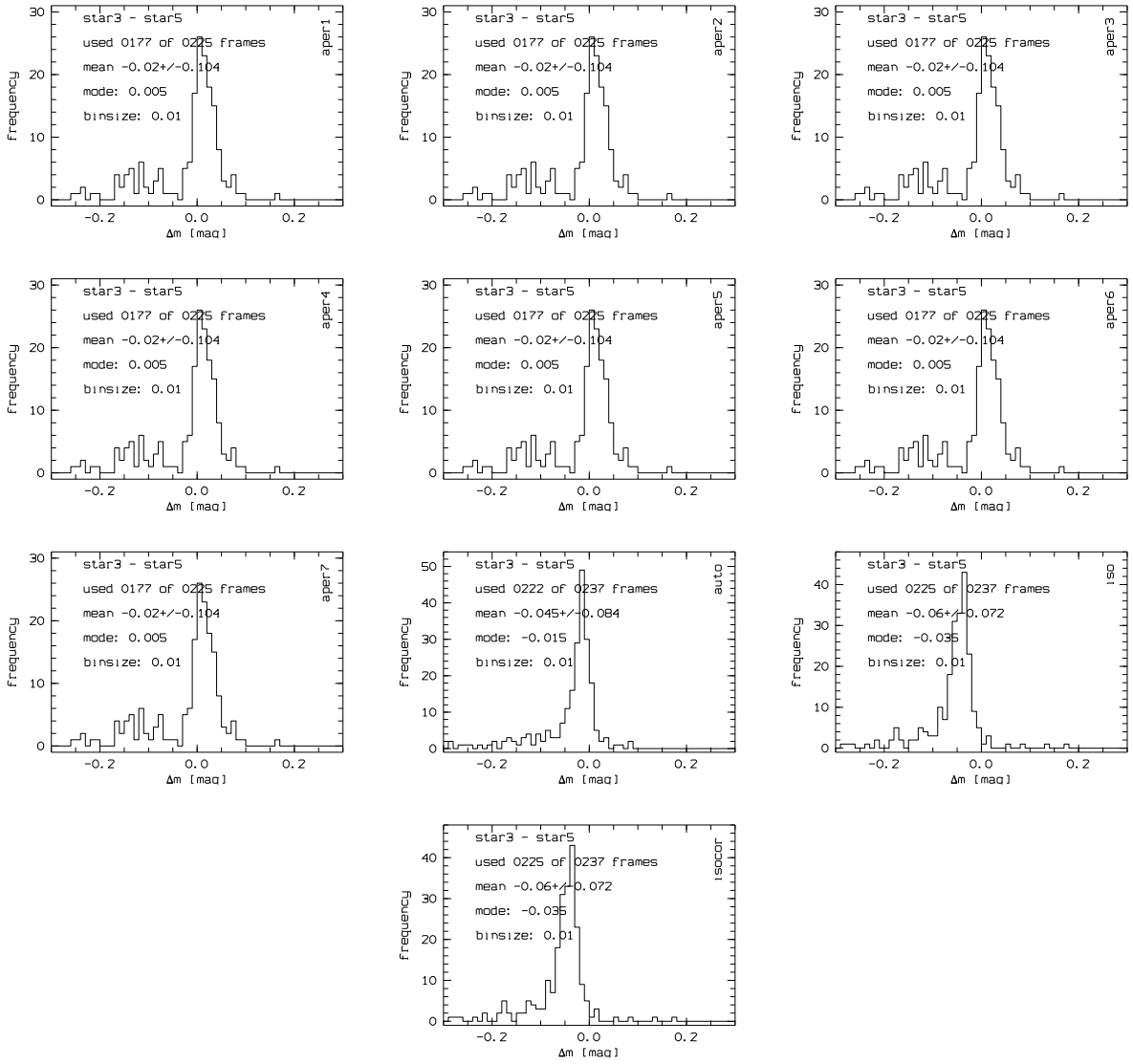

Figure G.5.: star3 minus star star5 in R band: aperture sizes of 2”, 4”, 6”, 8”, 10”, 15”, 20” fixed diameter and SExtractor specific `auto`, `iso`, and `isocor` variable size apertures.

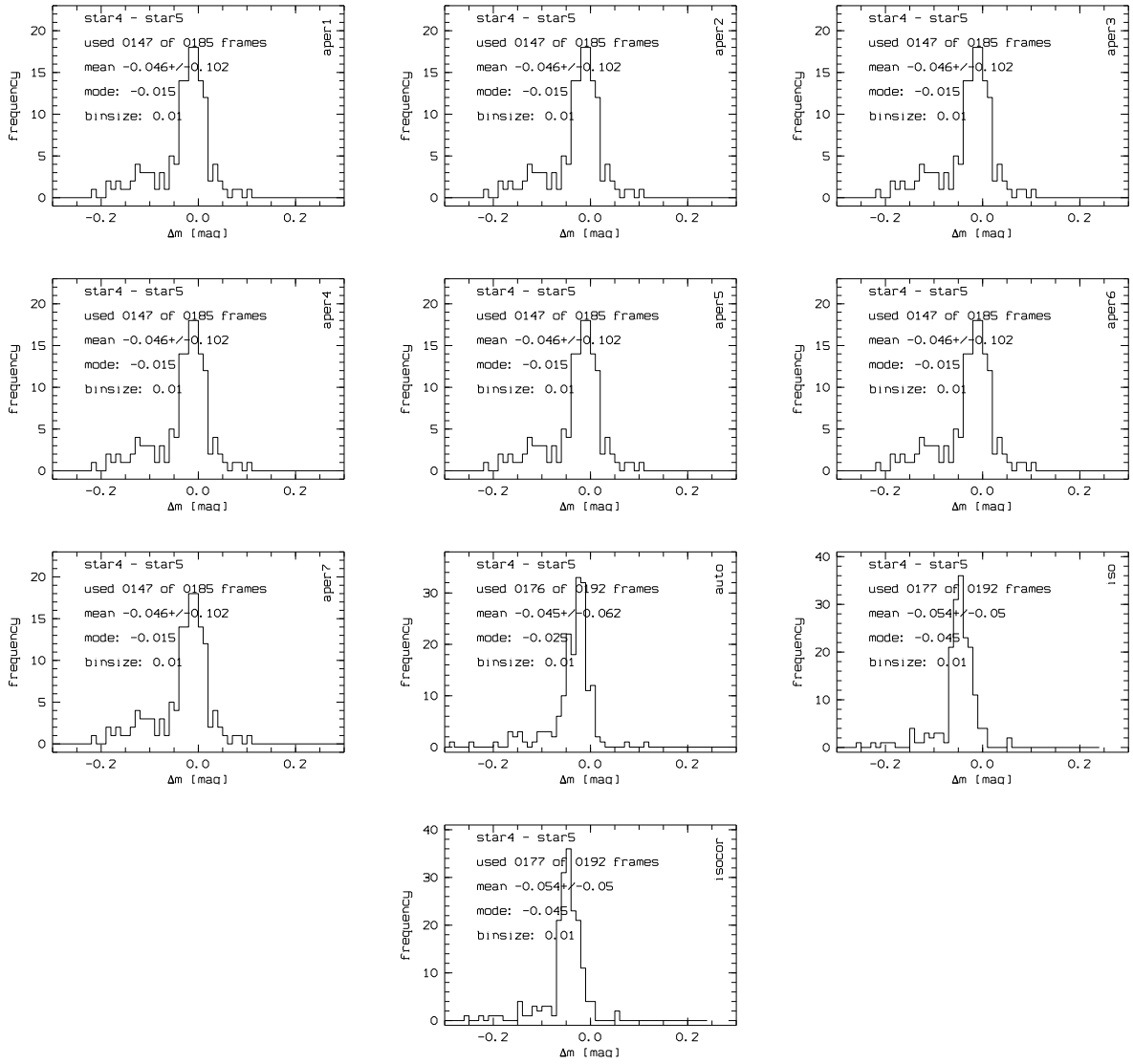

Figure G.6.: star 4 minus star 5 in R band: aperture sizes of 2”, 4”, 6”, 8”, 10”, 15”, 20” fixed diameter and SExtractor specific `auto`, `iso`, and `isocor` variable size apertures.

List of Figures

List of Tables

Index

Bibliography

Each reference is appened by the page numer it is cited in the text.

F. Aharonian, A. G. Akhperjanian, K.-M. Aye, ..., M. Hauser, and et al (H.E.S.S. collaboration). Discovery of VHE gamma rays from PKS 2005-489. A&A, 436:L17–L20, June 2005. doi: 10.1051/0004-6361:200500113. 127

F. Aharonian, A. G. Akhperjanian, A. R. Bazer-Bachi, ..., M. Hauser, and et al (H.E.S.S. collaboration). Observations of the Crab nebula with HESS. A&A, 457:899–915, October 2006. doi: 10.1051/0004-6361:20065351. 15, 16

F. Aharonian, A. G. Akhperjanian, U. Barres de Almeida, ..., M. Hauser, and et al (H.E.S.S. collaboration). New constraints on the mid-IR EBL from the HESS discovery of VHE γ-rays from 1ES 0229+200. A&A, 475:L9–L13, November 2007. doi: 10.1051/0004-6361:20078462. 113

F. Aharonian, A. G. Akhperjanian, U. Barres de Almeida, ..., M. Hauser, and et al (H.E.S.S. collaboration). Discovery of VHE γ-rays from the high-frequency-peaked BL Lacertae object RGB J0152+017. A&A, 481:L103–L107, April 2008. doi: 10.1051/0004-6361:200809603. 113, 125

F. Aharonian, A. G. Akhperjanian, G. Anton, Barres de Almeida, ..., M. Hauser, and et al (H.E.S.S. collaboration). Simultaneous Observations of PKS 2155-304 with HESS, Fermi, RXTE, and Atom: Spectral Energy Distributions and Variability in a Low State. ApJ, 696: L150–L155, May 2009. doi: 10.1088/0004-637X/696/2/L150. 14, 95, 113, 126

I. Appenzeller, K. Fricke, W. Fürtig, W. Gässler, R. Häfner, R. Harke, H.-J. Hess, W. Hummel, P. Jürgens, R.-P. Kudritzki, K.-H. Mantel, W. Meisl, B. Muschielok, H. Nicklas, G. Rupprecht, W. Seifert, O. Stahl, T. Szeifert, and K. Tarantik. Successful commissioning of FORS1 - the first optical instrument on the VLT. *The Messenger*, 94:1–6, December 1998. 99

B. Behera. *Effects of EBL extinction on the VHE spectra of blazars*. PhD thesis, Universität Heidelberg, 2010. 63, 138, 139, 146

A. S. Bennett. The revised 3C catalogue of radio sources. MmRAS, 68:163–+, 1962. 11

K. Bernlöhr. Impact of atmospheric parameters on the atmospheric Cherenkov technique*. *Astroparticle Physics*, 12:255–268, January 2000. doi: 10.1016/S0927-6505(99)00093-6. 16

K. Bernlöhr. Simulation of imaging atmospheric Cherenkov telescopes with CORSIKA and sim_telarray. *Astroparticle Physics*, 30:149–158, October 2008. doi: 10.1016/j.astropartphys.2008.07.009. 16

E. Bertin. *SExtractor users's manual*, 2006. v2.5. 77, 81

E. Bertin and S. Arnouts. SExtractor: Software for source extraction. A&AS, 117:393–404, June 1996. 69, 76

E. Bertin, Y. Mellier, M. Radovich, G. Missonnier, P. Didelon, and B. Morin. The TERAPIX Pipeline. In D. A. Bohlender, D. Durand, & T. H. Handley, editor, *Astronomical Data Analysis Software and Systems XI*, volume 281 of *Astronomical Society of the Pacific Conference Series*, pages 228–+, 2002. 130

M. S. Bessell. UBVRI passbands. PASP, 102:1181–1199, October 1990. 25

M. Böttcher, B. Hivick, J. Dashti, K. Fultz, S. Gupta, C. Gusbar, M. Joshi, A. Lamerato, T. Peery, D. Principe, A. Rajasingam, P. Roustazadeh, and J. Shields. Optical Spectral Variability of the Very High Energy Gamma-ray Blazar 1ES 1011+496. ApJ, 725:2344–2348, December 2010. doi: 10.1088/0004-637X/725/2/2344. 130

M. R. Calabretta and E. W. Greisen. Representations of celestial coordinates in FITS. A&A, 395:1077–1122, December 2002. doi: 10.1051/0004-6361:20021327. 75

F. D'Ammando, S. Vercellone, M. Tavani, G. Pucella, and et al. AGILE detection of the flaring gamma-ray blazar PKS 1510-089. *The Astronomer's Telegram*, 1957:1–+, March 2009. 127

C. D. Dermer and R. Schlickeiser. Model for the High-Energy Emission from Blazars. ApJ, 416: 458–+, October 1993. doi: 10.1086/173251. 12

E2V. *CCD47-10 Backthinned Compact Pack - High Performance AIMO Backthinned CCD Sensor*, June 2000. 24, 29, 38, 59

Eastman Kodak Company. *KAF- 0401E Full-Frame CCD Image Sensor Performance Specification*. Eastman Kodak Company, Rochester, New York 14650-2010, revision no. 0 edition, June 26 2000. 29, 54

D. Emmanoulopoulos. *Nonlinear Time Series Analysis of BL Lac Light Curves*. PhD thesis, Universität Heidelberg, 2007. 146

B. L. Fanaroff and J. M. Riley. The morphology of extragalactic radio sources of high and low luminosity. MNRAS, 167:31P–36P, May 1974. 11

G. Fossati, L. Maraschi, A. Celotti, A. Comastri, and G. Ghisellini. A unifying view of the spectral energy distributions of blazars. MNRAS, 299:433–448, September 1998. doi: 10.1046/j.1365-8711.1998.01828.x. 12

E. W. Greisen and M. R. Calabretta. Representations of world coordinates in FITS. A&A, 395: 1061–1075, December 2002. doi: 10.1051/0004-6361:20021326. 75

M. Hamuy and J. Maza. UBVRI photoelectric photometry in the fields of fifteen active galaxies. AJ, 97:720–725, March 1989. doi: 10.1086/115017. 76, 78

W. E. Harris, M. P. Fitzgerald, and B. C. Reed. Photoelectric photometry - an approach to data reduction. PASP, 93:507–517, August 1981. 99, 100

M. Hauser. *ATOM user manual*. Landessternwarte Heidelberg, 2006. 18, 30, 73

M. Hauser. *libEPOS - a linux SDK for the EPOS device*. LSW, 2006. http://www.lsw.uni-heidelberg.de/users/mhauser/libEPOS/. 25

M. Hauser, B. Behera, H. Hagen, and S. Wagner. Detection of an optical flare from PKS 2052-474. *The Astronomer's Telegram*, 2158:1–+, August 2009a. 146

M. Hauser, H. Hagen, and S. Wagner. Detection of an optical flare from 3EG J1429-4217. *The Astronomer's Telegram*, 2103:1–+, June 2009b. 136, 146

M. Hauser, H. Hagen, and S. Wagner. Detection of an optical flare from blazar PKS 1424-41. *The Astronomer's Telegram*, 2613:1–+, May 2010a. 126, 146

M. Hauser, S. Wagner, and H. Hagen. Detection of an optical flare from PKS 1222+216 (4C 21.35). *The Astronomer's Telegram*, 2436:1–+, February 2010b. 146

S. E. Healey, R. W. Romani, G. Cotter, P. F. Michelson, E. F. Schlafly, A. C. S. Readhead, P. Giommi, S. Chaty, I. A. Grenier, and L. C. Weintraub. CGRaBS: An All-Sky Survey of Gamma-Ray Blazar Candidates. ApJS, 175:97–104, March 2008. doi: 10.1086/523302. 129

HESS Collaboration, A. Abramowski, F. Acero, F. Aharonian, ..., M. Hauser, and et al. Multi-wavelength observations of H 2356-309. A&A, 516:A56+, June 2010. doi: 10.1051/0004-6361/201014321. 113, 126

HESS Collaboration, A. Abramowski, F. Acero, F. Aharonian, ..., M. Hauser, and et al. Simultaneous multi-wavelength campaign on pks 2005-489 in a high state. A&A, 2011. accepted. 127

J. A. Hinton. The status of the HESS project. *New Astronomy Review*, 48:331–337, April 2004. doi: 10.1016/j.newar.2003.12.004. 15

D. Hoffleit and C. Jaschek. *The Bright Star Catalogue*. The Bright Star Catalogue, New Haven: Yale University Observatory (4th edition), 1982, 1982. 65

B. Holwerda. *Sextractor for Dummies*, 2006. http://www-int.stsci.edu/~holwerda/Guide2source_extractor.pdf. 76

F. James. MINUIT - function minimization and error analysis. CERN Program Library Long Writeup D506, 1998. 100

K. I. Kellermann, R. Sramek, M. Schmidt, D. B. Shaffer, and R. Green. VLA observations of objects in the Palomar Bright Quasar Survey. AJ, 98:1195–1207, October 1989. doi: 10.1086/115207. 10

Brian W. Kernighan and Dennis M. Ritchie. *The C programming language*. Prentice-Hall software series. Prentice-Hall, Englewood Cliffs, N.J., 2. ed. edition, 1988. ISBN 0-13-110362-8 ; 0-13-110370-9. 43

A. U. Landolt. UBVRI photometric standard stars in the magnitude range 11.5-16.0 around the celestial equator. AJ, 104:340–371, July 1992. doi: 10.1086/116242. 99, 111

F. Longo, G. Iafrate, E. Hays, and M. Marelli. Fermi LAT detection of increasing gamma-ray activity of blazar PKS 1424-418. *The Astronomer's Telegram*, 2104:1–+, June 2009. 136, 146

K. Mannheim and P. L. Biermann. Gamma-ray flaring of 3C 279 - A proton-initiated cascade in the jet? A&A, 253:L21–L24, January 1992. 12

K. Mannheim, P. L. Biermann, and W. M. Kruells. A novel mechanism for nonthermal X-ray emission. A&A, 251:723–731, November 1991. 12

L. Maraschi, G. Ghisellini, and A. Celotti. A jet model for the gamma-ray emitting blazar 3C 279. ApJ, 397:L5–L9, September 1992. doi: 10.1086/186531. 12

maxon motors. *EPOS 24/1 Communication Guide*. maxon motors, january 2005 edition, a. 28

maxon motors. *EPOS Firmware Specification*. maxon motors, april 2006 edition, b. 30

maxon motors. *EPOS 24/1 Hardware reference*. maxon motors, february 2006 edition, c. 30

D. Mills. *Apogee camera driver - Linux User Guide*. The Random Factory, Tucson, AZ, USA, 2005. 24, 28, 30, 59

D. J. Mink. WCSTools: Image World Coordinate System Utilities. In *ASP Conf. Ser. 125: Astronomical Data Analysis Software and Systems VI*, pages 249–+, 1997. 75

D. J. Mink. WCSTools 4.0: Building Astrometry and Catalogs into Pipelines. In C. Gabriel, C. Arviset, D. Ponz, & S. Enrique, editor, *Astronomical Data Analysis Software and Systems XV*, volume 351 of *Astronomical Society of the Pacific Conference Series*, pages 204–+, July 2006. 75

D. B. A. Monet, B. Canzian, C. Dahn, H. Guetter, H. Harris, A. Henden, S. Levine, C. Luginbuhl, A. K. B. Monet, A. Rhodes, B. Riepe, S. Sell, R. Stone, F. Vrba, and R. Walker. The USNO-A2.0 Catalogue (Monet+ 1998). *VizieR Online Data Catalog*, 1252:0–+, October 1998. 76, 90

D. G. Monet, S. E. Levine, B. Canzian, H. D. Ables, A. R. Bird, C. C. Dahn, H. H. Guetter, H. C. Harris, A. A. Henden, S. K. Leggett, H. F. Levison, C. B. Luginbuhl, J. Martini, A. K. B. Monet, J. A. Munn, J. R. Pier, A. R. Rhodes, B. Riepe, S. Sell, R. C. Stone, F. J. Vrba, R. L. Walker, G. Westerhout, R. J. Brucato, I. N. Reid, W. Schoening, M. Hartley, M. A. Read, and S. B. Tritton. The USNO-B Catalog. AJ, 125:984–993, February 2003. doi: 10.1086/345888. 76

M. Mose Mariotti. MAGIC detects a VHE flare from 4C +21.35 (PKS 1222+21). *The Astronomer's Telegram*, 2684:1–+, June 2010. 128

A. Mücke, R. J. Protheroe, R. Engel, J. P. Rachen, and T. Stanev. BL Lac objects in the synchrotron proton blazar model. *Astroparticle Physics*, 18:593–613, March 2003. doi: 10.1016/S0927-6505(02)00185-8. 12

Andreas Müller. *Black Hole Astrophysics : Magnetohydrodynamics on the Kerr Geometry*. PhD thesis, Universität Heidelberg, http://www.ub.uni-heidelberg.de/archiv/5217, 2005. 13

M. Newberry. Measuring the gain of a ccd camera. Technical report, Axres, 1998. URL www.axres.com/technote1.html. 40

R. A. Ong. VERITAS Reports Markarian 421 in a High Flaring State. *The Astronomer's Telegram*, 2443:1–+, February 2010. 113

D. E. Osterbrock and R. W. Pogge. Optical spectra of narrow emission line Palomar-Green galaxies. ApJ, 323:108–117, December 1987. doi: 10.1086/165810. 127

N. Patat. Photometric solutions via one-step multilinear least squares fit. http://www.eso.org/observing/dfo/quality/FORS1/qc/photcoeff/photcoeff.ps, September 2000. 99, 102

M. J. Person, J. L. Elliot, A. S. Bosh, A. A. S. Gulbis, R. Jensen-Clem, M. F. Lockhart, A. M. Zangari, C. A. Zuluaga, S. E. Levine, J. M. Pasachoff, S. P. Souza, M. Lu, C. Malamut, P. Rojo, C. D. Bailyn, R. K. D. MacDonald, K. M. Ivarsen, D. E. Reichart, A. P. LaCluyze, M. C. Nysewander, and J. B. Haislip. Pluto's Atmosphere from the July 2010 Stellar Occultation. In *AAS/Division for Planetary Sciences Meeting Abstracts #42*, volume 42 of *Bulletin of the American Astronomical Society*, pages 983–+, October 2010. 176

M. Pohl and R. Schlickeiser. On the conversion of blast wave energy into radiation in active galactic nuclei and gamma-ray bursts. A&A, 354:395–410, February 2000. 12

G. Pühlhofer, S. Demgen, M Hauser, S. Wagner, J. Pforr, and W. Maneschg. Results and questions to andor about the ixon dv 887, arising from tests performed at lsw heidelberg. Technical report, Landessternwarte Heidelberg, Sep 2004. 41

B. Sicardy, F. Colas, L. Maquet, ..., M. Hauser, S. Wagner, and et.al. The 2010, February 19 stellar occultation by Varuna. In *AAS/Division for Planetary Sciences Meeting Abstracts #42*, volume 42 of *Bulletin of the American Astronomical Society*, pages 993–+, October 2010. 176

J. H. Simonetti, J. M. Cordes, and D. S. Heeschen. Flicker of extragalactic radio sources at two frequencies. ApJ, 296:46–59, September 1985. doi: 10.1086/163418. 119

N. Smith, A. O'Connor, J. Howard, A. Giltinan, S. O'Driscoll, S. Wagner, and M. Hauser. Observations of blazars using EMCCD technology. In C. M. Raiteri and M. Villata, editors, *Proceedings of the Second ENIGMA Meeting*, pages 13–25, November 2003. 41

N. Smith, C. Coates, A. Giltinan, J. Howard, A. O'Connor, S. O'Driscoll, M. Hauser, and S. Wagner. EMCCD technology and its impact on rapid low-light photometry. In J. D. Garnett and J. W. Beletic, editors, *Society of Photo-Optical Instrumentation Engineers (SPIE) Conference Series*, volume 5499 of *Society of Photo-Optical Instrumentation Engineers (SPIE) Conference Series*, pages 162–172, September 2004. doi: 10.1117/12.549789. 41

F. Tavecchio, L. Maraschi, and G. Ghisellini. Constraints on the Physical Parameters of TeV Blazars. ApJ, 509:608–619, December 1998. doi: 10.1086/306526. 12

C. M. Urry and P. Padovani. Unified Schemes for Radio-Loud Active Galactic Nuclei. PASP, 107:803–+, September 1995. doi: 10.1086/133630. 10, 11, 12

M. Villata, C. M. Raiteri, L. Lanteri, G. Sobrito, and M. Cavallone. BVR photometry of comparison stars in selected blazar fields. I. Photometric sequences for 10 BL Lacertae objects. A&AS, 130:305–310, June 1998. doi: 10.1051/aas:1998415. 114

S. Wagner and M. Hauser. Relations between optical synchrotron and gamma-ray variability. In *38th COSPAR Scientific Assembly*, volume 38 of *COSPAR, Plenary Meeting*, pages 2258–+, 2010. 138

S. J. Wagner. Fast flares of blazars during gamma-ray observations. Optical - gamma-ray correlations. A&AS, 120:C495+, December 1996. 138

S. J. Wagner and HESS collaboration. Detection of VHE Gamma-ray Emission from a Type 1 Quasar. In *AAS/High Energy Astrophysics Division no.11*, volume 11 of *AAS/High Energy Astrophysics Division*, pages 27.06–+, February 2010. 127

N. Zacharias, D. G. Monet, S. E. Levine, S. E. Urban, R. Gaume, and G. L. Wycoff. The Naval Observatory Merged Astrometric Dataset (NOMAD). In *American Astronomical Society Meeting Abstracts*, volume 36 of *Bulletin of the American Astronomical Society*, pages 1418–+, December 2004a. 76, 90

N. Zacharias, S. E. Urban, M. I. Zacharias, G. L. Wycoff, D. M. Hall, D. G. Monet, and T. J. Rafferty. The Second US Naval Observatory CCD Astrograph Catalog (UCAC2). AJ, 127: 3043–3059, May 2004b. doi: 10.1086/386353. 75

Danke!

Es ist nicht nur ein schöner Brauch, am Ende einer Arbeit „Danke“ zu sagen, sondern es ist mir auch ein Bedürfnis! Danke an alle, die zum letztendlichen Gelingen dieser Arbeit beigetragen haben!

Meinem Doktorvater Prof. Stefan Wagner für das interessante Thema, die langjährige Betreuung und die Möglichkeit, ATOM zu einem nützlichen Werkzeug für die H.E.S.S.-*community* zu machen. Und insbesondere auch für die immer mal wieder notwendigen Erinnerungen, neben der ganzen Instrumentrierungsarbeit die Astrophysik nicht zu vergessen.

Bedanken möchte ich mich auch bei Herrn Prof. Werner Hofmann für das Erstellen des Zweitgutachtens, sowie den Herren Prof. Wambsganß und Priv. Doz. Heidt für ihre Bereitschaft, meiner Prüfungskommision anzugehören.

Dr. Hans-Jürgen Hagen und Manfred Knoll von der Hamburger Sternwarte, die das Teleskop mit ihrer neuen Hard- und Software wieder zum Leben erweckt haben. Hans, ein ganz spezielles „Danke schön!“ an Dich für Deine Bereitschaft, mir im Laufe der Jahre bei allen aufgetretenen Problemen mit der Teleskopsteuerung mit Rat und Tat zur Seite zu stehen.

Nicht vergessen darf ich natürlich die Mechanikwerkstatt der LSW, insbesondere Ludwig Schäffner und Lutz Geuer. Eure Mitarbeit und die vielen Diskussionen und Ratschläge am Anfang der Arbeit zu dem Umbau des Teleskops und dem Aufbau des Instruments (und dessen Fertigung) waren wichtig! Ohne eure Hilfe hätte der Ab- und Aufbau in Heidelberg und Hamburg, und letztendlich der Zusammenbau und die Inbetriebnahme in Namibia nie so erfolgreich stattfinden können.

Vielen Dank auch an die Kollegen in Namibia: Toni Hanke, Albert Jahnke, Eben Tjingaete und Maveipi Kandji. Ein Teleskop über tausende Kilometer Entfernung zu betreiben funktioniert leider trotz aller Automatisierung nicht, wenn nicht von Zeit zu Zeit jemand vor Ort Hand anlegt, um das Eine oder Andere *„Wehwehchen“* zu beheben. Und dabei konnte ich mich immer auf euch verlassen! Und die gemeinsam durchgeführten Messreihen zur Bestimmung des Einflusses verschiedener thermischer Behandlungsverfahren auf die kulinarische Qualität von Teilen der namibianischen Fauna bleiben unvergessen.

Hier müsste jetzt eigentlich noch eine ganze Reihe von Namen kommen... liebe Freunde, seit großzügig und erlaubt mir, das so zusammenzufassen: Ich danke allen lieben Leuten aus dem Institut, meinen Freunden und Familie, für die ideelle Unterstützung während meiner *etwas* längeren Promotionszeit. Die vereinzelten Sticheleien sind entsprechend angekommen, und letztendlich haben auch sie dazu geführt, daß diese Arbeit jetzt fertig ist.

I thank all *contributers to the Debian GNU/Linux operating system* for making it that stable. Thanks also to *RMS and the Free Software Foundation* for providing the mighty editor *Emacs*. This research has made use of NASA's Astrophysics Data System, of the SIMBAD database, operated at CDS, Strasbourg, France and of SAOImage DS9, developed by Smithsonian Astrophysical Observatory.